Physical Chemistry in Action

Fabien Gatti *Editor*

Molecular Quantum Dynamics

From Theory to Applications

Springer

Physical Chemistry in Action

For further volumes:
http://www.springer.com/series/10915

Fabien Gatti
Editor

Molecular Quantum Dynamics

From Theory to Applications

Springer

Editor
Fabien Gatti
Institut Charles GERHARDT - CNRS 5253
Université Montpellier 2
Montpellier Cedex
France

ISSN 2197-4349 ISSN 2197-4357 (electronic)
ISBN 978-3-642-45289-5 ISBN 978-3-642-45290-1 (eBook)
DOI 10.1007/978-3-642-45290-1
Springer Heidelberg New York Dordrecht London

Library of Congress Control Number: 2014931787

Printed on acid-free paper

Springer is part of Springer Science+Business Media (www.springer.com)

Foreword

The word *dynamics* stands for motion as opposed to *statics* and being quantum and related to molecules implies that in this book the Schrödinger equation in its time-dependent form provides the central framework. In recent decades quantum dynamics has become an enormously diverse and active field of research ranging from entangled photons to biologically relevant response to laser light, covering thereby many, partly new, areas as cold atoms and molecules, Bose–Einstein condensates, atoms and molecules in external fields, coherent control of molecules, ultrafast processes like charge migration and energy transfer mediated by electron correlation, attosecond physics and may be also attosecond chemistry, and more. The availability of new light sources like free electron lasers and attosecond pulses produced via high-harmonic generation enlarge the range of possible quantum dynamics to be studied and pose further substantial requirements on the development of suitable theoretical methods. One should be aware that the high-harmonic generation itself is a quantum dynamics phenomenon.

At least in chemistry and biology, *structure* plays a major role within the realm of statics. Here, *complexity* typically tends to grow with the size of the system. This contrasts dynamics, in particular quantum dynamics, where complexity depends also on the forces leading to the dynamics. For instance, even the situations of hydrogen atoms in strong external crossed electric and magnetic fields or exposed to the intense free electron laser field represent nontrivial dynamics problems, while the same problems in weak fields are rather straightforward to solve. In quantum dynamics the measurement itself also adds to the complexity of the problem. To investigate the dynamics, one would, of course, like to follow it as a function of time. In femto-chemistry and several areas of physics this has been successfully achieved in many cases by employing so-called pump-probe methods. The field of time-dependent measurements is still in its infancy when one wishes to probe the faster electronic motion of atoms and molecules after a perturbation and, in particular, if the system is exposed to intense light.

Molecules are composed of *electrons and nuclei* and one often tends to forget that all of them participate in the dynamics. This stems from the Born–Oppenheimer approximation which is a milestone in the theory of molecules and of electronic matter in general. The much larger masses of the nuclei compared to that of electrons allow for an approximate separation of the electronic and nuclear motions, and this separation simplifies the quantum as well as classical treatment of molecules

substantially. One should be aware that even the notion of molecular electronic states is connected to this approximation. This approximation has been extremely useful in numerous applications and is generally widely applied. It has become a standard reference even in cases where it fails. And, indeed, this approximation does fail, often severely, in particular for polyatomic molecules whenever the potential energy surfaces belonging to different electronic states (defined by this approximation!) come close to each other. The most dramatic failure is encountered when these surfaces exhibit so-called conical intersections and the coupled motion on these surfaces has to be considered as well described in this book. Interestingly, one can express the *exact* wavefunction (or wavepacket) of the system as a product of electronic and nuclear wavefunctions and thus separate the respective motions exactly, but such an approach is nowadays still more complicated than solving the coupled equations for the coupled motion.

As long as only a few electronic states are excited and thus participate in the dynamics, one can solve the coupled electronic-nuclear dynamics by expanding the total wavepacket in the space of these electronic states (see also this book). Owing to advent of *ultrashort pulses*, many electronic states can be populated by such pulses and the description of the quantum dynamics, for instance, the ensuing hole migration, becomes extremely complicated. Here and in similar situations, the electronic and nuclear dynamics have to be described hand in hand when the process of observation exceeds the short time period at which only the electrons undergo motion and the nuclear motion did not set in yet. Treating both motions quantum dynamically is an important goal of future work. First steps have already been taken, for example, treating both kinds of motion within a fully time-dependent Born–Oppenheimer approximation and beyond.

This book covers a collection of important topics where *chemistry and physics* overlap. In most cases the methods and approaches employed are more physics-like, while the questions asked are more chemistry. In all these topics—excellently put into the frame of the book title in the introduction—quantum effects play a central role and the objects of study are molecules. The body of the book starts with gaining quantum insight into catalysis, a highly relevant subject in experimental chemistry, continues with tunneling and chemical reactions, comes to the subjects of vibrational and vibronic spectroscopies and the underlying quantum dynamics, and moves through non-adiabatic photodynamics and photochemistry phenomena to arrive at the control of molecular processes and the dynamics of molecular quantum computing. All in all, a collection of subjects which cannot be left out of a book with the title molecular quantum dynamics.

From the introduction chapter of the book and my short analysis displayed above, I anticipate that quantum dynamics is not only an exciting subject currently, but also has an enormous future potential. And, since molecules are the building blocks of everyday's life, molecular quantum dynamics will have a growing portion in the quantum dynamics world.

Heidelberg, Germany Lorenz Cederbaum
February 2014

Preface

Molecular quantum dynamics is an emerging field at the border between quantum physics and chemistry. There is growing evidence that a significant number of chemical reactions are impacted by strong quantum-mechanical effects and, even more importantly, that these quantum effects, such as quantum coherence, could be used to create radically new technologies involving molecular systems. For instance, since the invention of lasers, it has become a dream in chemistry to use these coherent sources for triggering photochemical reactions selectively and efficiently. In traditional industrial chemistry, this is achieved by adjusting external parameters such as temperature, pressure, concentration, and solvent, or by adding catalysts. In general, much energy is wasted and many undesired by-products are created, which may have negative effects on the environment. In this context, laser light offers the possibility to deposit energy in a molecule and to trigger chemical reactions in a fully controlled fashion and in a much cleaner and energetically efficient way.

Since the advent of femtochemistry, the possibility to manipulate chemical reactivity by excitation with laser pulses has already been experimentally demonstrated for several reactions in the gas phase and on surfaces. For instance, the excitation of the stretching modes of vibration of CH_4 accelerates the C–H bond breaking on a surface of Ni(100). But a precise control of quantum effects in molecular processes still remains challenging due to the large number of vibrational and rotational degrees of freedom that can rapidly dissipate the quantum coherence. However, major experimental developments have been achieved recently: the possibility to align and even orientate molecules in two or three dimensions and attospectroscopy that allows one to generate sub-femtosecond laser pulses for observing electrons on their natural time scale. The conjunction of femto- and atto-chemistry and of the alignment of molecules lets us hope that it will be possible to reach a much higher level of control of chemical reactivity at its most fundamental level including the quantum effects that govern the microscopic realm.

In addition, during the last 20 years, tremendous progress has been made in the development and applications of theoretical approaches to the full quantum-mechanical study of molecular processes. This development has been made possible by the availability of powerful workstations and massively parallel computers and even more importantly by the design of new and more efficient algorithms to solve the Schrödinger equation. Perhaps the most significant result of this is that full quantum-mechanical simulations have allowed the correct interpretation

of major experimental findings. This is the aim of the present book, written by theoreticians, to provide some illustrations in a wide range of areas: heterogeneous catalysis, reactive scattering, photodissociation, infrared or ultraviolet spectroscopy, photochemistry guided by laser pulses, and quantum computing.

I thank all the authors for their excellent contributions and the French National Centre for Scientific Research (CNRS) for its continuous support to this field. Finally, I am grateful to Tobias N. Wassermann from Springer Verlag for his constructive help and his efficiency.

Montpellier, France Fabien Gatti
November 2013

Contents

Introduction and Conceptual Background

1

Fabien Gatti and Benjamin Lasorne

Molecular Quantum Dynamics, often called "Quantum Dynamics," is the subfield of Theoretical Chemistry where both the electrons and the nuclei of a molecular system are treated with a quantum-mechanical approach. Molecular Quantum Dynamics can be seen as the encounter of Quantum Physics and Chemistry.

In general, the realm of quantum phenomena is not directly connected to chemistry but rather to physics, for instance atomic physics and quantum optics. These are domains that are now well understood and controlled, as recognized by the Nobel Prize in Physics 2012 awarded to Serge Haroche and David Jeffrey Wineland. Quantum mechanics deals with physical phenomena at the microscopic level, precisely where the action is of the order of magnitude of the Planck constant [1–7]. One of the most intriguing features of quantum mechanics is, as indicated by its name, the hypothesis of quantization. This notion implies that, under some particular conditions, physical observables measured experimentally can only take certain discrete values. These happen to be the eigenvalues of the operator associated with the physical observable. Another fundamental principle of quantum mechanics is the superposition principle, which holds that a quantum system can be in several eigenstates simultaneously. Formally, the corresponding wavefunction can be written as a linear superposition of several eigenfunctions of the operator corresponding to a given physical quantity. In particular, if the observable is the energy, such a linear combination will imply that the probability density, given by the square modulus of the normalized wavefunction at each point in space, will depend on time. The wavefunction is then referred to as a wavepacket, i.e., a coherent superposition of several eigenstates. When the physical quantity is measured, the wavepacket collapses. This results in the observation of only one of the possible eigenvalues. If there is no measurement, and if the system is isolated,

F. Gatti (✉) • B. Lasorne
Institut Charles Gerhardt Montpellier - CNRS - Université Montpellier 2, CC 15001 Place Eugène Bataillon, 34095 Montpellier, France
e-mail: gatti@univ-montp2.fr; blasorne@univ-montp2.fr

F. Gatti (ed.), *Molecular Quantum Dynamics*, Physical Chemistry in Action,
DOI 10.1007/978-3-642-45290-1_1, © Springer-Verlag Berlin Heidelberg 2014

the different components of the quantum superposition can interfere. This yields new properties that can be measured and that have no classical counterpart. This is illustrated by the famous Schrödinger cat that can be alive and dead simultaneously. In other words, the Schrödinger cat can be in a coherent superposition of both a dead state and an alive state. These two states can interfere to create new behaviors that cannot be observed for a cat that is either alive or dead. The Schrödinger cat can be seen as a paradox only because the cat is large-scale system and creating such a coherent superposition for a cat is not realistic. But for much smaller systems (photons, atoms, molecules, etc.) such coherent superpositions can be created. Perhaps the most surprising of the resulting effects is quantum entanglement, as predicted by Albert Einstein, Boris Podolsky, and Nathan Rosen in 1935, but seen at that time also as a paradox that was supposed to prove the inadequacy of quantum mechanics. After two particles have interacted, a measurement made on one of the particles can modify the quantum state of the second particle instantaneously, even if the distance between the two particles is large. However, in general, the system interacts with its environment, and a loss of coherence between the different quantum states occurs. This is what is called quantum decoherence. The quantum interference terms vanish locally, and the system is formally equivalent to a classical statistical mixture of states rather than a single coherent quantum superposition of them.

Such concepts are well known in physics, but chemistry is rarely interpreted within a full quantum-mechanical perspective. For instance, an elementary chemical process is generally not described as the evolution of a wavepacket. However, very early within the advent of quantum mechanics, quantization of the electronic states and the requirement of describing electrons with a delocalized wavefunction happened to be essential for many processes in chemistry, thus leading to the concepts of molecular orbitals, potential energy surfaces, and non-adiabatic couplings [8, 9]. The field of quantum chemistry was born, and its importance has been emphasized since then by Nobel prizes in Chemistry awarded to Linus Pauling in 1954, to Robert Mulliken in 1966, and to Walter Kohn and John A. Pople in 1998. Another significant illustration is found in Rudolph A. Marcus' theory, whereby the rates of electron transfer reactions are rationalized within a semi-classical formulation [10–12]. The latter describes the electron transfer process as a reaction where the system must undergo hops between two quantized electronic states. The hopping probability is estimated using an approximate analytical solution to the equations of motion governing the transition dynamics of a two-level quantum mechanical system (a Landau-Zener-type formula).

Consequently, electrons often are treated (at least partly) quantum-mechanically in theoretical chemistry except for very large systems (in the field of "Molecular Mechanics"). However, if the motion of the nuclei is added to the description of the system it is generally achieved through a classical treatment by solving Newton's equations, i.e., classically. This is the field known as "Molecular Dynamics" [13] (the development of models in this field has earned the Nobel prize in Chemistry to Martin Karplus, Michael Levitt, and Arieh Warshel in 2013). There are good reasons to support this strategy. The nuclei have a much larger mass than the electrons, and,

except for Hydrogen, they thus have a small de Broglie wavelength and generally move as mere mass points. In addition, since the nuclei are heavy, the difference of energy between the vibrational levels is much smaller than between the electronic states: quantization of the vibrational states can be neglected in many applications to reactivity. Besides, the coherence between the vibrational states is lost very quickly due to the very large density of states. The latter density is linked to the heavy mass of the nuclei and also to the fact that the system is entangled in a complex environment that destroys the interference effects [14]. Quantum effects for the nuclei are thus often expected to be weak in chemistry or at least negligible with respect to the other parameters that determine the characteristics of a molecular process.

One noticeable exception is molecular spectroscopy, more specifically infrared spectroscopy, where, almost by definition, quantization of the vibrational states cannot be neglected since it concerns the measurement of the transitions between the quantized vibrational states [15]. Due to its importance in chemistry, for instance for the detection of functional groups in organic chemistry, infrared spectroscopy is one of the very few domains where the students in both physics and chemistry experience the application of a full-quantum mechanical treatment for both the electrons and the nuclei in a molecular system. However, there is growing evidence that a significant number of various chemical reactions are impacted by strong quantum-mechanical effects involving nuclei [16].

In particular, chemical reaction rates can be greatly enhanced by quantum tunneling, namely the fact that particles can tunnel through a barrier that they could not surmount classically. This arises especially if the chemical reaction involves light atoms with large de Broglie wavelengths, such as protons, hydrogen atoms, and hydride ions. Tunneling is observed sometimes experimentally for heavy atoms but almost only at low temperature [17]. As stated by Robert J. McMahon in a paper of 2003 on chemical reactions involving quantum tunneling: "far from being mere curiosities or footnotes in the theory of chemical reaction rates, these quantum phenomena manifest themselves in 'ordinary' chemical reactions" [18]. In particular, tunneling is important not only at low, "cryogenic," temperatures but also at room temperature, in biological processes, for instance. Important changes of chemical reaction rates have been observed in chemical catalysis [19, 20] and interstellar chemistry [21]. It has also been suspected that tunneling plays a key role in some enzymatic reactions [22–28].

Another situation where quantum effects are essential occurs in the presence of strong vibronic couplings between several electronic states through the nuclear motion. The extreme case occurs around conical intersections, namely molecular geometries where two potential energy surfaces cross (the corresponding states are degenerate). These nonavoided crossings are called conical intersections because of the local shape of the two potential energy surfaces around the degeneracy point. In the vicinity of a conical intersection, the Born–Oppenheimer approximation breaks down, allowing non-adiabatic processes to take place. Conical intersections were predicted by John von Neumann and Eugene Wigner in 1929 and seem to be ubiquitous in polyatomic molecules [29, 30]. In particular, they are suspected

to play a key role during the first steps of photosynthesis [31] or vision [32,33], and in the photostability of DNA bases [34, 35]. As already mentioned about Rudolph A. Marcus' theory, the fact that a system can be transferred from one quantized state to another is per se a quantum effect. Besides this effect, the electronic states can remain coherent with respect to each other during a non-negligible period of time, leading to new quantum interference effects that are expected to exist even in living material [36]. For instance, a long-lived quantum superposition of (vibrational or vibronic) states has been observed experimentally in the photosynthetic system at low temperature [37] or at room temperature [38, 39], and in the chromophore of rodhopsin [40]. This does not mean that photosynthesis itself implies the same quantum interference effects since in the experiments this long quantum coherence is induced by pulsed coherent light. In contrast, photoinduced biological processes occur via one-photon absorption in natural light, which is incoherent [41]. As explained by Paul Brumer and Moshe Shapiro, "one-photon molecular excitation with pulsed coherent laser light and with natural incoherent light yield qualitatively different processes" [41]. In any case, the fact that photosynthetic systems can induce a long quantum coherence after excitation with laser pulses is a very important result on its own.

Another quantum effect is the so-called zero-point effect. The latter corresponds to the fact that a quantum molecular system has a zero-point energy greater than the minimum of its potential-energy well. It thus creates an effective uphill "shift" of the potential energy for a quantum particle along the minimum-energy path when compared to a classical particle [42, 43]. In addition, the wave properties of molecules have been revealed by diffraction experiments for systems as large as fullerene [44], perfluoroalkylated molecules, and complex derivatives of the tetraphenylporphyrin molecule with up to 430 atoms [45], and the subfemtosecond entanglement of protons with adjacent particles, such as other protons and electrons, has been highlighted by recent experiments [46]. As stated by Aris Chatzidimitriou-Dreismann and Markus Arndt as conclusions of a workshop on entanglement and decoherence of complex quantum systems: "in contrast to the popular view among chemists, atomic nuclei can not always be considered as classical mass points" [46].

On the experimental front, decisive progress has been achieved with the ability to use time-resolved pump-probe laser methods to study chemical processes on the femtosecond time scale (10^{-15}s), i.e., the typical period of molecular vibrations [47–49]. This was at the origin of the development of femtochemistry that earned Ahmed Zewail the Nobel Prize in Chemistry 1999. This technique allows experimentalists to follow the motion of the nuclei in real time: when chemical bonds break, form, or geometrically change. More recently, possibilities have emerged to generate sub-femtosecond or attosecond laser pulses [50–52] for observing electrons on their natural time scale. These techniques open the door to even measuring coupled electronic and nuclear dynamics [53–56]. Controlling the behavior of electrons and nuclei has become a key component to understand all sorts of quantum effects in molecular systems, in particular quantum coherence. It is also feasible with a closed-loop laboratory-learning procedure to create optimal ultrafast laser pulses that lead the molecular systems to a desired target outcome [57–60]. Another major

advance has been the possibility to orientate or align molecules, which allows one to excite molecular systems with laser pulses in a much more efficient way [61–64]. Polar molecules can be indeed (partially) oriented in the gas phase with a static field or with an external field that varies smoothly in a way that is concerted with the internal motion [65]. The introduction of crossed molecular beam methods mainly by Dudley Herschbach and Yuan T. Lee, for which they were awarded the Nobel Prize in Chemistry 1986 (along with John C. Polanyi for his work in chemical kinetics), has allowed experimentalists to measure collision cross sections strongly impacted by quantum effects [66,67], even when resonances, i.e., quantized metastable states, play a dominant role [68–70]. If one adds the fact that it is now possible to measure all the vibration-rotation-tunneling spectra even for very floppy systems such as water clusters [71–74], it appears clearly that it is now possible to detect, quantify precisely, and even manipulate most quantum effects in molecules.

In practice, one has to solve the time-dependent or the time-independent Schrödinger equation for the nuclei after having solved the Schrödinger equation for the electronic Hamiltonian that provides the potential energy surfaces and the couplings between the different electronic states. In principle, semiclassical theory is capable of describing all types of quantum effects [75–78] and is very efficient to add some quantum corrections to the description of very large systems [16]. The present book will however focus essentially on full quantum-mechanical methods. The latter not only give definitive comparisons with experimental results and validate more approximate theoretical approaches, but also provide the most complete characterization of a molecular process allowed by the basic laws of nature. In this context, fully-quantum-mechanical or semi-classical approaches can be seen as more complementary than in competition: quantum-mechanical methods offer quantitative benchmarks and, above all, a qualitative understanding of the quantum effects. Then, in a second step, variously elaborate semiclassical methods can be built, calibrated by the quantum methods, and applied to much larger systems.

Despite the considerable power of modern computers, the quantum-mechanical treatment of molecular dynamics is a formidable task when more than (only!) six nuclear degrees of freedom have to be taken into account. Indeed, the numerical effort scales exponentially with the number of degrees of freedom simply because the size of the basis set also grows exponentially with the dimension of the molecular system. Consequently, the development of molecular quantum dynamics has been directly linked to progress in computer power and even more importantly to the development of new algorithms to solve the Schrödinger equation. Joel M. Bowman, Tucker Carrington, and Hans-Dieter Meyer have given a short history of the quantum approaches in a recent review [79], albeit they focus on the computation of vibrational energies only. John Z. H. Zhang has also published a book describing the numerical methods in quantum dynamics and focusing more on reactive scattering [80]. Basically, the work can be divided into three main steps: (1) the numerical resolution of the (time-independent or time-dependent) Schrödinger equation for the nuclei, (2) the calculation of the potential energy surface(s), and (3) the choice of the set of coordinates to describe the system and the derivation of the corresponding kinetic energy operator.

The very first full quantum-mechanical approaches were undertaken in the early 1970s [81–85]. One major progress has been the definition of appropriate "primitive" basis functions to calculate the matrix elements of the Hamiltonian. The basis set must be complete and orthonormal in the space of its variable (which can be one or several degrees of freedom). In general, two basis sets of functions are employed that are related to one another by a unitary transformation. One basis corresponds to the so-called Finite Basis Representation (FBR) that is made of mathematical functions such as spherical harmonics, Hermite, sine, and exponential functions. The expression of the matrix elements of the kinetic energy operator in the FBR is analytical and simple [86]. The second representation is the so-called Discrete Variable Representation (DVR) in which the potential matrix is diagonal [87, 88]. Another important achievement has been the use of the Lanczos algorithm that allows one to calculate the eigenvalues of a given Hamiltonian without resorting to diagonalizing a full matrix [89,90]. Perturbative treatments have also been applied to calculate vibrational eigenvalues [91]. As regards the time-dependent Schrödinger equation, after pioneering works by Robert E. Wyatt and co-workers [81, 82, 92], the time-dependent picture has been popularized by several papers of Eric J. Heller [93–95]. After this preliminary stage, the community spent a lot of time in the 1980s on developing integrators to solve the time-dependent Schrödinger equation [96] (Chebyshev, Lanczos, Split Operator, etc.): they are listed in a review by Ronnie Kosloff [97] who played an important role in this domain [98]. Previously, the evolution of wavepackets was hardly studied in academic courses on quantum mechanics. David J. Tannor has recently published a book, "Introduction to Quantum Mechanics, a time-dependent perspective," that now fills in this lack. The book also presents some applications to molecular quantum dynamics. The development of robust integrators has thus been a great achievement, not only to study molecular systems, but also for any field where quantum mechanics is required.

Generally speaking, the fundamental problem faced in quantum-mechanical studies of large systems is the huge dimension of the primitive basis set, which is a product basis built from 1D bases for each degree of freedom. In order to tackle the exponential scaling of the numerical effort, several strategies have been developed, which are based on a "contraction" of the primitive basis. The contracted basis set is built in the primitive basis set but its size is much smaller. Some examples of contraction schemes are the Sequential Adiabatic Reduction (SAR) method of Z. Bačić and J. C. Light [87] or the contraction schemes developed by Tucker Carrington and co-workers that have emerged as optimal approaches to study rovibrational spectra [99–102]. One decisive step forward has been the systematic use of variational principles to build this intermediate "contracted" basis set. If we specifically turn to the time-independent picture, a systematic comparison between quantum dynamics and quantum chemistry can be made. The "contracted" functions obtained with the variational principle and primitive functions play the same role as the molecular orbitals and the atomic-orbital basis set functions in quantum chemistry, respectively. Several variants have been proposed. For the time-independent picture, one can cite Vibrational Self-Consistent Field (VSCF) methods

combined with perturbation theory [103–108]. Another approach is the VSCF procedure combined with a Configuration-Interaction (CI) method [109–111] that has given rise to the MULTIMODE package to calculate vibrational eigenvalues [112]: the subsequent CI procedure explicitly deals with the full correlation between the modes, yielding accurate results for five- or six-atom molecules and realistic results for much larger systems [113]. Vibrational Multi-Configuration Self-Consistent Field (MCSCF) methods have also been proposed that are similar to the Complete Active-Space SCF (CASSCF) method used in quantum chemistry [114–117]. The variational principle has also been applied to the time-dependent Schrödinger equation leading to the Time-Dependent Hartree (TDH) method [118, 119], and to multi-configuration time-dependent self-consistent field methods [120, 121] and more precisely to the Multi-Configuration Time-Dependent Hartree (MCTDH) method [122–125]. The Heidelberg MCTDH package [126] is probably the first software with a general character in the field of Molecular Quantum Dynamics. Its versatility is well illustrated by the fact that it has been applied to all the domains presented in the chapters of the present book: heterogeneous catalysis, reactive or non-reactive collisions, infrared spectroscopy, ultraviolet spectroscopy involving or not non-Born–Oppenheimer processes, photochemistry, processes guided by laser pulses, optimal control. Finally, it is worth noting that the calculation of metastable quantum states, in particular the calculation of their lifetimes, requires additional numerical techniques [127–132].

Molecular dynamics studies heavily depend on high-quality potential energy surfaces obtained from electronic structure calculations within the framework of quantum chemistry. These calculations and their global representation using analytical functions constitute a field on its own that is not the topic of the present book. Much progress has been achieved in this area in the last decades [133–135]. However, the description of systems by means of global potential energy surfaces is still limited to rather small systems. This limitation can be overcome, to some extent, by assuming that chemical phenomena can be described by a limited number of active coordinates that involve motions of large amplitude and that the other modes, the inactive ones, play a less important role. Under these conditions, it is possible to invoke simplifying approximations. For instance, a "reaction-path Hamiltonian" approach that makes use of a harmonic approximation defined along one or several active or "reactive" coordinates can be considered [136–142]. Another fruitful model has been devised by Cederbaum and co-workers to treat multistate-multimode vibronic couplings that uses a Taylor expansion of the different potential energy surfaces around the Franck–Condon geometry [143].

In molecular quantum dynamics, the choice of the set of coordinates to describe the physical system and to express the Hamiltonian operator is very important. As explained above, the main problem we have to face is the very large size of the basis sets, primitive or contracted, and this size is directly linked to the correlation between the coordinates. An inadequate set of coordinates can entail a strong artificial correlation and thus a poor convergence. Consequently, the set of coordinates must be carefully chosen to minimize as much as possible the size of the basis set. First, it is important to split the set of coordinates into two subsets,

one corresponding to the three Euler angles that define the Body-Fixed frame and that describe the overall rotation and one corresponding to the $3N-6$ internal coordinates, N being the number of atoms in the molecular system that describe the deformation of the system. The potential energy surfaces depend on the $3N-6$ internal degrees of freedom only, and if the molecular system is isolated one can take advantage of the fact that the quantum number associated with the total angular momentum is a constant of motion. As regards the choice of the $3N-6$ internal coordinates, for systems low in energy around a local minimum, the molecular system vibrates in a quasi-harmonic way and a description in terms of rectilinear normal coordinates that are linear combinations of the Cartesian coordinates of the atoms is correct. But higher in energy or for systems with large-amplitude motions such as systems undergoing scattering, dissociations, or isomerizations, a description with rectilinear coordinates is no longer adapted, and a description in curvilinear coordinates, i.e., involving angles, is required. Unfortunately, the use of curvilinear coordinates leads to very complicated expressions of the kinetic energy operator that are very specific to particular systems [144–147]. Recently, more general expressions of the kinetic energy operator have been given and general programs to provide them are now available [148, 149], in particular the formulation in polyspherical coordinates combined with a separation into subsystems [149–151] seems promising to treat large systems with curvilinear coordinates in a systematic way. The possibility to obtain the kinetic energy operators numerically in a systematic way is also an important achievement [148].

Typically, it is now possible in molecular quantum dynamics to treat systems with an ab initio potential energy surface and curvilinear coordinates up to 6–7 atoms in full dimensionality such as $(H_2)_3$ [152], CH_5^+ [102], and $H_5O_2^+$ [153, 154]. When a model is used for the potential and/or a description with normal coordinates is adopted, it is possible to deal with systems a little bit larger such as pyrazine, including two electronic states coupled through a conical intersection [155] or malonaldehyde [156]. One can also mention the $H + CH_4$ system that undergoes a reactive process [157]. We will see later that the recent Multi-Layer MCTDH approach will allow one to treat even larger systems. Note also that Feynman's path integral formulations have been applied to study condensed matter [158], but they will not be addressed in the present book.

The field of applications of molecular quantum dynamics covers broad areas of science not only in chemistry but also in physics and biology. Historically, due to the fact that the full quantum-mechanical simulation of molecular processes is limited to small systems, molecular quantum dynamics has given rise mainly to important applications of astrophysical and atmospheric relevance. In the interstellar medium or the Earth atmosphere, molecules are generally in the gas phase. Since many accurate spectroscopic data are available, these media have provided various prototype systems to study quantum effects in molecules and to calibrate the theoretical methods used to simulate these effects. In this context, it is not surprising that much theoretical effort is still directed toward modeling the full quantum-mechanical treatment of small molecules. Among others, one can cite the studies of the spectroscopy of water [159–161], and of the spectroscopy, photodissociation,

and formation of ozone, in particular the studies of the Hartley and Huggins bands that absorb most of the Sun medium-frequency ultraviolet light [162–164]. Molecular systems that are important for the greenhouse effect, ozone depletion, or for the study of the composition of the atmosphere of the Earth, planets in the solar system, or exoplanets have also been studied with full quantum-mechanical approaches: N_2O [165], NH_3 [140, 166–168], CH_4 [100, 169–173], etc.

But the most important goal of molecular quantum dynamics is probably to describe, understand, and control the elementary chemical processes at the most fundamental level, and it is the aim of the present book to provide some illustrations. This can be achieved by transferring all the methodology developed in quantum physics to the realm of molecular problems. In particular, the concepts of eigenstates, wavepackets, or even "dressed states" (dressed by an external field) used in quantum optics to describe atom-field interactions [174, 175] can be used to describe chemical phenomena. Such an approach can lead to new insights into the interpretation of chemical processes not available with a pure static picture or a classical or even a semi-classical picture of the motion of the nuclei (at least not directly in the latter case).

One central question in chemistry is how indeed to control reactivity and selectivity. A chemical reaction is often made of a series of several "elementary reactions" that can be described by using collision theory for bimolecular reactions since they can be seen as encounters between two chemical species [176]. The understanding of the dynamics of a system at the molecular level is the key to the interpretation of macroscopic kinetics, in particular to calculate thermal reaction rates, $k(T)$. As aforementioned, the development of crossed molecular beam methods allows the experimentalists to obtain an even more detailed information on the collisions, i.e., the state-to-state cross sections. Understanding all these elementary processes quantum-mechanically remains a very challenging task of tremendous practical importance, in particular for industrial reasons. Let us consider an example, the production of most synthetic compounds with heterogeneous catalysis involving the interaction of gas- or liquid-phase molecules with metal surfaces. In this context, the Nobel Prize in Chemistry 2007 was awarded to G. Ertl for his complete description of elementary molecule-surface reactions by which ammonia is produced for fertilizer [177]. But, for such a process, a detailed description of the mechanism behind each elementary act itself is still unavailable. In other words, if great progress has been achieved to produce new catalysts, the processes to find them remains empirical. It is what G.-J. Kroes and co-workers explain: "in many cases this progress [in the field of catalysis] is dictated by experience, intuition and trial and error" and thus "a full atomic scale picture of reaction dynamics at surfaces is desirable so that existing processes can be optimized and new and better catalysts can be designed" [178]. The ultimate goal is to reach a much higher level of control of the corresponding reactions. G.-J. Kroes mentions the fact that a demand for new catalysts is particularly strong in the automotive industry nowadays [178].

To determine in detail how molecules react on metals, many questions have to be answered [179]: how does the molecule dissipate or store internal vibrational energy during the collision with the surface? How does a bond of the incident

molecule break and how do the fragments bind chemically to the surface? How do the molecules scatter on the surface? What is the role of the phonons and electron-hole pair excitations in the process? etc. At this level of description, quantum effects can be dominant. In Chap. 2, Cristina Díaz et al. give some illustrations using a time-dependent quantum-mechanical approach. For instance, they present calculated reaction probabilities for $H_2 + Cu(111)$ and $D_2 + Cu(111)$ using all six molecular degrees of freedom and in excellent agreement with experiments [180]. They describe other simulations, for instance $H_2 + Pd(100)$, Pd(110) or Pd(111) [181]. The $H_2 + Pd(100)$ system has revealed the importance of the zero-point energy effect in the hydrogen dynamics: the quantum particles cannot propagate along the bottom of the valley of the potential energy surface since they require at least the zero-point energies perpendicular to the propagation direction. As a consequence, the sticking probability of H_2 on Pd(100) is much larger for the quantum particle than for a classical one [42]. In addition, the simulations given in Chap. 2 allow one to analyze the role played by the internal (vibrational or rotational) degrees of freedom for instance for the CH_4/Ni(100) system. They prove that the excitation of specific modes, for instance the C-H symmetric stretching mode for CH_4/Ni(100), can increase and guide the reactivity. This is the kind of information that cannot be obtained with a pure static description of a chemical process and that can be exploited to manipulate the reactivity by selectively exciting the corresponding modes of vibration using laser pulses. Such mode selectivity in chemistry has been experimentally demonstrated in the context of reactions on surfaces [182, 183].

A complete description of bimolecular reactions involving a moderate number of atoms is also very important for practical reasons, among others in atmospheric and combustion chemistry. U. Manthe and co-workers have, for instance, calculated the thermal rate constant, $k(T)$, for the $H + CH_4 \rightarrow H_2 + CH_3$ reaction [157, 184]. This H-atom abstraction reaction plays a central role in methane (CH_4/O_2) combustion [185]. U. Manthe and co-workers have performed a full-dimensional dynamics simulation using the MCTDH approach. By comparison with the classical transition-state theory, they have showed that quantum tunneling drastically fastens the reaction below 400 K. This simulation has been used as a benchmark to calibrate semi-classical methods, more precisely the transition state theory including corrections by Truhlar and co-workers, that could be used for much larger systems [186, 187]. An accurate determination of rates of combustion reactions requires to include quantum effects especially in the low-temperature regime [188]. This accurate determination is very important to point ways toward better fuel systems [189].

In Chap. 3, Hua Guo et al. stress the importance of tunneling in both unimolecular and bimolecular reactions. They have calculated the thermal rate constant, $k(T)$, for the exothermic $HO + CO \rightarrow H + CO_2$ reaction [190]. In combustion, this reaction is the main source of heat as the last step of hydrocarbon oxidation. They explain that it proceeds via the HOCO intermediate. In the last step of the reaction, the system has to surmount a transition state. There the reaction coordinate is essentially the H-O stretch and tunneling can dominate. This gives rise to a strong non-Arrhenius

kinetics: the rate constant is essentially flat up to 500 K and increases drastically higher. As shown by their calculations the presence of this plateau up to 500 K is due to tunneling.

Another intriguing quantum effect that has attracted great attention in the field of molecular quantum dynamics is the involvement of "quantum resonances." The resonant states are metastable states: the nuclei can be temporarily trapped during a reactive collision. Their lifetimes can be measured. They last typically for 10^{-13} to 10^{-12} s before they decay into reactants and products [191]. Scattering resonances can be classified in several types such as shape or Feshbach resonances [80]. In a shape resonance, the system is trapped in a one-dimensional well through which it can escape by tunneling. This well can be created by the centrifugal barrier of the system. The Feshbach resonance refers to an even more complex process with more than one dimension: during the collision, the energy associated with the scattering coordinate is partly transferred to other degrees of freedom. The system is temporarily stabilized and forms a metastable state. For instance, the calculated state-to-state probabilities show the existence of shape resonances and Feshbach resonances in $H + O_2 \rightarrow OH + O$ [192] and $H + H_2 \rightarrow H_2 + H$ [193,194] respectively. However, these short-lived states are extremely difficult to observe. Indeed, what is measured experimentally is a reaction cross section, which is a summation over all the probabilities corresponding to all values of the total angular momentum. This summation averages out the resonant contributions and masks their effect [76]. In Chap. 4, Zhigang Sun et al. present several reactive scattering systems involving Feshbach resonances. One of the most interesting results is the fact that they have been able to observe individual resonances in reactions such as $F + H_2$ [195] and $F + HD$ [70]. They have carried out wavepacket propagations in full dimensionality. For $F + H_2$, the usual way used in chemistry to explain the reaction rates of elementary chemical reactions (mainly based on transition state theory) must be abandoned: the system tunnels below the transition state energy and for certain energies remains temporarily trapped, although the potential is strongly repulsive along the reaction path! The results for $F + HD$ are even more interesting since each of the three peaks observed experimentally in the differential cross sections have been assigned to one Fesbach resonance only. At "normal" temperatures, the effect of these metastable states is masked. But detecting individual resonances is not only an exotic result since "ultracold" chemistry is precisely emerging as a very important field of research [196–201]. Measuring and controlling the reactivity of "cold" (1 mK $< T <$ 1 K) and "ultracold" ($T <$ 1 mK) molecules are now possible. At these temperatures, wavelike properties of molecules start dominating reaction dynamics and the quantum effects are strongly amplified. Tunneling through potential barriers becomes the dominant reaction mechanism: for instance, two atoms with a large mass such as Cesium can be combined through tunneling to form Cs_2 at around 300 μK [202–204]. As a consequence, chemical reactions at hyperthermal energies can occur along pathways that deviate far from the minimum-energy path [205]. The resulting chemistry is very rich and could give rise to many applications that are not possible otherwise. In particular, thermochemistry at cold temperature can no longer be described by the

paradigms of reaction path and transition states. In this context, it is conceivable to target the resonant states [191] and to guide the chemical reactions in a way that is completely different from chemistry at higher temperature.

When elementary reactions are not bimolecular, they are generally unimolecular. Among the latter, many are induced by the absorption of light. But before describing the photochemistry of molecules, it is necessary to understand how they interact with light. Photoabsorbtion spectra lead to information about the actual values of the eigenvalues of the Hamiltonian of the system and indirectly to the nature of the corresponding quantum eigenstates. In infrared or microwave spectroscopy, the fact that the rotational and vibrational states are quantized must be taken into account since transitions are resonant only if the energy of the photon corresponds to the energy difference between two rovibrational eigenvalues. The accurate knowledge of infrared or microwave spectra of small molecules is important not only for the spectroscopy of the atmosphere or in astrophysics, but it also provides invaluable information to identify molecular properties that can be exploited in different domains of chemistry [206]. Let us consider an example: the water dimer is the archetype for aqueous hydrogen bonding and the dimer interaction constitutes the leading and most important term in a many-body expansion for water clusters and condensed phases of water [73]. Most simulations of water use empirical pair potentials fitted to reproduce some properties obtained with approximate methods (molecular dynamics or Monte Carlo). It is suspected that many simulations suffer from an inadequate representation of the force field since these effective potentials describe very poorly the experimental data of small water clusters [207]. The vibrations and rotations of the monomers in the water dimer have large amplitudes and are highly anharmonic. In addition, the rovibrational levels are all split by quantum tunneling so that nearly exact quantum dynamics is necessary to describe quantitatively the rovibrational spectrum. C. Leforestier and co-workers have developed a code that solves the time-independent Schrödinger equation to calculate the latter [208, 209]. Since very accurate experimental data are available for this system [73], the code has allowed one to provide a test for the different potentials, the two most recent ones [209, 210] giving a very good agreement with experiments [209, 211]. It will allow a much more accurate description of interactions between molecules of water and will result in better models of the liquid or solid phase, which can be used, for instance, to study solvation and reactions in aqueous environments. More generally, it will help for a better understanding of hydrogen bonds that play an important role in many chemical processes [212].

In Chap. 5, Oriol Vendrell et al. give a similar example: the infrared spectrum of the protonated dimer or Zundel cation, $H_5O_2^+$. Using a time-dependent description with the MCTDH approach including all 15 internal degrees of freedom, they have been able to completely characterize the infrared spectra in the gas phase for this system as well as all its analogues where the hydrogen atoms have been replaced by deuterium atoms [153, 154]. They have also performed time-dependent simulations of the dynamics of a proton between the two water molecules [213]. As explained by S. S. Xantheas, the scope of this work exceeds the simple description of this small cluster alone since hydrogen cations are ubiquitous in nature [214]. The

protonated dimers are important for environmental reasons since, for instance, "they take part in acid-base reactions that determine the formation, fate and transport of the main environmental pollutants that cause acid rain"; they are important also for biological processes since "they are pumped across cell membranes by dedicated proteins, creating gradients in pH and charge that act as energy reservoirs for the cell," etc. [214]. Describing correctly the potential interaction of this system and the underlying vibrational quantum dynamics has thus a general character. In particular, the time-dependent evolution of the proton obtained with MCTDH can serve as a reference to calibrate more approximate methods [215, 216], which can, in turn, be used to treat much larger clusters. This work can be seen as a first step in a so-called bottom-up approach in nanotechnologies for instance, where a precise description of chemical properties of small components can help to understand much more complex structures created by the self-organization of these components, in this particular case the collective physical phenomena involved when hydrogen ions move through water. In the same vein, Vendrell et al. present simulations concerning the infrared spectrum of malonaldehyde, a prototype for the description of the intramolecular hydrogen bond and the corresponding proton transfer [212, 217–220]. The field of infrared spectroscopy is also linked to the studies of Intramolecular Vibrational Redistribution (IVR). The knowledge of the couplings between the vibrational modes and the time scales of the vibrational energy redistribution in molecules is important to understand the rates and the efficiency of chemical reactions [221–223]. As stated by A. Zewail during his Nobel lecture, knowing and controlling the time scales of IVR are a prerequisite of mode-selective chemistry with lasers [224]. It may happen that the vibrational energy given to a chemical bond for instance is redistributed within the molecule in a statistical way, but IVR can also proceed via very specific pathways. In the latter case and if these specific channels lead to important processes, this opens the way to the induction of isomerizations (or dissociations) by laser pulses in the electronic ground state: the lasers can excite one mode of vibration creating a coherent superposition of several vibrational eigenstates, and the resulting wavepacket moves, in a second step, into the direction of the other isomer [225–227].

If the energy of the photons is higher, in the ultraviolet-visible region, the molecule can also be excited electronically. From the electronic excited state, the molecule can release its excess energy and return to the electronic ground state through light emission: fluorescence from a singlet state or phosphorescence from a triplet state. However, in many cases, the light emission is quenched by a much faster radiationless process that is often due to the presence of a non-adiabatic coupling between the excited electronic state and the electronic ground state. In addition, a photochemical reaction (photo-isomerization or photodissociation) may occur during the deactivation time leading to new photoproducts. In polyatomic molecules, this non-Born–Oppenheimer process is generally due to the presence of a conical intersection [29, 30]. Understanding the physics around these conical intersections is very important for at least two reasons: (1) a transfer through a conical intersection corresponds to a fast change in the electronic wavefunction so that the system can rapidly jump from one chemical state to a very different

one. A conical intersection can be seen as a funnel through which a new chemical reaction can occur. Conical intersections are a central paradigm for understanding reaction mechanisms in photochemistry, as important as transitions states in thermal chemistry [228]. (2) As explained above, the presence of conical intersections can be at the origin of strong quantum-mechanical effects since the two nuclear wavefunctions associated with the two electronic states can interfere. Thus, the determination of the corresponding ultraviolet spectra in the gas phase is not only important for astrophysical applications, but it is also an essential test for the description of the quantum effects in molecules, which paves the way to photochemistry induced by strong vibronic couplings. The illustrations given in Chap. 6 by Horst Köppel prove that quantum physics around conical intersections is now perfectly mastered. Time-dependent methods allow one to perfectly reproduce the envelops of the experimental absorption spectra. The calculation of the eigenstates with a time-independent approach allows the assignment of the main peaks of the spectra. In particular it allows the assignment of those corresponding to "vibronic" states, i.e., vibrational eigenstates with components extending over more than one electronic states such as those corresponding to the "mystery band" in the photoelectron spectrum of the butatriene molecule. The simulations can also capture the most subtle interference effects that characterize the physics around a conical intersection, among others the "geometric phase phenomenon." The spectroscopy of molecules can also be complicated by the presence of spin–orbit couplings, which is a special class of non-adiabatic coupling, especially for open-shell systems, since the latter have unpaired electrons and an electronic spin that is different from zero [229, 230]. The inclusion of the spin–orbit coupling is performed by adding relativistic coupling terms in the molecular Hamiltonian operator.

In Chap. 7, Benjamin Lasorne et al. present studies of photochemistry around conical intersections. Of course, the spectral position, shape, and width of the absorption (or emission) spectra depend on all the competing events that dominate the short-timescale dynamics of the system. In other words, there is a link between the spectroscopy and the photochemistry of the molecule. But photochemistry has to go one step further than spectroscopy since the conical intersection can be far from the Franck–Condon region, the latter playing the dominant role for the photoabsorption spectrum. As explained by M. Robb and co-workers, taking into account explicitly the motion of the nuclei is essential for photochemical reactions, in contrast with thermal reactions [228]. The latter are much better described by the concept of minimum energy path and intrinsic reaction coordinate since the system has time to equilibrate and redistribute the nuclear kinetic energy to the surrounding environment. On the other hand, most photochemical reactions are ultrafast, and the most straightforward path leading to the conical intersection can be very different from the minimum energy path. To simulate explicitly the time evolution, Lasorne et al. have adopted several approaches including a Gaussian wavepacket version of the MCTDH algorithm: instead of using a contracted basis set that is fully optimized variationally as in the MCTDH approach, the contracted bases are constrained to keep a Gaussian shape. This allows one to associate, to the propagation of each Gaussian function, a trajectory as in classical mechanics. Along

the trajectory, the electronic potential can be calculated "on-the-fly," i.e., for each geometry, thus avoiding an explicit calculation of the potential energy surface. In its most elaborate version [231], this Gaussian approach is "variational" in the sense that all the quantum effects can be captured provided that the number of Gaussian functions is very large. In practice, the number of Gaussian functions is limited for numerical reasons, and this approach can be seen as an intermediate stage between a full quantum-mechanical approach (i.e., using ab initio potential energy surfaces and an algorithm such as MCTDH) and an approximate semi-classical method. This approach allows one to see the quantum effects appearing step-by-step by adding more Gaussian functions in the propagation. It is illustrated by the nonlocal transfer from one electronic state to another in the case of the photoisomerization of a cyanine model. In the latter case, a nonlocal transfer appears: as for tunneling, the wavefunction disappears in one electronic state and instantaneously reappears in the other electronic state with no indication of physically transiting the intermediate geometries [232]. This effect is due to the presence of a conical intersection and not to tunneling. In the same manner, when the wavepacket goes through the conical intersection, it can split into several components. The latter can then meet again and create strong interferences that can change the dynamics of the system [233]. These effects can be rendered by the Gaussian propagation methods [233]. One of the most important results brought to the fore by these quantum studies has been the impact of the topology of the conical intersection. As stated by M. Robb and co-workers "sloped conical intersections tend to favor regeneration of the starting material (photostability) because both excited-state and ground-state gradients point toward the reactant side of the potential energy surfaces, whereas peaked conical intersections are more likely to lead to photoproducts as one of the two gradients leads to a new reactive channel on the ground-state surface" [228]. It is a sloped topology that probably explains the photostability of DNA bases [34, 35, 234, 235] and a peaked topology the isomerization of retinal in the first step of vision [236] and the electron transfer in the linked porphyrin-quinone molecule that is responsible for the first step of photosynthesis [31]. Conical intersections are perhaps the tools used in nature to transform the energy of light into chemical energy because of the efficiency and the rapidity of the effect they induce.

Explaining the cross sections of collisions and the photoabsorption spectra of molecules is fundamental to understand the properties of materials, but it is even more important to be able to manipulate and control these properties. In traditional chemistry, this is achieved by adjusting external parameters such as temperature, pressure, concentration, solvent, or by adding catalysts. A higher selectivity and precision could be obtained by a systematic use of lasers. In addition, the latter can offer the possibility to control quantum effects such as quantum coherence. In traditional chemistry, the quantum states involved in the chemical process are, in general, populated in a incoherent way described as a "mixed state" in quantum statistical mechanics. The systematic use of laser pulses to induce chemical process opens the possibility to create coherent superpositions of the same quantum states, what is called a "pure state" in quantum statistical mechanics. Such coherent superpositions might drastically increase the efficiency and the control of

the corresponding chemical processes and at a much lower energetical cost. The exploitation of this quantum coherence in molecular processes is seen as one of the main challenges in basic energy sciences [237]. This leads to the concept of coherent control that is presented in Chap. 8 by Sebastian Thallmair et al. The studies presented in Chap. 7 are a first step in the direction of coherent control. For instance, it is observed that a sloped or a peaked topology at the conical intersection leads preferentially to photostability or photoreactivity, respectively. But since a conical intersection is not an isolated point but a subspace of $3N-8$ dimensions, N being the number of atoms of the molecule, the topology can be sloped in some regions, while peaked elsewhere [238,239]. By selecting the initial vibrations that are excited by a laser pulse, the system can be guided in a specific direction and access the conical intersection in different regions leading to different processes, photostable or photoreactive for instance [238, 239]. Consequently, if it is important to understand the intramolecular vibrational energy redistribution in molecules and the quantum physics around conical intersections, it is even more important to understand the two at the same time since, in polyatomic molecules, excitations result in a rapid mixing of vibrational and electronic motions, which induces both charge redistribution and energy flow in the molecule [240]. The fact that the electronic and nuclear motions can be coupled in the most subtle way is observed even in physiological processes. For instance, as aforementioned, a quantum coherence between two electronic states has been evidenced in photosynthetic systems. In such biological systems, the number of modes of vibration is huge and these vibrations should destroy the quantum interferences very fast [36]. In other words, a quantum decoherence between the two electronic states should be almost instantaneous due to the presence of the "environment" of the numerous vibrations. But since a much longer coherence is observed experimentally, it probably means that a subset of modes of vibrations must themselves be in coherence with the electronic motion and enhance the interferences instead of destroying them, while the other modes of vibration are less coupled to the electronic motion and will play the role of an environment that dissipates the coherence only in a second stage [36, 241]. In this context, understanding the coupled quantum behavior between electrons and nuclei is particularly important in molecular quantum dynamics especially with the advent of "attosecond spectroscopy" that allows scientists to measure all the corresponding quantum effects [237]. Understanding how light is converted into chemical energy and the corresponding quantum effects can have many applications [242]. In particular, as stated by C. A. Rozzi et al: "One of the key challenges for the future will be to learn how to construct artificial devices enabling to the harvesting of sunlight and their use either for direct electric power generation (photovoltaic approach) or to drive fuel-producing photochemical reactions (photosynthetic approach)" [243]. In this context, "a fascinating, but so far unexplored, perspective would be to exploit such quantum coherence effects in artificial photosynthetic/photovoltaic systems to improve their performance," although the quantum effects induced by sunlight or by laser pulses in experiments must be clearly distinguished [41].

A full quantum description of molecules in interaction with laser pulses is a difficult task. In practice, in molecular quantum dynamics, the light is not described

quantum-mechanically with quantum electrodynamics but classically. But even with this approximation, all the information gained on the isolated systems (i.e., without any external field) about the topology of the potential energy surfaces or the eigen or metastable states cannot be directly transposed to the study of the system in interaction with pulses. Indeed, the presence of the external fields modifies the molecular systems themselves. When the pulse is periodic or when the envelop of the pulse changes smoothly, i.e., "adiabatically" according to precise criteria, it is the Floquet states that play an analogous role to that of the energy eigenstates in time-dependent systems [244, 245]. Since the calculation of the Floquet states is even more complicated than the calculation of the eigenstates, some approximations are often invoked to rationalize the interaction of the system with light. Two extreme cases can be distinguished. If ω, the carrier frequency of the laser pulse, is quasiresonant with respect to the transition of interest, the problem can be reformulated in terms of "dressed" states, i.e., eigenstates dressed by the external field. The dressed energies are simply the eigenvalues of the time-independent problem, $\pm\hbar\omega$. If the frequency is completely non-resonant, the interaction with the pulse can be reduced to a dynamic Stark effect, i.e., the effective potential seen by the system is simply the electronic potential plus the contributions of the dipole moment and the polarizability that depend on time only through the envelope of the pulse. The eigenstates must be replaced by the eigensolutions for each time t of the effective Hamiltonian with the effective potential. In this context, joining clearly the targeted chemical properties of systems and the parameters of the laser pulses is still challenging.

As explained by Sebastian Thallmair et al. in Chap. 8, the coherent control of quantum systems, two complementary approaches can be distinguished: the "rational" control (or "single-parameter" control) and the "optimal" control (or "multi-parameter" control). In the first approach, a single parameter (pulse duration, intensity, wavelength, pulse delay, chirp) is used to control the chemical process [246–250]. The second approach is more systematic: several parameters are optimized at the same time using an appropriate control scheme to find an "optimal" laser field in order to reach a predefined target [251, 252]. It is indeed possible experimentally to tailor the driving laser pulse with a pulse-shaping device using a closed-loop laboratory-learning procedure. These two approaches are complementary: the second one is more efficient but is somewhat "blind" since the intrinsic information about the physics of the system is concealed in the optimal pulse [253, 254]. It is precisely the role of rational control to make the link between the physical properties of the system and the parameters used in the field to control the process and to bring out general rules that govern the dynamics. For this, one can split the processes into several categories. First, one focuses on the control of the nuclear motion only, i.e., on chemical processes in one electronic state, typically the electronic ground state, and one uses the Born–Oppenheimer approximation. The understanding and the control of tunneling and of IVR are then the main issues. Second, one adds the possibility to switch from one electronic state to another through a non-adiabatic process induced by the presence of a conical intersection for instance. In this context, the topology of the

potential surfaces around the conical intersection plays a crucial role in the physical process as explained in Chap. 7. Control of the reactivity can then be obtained by changing this topology, for instance, by using a non-resonant laser that creates a Stark effect and shifts the energy of one electronic state with respect to the other one. However, IVR can interfere in the dynamics and the full control of the reactivity can only be achieved by controlling the coupled nuclear and electron dynamics. In Chap. 8, Sebastian Thallmair et al. present several strategies they have employed to control chemical processes with laser pulses, special emphasis being placed on subfemtosecond coherent control of coupled electronic and nuclear dynamics. They present an example of possible optimal control for a molecular switch made of an electrocyclic reaction of fulgides [254]. Molecular switches can be used as versatile devices in nanotechnology and for logic gates in molecular computation. But the most important results they present are probably those concerning the control of the electron localization in the diatomics D_2, CO, K_2. Their simulations explain the recent experiments realized for these systems using laser pulses at the sub-femtosecond time scale [53, 255, 256]. These works prove that it is now possible not only to control the motion of the nuclei with laser pulses as in femto-chemistry but, even more importantly, to also control and to "shape" the electronic density by creating an electronic wave packet that is a coherent superposition of several molecular electronic states.

Finally, Alex Brown et al. present in Chap. 9 some applications in the context of quantum computing. The possibilities offered through quantum computation have been well known for many years now [257, 258]. A quantum computer is a computation device that makes direct use of quantum-mechanical phenomena, mainly the fact that the system can be in a coherent superposition of different eigenstates due to the superposition principle. This has no classical counterpart as illustrated by the famous Schrödinger cat as explained above. In classical computers, the basic unit of information is a "bit" that can have only two values often denoted 0 and 1. As explained by Brown et al, in quantum computers, the unit of information is a "qubit" that is a coherent superposition of two quantum sates denoted 0 and 1. More precisely, it is a two-state quantum-mechanical system that can be written as: $\alpha|0> + \beta|1>$. The advantage of a quantum computer can be understood straightforwardly: whereas a bit must be either 0 or 1, a qubit can be in any superposition of both (due to the superposition principle), and the number of possible combinations is much larger. This possibility to superpose several states offers new possibilities of combinatorial calculations that do not exist with computers based on classical laws. In particular, it is expected that quantum computers could solve certain problems much faster than any classical computer. One of the main challenges in quantum computing is controlling quantum decoherence since the latter destroys the properties that are exploited in quantum computing. In addition to the superposition principle, quantum computers could exploit other quantum properties such as entanglement (for quantum teleportation, i.e., to transmit quantum information from one location to another) or wave function collapse (for cryptography [259]). In the context of molecular quantum dynamics, it has been proposed that electronic vibrational or rotational states of molecules

could be used for quantum computation processes [260–263]. Vibrationally excited molecules in the gas phase could be possible candidates to encode qubits since decoherence could be controlled easily [260, 264]. The final chapter on quantum computing highlights that one key issue in molecular quantum dynamics is the creation of a coherent superposition of quantum states and its conservation over time since quantum decoherence can occur very fast upon interaction with the environment.

References

1. Messiah A (1962) Quantum mechanics, vol 1. Wiley, New York
2. Cohen-Tannoudji C, Diu B, Laloe F (1992) Quantum mechanics. Wiley, New York
3. Basdevant J-L, Dalibard J (2005) Quantum mechanics. Springer, Heidelberg
4. Tannor DJ (2007) Introduction to Quantum Dynamics: A Time-Dependent Perspective. University Science Books, Sausalito, CA
5. Fox M (2006) Quantum optics: An introduction. Oxford University Press, Oxford
6. Cohen-Tannoudji C, Grynberg G, Aspect A, Fabre C (2010) Introduction to quantum optics: From the semi-classical approach to quantized light. Cambridge University Press, Cambridge
7. Haroche S, Raimond J-M (2006) Exploring the quantum: Atoms, cavities, and photons. Oxford University Press, Oxford
8. Pauling L, Wilson EB (1985) Introduction to quantum mechanics with applications to chemistry. Dover Publications, New York
9. Smith VH, Schaefer HF, Morokuma K (eds) (1986) Applied quantum chemistry. Springer, Heidelberg
10. Marcus RA (1952) Unimolecular dissociations and free radical recombination reactions. J Chem Phys 20:359
11. Marcus RA (1965) On the theory of electron-transfer reactions. VI. Unified treatment for homogeneous and electrode reactions. J Chem Phys 43:679
12. Marcus RA (1993) Electron transfer reactions in chemistry. Theory and experiment. Rev Mod Phys 65:599
13. Griebel M, Knapek S, Zumbusch G (2007) Numerical simulation in molecular dynamics. Springer, Heidelberg
14. Onuhic JN, Wolynes PG (1988) Classical and quantum pictures of reaction dynamics in condensed matter: Resonances, dephasing, and all that. J Phys Chem 92:6495
15. Herzberg G (1992) Molecular spectra and molecular structure. Krieger, Malabar
16. Miller WH (2006) Including quantum effects in the dynamics of complex (i.e., large) molecular systems. J Chem Phys 125:132305
17. Zuev PS, Sheridan RS, Albu TV, Truhlar DG, Hrovat DA, Borden WT (2003) Carbon tunneling from a single quantum state. Science 299:867
18. McMahon RJ (2003) Chemical reactions involving quantum tunneling. Science 299:833
19. Espinosa-García J, Corchado JC, Truhlar DG (1997) The importance of quantum effects for C-H bond activation reactions. J Am Chem Soc 119:9891
20. Wonchoba SE, Hu W-P, Truhlar DG (1995) Surface diffusion of H on Ni(100). Interpretation of the transition temperature. Phys Rev B 51:9985
21. Hiraoka K, Sato T, Takayama T (2001) Tunneling reactions in interstellar ices. Science 292:869
22. Cha Y, Murray CJ, Klinman JP (1989) Hydrogen tunneling in enzyme-reaction. Science 243:1325
23. Kohen A, Cannio R, Bartolucci S, Klinman JP (1999) Enzyme dynamics and hydrogen tunnelling in a thermophilic alcohol dehydrogenase. Nature 399:496

24. Truhlar DG, Gao J, Alhambra C, Garcia-Viloca M, Corchado J, Sánchez ML, Villà J (2002) The incorporation of quantum effects in enzyme kinetics modeling. Acc Chem Res 35:341
25. Truhlar DG, Gao J, Alhambra C, Garcia-Viloca M, Corchado J, Sánchez ML, Villà J (2004) Ensemble-averaged variational transition state theory with optimized multidimensional tunneling for enzyme kinetics and other condensed-phase reactions. Int J Quant Chem 100:1136
26. Hammer-Schiffer S (2002) Impact of enzyme motion on activity. Biochemistry 41:13335
27. Antoniou D, Caratzoulas S, Mincer J, Schwartz SD (2002) Barrier passage and protein dynamics in enzymatically catalyzed reactions. Eur J Biochem 269:3103
28. Ball P (2012) The dawn of quantum biology. Nature 474:272
29. Domcke W, Yarkony DR, Köppel H (eds) (2004) Conical intersections, electronic strucutre, dynamics and spectroscopy. World Scientific, New Jersey
30. Domcke W, Yarkony DR, Köppel H (eds) (2004) Conical intersections, theory, computation and experiment. World Scientific, New Jersey
31. Worth GA, Cederbaum LS (2001) Mediation of ultrafast electron transfer in biological systems by conical intersections. Chem Phys Lett 338:219–223
32. González-Luque M, Garavelli M, Bernardi F, Mechán M, Robb MA, Olivucci M (2010) Computational. Proc Natl Acad Sci USA 97:9379
33. Polli D, Altoè P, Weingart O, Spillane KM, Manzoni C, Brida D, Tomasello G, Orlandi G, Kukura P, Mathies RA, Garavelli M, Cerullo G (2010) Conical intersection dynamics of the primary photoisomerization event in vision. Nature 467:440
34. Lan Z, Frutos LM, Sobolewski AL, Domcke W (2008) Photochemistry of hydrogen-bonded aromatic pairs: quantum dynamical calculations for the pyrrole-pyridine complex. Proc Natl Acad Sci USA 105:12707
35. Schultz T, Samoylova E, Radloff W, Hertel IV, Sobolewski AL, Domcke W (2004) Efficient deactivation of a model base pair via excited-state hydrogen transfer. Science 306:1765
36. Wolynes PG (2009) Some quantum weirdness in physiology. Proc Natl Acad Sci USA 106:17247–17248
37. Engel GS, Calhoun TR, Read EL, Ahn T-K, Mancal T, Cheng Y-C, Blankenship RE, Fleming GR (2007) Evidence for wavelike energy transfer through quantum coherence in photosynthetic systems. Nature 446:782–786
38. Lee H, Cheng Y-C, Fleming GR (2007) Coherence dynamics in photosynthesis: Protein protection of excitonic coherence. Science 316:1462
39. Collini E, Wong CY, Wilk KE, Curmi PMG, Brumer P, Scholes GD (2010) Coherently wired light-harvesting in photosynthetic marine algae at ambient temperature. Nature 463:644
40. Wang Q, Schoenlein RW, Peteanu LA, Shank RA (1994) Vibrationnaly coherent photochemistry in the femtosecond primary event of vision. Science 266:422–424
41. Brumer P, Shapiro M (2012) Molecular response in one-photon absorption via natural thermal light vs. pulsed laser excitation. Proc Natl Acad Sci USA 109:19575
42. Gross A, Scheffer M (1998) Ab initio quantum and molecular dynamics of the dissociative adsorption on Pd(100). Phys Rev B 57:2493
43. Marx D, Parrinello M (1996) The effect of quantum and thermal fluctuations on the structure of the floppy molecule $C_2H_3^+$. Science 271:179
44. Arndt M, Nairz O, Voss-Andreae J, Keller C, van der Zouw G, Zeillinger A (1999) Wave-particle duality of c_{60} molecules. Nature 401:680
45. Gerlich S, Eibenberger S, Tomand M, Nimmrichter S, Hornberger K, Fagan PJ, Tüxen J, Mayor M, Arndt M (2011) Quantum interference of large organic molecules. Nat Phys 2:263
46. Chatzidimitriou-Dreismann A, Arndt M (2004) Quantum mechanics and chemistry: The relevance of nonlocality and entanglement for molecules. Angew Chem Int Ed 335:144
47. Chergui M (ed) (1996) Femtochemistry. World Scientific, Singapore
48. Zewail AH (1994) Femtochemistry: ultrafast dynamics of the chemical bond. World Scientific, Singapore
49. Ihee H, Lobastov V, Gomez U, Goodson B, Srinivasan R, Ruan C-Y, Zewail AH (2001) Science 291:385

50. Drescher M, Hentschel M, Kienberger R, Uiberacker M, Scrinzi A, Westerwalbesloh T, Kleineberg U, Heinzmann U, Krausz F (2002) Time-resolved atomic inner-shell spectroscopy. Nature 419:803
51. Goulielmakis E, Loh Z-H, Wirth A, Santra R, Rohringer N, Yakovlev VS, Zherebtsov S, Pfeifero T, Azzeer AM, Kling MF, Leone SR, Krausz F (2010) Real-time observation of valence electron motion. Nature 466:739
52. Krausz F, Ivanov M (2009) Attosecond physics. Rev Mod Phys 81:163–234
53. Kling MF, Siedschlag C, Verhoef AJ, Khan JI, Schultze M, Uphues T, Ni Y, Uiberacker M, Drescher M, Krausz F, Vrakking MJJ (2006) Control of electron localization in molecular dissociation. Science 312:246
54. Niikura H, Légaré F, Hasbani R, Bandrauk AD, Ivanov MY, Villeneuve DM, Corkum PB (2002) Sub-laser-cycle electron pulse for probing molecular dynamics. Nature 417:917
55. Stolow A, Jonas DM (2004) Muldimensional snapshots of chemical dynamics. Science 305:1575
56. Kahra S, Leschhorn G, Kowalewski M, Schiffrin A, Bothschafter E, Fuss W, de Vivie-Riedle R, Ernstorfer R, Krausz F, Kienberger R, Schaetz T (2012) Controlled delivery of single molecules into ultra-short laser pulses: a molecular conveyor belt. Nat Phys 8:238
57. Asssion A, Baumert T, Bergt M, Brixner T, Kiefer B, Seyfried V, Strehle M, Gerber G (1998) Control of chemical reactions by feedback-optimized phase-shaped femtocecond laser pulses. Science 282:919
58. Brixner T, Damreuer NH, Niklaus P, Gerber G (2001) Photoselective adaptative femtosecond quantum control in the liquid phase. Nature 414:57
59. Herek JL, Wohlleben W, Cogdell RJ, Zeidler D, Motzus M (2002) Quantum control of energy flow in light harvesting. Nature 417:533
60. Levis RJ, Menkir GM, Rabitz H (2001) Selective bond dissociation and rearrangement with optimally tailored, strong-field laser pulses. Science 292:709
61. Daems D, Guérin S, Hertz E, Jauslin HR, Lavorel B, Faucher O (2005) Field-free two-direction alignement alternation of linear molecules by elliptic laser pulses. Phys Rev Lett 95:063005
62. Madsen CB, Madsen LB, Viftrup SS, Johansson MP, Poulsen TB, Holmegaard L, Kumarappan V, Jorgensen KA, Stapelfeldt H (2009) Manipulating the torsion of molecules by strong laser pulses. Phys Rev Lett 102:073007
63. Holmegaard L, Hansen JL, Kalhøj L, Kragh SL, Stapelfeldt H, Filsinger F, Küpper J, Meijer G, Dimitrovski D, Martiny C, Madsen LB (2010) Photoelectron angular distributions from strong-field ionization of oriented molecules. Nat Phys 6:428
64. Bisgaard CZ, Clarkin OJ, Wu G, Lee AMD, Gessner O, Hayden CC, Stolow A (2009) Time-resolved molecular frame dynamics of fixed-in-space CS_2 molecules. Science 323:1464
65. Bethlem HL, Berden G, Crompvoets FM, Jongma RT, van Roij AJA, Meijer G (2000) Electrostatic trapping of ammonia molecules. Nature 406:491
66. Kreckel H, Bruhns H, Čížek M, Glover SCO, Miller KA, Urbain X, Savin DW (2010) Experimental results for H_2 formation from H^- and H and implications for first star formation. Science 329:69
67. Clary DC (1998) Quantum theory of chemical reaction dynamics. Science 279:1879
68. Schnieder L, Seekamp-Rahn K, Borkowski J, Wrede E, Welge KH, Aoiz FJ, Bañares L, D'Mello MJ, Herrero VJ, Rábanos VS, Wyatt RE (1995) Experimental studies and theoretical predictions for the $H + D_2 \rightarrow HD + D$ reaction. Science 269:207
69. Qui M, Ren Z, Che L, Dai D, Harich SA, Wang X, Yang X, Xu C, Xie D, Gustafsson M, Skodje RT, Sun Z, Zhang DH (2006) Observation of Feshbach resonances in the $F + H_2 \rightarrow HF + H$ reaction. Science 311:1440
70. Dong W, Xiao C, Wang T, Dai D, Yang X, Zhang DH (2010) Transition-state spectroscopy of partial wave resonances in the F + HD. Science 327:1501
71. Dyke TR, Howard BJ, Klemperer W. Radiofrequency and microwave spectrum of the hydrogen fluoride dimer; a nonrigid molecule. J Chem Phys 56:2442

72. Howard BJ, Dyke TR, Klemperer W (1984) The molecular beam spectrum and the structure of the hydrogen fluoride dimer. J Chem Phys 81:5417
73. Fellers RS, Leforestier C, Braly LB, Brown MG, Saykally RJ (1999) Spectroscopic Determination of the Water Pair Potential. Science 284:945
74. Saykally RJ, Blake GA (1993) Molecular interactions and hydrogen bond tunneling dynamics: Some new perspectives. Science 259:1570
75. Miller WH (1974) Quantum mechanical transition state theory and a new semiclassical model for reaction rate constants. J Chem Phys 61:1823–1834
76. Miller WH (1993) Beyond transition-state theory: a rigorous quantum theory of chemical reaction rates. Acc Chem Res 26(4):174
77. Thoss M, Miller WH, Stock G (2000) Semiclassical description of nonadiabatic quantum dynamics: Application to the S_1 – S_2 conical intersection in pyrazine. J Chem Phys 112:10282–10292
78. Wang HB, Thoss M, Sorge KL, Gelabert R, Gimenez X, Miller WH (2001) Semiclassical description of quantum coherence effects and their quenching: A forward-backward initial value representation study. J Chem Phys 114:2562–2571
79. Bowman JM, Carrington Jr. T, Meyer H-D (2008) Variational quantum approaches for computing vibrational energies of polyatomic molecules. Mol Phys 106:2145–2182
80. Zhang JZH (1999) Theory and application of uantum molecular dynamics. World Scientific, Singapore
81. McCullough EA, Wyatt RE (1969) Quantum dynamics of the collinear (H,H_2) reaction. J Chem Phys 51:1253
82. McCullough EA, Wyatt RE (1971) Dynamics of the collinear (H,H_2) reaction. I. Probability density and flux. J Chem Phys 54:3578
83. Whitehead RJ, Handy NC (1975) J Mol Spec 55:356
84. Schatz GC, Kuppermann A (1976) Quantum mechanical reactive scattering for three-dimensional atom plus diatom systems. I. Theory. J Chem Phys 65:4642
85. Schatz GC, Kuppermann A (1976) Quantum mechanical reactive scattering for three-dimensional atom plus diatom systems. II. Accurate cross sections for $H + H_2$. J Chem Phys 65:4668–4692
86. Carter S, Handy NC (1986) An efficient procedure for the calculation of the vibrational energy levels of any triatomic molecule. Mol Phys 57:175
87. Bačić Z, Light JC (1986) Highly excited vibrational levels of "floppy" triatomic molecules: A discrete variable representation – Distributed Gaussian approach. J Chem Phys 85:4594
88. Bačić Z, Light JC (1987) Accurate localized and delocalized vibrational states of HCN/HNC. J Chem Phys 86:3065
89. Köppel H, Cederbaum LS, Domcke W (1982) Strong nonadiabatic effects and conical intersections in molecular spectroscopy and unimolecular decay: $C_2H_4^+$. J Chem Phys 77:2014
90. Nauts A, Wyatt RE (1983) New approach to many-state quantum dynamics: the recursive-residue-generation method. Phys Rev Lett 51:2238
91. Sibert EL (1990) Variational and perturbative descriptions of highly vibrationally excited molecules. Int Rev Phys Chem 9:1
92. Elkowitz AB, Wyatt RE (1975) Quantum-mechanical reaction cross-section for 3-dimensional hydrogen-exchange reaction. J Chem Phys 62:2504
93. Heller EJ. Time-dependent approach to semiclassical dynamics. J Chem Phys 62:1544
94. Heller EJ. Time-dependent variational approach to semiclassical dynamics. J Chem Phys 64:63
95. Heller EJ () Wigner phase space method: Analysis for semiclassical applications. J Chem Phys 65:1289
96. Leforestier C, Bisseling RH, Cerjan C, Feit MD, Friesner R, Guldenberg A, Hammerich A, Jolicard G, Karrlein W, Meyer HD, Lipkin N, Roncero O, Kosloff R (1991) A comparison of different propagation schemes for the time dependent Schrödinger equation. J Comput Phys 94:59

97. Kosloff R (1988) Time-dependent quantum-mechanical methods for molecular dynamics. J Phys Chem 92:2087
98. Kosloff D, Kosloff R (1983) A Fourier-method solution for the time-dependent Schrödinger equation as a tool in molecular dynamics. J Comput Phys 52:35
99. Wang X-G, Carrington Jr T (2003) A contracted basis-Lanczos calculation of vibrational levels of methane: Solving the Schrödinger equation in nine dimensions. J Chem Phys 119:101
100. Wang X-G, Carrington Jr T (2004) Contracted basis lanczos methods for computing numerically exact rovibrational levels of methane. J Chem Phys 121(7):2937–2954
101. Tremblay JC, Carrington Jr T (2006) Calculating vibrational energies and wave functions of vinylidene using a contracted basis with a locally reorthogonalized coupled two-term lanczos eigensolver. J Chem Phys 125:094311
102. Wang X, Carrington Jr T (2008) Vibrational energy levels of CH_5^+. J Chem Phys 129:234102
103. Norris LS, Ratner MA, Roitberg AE, Gerber RB (1996) Moller-plesset perturbation theory applied to vibrational problems. J Chem Phys 105:11261
104. Christiansen O (2003) Moller-plesset perturbation theory for vibrational wave functions. J Chem Phys 119:5773
105. Christiansen O (2004) Vibrational coupled cluster theory. J Chem Phys 120:2149
106. Christiansen O, Luis J (2005) Beyond vibrational self-consistent-field methods: Benchmark calculations for the fundamental vibrations of ethylene. Int J Quant Chem 104:667
107. Scribano Y, Benoit D (2007) J Chem Phys 127:164118
108. Barone V (2005) Anharmonic vibrational properties by a fully automated second-order perturbative aproach. J Chem Phys 122:014108
109. Bowman J (1978) Self-consistent field energies and wavefunctions for coupled oscillators. J Chem Phys 68:608
110. Bowman J, Christoffel K, Tobin F. Application of SCF-SI theory to vibrational motion in polyatomic molecules. J Phys Chem 83:905
111. Bégué D, Gohaud N, Pouchan C, Cassam-Chenaï P, Liévin J (2007) A comparison of two methods for selecting vibrational configuration interaction spaces on a heptatomic system: Ethylene oxide. J Chem Phys 127:164115
112. Carter S, Bowman JM, Handy NC (1998) Extensions and tests of "multimodes": a code to obtain accurate vibration/rotation energies of many-mode molecules. Theor Chem Acc 100:191
113. Bowman JM (2000) Chemistry—beyond platonic molecules. Science 290:724
114. Culot F, Laruelle F, Liévin J (1995) A vibrational CASSCF study of stretch-bend interactions and their influence on infrared intensities in the water molecule. Theor Chem Acc 92:211
115. Heislbetz S, Rauhut G (2010) Vibrational multiconfiguration self-consistent field theory: Implementation and test calculations. J Chem Phys 132:124102
116. Meyer H-D, Le Quéré F, Léonard C, Gatti F (2006) Calculation and selective population of vibrational levels with the Multiconfiguration Time-Dependent Hartree (MCTDH) algorithm. Chem Phys 329:179–192
117. Joubert Doriol L, Gatti F, Iung C, Meyer H-D (2008) Computation of vibrational energy levels and eigenstates of fluoroform using the multiconfiguration time-dependent Hartree method. J Chem Phys 129:224109
118. Gerber RB, Buch V, Ratner MA (1982) Time-dependent self-consistent field approximation for intramolecular energy transfer. I. Formulation and application to dissociation of van der Waals molecules. J Chem Phys 77:3022
119. Gerber RB, Ratner MA (1988) Self-consistent-field methods for vibrational excitations in polyatomic systems. Adv Chem Phys 70:97
120. Makri N, Miller WH (1987) Time-dependent self-consistent (TDSCF) approximation for a reaction coordinate coupled to a harmonic bath: Single and multiconfiguration treatments. J Chem Phys 87:5781

121. Kotler Z, Nitzan A, Kosloff R (1988) Multiconfiguration time-dependent self-consistent field approximation for curve crossing in presence of a bath. A Fast Fourier Transform study. Chem Phys Lett 153:483
122. Meyer H-D, Manthe U, Cederbaum LS (1990) The multi-configurational time-dependent Hartree approach. Chem Phys Lett 165:73–78
123. Manthe U, Meyer H-D, Cederbaum LS (1992) Wave-packet dynamics within the multi-configuration Hartree framework: General aspects and application to NOCl. J Chem Phys 97:3199–3213
124. Beck MH, Jäckle A, Worth GA, Meyer H-D (2000) The multi-configuration time-dependent Hartree (MCTDH) method: A highly efficient algorithm for propagating wave packets. Phys Rep 324:1–105
125. Meyer H-D, Gatti F, Worth GA (eds) (2009) Multidimensional quantum dynamics: MCTDH theory and applications. Wiley, Weinheim
126. Worth GA, Beck MH, Jäckle A, Meyer H-D (2007) The MCTDH Package, Version 8.2, (2000). Meyer HD, Version 8.3 (2002), Version 8.4 (2007). See http://mctdh.uni-hd.de/
127. Jolicard G, Austin E (1985) Optical potential stabilisation method for predicting resonance level. Chem Phys Lett 121:106
128. Jolicard G, Austin E (1986) Optical potential method of caculating resonance energies and widths. Chem Phys 103:295
129. Riss UV, Meyer H-D (1993) Calculation of resonance energies and widths using the complex absorbing potential method. J Phys B 26:4503
130. Riss UV, Meyer H-D (1996) Investigation on the reflection and transmission properties of complex absorbing potentials. J Chem Phys 105:1409
131. Moiseyev N (1998) Quantum theory of resonances: calculating energies, widths and cross-sections by complex scaling. Phys Rep 302:211
132. Moiseyev N (2011) Non-Hermitian quantum mechanics. Cambridge University Press, Cambridge, UK
133. Thompson KC, Jordan MJT, Collins MA (1998) Polyatomic molecular potential energy surfaces by interpolation in local internal coordinates. J Chem Phys 108:8302–8316
134. Varandas AJC (2004) Modeling and interpolation of global multi-sheeted potential energy surfaces. In: Domcke W, Yarkony DR, Köppel H (eds), Conical Intersections. World Scientific, Singapore p 205
135. Huang X, Braams BJ, Bowman JM (2005) *Ab initio* potential energy and dipole moment surfaces for $H_5O_2^+$. J Chem Phys 122:044308
136. Miller WH, Handy NC, Adams JE (1980) Reaction path hamiltonian for polyatomic molecules. J Chem Phys 72:99
137. Ruf BA, Miller WH (1988) A new (cartesian) reaction-path mode for dynamics in polyatomic systems, with application to h-atom transfer in malonaldehyde. J Chem Soc Faraday Trans 84:1523
138. Tew D, Handy N, Carter S (2003) A reaction surface hamiltonian study of malonaldehyde. J Chem Phys 125:084313
139. Lauvergnat D, Nauts A, Justum Y, Chapuisat X (2001) A harmonic adiabatic approximation to calculate highly excited vibrational levels of "floppy molecules". J Chem Phys 114:6592
140. Lauvergnat D, Nauts A (2004) A harmonic adiabatic approximation to calculate vibrational states of ammonia. Chem Phys 305:105
141. Gromov EV, Trofimov AB, Gatti F, Köppel H (2010) Theoretical study of photoinduced ring-opening in furan. J Chem Phys 133:164309
142. Gromov EV, Leveque C, Gatti F, Burghardt I, Köppel H (2011) Ab initio quantum dynamical study of photoinduced ring-opening in furan. J Chem Phys 135:164305
143. Köppel H, Domcke W, Cederbaum LS (1984) Multimode molecular dynamics beyond the Born-Oppenheimer approximation. Adv Chem Phys 57:59
144. Brocks G, Avoird AVD, Sutcliffe BT, Tennyson J (1983) Mol Phys 50:1025

145. Nauts A, Chapuisat X (1985) Momentum, quasi-momentum and hamiltonian operators in terms of arbitrary curvilinear coordinates, with special emphasis on molecular hamiltonians. Mol Phys 55:1287
146. Sutcliffe BT, Tennyson J (1986) A generalized approach to the calculation of ro-vibrational spectra of triatomic molecules. Mol Phys 58:1053–1066
147. Handy NC (1987) The derivation of vibration-rotation kinetic energy operators, in internal coordinates. Mol Phys 61:207
148. Lauvergnat D, Nauts A (2002) Exact numerical computation of a kinetic energy operator in curvilinear coordinates. J Chem Phys 116:8560
149. Ndong M, Joubert Doriol L, Meyer H-D, Nauts A, Gatti F, Lauvergnat D (2012) Automatic computer procedure for generating exact and analytical kinetic energy operators based on the polyspherical approach. J Chem Phys 136:034107
150. Gatti F, Iung C, Menou M, Justum Y, Nauts A, Chapuisat X (1998) Vector parametrization of the n-atom problem in quantum mechanics. I. Jacobi vectors. J Chem Phys 108:8804
151. Gatti F, Iung C (2009) Exact and constrained kinetic energy operators for polyatomic molecules: The polyspherical approach. Phys Rep 484:1–69
152. Yu H-G (2004) Full-dimensional quantum calculations of vibrational spectra of six-atom molecules. i. theory and numerical results. J Chem Phys 120:2270
153. Vendrell O, Gatti F, Meyer H-D. Dynamics and infrared spectroscopy of the protonated water dimer. Angew Chem Int Ed 46:6918–6921
154. Vendrell O, Gatti F, Meyer H-D. Strong isotope effects in the infrared spectrum of the zundel cation. Angew Chem Int Ed 48:352–355
155. Raab A, Worth G, Meyer H-D, Cederbaum LS. Molecular dynamics of pyrazine after excitation to the S_2 electronic state using a realistic 24-mode model Hamiltonian. J Chem Phys 110:936–946
156. Hammer T, Manthe U (2011) Intramolecular proton transfer in malonaldehyde: Accurate multilayer multi-configurational time-dependent Hartree calculations. J Chem Phys 134:224305
157. Huarte-Larrañaga F, Manthe U (2000) Full dimensional quantum calculations of the $CH_4 + H \rightarrow CH_3 + H_2$ reaction rate. J Chem Phys 113:5115
158. Makri N (2008) Equilibrium and dynamical path integral methods in bacterial photosynthesis. In: Aartsma TJ, Matysik J (eds) Biophysical techniques in photosynthesis. Series advances in photosynthesis and respiration, vol 2. Springer, Dordrecht
159. Polyansky OL, Zobob NF, Viti S, Tennyson J, Bernath PF, Wallace L (1997) Water on the sun. Science 277:346
160. Callegari A, Theulé P, Muenter JS, Tolchenov RN, Zobov NF, Polyansky OL, Tennyson J, Rizzo TR (2002) Dipole moments of higly vibrationnally excited water. Science 297:993
161. Polyansky OL, Császár AG, Shririn SV, Zobob NF, Barletta P, Tennyson J, Schenke DW, Knowles PJ (2003) High-accuracy ab initio rotation-vibration transitions for water. Science 299:539
162. Ndengué SA, Gatti F, Schinke R, Meyer H-D, Jost R (2010) Absorption cross section of ozone Isotopologues calculated with the multiconfiguration time-dependent Hartree (MCTDH) method: I. The Hartley and Huggins bands. J Phys Chem A 114:9855–9863
163. Ndengué SA, Schinke R, Gatti F, Meyer H-D, Jost R (2012) Comparison of the Huggins band for six ozone isotopologues: vibrational levels and Absorption Cross Section. J Phys Chem A 116:12260
164. Ndengué SA, Schinke R, Gatti F, Meyer H-D, Jost R (2012) Ozone photodissociation: isotopic and electronic branching ratios for asymmetric isotopologues. J Phys Chem A 116:12271
165. Schinke R (2011) Photodissociation of N_2O: Potential energy surfaces and absorption spectrum. J Chem Phys 134:064313
166. Gatti F, Iung C, Leforestier C, Chapuisat X (1999) Fully coupled 6D calculations of the ammonia vibration-inversion-tunneling states with a split hamiltonian pseudospectral approach. J Chem Phys 111:7236–7243

167. Rajamaki T, Miani A, Halonen L (2003) Vibrational energy levels for symmetric and asymmetric isotopomers of ammonia with an exact kinetic energy operator and new potential energy surfaces. J Chem Phys 118:2003
168. Léonard C, Carter S, Handy NC (2003) The barrier to inversion of ammonia. Chem Phys Lett 370:360
169. Wang X-G, Sibert III EL (1999) A nine-dimensional perturbative treatment of the vibrations of methane and its isotopomers. J Chem Phys 111:4510
170. Venuti E, Halonen L, Della Valle RG (1999) High dimensional anharmonic potential energy surfaces: The case of methane. J Chem Phys 110:7339
171. Carter S Bowman JM (2000) Variational calculations of rotational-vibrational energies of CH_4 and isotopomers using an adjusted ab initio potential. J Phys Chem A 104:2355
172. Yu H-G (2004) Converged quantum dynamics calculations of vibrational energies of CH_4 and CH_3D using an ab initio potential. J Chem Phys 121:6334
173. Cassam-Chenaï P, Liévin J (2012) Ab initio calculation of the rotational spectrum of methane vibrational ground state. J Chem Phys 136:174309
174. Cohen-Tannoudji C, Dupont-Roc J, Grynberg G (1997) Photons and atoms: introduction to quantum electrodynamics. Wiley, New York
175. Cohen-Tannoudji C, Dupont-Roc J, Grynberg G (1998) Atom-photon interactions. Wiley Science Paperback Series. Wiley, New York
176. Levine RD, Bernstein RB (1987) Molecular reaction dynamics and chemical reactivity. Oxford University Press, New York,Oxford
177. Ertl G (1983) Primary steps in catalytic synthesis of ammonia. J Vac Sci Tech A 1:1247–1253
178. Bonn M, Kleyn AW, Kroes G-J (2002) Real time chemical dynamics at surfaces. Surf Sci 500:475
179. Kroes G-J. Frontiers in surface scattering simulations. Science 321:794
180. Díaz C, Pijper E, Olsen RA, Busnengo HF, Auerbach DJ, Kroes GJ (2009) Chemically accurate simulation of a prototypical surface reaction: H_2 dissociation on Cu(111). Science 326:832
181. Farías D, Díaz C, Rivière P, Busnengo HF, Nieto P, Somers MF, Kroes G-J, Salin A, Martín F (2004) In-plane and out-of-plane diffraction of H_2 from metal surfaces. Phys Rev Lett 93:246104
182. Beck R, Maroni P, Papageorgopoulos DC, Dang TT, Schmid MP, Rizzo TR (2003) Vibrational mode-specific reaction of methane on a nickel surface. Science 302:98–100
183. Juurlink LBH, Killelea DR, Utz AL (2009) State-resolved probes of methane dissociation dynamics. Progr Surf Sci 84:69
184. Wu T, Werner H-J, Manthe U (2004) First-principles theory for the $H + CH_4 \rightarrow H_2 + CH_3$ reaction. Science 306:2227–2229
185. Zhang W, Zhou Y, Wu G, Lu Y, Pan H, Fu B, Shuai Q, liu L, Liu S, Zhang L, Jiang B, Dai D, Lee S-Y, Xie Z, Braams BJ, Bowman JM, Collins MA, Zhang DH, Yang X (2010) Depression of reactivity by the collision energy in the single barrier $H + CD_4 \rightarrow HD + CD_3$ reaction. Proc Natl Acad Sci USA 107:12782
186. Pu JZ, Corchado JC, Truhlar DG (2001) Test of variational transition state theory with multidimensional tunneling contributions against an accurate full-dimensional rate constant calculation for a six-atom system. J Chem Phys 115:6266–6267
187. Pu JZ, Truhlar DG (2002) Parameterized direct dynamics study of rate constants of H with CH_4 from 250 to 2400 K. J Chem Phys 116:1468
188. Chakraborty A, Zhao Y, Lin H, Truhlar DG (2006) Combined valence bond-molecular mechanics potential-energy surface and direct dynamics study of rate constants and kinetic isotope effects for the $H + C_2H_6$ reaction. J Chem Phys 124:044315
189. Seal P, Oyedepo G, Truhlar DG (2013) Kinetics of the hydrogen atom abstraction reactions from 1-Butanol by hydroxyl radical: Theory mathces experiments and more. J Phys Chem A 117:275
190. Ma J, Li J, Guo H (2012) Quantum dynamics of the $HO + CO \rightarrow H + CO_2$. J Phys Chem Lett 3:2482

191. Althorpe SC (2010) Setting the trap for reactive resonances. Science 327:1460
192. Dobbyn AJ, Stumpf M, Keller H-M, Schinke R (1996) Theoretical study of the unimolecular dissociation $HO_2 \rightarrow H + O_2$. II. Calculation of resonant states, dissociation rates, and O_2 product state distributions. J Chem Phys 104:8357
193. Miller WH (1990) Recent advances in quantum mechanical reactive scattering theory (Including comparison of recent experiments with rigorous calculations of state-to-state cross sections for the $H/D + H_2 \rightarrow H_2/HD + H$ reactions). Ann Rev Phys Chem 41:245
194. D'Mello MJ, Manolopoulos DE, Wyatt RE (1994) Theory, experiment, and the $H + D_2$ reaction. Science 263:102
195. Qiu M, Ren Z, Che L, Dai D, Harich SA, Wang X, Yang X, Xu C, Xie D, Gustafsson M, Skoedje RT, Sun Z, Zhang D-H (2006) Observation of feshbach resonances in the $F + H_2 \rightarrow HF + H$ reaction. Science 311:1440
196. Dulieu O, Krems R, Weidemüller M, Willitsch S (2011) Physics and chemistry of cold molecules. Phys Chem Chem Phys 13:18703
197. Quéméner G, Julienne PS (2012) Ultracold molecules under control! Chem Rev 112:4949
198. Jin DS, Ye J (2012) Introduction to ultracold molecules: New frontiers in quantum and chemical physics. Chem Rev 112:4801
199. Baranov MA, Dalmonte M, Pupillo G, Zoller P (2012) Condensed matter theory of dipolar quantum gases. Chem Rev 112:5012
200. Narevicius E, Raizen MG (2012) Toward cold chemistry with magnetically decelerated supersonic beams. Chem Rev 112:4879
201. Stuhl BK, Hummon MT, Yeo M, Quéméner G, Bohn JL, Ye J (2012) Evaporative cooling of the dipolar hydroxyl radical. Nature 492:396.
202. Fioretti A, Comparat D, Crubellier A, Dulieu O, Masnou-Seuuws F, Pillet P (1998) Formation of cold Cs_2 molecules through photoassociation. Phys Rev Lett 80:4402
203. Vatasescu M, Dulieu O, Amiot C, Comparat D, Drag C, Kokooline V, Masnou-Seeuws F, Pillet P (2000) Multichannel tunneling in the Cs_2 $O_{(g)}^{(-)}$ photoassociation spectrum. Phys Rev A 61:044701
204. Dion CM, Drag C, Dulieu O, Torla BL, Masnou-Seuuws F, Pillet P (2001) Resonant coupling in the formation of ultracold ground state molecules via photoassociation. Phys Rev Lett 86:2253
205. Jankunas J, Zare RN, Bouakline F, Althorpe SC, Herràez-Aguilar D, Aoiz FJ (2012) Seemingly anomalous angular distribution in $H + D_2$ reactive scattering. Science 336:1687
206. Melnik DG, Miller TA (2008) The changing shapes of molecules. Science 320:881
207. Bukowski R, Szalewicz K, Groenenboom GC, van der Avoird A (2007) Predictions of the properties of water from first principles. Science 315:1249
208. Leforestier C, Gatti F, Fellers RS, Saykally RJ (2002) Determination of a flexible (12D) water dimer potential via direct inversion of spectroscopic data. J Chem Phys 117:8710
209. Leforestier C, Szalewicz K, van der Avoird A (2012) Spectra of water dimer from a new ab initio potential with flexible monomers. J Chem Phys 137:014305
210. Huang XC, Braams BJ, Bowman JM (2006) Ab initio potential energy and dipole moment surfaces of $(H2O)_{(2)}$. J Chem Phys 110:445
211. Leforestier C (2012) Infrared shifts of the water dimer from the fully flexible ab initio hbb2 potential. Phil Trans R Soc A 370:2675
212. Giese K, Petković M, Naundorf H, Kühn O (2006) Multidimensional quantum dynamics and infrared spectroscopy of hydrogen bonds. Phys Rep 430:211
213. Vendrell O, Meyer H-D (2008) A proton between two waters: insight from full-dimensional quantum-dynamics simulations of the $[H_2O\text{-}H\text{-}OH_2]^+$ cluster. Phys Chem Chem Phys 10:4692–4703
214. Xantheas SS (2009) Computational chemistry dances with hydrogen cations. Nature 457:673–674
215. Vuilleumier R, Borgis D (1999) Transport and spectroscopy of the hydrated proton: A molecular dynamics study. J Chem Phys 111:4251

216. Vuilleumier R, Borgis D (2012) Proton conduction: Hopping along hydrogen bonds. Nat Phys 119:432
217. Wassermann TN, Luckhaus D, Coussan S, Suhn MA (2006) Proton tunneling estimates for malonaldehyde vibrations from supersonic jet and matrix quenching experiments. Phys Chem Chem Phys 8:2344
218. Lüttschwager NOB, Wassermann TN, Coussan S, Suhm MA (2010) Periodic bond breaking and making in the electronic ground state on a sub-picosecond timescale: OH bending spectroscopy of malonaldehyde in the frequency domain at low temperature. Phys Chem Chem Phys 12:8201
219. Trivella A, Wassermann TN, Mestdagh JM, Manca Tanner C, Marinelli F, Roubin P, Coussan S (2010) New insights into the photodynamics of acetylacetone: isomerization and fragmentation in low-temperature matrixes. Phys Chem Chem Phys 12:8300
220. Lüttschwager NOB, Wassermann TN, Coussan S, Suhm MA (2013) Vibrational tuning of the hydrogen transfer in malonaldehyde—a combined FTIR and raman jet study. Phys Chem Chem Phys 14:2211
221. Marquardt R, Quack M (2001) Energy redistribution in reacting systems. In: Moore J, Spencer N (eds) Encyclopedia of chemical physics and physical chemistry. IOP publishing, Bristol, p 897
222. Wyatt RE, Iung C (1996) Quantum mechanical studies of molecular sepctra and dynamics. In: Wyatt RE, Zhang JZH (eds) Dynamics of molecules and chemical reactions. Marcel Dekker, New York, pp 59–122
223. Gatti F, Iung C (2009) Intramolecular vibrational energy redistribution and infrared spectroscopy. In: Meyer H-D, Gatti F, Worth GA (eds) Multidimensional quantum dynamics: MCTDH theory and applications. Wiley, Weinheim, pp 275–291
224. Zewail AH (2001) Nobel lecture. In: De Schryver FC, De Feyter S, Schweitzer G (eds) Femtochemistry. Wiley, Weinheim, p 58
225. Botan V, Hamm P (2008) Intramolecular vibrational energy relaxation in nitrous acid (HONO). J Chem Phys 129:234511
226. Botan V, Hamm P (2008) Temperature dependence of the IR driven cis-trans isomerization of nitrous acid (HONO). J Chem Phys 129:114510
227. Richter F, Gatti F, Léonard C, Le Quéré F, Meyer H-D (2007) Time–dependent wave packet study on trans–cis isomerisation of HONO driven by an external field. J Chem Phys 127:164315
228. Lasorne B, Worth GA, Robb MA (2011) Excited-state dynamics. Wires Comput Mol Sci 1:460–475
229. Schuurman MS, Weinberg DE, Yarkony DR (2007) On the simulation of photoelectron spectra in molecules with conical intersections and spin-orbit coupling: the vibronic spectrum of CH_3S. J Chem Phys 127:104309
230. Poluyanov LV, Domcke W (2009) Spin-orbit vibronic coupling in Jahn-Teller and Renner systems. In: Köppel H, Yarkony DR, Barentzen H (eds) The Jahn-Teller effect, fundamentals and implications for physics and chemistry. Springer series in chemical physics, vol 97. Springer, Heidelberg, pp 77–97
231. Burghardt I, Meyer H-D, Cederbaum LS (1999) Approaches to the approximate treatment of complex molecular systems by the multiconfiguration time-dependent Hartree method. J Chem Phys 111:2927–2939
232. Allan CSM, Lasorne B, Worth GA, Robb MA (2010) A straightforward method of analysis for direct quantum dynamics: Application to the photochemistry of a model cyanine. J Chem Phys 114:8713
233. Worth GA, Robb MA, Burghardt I (2004) Non-adiabatic direct dynamics using variational gaussian wavepackets: The $\tilde{X}/\tilde{A}$ manifold of the butatriene cation. Farad Discuss 127:307–323
234. Sobolewski AL, Domcke W, Hättig C (2005) Tautomeric selectivity of the excited-state lifetime of guanine / cytosine base pairs: The role of electron-driven proton-transfer processes. Proc Natl Acad Sci 102:17903–17906

235. Asturiol D, Lasorne B, Robb MA, Blancafort L (2009) Photophysics of the pi,pi* and n,pi* states of thymine: Ms-caspt2 minimum-energy paths and casscf on-the-fly dynamics. J Phys Chem A 113:10211
236. Abe M, Ohtsuki Y, Fujimura Y, Domcke W (2005) Optimal control of ultrafast cis-trans photisomerisation of retinal in rhodopsin via a conical intersection. J Chem Phys 123:144508
237. Fleming GR, Ratner MA (2008) Grand challenges in basic energy sciences. Phys Today 61:28
238. Lasorne B, Bearpark MJ, Robb MA, Worth GA (2008) Controlling S_1/S_0 decay and the balance between photochemistry and photostability in benzene: A direct quantum dynamics study. J Phys Chem A 112:13017–13027
239. Asturiol D, Lasorne B, Worth GA, Robb MA, Blancafort L. Exploring the sloped-to-peaked S_2/S_1 seam of intersection of thymine with electronic structure and direct quantum dynamics. Phys Chem Chem Phys 12:4949
240. Blanchet V, Zgierski MZ, Seideman T, Stolow A (1999) Discerning vibronic molecular dynamics using time-resolved photoelectron spectroscopy. Science 401:52
241. Gelin MF, Sharp LZ, Egorova D, Domcke W (2012) Bath-inudced correlations and relaxation of vibronic dimers. J Chem Phys 136:034507
242. Scholes GD, Fleming GR, Olaya-Castro A, van Grondelle R (2012) Lessons from nature about solar light harvesting. Natl Chem 3:763
243. Rozzi CA, Falke SM, Spallanzani N, Rubio A, Molinari E, Brida D, Maiuri M, Cerullo G, Schramm H, Christophers J, Lienau C (2013) Quantum coherence controls the charge separation in a prototypical artificial light-harvesting system. Nat Commun 4:1603
244. Bayfield JE (1999) Quantum evolution. Wiley, New York
245. Guerin S, Jauslin HR (2003) Control of quantum dynamics by laser pulses: adiabatic floquet theory. Adv Chem Phys 125:147–267
246. Brumer P, Shapiro M (1986) Control of unimolecular reactions using coherent light. Chem Phys Lett 126:541
247. Gaubatz U, Rudecki P, Becker M, Schiemann S, Külz M, Bergmann K (1988) Population switching between vibrational levels in molecular-beams. Chem Phys Lett 149:463
248. Gaubatz U, Rudecki P, Schiemann S, Bergmann K (1990) Population transfer between molecular vibrational levels by stimulated raman-scattering with partially overlapping laserfields - a new concept and experimental results. J Chem Phys 92:5363
249. Tannor DJ, Rice SA (1985) Control of selectivity of chemical-reaction via control of wave packet evolution. J Chem Phys 83:5013
250. Tannor DJ, Kosloff R, Rice SA (1986) Coherent pulse sequence induced control of selectivity of reaction - exact quatum-mechanical calculations. J Chem Phys 85:5805
251. Judson RS, Rabitz H (1992) Teaching lasers to control molecules. Phys Rev Lett 68:1500
252. Rabitz H, de Vivie-Riedle R, Motkuz M, Kompa K (2000) Chemistry—whither the future of controlling quantum phenomena? Science 288:824
253. Daniel C, Full J, González L, Lupulescu C, Manz J, Merli A, Vajda S, Wöste L (2003) Deciphering the reaction dynamics underlying optimal control laser fields. Science 299:536–539
254. von den Hoff P, Thallmair S, Kowalewski M, Siemering R, de Vivie-Riedle R (2012) Optimal control theory -closing the gap between theory and experiment. Phys Chem Chem Phys 14:14460
255. Znakovskaya I, von den Hoff P, Zherebtsov S, Wirth A, Herrwerth O, Vraking MJJ, de Vivie-Riedle R, Kling MF (2009) Phys Rev Lett 103:103002
256. Bayer T, Braun H, Sarpe C, Siemering R, von den Hoff P, de Vivie-Riedle R, Baumert T, Wollenhaupt M (2013) Phys Rev Lett 110:123003
257. Feynman RP (1982) Simulating physics with computers. Int J Theo Phys 21:467
258. Deutsch D (1985) Quantum theory, the church-turing principle and the universal quantum computer. Proc Natl Acad Sci USA 400:97
259. Barz S, Kashefi E, Broadbent A, Fitzsimons JF, Zeilinger A, Walther P (2012) Demonstration of blind quantum computing. Science 335:303

260. Tesch CM, de Vivie-Riedle R (2002) Quantum computation with vibrationally excited molecules. Phys Rev Lett 89:57901
261. Bihary Z, Glenn D, Lidar D, Apkarian VA (2002) An implementation of the deutsch-jozsa algorithm on molecular vibronic coherences through four-wave mixing: a theoretical study. Chem Phys Lett 360:62316
262. Zadoyan R, Kohen D, Lidar D, Apkarian VA (2001) The manipulation of massive ro-vibronic superpositions using time-frequency-resolved coherent anti-stokes raman scattering (tfrcars): from quantum control to quantum computing. Chem Phys 266:323
263. Vala J, Amitay Z, Zhang B, Leone S, Kosloff R (2002) Experimental implementation of the deutsch-jozsa algorithm for three-qubit functions using pure coherent molecular superpositions. Phys Rev A 66:62316
264. Zaari RR, Brown A (2011) Effect of diatomic molecular properties on binary laser pulse optimizations of quantum gate operations. J Chem Phys 135:044317

Elementary Molecule–Surface Scattering Processes Relevant to Heterogeneous Catalysis: Insights from Quantum Dynamics Calculations

2

Cristina Díaz, Axel Gross, Bret Jackson, and Geert-Jan Kroes

Abstract

We show some examples of molecule/surface systems that have been recently described using quantum dynamics simulations, such as H_2/metal surfaces and CH_4/metal surfaces. Quantum simulations performed on these systems have yielded results in excellent agreement with independent experimental measurements. These simulations have allowed, for example, the analysis of the role of the internal degrees of freedom of the molecule, the interpretation of puzzling controversial experimental results, and the suggestion of novel experiments.

2.1 Introduction

Although we do not notice it often, in everyday life we are surrounded by phenomena involving molecule–surface interactions: for instance, the corrosion of a coin (or any other metallic object). Considering the coin, the O_2 molecules in the air interact with the metal surface atoms causing a structural damage, leaving a layer

C. Díaz (✉)
Departamento de Química, Módulo 13, Universidad Autónoma de Madrid, 28049 Madrid, Spain
e-mail: cristina.diaz@uam.es

A. Gross
Institut für Theoretische Chemie, Universität Ulm, 89069 Ulm, Germany
e-mail: axel.gross@uni-ulm.de

B. Jackson
Department of Chemistry, University of Massachusetts, Amherst, MA 01003, USA
e-mail: jackson@chem.umass.edu

G.-Jan Kroes
Leiden Institute of Chemistry, Gorlaeus Laboratories, Leiden University, 2300 RA Leiden, The Netherlands
e-mail: g.j.kroes@chem.univleiden.nl

F. Gatti (ed.), *Molecular Quantum Dynamics*, Physical Chemistry in Action,
DOI 10.1007/978-3-642-45290-1_2,

of oxidized material (rust) on the coin. Another example is the green appearance on the domes of some old buildings. This latter phenomenon is due to the oxidation of copper, material from which the domes are made.

Interactions of molecules with surfaces also play an important role in wide range of technologically relevant applications. For example, the dissociative adsorption of a molecule on a metal surface is the first and one of the fundamental reaction steps occurring in heterogeneous catalysis—about 90 % of the chemical manufacturing processes employed worldwide use catalysts in one form or another [10]. For example, the industrial synthesis of ammonia, from N_2 and H_2, is mediated by a hydrogenation reaction where an iron or a ruthenium surface catalyzes the reaction. Furthermore, N_2 dissociation is considered the rate-limiting step in this process. At the point, we should point out that most of the ammonia produced is used for fertilizers, making ammonia essential for our society. Another example closely related to our daily life can be found in the exhaust systems of cars, where platinum, rhodium, and palladium surfaces are used as catalysts to convert poisonous gasses expelled directly from the engine, like CO and NO_x, harmful to the environment, into a less harmful exhaust mixture of CO_2, H_2O, N_2, and O_2, before being ejected into the air. Platinum surfaces are also used as catalysts in the process of dehydrogenation of butane (C_4H_{10}) to butadiene (C_4H_6), which is used in the production of synthetic rubber or in the upgrading of the octane rating of gasoline [84]. Other examples of chemical reactions of industrial importance in which surfaces play the role of catalyst are: (1) the synthesis of methanol (CH_3OH) from CO and H_2, (2) the oxidation of ethylene to ethylene oxide, which is used in the production of antifreezes, (3) lubrication processes that influences the durability of mechanical systems, and (4) crystals growth, which determines, e.g., the quality of semiconductor devices. Special mention deserves the steam reforming process, through which methane (CH_4) and water molecules react over a Ni catalyst producing hydrogen [4, 79].[1] Due to its industrial significance, CH_4 dissociation in CH_3 and H is one of the most studied reaction in surface science [48, 60]. To conclude with this, by no means exhaustive, list of molecule/surfaces interaction processes relevant to heterogeneous catalysis we would like to point out that their importance was worldwide recognized in 2007 when the Nobel Prize in Chemistry was awarded to Gerhard Ertl for the detailed description of the sequence of elementary molecule/surface reactions by which ammonia is produced, unraveling the fundamental mechanisms of the Haber–Bosch process [25].

The reactions involved in these processes are usually too complicated to be studied in detail as a whole. Therefore surface scientists try to understand reaction mechanisms by breaking them up into simpler steps, which are studied under well-defined conditions. In this respect, accurate quantum dynamics simulations are essential to gain deeper insight into this elementary steps, and thereby to progress in modeling and improving heterogeneous catalysis. Nowadays, quantum dynamics studies including explicitly all molecular degrees of freedom (DOFs) can be

[1] Hydrogen may be considered the energy carrier of the future.

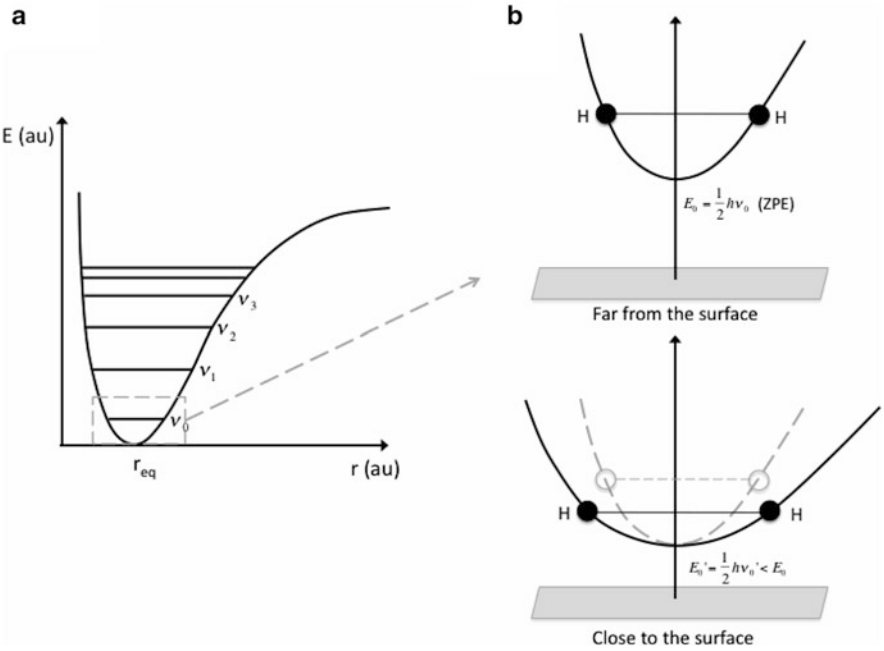

Fig. 2.1 Schematic representation of (**a**) vibrational states of a diatomic molecules and (**b**) vibrational softening

performed almost routinely for H_2 and its isotopes [32,53–55,57]. Full-dimensional quantum dynamics simulations based on coupled-channel (CC) and time-dependent wave packet (TDWP) methods have already been performed for reactive and nonreactive scattering of H_2 on low-index surfaces of various metals: Pd(100) [36, 38], Cu(100) [56], sulfur-precovered/Pd(100) [37], Pd(110) [15], Cu(111) [14,20], Cu(100) [86], Pt(111) [74], Pd(111) [7,8,18,29], Rh(111) [16], NiAl(110) [78], Cu(110) [58], CO-precovered/Ru(0001) [31], and c(2×2i)-Ti/Al(100) [9].

In order to test their theoretical models, the strategy used by surface scientists is to perform studies on benchmark systems for which experimental as well as theoretical analysis can be performed with similar accuracy. Throughout this chapter we will discuss six-dimensional quantum dynamics simulations performed on several of these H_2/metal surface benchmark systems, and we will analyze the results with the focus on the role played by the different DOFs. We will pay special attention to the effect that preexciting the vibrational DOFs has on molecular reactivity. As dissociative chemisorption involves stretching bonds until they rupture, reactivity of molecules on surfaces is closely related to energy transfer to and from the vibrational DOF. This energy transfer occurs not only for vibrationally excited molecules, where a deexcitation to the ground state causes an energy flux to the other DOFs. In fact, as we will discuss in the following section, the zero point energy (ZPE) of the molecule, the vibrational energy of the molecule ground state (see Fig. 2.1), can have a key effect on the reactivity of the so-called non-activated systems. In this case,

there can be an energy transfer from vibration to translation induced by vibrational softening. This vibrational softening occurs whenever a molecule approaches an attractive surface, and the attractive force between the surface and the atoms of the molecule becomes larger than the intramolecular force. This leads to a reduction of the force constant associated with the vibrational motion and, therefore, to the relaxation of the intramolecular bond. This bond relaxation induces a decrease in the potential well curvature, and, therefore, a decrease in the ZPE value (see Fig. 2.1).

We will also discuss first progress in the quantum dynamical treatment of polyatomic molecules (methane) reacting on surfaces, which has come possible, thanks to the development of reduced dimensionality models treating at least one vibrational mode of the molecule, and modeling the surface motion.

Finally, we should point out that quantum dynamics simulations represented throughout this chapter have been performed taking advantage of the Born–Oppenheimer approximation (BOA). In applying the BOA it is assumed that the interaction between the molecule and the surface takes place on the electronic ground state, i.e., that the electronic non-adiabatic effects are very small. Thus, these kind of studies are performed in two consecutive steps. First, the potential energy surface (PES), i.e., the electronic structure of the system, is computed, generally, using Density Functional Theory (DFT) [41, 51]. Quantum (and also classical) dynamics needs a continuous representation of the PES. Hence as an intermediate step the interpolation of the PES, for example with the corrugation reducing procedure [5], the modified Shepard method [13] or neural networks [62], is needed. Second, the motion of the nuclei on these PES is simulated. In this chapter, we will focus on this second step, the dynamics. At that point, we should also remark that most of the results presented here have been obtained by keeping the surface atoms fixed in the calculations, i.e., the energy transfer to and from phonons are neglected.

2.2 Reactive and Nonreactive Scattering of Molecules from Metal Surfaces

Molecule/surface systems are typically divided into two main groups, activated and non-activated systems. Activated systems are those in which the molecule needs a minimum energy to dissociate on the surface, i.e., those which present a minimum reaction barrier. On the other hand, systems with at least one barrierless reaction path are called non-activated. In the following, we show some representative quantum dynamics studies for prototypical activated and non-activated systems.

2.2.1 H_2/Metal Surfaces

2.2.1.1 Non-activated Systems

The first full-dimensional quantum dynamical calculations on dissociative adsorption were carried out on H_2/Pd(100) [38] (a non-activated system). These

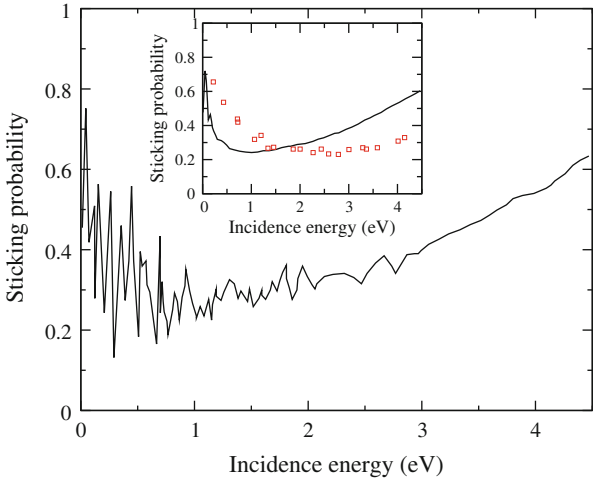

Fig. 2.2 Sticking probability versus incidence energy, under normal incidence, for $H_2(v = 0, J = 0)$/Pd(100) [38]. The *inset* show the convoluted sticking probability that account for the experimental molecular beam characteristics (*solid line*), and, for the sake of completeness, the experimental data from [75] (*square symbols*)

calculations showed a non-monotonous behavior of the dissociative adsorption (or sticking) probability as a function of the incidence energy of the molecule. This behavior was not unexpected for non-activated systems [75], but the sticking features are that the first it is not due to a precursor mechanism (see below) and second a strong oscillatory structure for low incidence energies (see Fig. 2.2), which, to present, has not been found experimentally. Before discussing the origin of these oscillations, it is worth mentioning that similar oscillations have been found later for other non-activated systems, such as H_2/Pd(110) [15], H_2/Pd(111) [7] and H_2/W(100) [49]. These oscillations have been attributed to the opening up of new diffraction and rotational excitation channels [35], which could explain why they are not obtained from classical (or quasiclassical) calculations, where neither the parallel momenta nor the energy take on discrete values, but change gradually. On the other hand, one may wonder why these oscillations are not observed experimentally. To answer this question we have to take into account the practical limitations of experimental setups. Whereas quantum calculations are performed considering a monoenergetic molecular beam containing H_2 in a well-defined quantum state (v, J) colliding with a frozen surface, the experimental molecular beams are not monochromatic, but display an energy spread, and the molecules are not only in the rovibrational ground state, but also occupy several rovibrational states according to a Boltzmann distribution. Furthermore, once the first impinging molecules are adsorbed, the perfect periodicity of the PES of the clean surface is destroyed. It should be also taken into account that the surface has a finite temperature, which reduces the coherence of the scattering process. And one should

also consider the influence of the incidence angle—usually >0 deg in experiments. All these factors smooth the experimental sticking curve. In fact, if the Boltzmann rovibrational distribution and the energy width of the experimental molecular beam are taken into account in the theoretical simulations, the quantum curve also shows a smooth appearance (see inset Fig. 2.2).

As shown in Fig. 2.2, quantum results on H_2/Pd(100) reproduce the initial decrease of the sticking probabilities observed experimentally in non-activated systems quite well. These results proved for the first time that this behavior is not due to any precursor state, as previously hypothesized, but to a purely dynamical mechanism. Initially it was suggested to be a pure steering mechanism, but later it was shown using classical trajectories that dynamics trapping contributes significantly to this behavior [6]. On the other hand, a comparison with quasi-classical dynamics simulations showed the key role played by the zero-point energy (ZPE) in the hydrogen dynamics [36]. Quasi-classical simulations suffer from the so-called violation of the ZPE: the initial ZPE can flow freely between all the molecular DOFs, which is not allowed in a quantum calculation. And as a result of this classical phenomenon the nonmonotonic behavior disappears in the quasi-classical results. The nonmonotonic behavior can be retrieved from classical calculations by leaving out the ZPE, i.e., by performing pure classical calculations, but in this case the sticking probability may be too low, because then the vibrational softening cannot be taken into account. It should be noted here that later it was shown that the parametrization of the PES used for the quantum dynamics simulations contained an artificial symmetry, which caused a lowering of the sticking probability [33]. However, all qualitative conclusions drawn from the quantum simulations [36, 38] still remain valid.

Thanks to the quantum dynamics simulations the role played by the internal degree of freedom of the molecule could also be analyzed, for both the rotational [24, 38] and the vibrational [34] mode. Quantum calculations have shown that molecular rotation suppresses the sticking of H_2 on Pd(100); the faster the molecules are rotating, the more the dissociative adsorption is suppressed. A closer inspection of these $J > 0$ results reveals that the suppression of sticking is due to molecules rotating in the so-called cartwheel rotation mode, $m_J = 0$. A similar result has been obtained for another non-activated system H_2/Rh(100) [24]. According to detailed balance, the consequence of these results, taken into account the principle of microscopic reversibility, is that the populations of rotational states in associative desorption is lower than expected for molecules in thermal equilibrium with the surface temperature (see Fig. 2.3). This rotational cooling was also found experimentally [81]. However, this behavior is not general for non-activated systems. Indeed, quantum calculations performed on H_2/Pd(110) [15] show a strong rotational enhancement in dissociative adsorption, which leads to rotational heating in associative desorption (see Fig. 2.3). In the case of Pd(111) [88] the scenario is even more complicated. At low incidence energy the dissociative adsorption probability first decreases with J and then increases, in agreement with experiments [30].

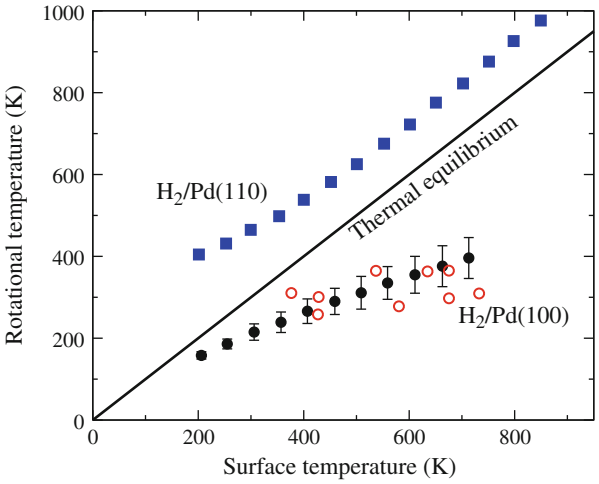

Fig. 2.3 Rotational temperatures of desorbing H_2 molecules from Pd(100): *solid black circles* theory from [38] and *red open circles* experiment from [81]. And from Pd(110): *solid blue squares* theory from [15]. The *solid line* corresponds to molecules in equilibrium with the surface temperature

As mentioned above, the suppression of sticking in H_2/Pd(100) by rotation is due to the cartwheel mode ($m_J = 0$), whereas the helicopter ($|m_J| = J$) mode enhances reactivity, i.e., quantum results suggest a strong steric effect. In order to verify this steric effect, the rotational quadrupole alignment parameter defined as:

$$A_0^{(2)}(J) = \left\langle \frac{3m_j^2 - J^2}{J^2} \right\rangle, \tag{2.1}$$

was computed from the fully initial-state resolved quantum sticking probabilities. $A_0^{(2)}(J)$ can change from -1 (molecules rotating in cartwheel fashion) to 2 (molecules rotating in helicopter fashion). In Fig. 2.1 the rotational alignment parameter as a function of the rotational quantum number, as obtained in [24], is shown. From this figure it can be seen that the $A_0^{(2)}(J)$ values are positive, and very similar to the experimental ones [90], confirming the steric effect. Results for H_2/Pd(110), shown in Fig. 2.4, show positive values [15], but much smaller than the ones computed for Pd(100).

The role of the initial vibrational state of the H_2 molecule has been also analyzed. This was done by means of the so-called vibrational efficacy, which gives a measure of the effectiveness of the vibrational energy to promote the dissociative adsorption. The vibrational efficacy can be computed using the simple formula:

$$\eta_v = \frac{E_0(v = 0, J = 0) - E_0(v = 1, J = 0)}{\hbar\omega_{\text{vib}}}, \tag{2.2}$$

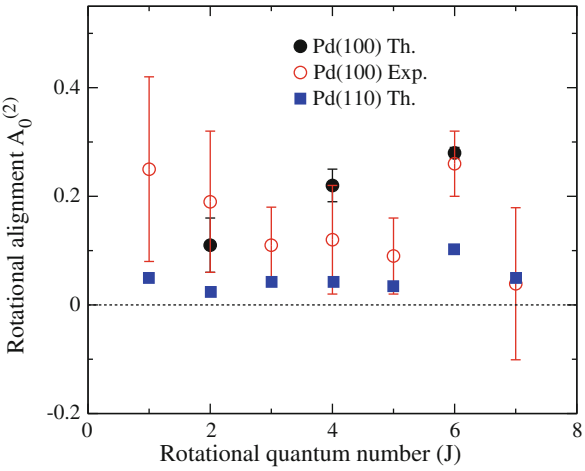

Fig. 2.4 Rotational quadrupole alignment parameter for desorbing H_2 molecules as a function of the rotational quantum number for a surface temperature $T = 700$ K. *Solid black circles*: theoretical results for Pd(100) from [24]. *Red open circles*: experimental results for Pd(100) from [90]. *Solid blue squares*: theoretical for Pd(110) from [15]

where E_0 is the translational energy required to obtain a dissociative adsorption probability S, so that η_v represents the separations of the sticking curves for a certain sticking probability divided by the gas-phase vibrational quantum $\hbar\omega_{\text{vib}} = 516$ meV. The value of η_v obtained for H_2/Pd(100), computed for $S = 0.7$, was 0.75, i.e., of the vibrational energy is 0.75 times as effective in promoting the dissociative adsorption as translational energy. This value is strikingly high compared with values obtained for other H_2/metal surface systems. Still higher values have been found for other molecules reacting on metal surfaces such as N_2 on Ru(0001) [17] and CH_4 on Ni(111) [85].

A detailed analysis allowed the mechanism behind the high effectiveness of vibration in promoting sticking to be revealed. Contrary to previous suggestions, this is not necessarily due to a strong curvature of the reaction path and to a late minimum reaction barrier to dissociative adsorption. It can also arise from a strong lowering of the molecular vibrational frequency during the adsorption and to the multi-dimensional character of the relevant phase space with its broad distribution of barrier heights [34]. At this point, it is worthy mentioning that this analysis could not be performed using classical simulations for the reasons discussed above.

Quantum dynamics simulations have also allowed the study of a purely quantum effect, molecular diffraction [18,22,29]. Molecular diffraction, observed experimentally for the first time in the 1930s [26], revealed the wave nature of the molecular motion. If we take into account the relationship between the de Broglie wavelength associated with the molecular beam, λ, and its wave vector, k, ($\lambda = 2\pi/k$) according to the Bragg condition for diffraction [27], molecular diffraction from a periodic surface occurs when the variation of the parallel wave vector **K** coincides

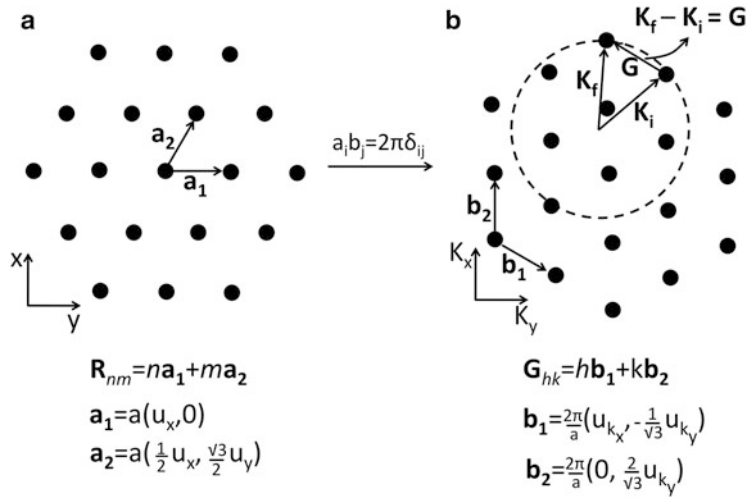

Fig. 2.5 (**a**) Schematic representation of a hexagonal real space. (**b**) Schematic representation of the corresponding reciprocal space and the Ewald sphere for diffraction

with a vector of the reciprocal lattice **G** (see Fig. 2.5). That is, diffraction occurs whenever

$$\mathbf{K}_i + \mathbf{G}_{n,m} = \mathbf{K}_f, \tag{2.3}$$

with $\mathbf{G}_{n,m} = n\mathbf{b}_1 + m\mathbf{b}_2$, where $\mathbf{b}_1$ and $\mathbf{b}_2$ are the basis vectors of the reciprocal lattice. For the sake of completeness, we point out that, taking into account the variation of the internal energy (rotational excitation and deexcitation), the molecular diffraction condition can be written as

$$k_{z,f}^2 = k_i^2 - \frac{4M\Delta E_{\text{rot}}}{\hbar^2} - (\mathbf{K}_i + \mathbf{G}_{n,m})^2 > 0. \tag{2.4}$$

where M being the mass of the molecule, $k_{z,f}$ the final perpendicular wave vector, k_i the initial total wave vector, and ΔE the change of the rotational energy. In the equation above, we have taken into account that, at the typical experimental impact energies, vibrational excitation is not possible.

Diffraction of molecules from metal surfaces has been widely studied experimentally for activated molecule/surface systems [27]. But, due to their complexity, only few 6D theoretical results are available in the literature. Here, we discuss the first 6D calculations on a non-activated system, H_2/Pd(111), published in 2004 [29]. Molecular diffraction from a non-activated system represents a challenge not only from a theoretical point of view, but also for experiments, because in this case most of the molecules dissociate on the surface, even for very low incidence energies. Therefore, in order to prevent the building-up of an adsorbed layer of hydrogen

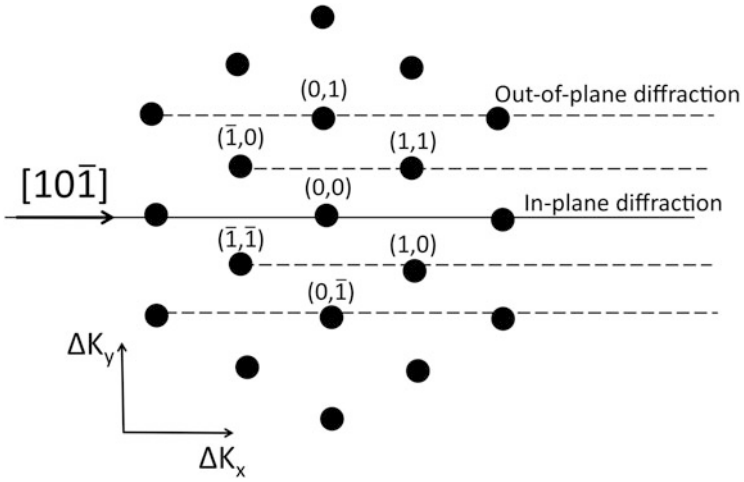

Fig. 2.6 Schematic representation of in-plane and out-of-plane diffraction

during the experiment, the surface temperature has to be kept at about 430 K, which enhances the surface atom vibrations, causing destructive inferences that quench diffraction. Furthermore, as these non-activated systems are very corrugated, inelastic diffraction is expected to dominate the spectra, increasing the number of diffraction peaks and decreasing their probabilities. These two phenomena explain why there were no attempts to measure diffraction in non-activated systems before 2004. But 6D quantum dynamics calculations, which suggested that the H_2/Pd(111) diffraction spectrum is dominated by first order out-of-plane diffraction peaks (see Fig. 2.6 for out-of-plane definition), stimulated the carrying out of diffraction experiments on this system. The experimental measurements corroborated theoretical results (see Fig. 2.7). Digging deeper into theoretical data, it was noticed that the out-of-plane peaks present in the spectra[2], associated with changes of K perpendicular to the incidence direction (parallel to the surface), were much larger than the peaks representing changes in the longitudinal direction. For example, if the incident molecular beam is aligned with the [10$\bar{1}$] direction (see Fig. 2.6), an out-of-plane diffraction peak observed in the spectrum is the (0,1) one (see Fig. 2.7): this peak is associated with $\Delta K_y = K_y$ and $\Delta K_x = 0$. It should be also noticed that in both experiments and theoretical simulations, the angle between the molecular beam incidence direction and the normal to the surface is quite high, $\theta_i = 50°$. Theoretical simulations considering low incidence angles did not show such transversal out-of-plane diffraction predominance. A complete analysis of the quantum theoretical simulations reveals that there is a direct relationship between the incidence angle

[2]Several initial conditions of the molecular beam were analyzed.

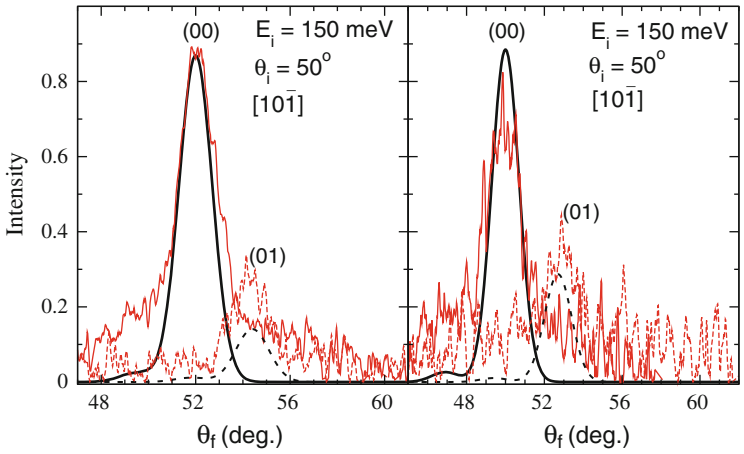

Fig. 2.7 Typical diffraction spectra for H_2/Pd(111). *Black line*: quantum results and *red line* experimental measurements; *solid line*: in-plane-diffraction; and *dashed line*: out-of-plane diffraction

and the transversal out-of-plane diffraction probability. This phenomenon is due to the periodicity of the potential[28]: the higher the incidence angles, the higher the periodicity of the potential felt by the molecules along the incidence direction, and in the extreme case of $\theta_i = 90°$ the molecule will feel a perfectly periodic potential and therefore along this direction $\Delta K = 0$, and, therefore, only changes of K in the perpendicular direction are possible.

Although this prominent out-of-plane diffraction has been observed for a non-activated system, it is a general phenomenon that is expected to be observed whenever the incidence angle is high enough, for example, prominent out-of-plane diffraction have been observed later on for H_2/Pt(111) [71] H_2/Ru(0001) [72] and H_2/Cu/Ru(0001) [22]. Furthermore, [28, 29] hypothesized that at grazing incidence and high incidence energy only out-of-plane transversal diffraction peaks could be observed. This hypothesis was confirmed experimentally a few years later [80, 82].

2.2.1.2 Activated Systems

Quantum dynamics on dissociative adsorption of the prototype activated system $H_2(D_2)$/Cu(111) have been essential, together with an accurate potential energy surface [21], to reproduce experimental observables with chemical accuracy [19].

As already mentioned in Sect. 2.2.1.1 to perform a meaningful comparison with experimental results, both the rovibrational distribution and the energy width of the molecular beam have been taken into account [20]. In order to do so, first the quantum monoenergetic state-resolved sticking probabilities, $S(v, J; E)$, are computed for a large range of incidence energies and the rovibrational states populated in molecular beams experiments. These probabilities are used to compute the

monoenergetic probabilities $S(T_n; E)$, which only depend on the incidence energy and on the nozzle temperature—this later one determines the rovibrational state distribution of the molecules in the molecular beam. $S(T_n; E)$ can be computed as:

$$S(T_n; E) = \sum_{v,J} F_{\mathrm{B}}(v, J; T_n) S(v, J; E), \tag{2.5}$$

where the Boltzmann factor, F_{B}, of each (v, J) state is given by:

$$F_{\mathrm{B}}(v, J; T_n) = (2J + 1) \exp[-E_{\mathrm{vib}}/kT_n] \times w(J) \exp[-E_{\mathrm{rot}}/0.8kT_n]/N, \tag{2.6}$$

where N is the normalization factor and $w(J)$ is the factor describing the nuclear spin statistics. From these computed monoenergetic reaction probabilities, molecular beam experimental results can be simulated by convolution over the distribution of the molecular beam, according to the expression:

$$S(T_n) = \frac{\int_{v=0}^{v=\infty} f(v; T_n) S(E, T_n) dv}{\int_{v=0}^{v=\infty} f(v; T_n)}, \tag{2.7}$$

where $E = \frac{1}{2} M v^2$, v being the velocity of the molecule and M its total mass. The flux weighted velocity distribution $f(v; T_n)$ is given by:

$$f(v; T_n) dv = C v^3 \exp[-(v - v_0)^2/\alpha^2] dv. \tag{2.8}$$

This latter equation includes the parameters describing the energy (or velocity) distribution of the molecular beam, the stream velocity v_0, and the width of the velocity distribution α, C being a constant.

Beyond simulating the experimental molecular beam characteristics, to be able to properly reproduce experimental results, an accurate PES has to be used [19]. At present, the only quantum electronic method able to treat the huge number of electrons involved in a molecule/surface system is DFT[3] (density functional theory), of which the accuracy depends on the accuracy of the exchange-correlation functional that was chosen. A sound strategy to choose the functional consists in fitting experimental results for one specific case to theoretical simulations based on PESs using different functionals, in an approach called the specific reaction parameter (SRP) approach to DFT [11]. An innovation applied to H_2/metal systems has been to take the SRP functional as a weighted average of GGA functionals [19]. In the study performed in [19] on $H_2(D_2)$/Cu(111), the functionals used were PW91 (Perdew–Wang 1991) [73] and RPBE (Revised Perdew–Burke–Ernzerhof) [39]. In this case, the specific experiment chosen was the dissociative

[3]The description of the method is beyond the scope of this chapter.

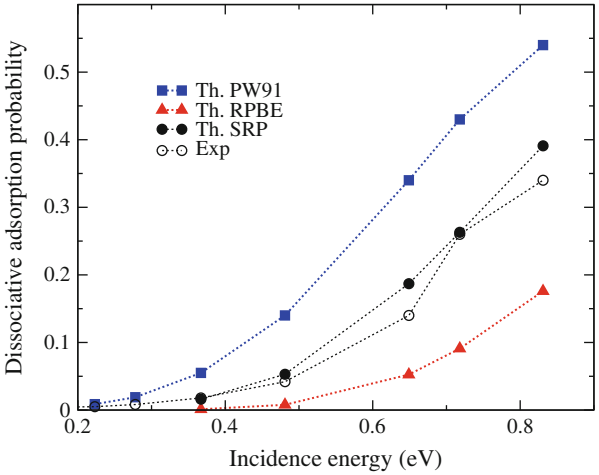

Fig. 2.8 Dissociative adsorption probabilities as a function of incidence energy for D_2/Cu(111), for a nozzle temperature T_n =2,100 K. Experimental data from [77]. Quasi-classical theoretical data from [19]

adsorption probability of D_2 for a nozzle temperature equal to 2,100 K, seeding in H_2 (see Fig. 2.8). The comparison between the theoretical and the experimental results showed that PW91-based theoretical results overestimated the experimental sticking probabilities, whereas the RPBE-based results underestimated them. Thus, none of these functionals yielded chemical accurate results, but a more accurate potential was obtained by combining these two functionals, using a specific reaction parameter (SRP) strategy, in such a way that the exchange-correlation part of the new functional is written as:

$$E_{\mathrm{xc}}^{\mathrm{SRP}} = xE_{\mathrm{xc}}^{\mathrm{PW91}} + (1-x)E_{\mathrm{xc}}^{\mathrm{RPBE}}, \tag{2.9}$$

where x being the mixing parameter chosen to accurately simulate the experimental results, as shown in Fig. 2.8.

This new SRP functional yielded chemically accurate (errors $\leq$1 kcal/mol $\approx$ 0.043 eV) results for a number of experimental observables. For example, in Fig. 2.9, dissociative adsorption probabilities as a function of the incidence energy, in comparison with experimental data, are shown for H_2/Cu(111). In this figure the theoretical results were obtained by using the SRP-PES and the corresponding parameters characteristic of each experimental molecular beam measurement. The theoretical results agree within chemical accuracy with the experimental ones. Furthermore, this study, published in 2009 [19], allowed to unravel a previous unsolved puzzle: why, at similar translational energies, did the two sets of experimental sticking probabilities, shown in Fig. 2.9, differ by an order of magnitude?

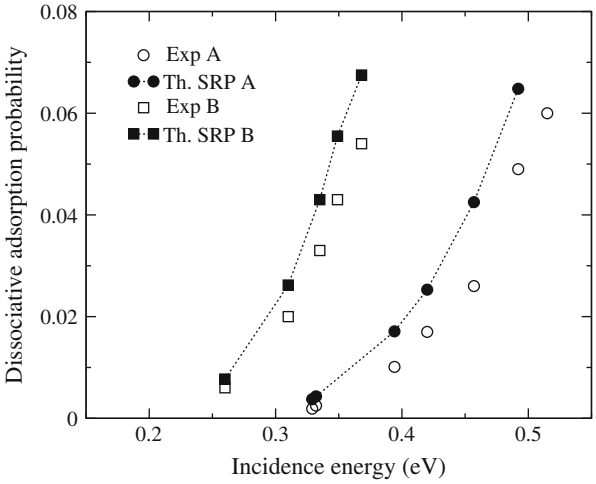

Fig. 2.9 Dissociative adsorption probabilities as a function of the incidence energy for a pure H_2 molecular beam on Cu(111). Experimental data A (*solid circles*) from [77]. Experimental data B (*solid squares*) from [3]. Theoretical data from [19]

The solution came from a detailed analysis of the molecular beam, which was needed to perform a meaningful comparison with theoretical simulations. The experimental sticking probabilities of [3] were larger because this group used molecular beams with wider energy distributions, the tails of which overlap to a greater extent with the portion of the energy-resolved reaction probability curve that steeply rises above threshold.

Quantum state-to-state scattering calculations also reproduced the rotationally inelastic scattering [19, 20] trend observed experimentally [40], according to which the rotationally inelastic scattering probability from $H_2(v = 1, J = 0)$ to $H_2(v = 1, J = 2)$ first increases with translational energy, E, reaching a maximum at around 0.14 eV, and then decreases when E increases. Quantum results show the same nonmonotonic behavior (see Fig. 2.10), but with the maximum at around 0.18 eV. As shown in Fig. 2.10 the theoretical data are shifted to higher values of E by about 0.039 eV, i.e., once again the agreement is within chemical accuracy. Additionally, quantum results showed that a further increase in the translational energy induces an increase of the rotational inelastic scattering probabilities.

A detailed comparison between experiments and quantum dynamics and AIMD (ab initio molecular dynamics) simulations has also been used to hypothesize about the prominent role that surface degrees of freedom (SDOFs) may have. For example, quantum vibrational excitation probabilities for H_2/Cu(111) and rotational alignment parameters for D_2/Cu(111) [20] do not show chemical accuracy, contrary to the case of the observables discussed above. However, these less accurate results could be attributed to a failure of the static surface approximation [59]. In Fig. 2.11

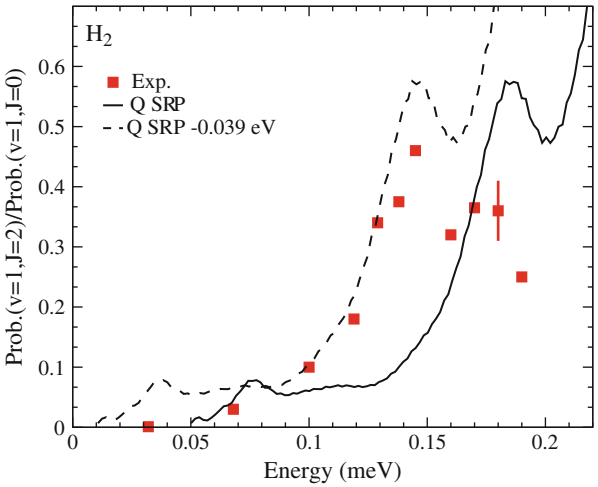

Fig. 2.10 Ratios of rotationally inelastic probabilities for $H_2(v = 1, J = 2)$ scattered from Cu(111). Experimental data from [40]. Theoretical data from [19]

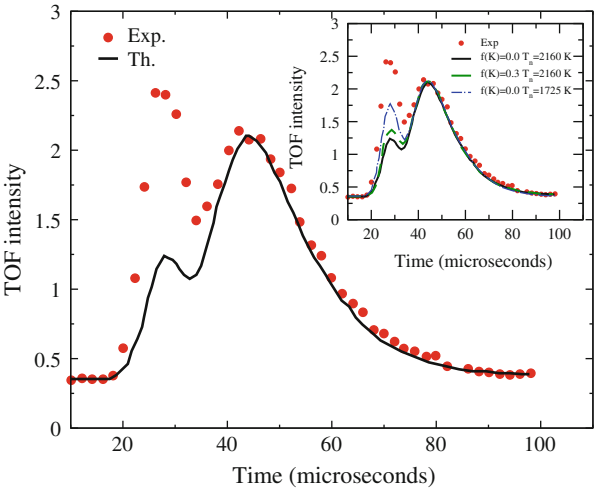

Fig. 2.11 TOF spectrum of H_2 scattered from Cu(111) into the state $(v = 1, J = 3)$. Experimental data, with T_s =400 k, from [76]. Theoretical data from [59] assuming total energy scaling. *Inset* also shows theoretical data as a function of the nozzle temperature, T_n, and as a function of the translational energy loss, $f(K)$

the experimental and theoretical time-of-flight (TOF) spectrum for $H_2(v, J \rightarrow v = 1, J = 3)$/Cu(111) are shown. In order to simulate theoretically the experimental TOF spectrum the expression

$$f(t,T_n) = c + N \times \left[\left(\frac{v_i}{v_0}\right)^4 \times \left[-\left(\frac{v_i - v_0}{\alpha}\right)^2\right] \times P(v = v', J = J' \rightarrow v', J')\right.$$
$$+x_t \times \left(\sum_{vJ,v'J' \neq} \left(\frac{v_i^3}{v_s v_0^4}\right) \times \left(\frac{1}{x_i v_i^{-2} + x_s v_i v_s^{-3}}\right) \times \exp\left[-\left(\frac{v_i - v_0}{\alpha}\right)^2\right]\right.$$
$$\left.\left.\times w_{vJ} \times P(v, J \rightarrow v'J')\right)\right] \tag{2.10}$$

was used. In this equation v_s represents the velocity of the scattered molecule, the parameter $x_i(x_s)$ describes the distance traveled by the molecule from the chopper (from the surface) to the surface (to the detecting laser), and w_{vJ} is the Boltzmann population of the initial (v, J) state in the incidence beams divided by the Boltzmann populations of the final (v', J') state in the incident beam, at the nozzle temperature used in the experiments.

From Fig. 2.11 it can be seen that there is a good agreement between the experimental and the theoretical *loss peak* exhibited by the spectra at long times. This *loss peak* reflects the loss of $H_2(v = 1, J = 3)$ due to dissociative adsorption, vibrational deexcitation, and rotational redistribution within $v = 1$. Thus, this excellent agreement showed that the Born–Oppenheimer static surface model provides an accurate simultaneous description of these processes. On the other hand, the *gain peak* at short times, due to vibrational excitation from $H_2(v = 0)$ to $H_2(v = 1, J = 3)$, is strongly underestimated by quantum simulations. The factors that may contribute to this disagreement between theoretical and experimental TOF spectrum have been discussed in [59]. The first one concerns the fraction of translational energy lost $(f(K))$ by H_2 and D_2 molecules scattered from Cu surfaces, estimated, from experimental measurements on vibrational deexcitation [89], to be of the order of 30 %. This energy loss is not taken into account in the static surface approximation. In fact, taking this phenomenon into account increases the agreement between theory and experiment, as shown in the inset of Fig. 2.11. A second factor is related to the uncertainties of the experimental nozzle temperature. As shown in the inset of Fig. 2.11 the intensity of the gain peak increases when T_n decreases. Eventually, the surface temperature (T_s) also plays a role in the vibrational excitation. A detailed analysis of experimental data on H_2 vibrational excitation as a function of the surface temperature [76] shows that increasing T_s from 400 to 700 K increases the contribution of vibrational excitation by about 20 %.

Rotational quadrupole alignment parameters $(A_0^{(2)})$ as a function of the translational energy represent another example of the role of the SDOFs. In Fig. 2.12 experimental and quantum simulated $A_0^{(2)}$ for D_2 as a function of the translations energy are shown. This figure shows the good agreement between experiments [42] and quantum theory [20]. But, this agreement is not within chemical accuracy as in the case of dissociative adsorption or vibrational deexcitation, despite the fact that the same accurate SRP-PES is used in all the cases. In order to explore the role played by the SDOFs, AIMD calculations [33] have shown themselves to be a very useful tool [68]. AIMD simulations, which include the SDOFs, yielded $A_0^{(2)}$ values

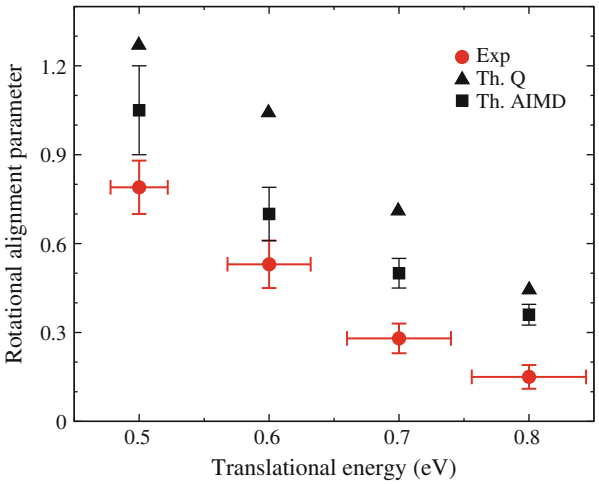

Fig. 2.12 Rotational alignment parameters as a function of the translational energy. Experimental data from [42]. Quantum dynamics data from [20]. AIMD data from [68]

in better agreement with experiments (see Fig. 2.12), showing the non-negligible role played by the surface motion in this physical process. In this case, quantum dynamics simulations results were used as reference data to evaluate the effect of surface motion.

Finally quantum dynamics simulations on dissociative adsorption and molecular diffraction for H_2/Pt(111) [74] allowed the solution of a long-standing experimental paradox regarding the corrugation of the system. On one hand, Luntz et al. [64] suggested a quite corrugated PES based on molecular beam experiments on sticking of D_2 and H_2, showing the dependence of the sticking on the initial momentum of the molecule parallel to the surface. On the other hand, experiments on rotationally inelastic diffraction for HD, carried out by Cowin et al. [12], which showed almost no diffraction, suggested a quite flat PES. Quantum calculations performed by Pijper et al. [74] show that, in fact, increasing the initial parallel energy of the H_2 molecule inhibits reaction for low normal energy (see Fig. 2.13). This phenomenon has been explained in terms of the barrier heights encountered by the molecule. Due to the parallel momentum, the incident molecule samples barriers across the whole unit cell. Thus, increasing the parallel momentum increases the probability that the incident molecule encounters a higher barrier, leading to a decrease in reactivity.

An analysis of the complementary channel, molecular scattering, in terms of diffraction probabilities (see Fig. 2.14) reveals that the most populated first order diffraction peaks are not in-plane, but out-of-plane, (01) and $(0\bar{1})$ (see Fig. 2.6), which explains the very low diffraction probability found experimentally [12]. These experiments considered only for in-plane diffraction.

Later in [71], a detailed comparison, i.e., taking into account the rovibrational distribution of the molecular beam, with experiment, measuring both in-plane and

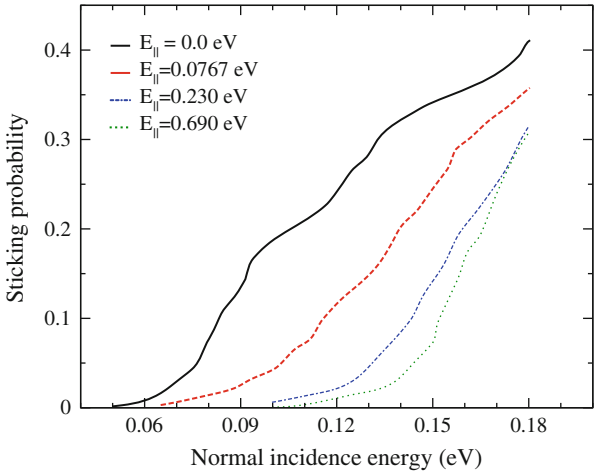

Fig. 2.13 Quantum reaction probabilities, for $H_2(v = 0, J = 0)$/Pt(111), for off-normal incidence as a function of the normal incidence energy. Results are for the rovibrational ground state ($v = 0, J = 0$), for incidence along the $[10\bar{1}]$ direction, and four different initial parallel energies

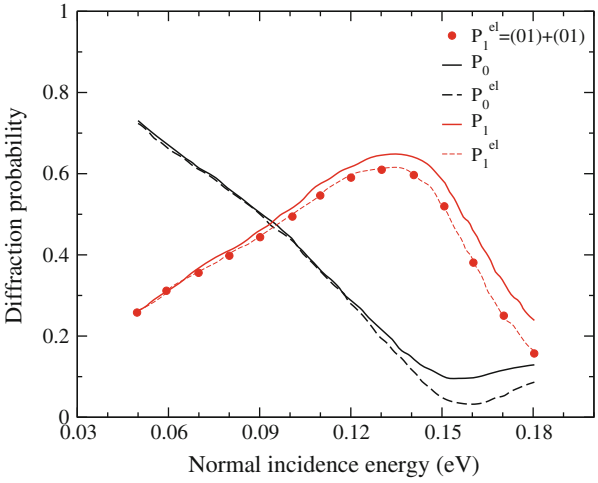

Fig. 2.14 Quantum diffraction probabilities versus normal incidence energy, for $H_2(v = 0, J = 0)$/Pt(111), for the zeroth and the first diffraction order, P_0 and P_1, along the incidence direction $[10\bar{1}]$. Rotationally elastic diffraction probability into the zeroth and first order, P_0^{el} and P_1^{el}, is also shown. $\tilde{P}_1^{el}$ refers to the part of P_0^{el} due to diffraction into the (01) and $(0\bar{1})$ out-of-plane diffraction peaks. These results correspond to $E_n = 0.69$ eV

out-of-plane diffraction, corroborated the importance of out-of-plane diffraction in the scattering of H_2 from Pt(111) (see Fig. 2.15). Furthermore, the good agreement obtained between quantum results and experiments, for both dissociative adsorption

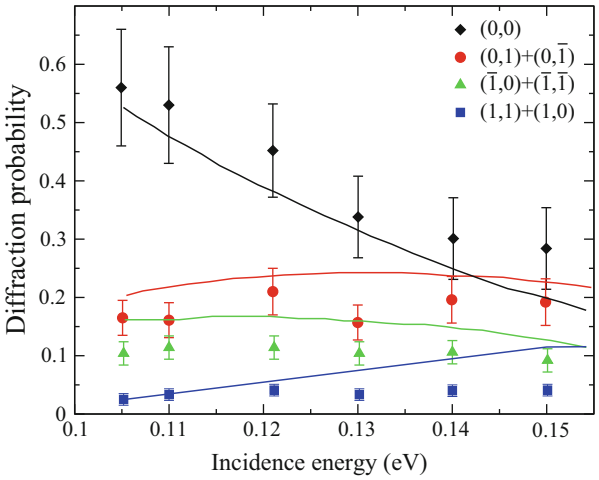

Fig. 2.15 Diffraction peaks probabilities versus incidence energy, for incidence along the $[10\bar{1}]$ direction. The experimental results are shown with *symbols*; the theoretical results are shown with *solid lines*

and scattering, has been considered a proof of the high accuracy of the Born–Oppenheimer approximation for H_2/metal systems.

2.2.2 CH_4/Metal Surfaces

Quantum dynamics calculations have also been performed on more complex systems, such as CH_4/metal surfaces. In fact, from an experimental point of view, the dissociation of methane on metals is one of the most studied reactions in surface science [2, 47, 60, 66, 85] because of its industrial relevance.

To simulate the reactivity of methane on metal surfaces a quantum treatment is preferred because the high barriers present on the PES lead to low reaction probabilities at lower energies, where tunneling is important. This is a real challenge for theoretical studies, given the large number of molecular DOFs. But this is not the only problem that theoretical studies have to face. At the high collision energies required for reaction, the interaction between the molecule and the atoms of the metal lattice is strong, and lattice motion has to be included in the calculation. Quantum dynamics calculations for dissociation of CH_4 on Ni(111) were performed by Jackson and others [69] using a reduced dimensionality scheme, where only one of the H-CH_3 bonds, the distance between the molecular center of mass and surface, and the rotation of the molecule, are considered. But, in addition to these molecule DOFs, the lattice motion was modeled by allowing the Ni atom over which the reaction occurs to move normal to the surface (Q). Dissociative adsorption probabilities obtained using this lattice relaxation (LR) model are shown in Fig. 2.16. The LR results shown in this figure, obtained by Boltzmann averaging

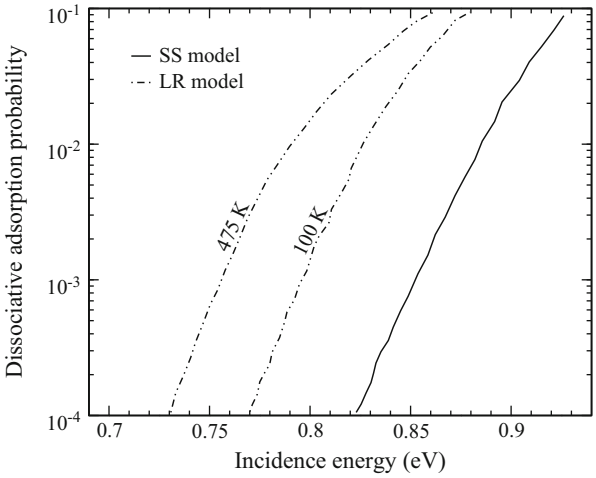

Fig. 2.16 Quantum dissociative adsorption probabilities as a function of translational energy for CH_4/Ni(111), for the molecular vibrational ground state. *Solid line*: SS model; *dot-dashed line*: LR model. For the later case two surface temperatures are shown, 100 and 475 K

over many lattice vibrational modes, are representative of the main results obtained in that study: (1) the LR model yielded higher reactivity than the static surface (SS) model; (2) the effects of lattice motion and relaxation on reactivity are strong at low translational energies where tunneling dominates. In spite of the approximations made in the LR model, the results were found to be in reasonable agreement with experiments. For example, the reactivity measured by Utz and others [85] for CH_4 in its vibrational ground state for $T_s = 475\,\text{K}$ and $E = 0.75\,\text{eV}$ is equal to 10^{-4}. The LR model gives the same reactivity at 0.73 eV.

Subsequent studies of CH_4 dissociation on Ni(111) [87], using both a mixed quantum/classical approach and the fully quantum model described above, showed that the motion of the lattice is relatively unperturbed by the incident molecule. In fact, Jackson and others [87] showed that a sudden treatment of the lattice motion reproduced fairly well the full-dimensional quantum results (see Fig. 2.17), but with a much lower computational effort. These studies also showed that the reactivity is dominated by collisions with metal atoms that are puckered out of the plane of the surface at the time of impact, as the barrier to methane dissociation is lower for these lattice configurations.

Without any doubt, the most striking results of the dissociative adsorption measurements of CH_4 on Nickel is the significant enhancement of reactivity for vibrationally excited molecules. For example, for CH_4/Ni(100), experiment [47,66] reveals that the ν_1 vibrational state (see Fig. 2.18) has the largest efficacy (η_ν) for promoting reaction. To analyze this observed behavior, and to shed some light on the physical mechanisms behind these observations, full-dimensional quantum simulations were performed [44, 70]. To carry out these simulations the Reaction

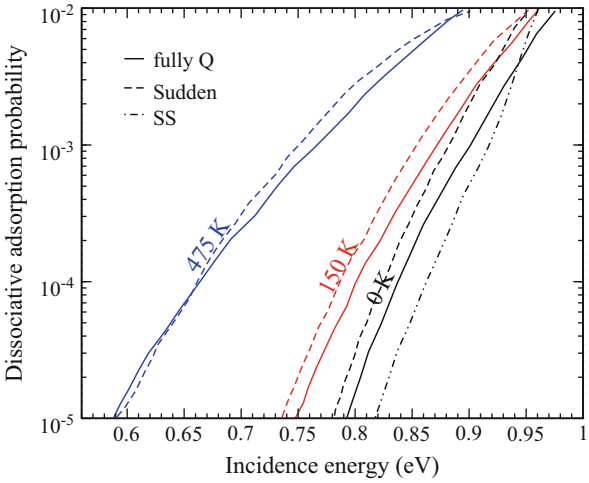

Fig. 2.17 Quantum dissociative adsorption probabilities as a function of the incidence energy for CH_4/Ni(111), for the molecular vibrational ground state. *Solid line*: fully quantum calculations; *dashed line*: sudden approximations; *dot-dashed line*: surface static approximations. Three surface temperatures are shown: 0, 100, and 475 K

Path Hamiltonian (RPH) [65,67] was used, including all 15 molecular DOFs within the harmonic approximation. In order to allow the evolution of the system and observe the possible transitions between different vibrational states, due to the non-adiabatic coupling that arises from the interaction between the molecule and surface, the total wavefunction was expanded in the adiabatic vibrational states of the molecule. Close-coupled equations were derived for wave packets propagating on a vibrationally adiabatic potential energy surfaces, with vibrationally non-adiabatic couplings linking these states to each other. In spite of the approximations made in deriving this quantum model, the theoretical results for the full-dimensional finite temperature dissociative adsorption probability are in very good agreement with experiments (see Fig. 2.19). As also shown in Table 2.1 the larger efficacy of the ν_1 state relative to the ν_3 state is reproduced.

A detailed analysis of the quantum results revealed the origin of this behavior. The increased efficacy of the ν_1 state arises from both mode softening and vibrationally non-adiabatic couplings. Furthermore this analysis revealed that most of the reactivity at the experimental surface temperature (475 K) is due to thermally assisted over-the-barrier processes, and not to tunneling. Tunneling becomes important at lower incidence energies and lower surface temperatures.

Low-dimensional quantum dynamics studies of the dissociative adsorption of CH_4 on Ni(111), as a function of the vibrational initial state, have also been carried out [52]. In this case, quantum dynamics simulations were performed using the multiconfiguration time-dependent Hartree (MCTDH) method [1]. Results obtained from this study are similar to those obtained for Ni(100): the efficacies of the stretching modes are larger than those of the bending modes, also in good agreement with experiments.

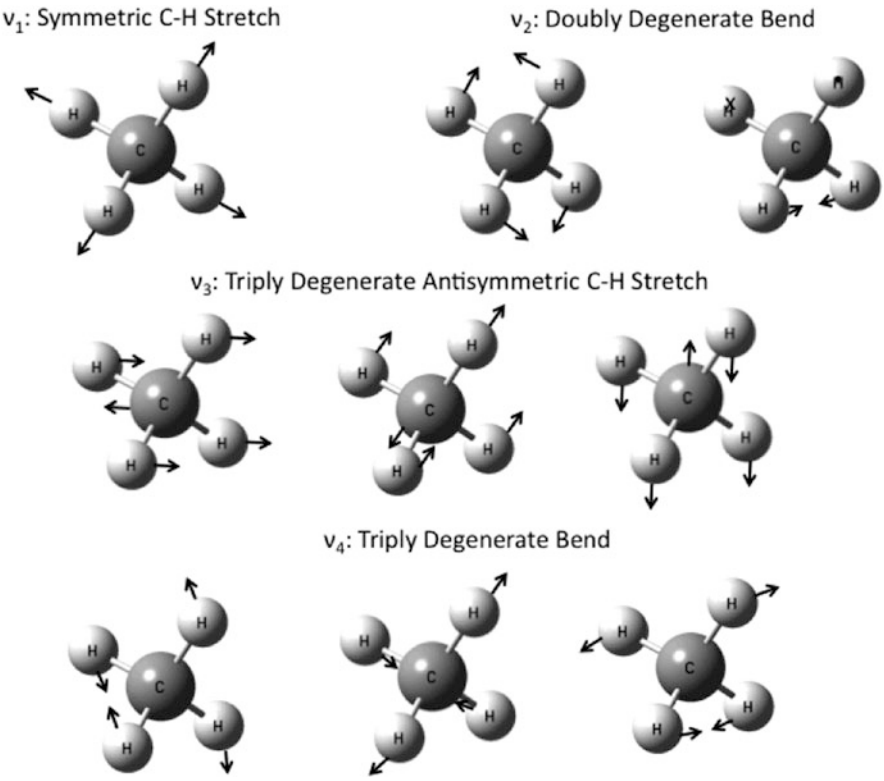

Fig. 2.18 Methane vibrational normal modes

2.3 Conclusions and Outlook

Throughout this chapter we have shown that quantum dynamics simulation on molecule/metal surface interactions have allowed the description of a significant number of physical phenomena related to both the molecular and the surface DOFs. In the case of the molecular DOF their role is investigated directly through quantum calculations, whereas the surface DOF has been investigated indirectly by using quantum data as reference ones. We have shown that nowadays state-of-the-art quantum simulations allow one to treat, fully quantum mechanically, light diatomic molecules (H_2, D_2 and HD) interacting with metal surfaces including the six DOFs of the molecule. Beyond these simple molecules, quantum dynamics simulations have been used to study the reactivity of methane on Ni surfaces, including only the relevant molecular DOFs. But, in spite of the reduce dimensionality of the simulations, they have allowed the identification of the physical mechanisms behind the observed experimental measurements.

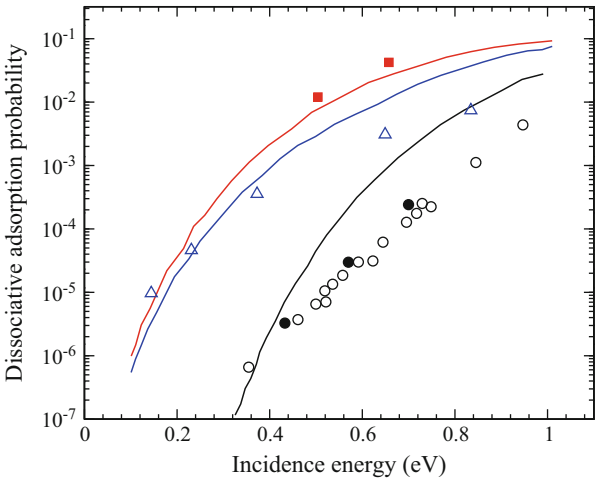

Fig. 2.19 Dissociative adsorption probabilities as a function of the incidence energy for CH_4/Ni(100), for several vibrational states. Theory from [44], *black line* for ν_0, *red line* for ν_1 and *blue line* for ν_3. *Black solid circles*: experimental data for ν_0 from [2]; *red solid squares*: experimental data for ν_1 from [2]; *black open circles*: experimental data for ν_0 from [46]; *blue open triangles*: experimental data for ν_3 from [46]

Table 2.1 Vibrational efficacies for CH_4/Ni(100)

Mode	η_{exp}	η_{th}
ν_1	1.4	0.93
ν_3	0.94	0.80

Experimental modes ν_1 and ν_3 taken from [47] and [46]. Theoretical data from [70]

In spite of the notable success of quantum dynamics achieved with describing molecule/surface interactions during the last few decades, surface scientists will have to face important challenges in the next future. Although at present state-of-the-art quantum dynamics simulations allow one to treat diatomic molecules with essentially no approximations relative to the molecular DOFs, still some effects cannot be included accurately. In this respect, the greatest challenge facing theorists in the field is to come up with a model that can yield accurate predictions for molecule–metal surface reactions involving excited electronic states with potential curve crossings [54]. These electronic excitations have been suggested, based on experimental measurements, to play a key role in phenomena such as vibrational quenching in associative desorption of N_2 from Ru(0001) [23] or multi-quantum vibrational relaxation of NO scattering from metal surfaces [43]. Till present day, several models have been developed to take into account non-adiabatic effects, with moderate success [45,63,83]. But a complete accurate description is most desirable. Time-dependent Density Functional Theory (TDDFT) [61] and embedding schemes involving high-level ab initio methods and DFT [50] may be of help. Also relative

to diatomic/molecule surfaces, an accurate description of the surface motion would be necessary.

Full dimensional quantum dynamics calculations on polyatomic molecules will hopefully lead to a deeper understanding on molecule/surface interactions mechanisms, as the six-dimensional quantum dynamics calculations have already done for H_2/metal surfaces. These kind of simulations are required to describe accurately processes involving the breaking of a X-R bond, beyond dissociation of CH_4 on H and CH_3. A description along the lines of the MCTDH (multi-configurational time-dependent Hartree) method would be worth exploring. For these polyatomic molecules, a better description of the molecule–lattice coupling is also desirable.

Acknowledgements C. Díaz acknowledges support under MICINN project FIS2010-25127.

References

1. Beck MH, Jäckle A, Worth GA, Meyer HD (2000) The multiconfiguration time-dependent Hartree (MCTDH) method: a highly efficient algorithm for propagating wavepackets. Phys Rep 324:1
2. Beck RD, Maroni P, Papageorgopoulos DC, Dang TT, Schmid MP, Rizzo TR (2003) Vibrational mode-specific reaction of methane on a nickel surface. Science 302:98
3. Berger HF, Leisch M, Winkler A, Rendulic KD (1990) A search for vibrational contributions to the activated adsorption of H_2 on copper. Chem Phys Lett 175:425
4. Besenbacher F, Chorkendorff I, Clausen BS, Hammer B, Malenbroek AM, Norskov JK, Stensgaard I (1998) Design of a surface alloy catalyst for steam reforming. Science 279:1913
5. Busnengo HF, Salin A, Dong W (2000) Representation of the 6D potential energy surface for a diatomic molecule near a solid surface. J Chem Phys 112:7641
6. Busnengo HF, Crespos C, Dong W, Rayez JC, Salin A (2002) Classical dynamics of dissociative adsorption for a nonactivated system: The role of zero point energy. J Chem Phys 116:9005
7. Busnengo HF, Pijper E, Somers MF, Kroes GJ, Salin A, Olsen RA, Lemoine D, Dong W (2002) Six-dimensional quantum and classical dynamics study of $H_2(v = 0,J = 0)$ scattering from Pd(111). Chem Phys Lett 356:515
8. Busnengo HF, Pijper E, Kroes GJ, Salin A (2003) Rotational effects in dissociation of H_2 on Pd(111): Quantum and classical study. J Chem Phys 119:12553
9. Chen JC, Juanes-Marcos JC, Woittequand S, Somers MF, Díaz C, Olsen RA, Kroes GJ (2011) Six-dimensional quasiclassical and quantum dynamics of H_2 dissociation on the c(2×2)-Ti/Al(100) surface. J Chem Phys 134:114708
10. Chorkendorff I, Niemantsverdriet JW (2003) Concepts of modern catalysis and kinetics. Wiley-VCH, Weinheim
11. Chuang YY, Radhakrisnan ML, Fast PL, Cramer CJ, Truhlar DG (1999) Direct dynamics for free radical kinetics in solution: solvent effect on the rate constant for the methanol with atomic hydrogen. J Phys Chem A 103:4893
12. Cowin JP, Yu CF, Sibener SJ, Wharton L (1983) HD scattering from Pt(111): Rotational excitation probabilities. J Chem Phys 79:3537
13. Crespos C, Collins MA, Pijper E, Kroes GJ (2004) Application of the modified Shepard interpolation method to the determination of the potential energy surface for a molecule-surface reaction:H_2+ Pt(111). J Chem Phys 120:2392
14. Dai J, Light JC (1997) Six dimensional quantum dynamics study for dissociative adsorption of H_2 on Cu(111) surface. J Chem Phys 107:1676

15. Dianat A, Gross A (2004) High-dimensional quantum dynamical study of the dissociation of H_2 on Pd(110). J Chem Phys 120:5339
16. Dianat A, Sakong S, Gross A (2005) Quantum dynamics of the dissociation of H_2 on Rh(111). Eur Phys J B 45:425
17. Díaz C, Olsen RA (2009) A note on the vibrational efficacy in molecule-surface reactions. J Phys Chem 130:094706
18. Díaz C, Somers MF, Kroes GJ, Busnengo HF, Salin A, Martín F (2005) Quantum and classical dynamics of H_2 scattering from Pd(111) at off-normal incidence. Phys Rev B 72:035401
19. Díaz C, Pijper E, Olsen RA, Busnengo HF, Auerbach DJ, Kroes GJ (2009) Science 326:832
20. Díaz C, Olsen RA, Auerbach DJ, Kroes GJ (2010) Six-dimensional dynamics study of reactive and non reactive scattering of H_2 from Cu(111) using a chemically accurate potential energy surface. Phys Chem Chem Phys 12:6499
21. Díaz C, Olsen RA, Busnengo HF, Kroes GJ (2010) Dynamics on six-dimensional potential energy surfaces for H_2/Cu(111): Corrugation reducing procedure versus modified Shepard interpolation method and PW91 versus RPBE. J Phys Chem C 114:11192
22. Díaz C, Martín F, Kroes GJ, Minniti M, Farías D, Miranda R (2012) H_2 diffraction from a strained pseudomorphic monolayer of Cu deposited on Ru(0001) J Phys Chem C 116:13671
23. Diekhöner L, Honekaer L, Mortensen H, Jensen E, Baurichter A, Petrunin VV, Luntz AC (2002) Indirect evidence for strong nonadiabatic coupling in N_2 associative desorption from and dissociative adsorption on Ru(0001). J Chem Phys 117:5018
24. Eichler A, Hafner J, Gross A, Scheffler M (1999) Rotational effects in the dissociation of H_2 on metal surfaces studies by ab initio quantum-dynamics calculations. Chem Phys Lett 311:1
25. Ertl G (1983) Primary steps in catalytic synthesis of ammonia. J Vac Sci Technol A 1:1247
26. Estermann I, Stern O (1930) Z Phys 63:95
27. Farías D, Rieder KH (1998) Atomic beam diffraction from solid surfaces. Rep Prog Phys 61:1575
28. Farías D, Díaz C, Nieto P, Salin A, Martín F (2004) Pronounced out-of-plane diffraction of H_2 molecules from a Pd(111) surface. Chem Phys Lett 390:250
29. Farías D, Díaz C, Rivière P, Busnengo HF, Nieto P, Somers MF, Kroes GJ, Salin A, Martín F (2004) In-plane and out-plane diffraction of H_2 from metal surfaces. Phys Rev Lett 93:246104
30. Gostein HG, Sitz GO (1997) Rotational state-resolved sticking coefficients for H_2 on Pd(111): Testing dynamical steering in dissociative adsorption. J Chem Phys 106:7378
31. Groot IMN, Juanes-Marcos JC, Díaz C, Somers MF (2010) Dynamics of dissociative adsorption of hydrogen on CO-precovered Ru(0001) surface: a comparison of theoretical and experimental results. R. A. Olsen and G. J. Kroes, Phys Chem Chem Phys 12:1331
32. Gross A (1998) Reactions at surfaces studied by ab initio dynamics calculations. Surf Sci Rep 32:291
33. Gross A, Dianat A (2007) Hydrogen dissociation dynamics on precovered Pd surfaces: Langmuir is still right. Phys Rev Lett 98:206107
34. Gross A, Scheffler M (1996) Influence of molecular vibrations on dissociative adsorption. Chem Phys Lett 256:417
35. Gross A, Scheffler M (1996) Scattering of hydrogen molecules from a reactive surface: Strong off-specular and rotationally inelastic diffraction. Chem Phys Lett 263:567
36. Gross A, Scheffler M (1998) Ab initio quantum and molecular dynamics of the dissociative adsorption of hydrogen on Pd(100). Phys Rev B 57:2493
37. Gross A, Scheffler M (2000) Dynamics of hydrogen dissociation at the sulfur-covered Pd(100) surface. Phys Rev B 61:8425
38. Gross A, Wilke S, Scheffler M (1995) Six-dimensional quantum dynamics of adsorption and desorption of H_2 at Pd(100): steering ans steric effects. Phys Rev Lett 75:2718
39. Hammer B, Hansen LB, Norskov JK (1999) Improved adsorption energetics within density-functional theory using revised Perdew-Burke-Ernzerhof functionals. Phys Rev B 59:7413
40. Hodgson A, Samson P, Wight A, Cottrell C (1997) Rotational excitation and vibrational relaxation of $H_2(\nu = 0, J = 0)$ scattered from Cu(111). Phys Rev Lett 78:963
41. Hohenberg P, Kohn W (1964) Inhomogeneous electron. Gas Phys Rev 136:B864

42. Hou H, Gulding SJ, Rettner CT, Wodtke AM, Auerbach DJ (1997) The stereodynamics of a gas-surface reaction. Science 277:80
43. Huang Y, Rettner CT, Auerbach DJ, Wodtke AM (2000) Vibrational promotion of electron transfer. Science 290:111
44. Jackson B, Nave S (2011) The dissociative chemisorption of methane on Ni(100): Reaction path description of mode-selective chemistry. J Chem Phys 135:114701
45. Juaristi JI, Alducin M, Díez-Muiño R, Busnengo HF, Salin A (2008) Role of electron-hole pair excitations in the dissociative adsorption of diatomic molecules on metal surfaces. Phys Rev Lett 100:116102
46. Juurlink LBF, McCabe PR, Smith RR, DiCologero CL, Utz AL (1999) Eigenstate-resolved studies of gas-surface reactivity: $CH_4(\nu_3)$ dissociation on Ni(100). Phys Rev Lett 83:868
47. Juurlink LBF, Smith RR, Killelea DR, Utz AL (2005) Comparative study of C-H stretch and bend vibrations in methane activation on Ni(100) and Ni(111). Phys Rev Lett 94:208303
48. Juurlink LBF, Killelea DR, Utz AL (2009) State-resolved probes of methane dissociation dynamics. Prog Surf Sci 84:69
49. Kay M, Darling GR, Holloway S, White JA, Bird DM (1995) Steering effects in non-activated adsorption. Chem Phys Lett 245:311
50. Klüner T, Govind N, Wang YA, Carter EA (2002) Periodic density functional embedding theory for complete active space self-consistent field and configuration interaction calculations: ground and excited states. J Chem Phys 116:42
51. Kohn W, Sham LJ (1965) Self-consistent equations including exchange and correlation effects. Phys Rev 140:A1133
52. Krishnamohan GP, Olsen RA, Kroes GJ, Gatti F, Woittequand S (2010) Quantum dynamics of dissociative chemisorption of CH_4 on Ni(111): Influence of the bending vibration J Chem Phys 133:144308
53. Kroes GJ (1999) Six-dimensional quantum dynamics of dissociative chemisorption of H_2 on metal surfaces. Prog Surf Sci 60:1
54. Kroes GJ (2008) Frontiers in surface scattering simulations. Science 321:794
55. Kroes GJ, Somers MF (2005) Six-dimensional dynamics of dissociative chemisorption of H_2 on metal surfaces. J Theor Comput Chem 4:493
56. Kroes GJ, Baerends EJ, Mowrey RC (1997) Six-dimensional quantum dynamics of dissociative chemisorption of ($v = 0$,$J = 0$) H_2 on Cu(100). Phys Rev Lett 78:3583
57. Kroes GJ, Gross A, Baerends EJ, Scheffler M, McCormack DA (2002) Quantum theory of dissociative chemisorption on metal surfaces. Acc Chem Res 35:193
58. Kroes GJ, Pijper E, Salin A (2007) Dissociative chemisorption of H_2 on the Cu(110) surface: A quantum and quasiclassical dynamical study. J Chem Phys 127:164722
59. Kroes GJ, Díaz C, Pijper E, Olsen RA, Auerbach DJ (2010) Apparent failure of the Born-Oppenheimer static surface model for vibrational excitation of molecular hydrogen on copper. PNAS 107:20881
60. Larsen JH, Chorkendorff I (1999) From fundamental studies of reactivity on single crystals to the design of catalysts. Surf Sci Rep 35:163
61. Lindenblatt M, Pehlke E (2006) Ab initio simulation of the spin transition during chemisorption: H/Al(111). Phys Rev Lett 97:216101
62. Lorenz S, Gross A, Scheffler M (2004) Representing high-dimensional potential-energy surfaces for reactions at surfaces by neural networks. Chem Phys Lett 395:210
63. Luntz AC, Persson M (2005) How adiabatic is activated adsorption/associative desorption? J Chem Phys 123:074704
64. Luntz AC, Brown JK, Williams MD (1990) Molecular beam studies of H_2 and D_2 dissociative chemisorption on Pt(111). J Chem Phys 93:5240
65. Marcus RA (1966) On the analytical mechanics of chemical reactions. Classical mechanics of linear collisions. J Chem Phys 45:4500
66. Maroni P, Papageorgopoulos DC, Sacchi M, Dang TT, Beck RD, Rizzo TR (2005) State-resolved gas-surface reactivity of methane in the symmetric C-H stretch vibration on Ni(100). Phys Rev Lett 94:246104

67. Miller WH, Handy NC, Adams JE (1980) Reaction path Hamiltonian for polyatomic molecules. J Chem Phys 72:99
68. Nattino F, Díaz C, Jackson B, Kroes GJ (2012) Effect of surface motion on the rotational quadrupole alignment parameter of D_2 reacting on Cu(111). Phys Rev Lett 108:236104
69. Nave S, Jackson B (2007) Methane dissociation on Ni(111): The role of lattice reconstruction. Phys Rev Lett 98:173003
70. Nave S, Jackson B (2010) Vibrational mode-selective chemistry: Methane dissociation on Ni(100). Phys Rev B 81:233408
71. Nieto P, Pijper E, Barredo D, Laurent G, Olsen RA, Baerends EJ, Kroes GJ, Farías D (2006) Reactive ans nonreactive scattering of H_2 from a metal surface is electronically adiabatic. Science 312:86
72. Nieto P, Farías D, Miranda R, Luppi M, Baerends EJ, Somers MF, van der Niet MJTC, Olsen RA, Kroes GJ (2011) Diffractive and reactive scattering of H_2 from Ru(0001): experimental and theoretical study. Phys Chem Chem Phys 13:8583
73. Perdew JP, Chevary JA, Vosko SH, Jackson KA, Pederson MR, Singh DJ, Fiolhais C (1992) Atoms, molecules, solids, and surfaces: applications of the generalized gradient approximation for exchange ans correlation. Phys Rev B 46:6671
74. Pijper E, Kroes GJ, Olsen RA, Baerends EJ (2002) Reactive and diffractive scattering of H_2 from Pt(111) studied using a six-dimensional wave packet method. J Chem Phys 117:5885
75. Rendulic KD, Anger G, Winkler A (1989) Wide range nozzle beam adsorption data for the system H_2/nickel and H_2/Pd(100). Surf Sci 208:404
76. Rettner C, Michelsen HA, Auerbach DJ (1993) Determination of quantum-state-specific gas-surface energy transfer and adsorption probabilities as a function of kinetic energy. Chem Phys 175:157
77. Rettner C, Michelsen HA, Auerbach DJ (1995) Quantum-state-specific dynamics of the dissociative adsorption and associative desorption of H_2 at a Cu(111) surface. J Chem Phys 102:4625
78. Rivière P, Somers MF, Kroes GJ, Martín F (2006) Quantum dynamical study of the H_2 and D_2 dissociative adsorption and diffraction from the NiAl(110) alloy surface. Phys Rev B 73:205417
79. Rostrup-Nielsen JR (1984) Catalysis: science technology. In: Boudart M, Anderson JR (eds). Springer, Berlin
80. Rousseau P, Khemliche H, Borisov AG, Roncin P (2007) Quantum scattering of fast atoms and molecules on surfaces. Phys Rev Lett 98:016104
81. Schröter L, David R, Zacharias H (1991) Rotational state distribution of recombinatively desorbing hydrogen from clean ans S-covered Pd(100). Surf Sci 258:259; Laser spectroscopy of hydrogen desorption from Pd(100). J Vac Sci Technol A 9:1712 (1991)
82. Schüller A, Wethekam S, Winter H (2007) Diffraction of fast atomic projectiles during grazing scattering from a LiF(001) surface. Phys Rev Lett 98:016103
83. Shenvi N, Roy S, Tully JC (2009) Dynamical steering ans electronic excitation in NO scattering from a gold surface. Science 326:829
84. Sinfelt JH (1979) Structure of metal catalysts. Rev Mod Phys 51:569
85. Smith RR, Killelea DR, DelSesto DF, Utz AL (2004) Preference for vibrational over translational energy in a gas-surface reaction. Science 304:992
86. Somers MF, McCormack DA, Kroes GJ, Olsen RA, Baerends EJ, Mowrey RC (2002) Signatures of site-specific reaction of H_2 on Cu(100). J Chem Phys 117:6673
87. Tiwari AK, Nave S, Jackson B (2009) Methane dissociation on Ni(111): a new understanding of the lattice effect. Phys Rev Lett 103:253201
88. van Willingen RT, Somers MF, Busnengo HF, Kroes GJ (2004) The dependence of dissociative chemisorption of H_2 on Pd(111) on H_2 rotation: a six-dimensional quantum dynamics study. Chem Phys Lett 393:166

89. Watts E, Sitz GO (2001) State-to-state scattering in a reactive system $H_2(\nu = 1,J = 1)$ from Cu(100). J Chem Phys 114:4171
90. Wetzig D, Rutkowski M, Ettrich W, David R, Zacharias H (1996) Rotational alignment in associative desorption of H_2 from Pd(100). Surf Sci 402:232

Tunneling in Unimolecular and Bimolecular Reactions

3

Hua Guo, Jianyi Ma, and Jun Li

Abstract

Tunneling is an important quantum phenomenon in reaction dynamics. In this chapter, the effects of tunneling on photodissociation and reactive scattering are discussed using two prototypical examples. The first deals with a unimolecular decomposition reaction, namely the photodissociation of NH_3 in its first (A) absorption band and the second is concerned with an important bimolecular reaction in combustion: $HO + CO \rightarrow H + CO_2$. In the former case, the lifetimes of low-lying vibrational resonances in the predissociative excited state are influenced by tunneling through a small barrier in the dissociation (N–H) coordinate, which is also responsible for a strong H/D isotope effect. The latter, on the other hand, is affected by tunneling through a tight barrier in the exit channel primarily along the H–O dissociation coordinate, which is manifested by the non-Arrhenius rate constant at low temperatures, kinetic isotope effects, and vibrational mode selectivity. In addition, the photodetachment of $HOCO^-$ produces metastable HOCO species, the decomposition of which is dominated by deep tunneling to the $H + CO_2$ products. Since both systems are influenced by multidimensional tunneling, an accurate characterization of the dynamics requires a quantum mechanical (QM) treatment, preferably with full dimensionality. In this chapter,

H. Guo (✉) • J. Li
Department of Chemistry and Chemical Biology, University of New Mexico, Albuquerque, NM 87131, USA
e-mail: hguo@unm.edu; junli11@unm.edu

J. Ma
Department of Chemistry and Chemical Biology, University of New Mexico, Albuquerque, NM 87131, USA

Institute of Atomic and Molecular Physics, Sichuan University, Chengdu, Sichuan 610065, China
e-mail: jianyi.m@gmail.com

F. Gatti (ed.), *Molecular Quantum Dynamics*, Physical Chemistry in Action,
DOI 10.1007/978-3-642-45290-1_3, © Springer-Verlag Berlin Heidelberg 2014

we review the recent advances in understanding the effects of tunneling in these two reactive systems.

3.1 Introduction

Tunneling is an important quantum effect, which stems from the particle-wave duality in quantum mechanics. A light quantum particle, which has a long de Broglie wavelength, is capable of having substantial non-zero probability amplitudes in classically forbidden regions. For many chemical reactions that possess a reaction barrier, for example, tunneling facilitates reactivity by penetrating the barrier at energies below the barrier height [1, 2]. Tunneling manifests in many observables such as non-Arrhenius behaviors of thermal rate constants at low temperatures and kinetic isotope effects, but an unambiguous and precise quantification of tunneling is not always straightforward for bimolecular reactions since the classical limit without tunneling is difficult to define. Tunneling is particularly facile if the reaction coordinate involves the motion of light atoms, such as hydrogen. A good example is the $H + H_2$ reaction [3], which has been shown by accurate quantum reactive scattering and transition-state theory calculations to exhibit strong non-Arrhenius effects at low temperatures and large kinetic isotope effects [4–6], thanks to tunneling as well as other quantum effects such as zero-point energy and resonances. The enhancement of the rate constant relative to the Arrhenius prediction at low temperatures is a tell-tale sign of tunneling, as it reduces the effective reaction barrier.

Since it is a quantum effect, a proper account of tunneling dynamics requires a QM treatment. While such a treatment has become routine for bound-state calculations in small polyatomic systems [7, 8], an accurate description of the tunneling affected reaction dynamics is much more difficult [9–11]. Apart from the exponential scaling of the number of degrees of freedom, the other main obstacles include the lack of an optimal coordinate system to describe the both reactant and product arrangement channels, the involvement of a large phase space, and the possible long lifetime when a reaction intermediate is involved. In addition, reliable multidimensional global potential energy surfaces (PESs) are often scarce, which prevent accurate QM calculations of the dynamics. Despite these challenges, significant progress has been made in QM treatments of tunneling and reaction dynamics in polyatomic reactive systems. In this chapter, we will focus on the role of tunneling in chemical reactions using two prototypical examples. The first is a unimolecular decomposition process, which involves the predissociation of ammonia (NH_3) in its first excited electronic state. The other is concerned with a bimolecular reaction: $HO + CO \rightarrow H + CO_2$, which plays an important role in many gas phase environments. These two prototypical systems share some important features. First, with six internal degrees of freedom these tetra-atomic systems offer much richer dynamics than the extensively studied triatomic reactions, but are more challenging to study quantum mechanically. Second and more relevant

to this chapter, the dynamics of these bond breaking and forming processes are significantly affected by tunneling.

3.2 Photodissociation of NH_3

The photo-induced dissociation of NH_3 to $NH_2(\tilde{A})/NH_2(\tilde{X}) + H$ has served as a prototype for understanding photodissociation dynamics in polyatomic systems [12, 13]. The first (A) absorption band between 45,000 and 67,000 cm^{-1} consists of a long series of nearly equidistant diffuse peaks, which have been assigned to excitations in the umbrella (2^n) vibration [14–16]. This progression reflects the dramatic change from the trigonal pyramidal (C_{3v}) equilibrium geometry of NH_3 in the ground electronic ($\tilde{X}^1A_1'$) state to the trigonal planar (D_{3h}) structure on the first excited electronic ($\tilde{A}^1A_2''$) state. The diffuse nature of the peaks suggests strong predissociation and the widths of these metastable resonances have been measured by many authors [17–24]. It was found that the line width, which is inversely proportional to the lifetime, of these vibrational levels depends on the vibrational quantum number (n). In addition, the widths of the ND_3 peaks are significantly narrower than their NH_3 counterparts, strongly suggesting tunneling.

The predissociation of ammonia stems from the quasi-bound nature of the vibrational states in the Franck–Condon region of the $\tilde{A}$-state PES. Ab initio calculations indicated a small barrier along the dissociation (N–H) coordinate immediately outside the Franck–Condon region [25–27], due primarily to the interaction between the N(3s) Rydberg state and the σ^* antibonding state. The existence of this barrier is consistent with the diffuse nature of the 2^n peaks and with the isotope effect, as the predissociation, at least for low energies, proceeds via tunneling. At higher energies, the lifetime is presumably influenced by a number of other factors, including intramolecular vibrational energy redistribution (IVR) among the various vibrational modes in NH_3. Beyond the barrier, the excited $\tilde{A}$-state forms a seam of conical intersections with the ground $\tilde{X}$-state [25–29], which are responsible for non-adiabatic transitions leading to the dominant $NH_2(\tilde{X}) + H$ fragmentation channel observed in experiment. The schematic $\tilde{X}/\tilde{A}$ PESs for ammonia are illustrated in Fig. 3.1.

The quasi-bound nature of $NH_3(\tilde{A}^1A_2'')$ in the Franck–Condon region provides an ideal case for studying tunneling dynamics in unimolecular reactions [27, 30–33]. As expected, the lifetime of a metastable quantum resonance state depends sensitively on the shape and height of the barrier, as well as other factors such as intermodal coupling. Indeed, the measured lifetimes of both NH_3 and ND_3 exhibit some surprising trends. For example, the first overtone of the umbrella vibration (2^1) of both NH_3 and ND_3 has a longer lifetime than the ground vibrational state (2^0) and the second overtone (2^2), although higher overtones typically have shorter lifetimes [15–17, 19, 22]. In order to quantitatively understand the unique dissociation dynamics, much effort has been devoted to the accurate determination of the PES of the excited as well as the ground states of NH_3 [25–29, 34]. However, it is only recently that ab initio-based full-dimensional PESs have become available.

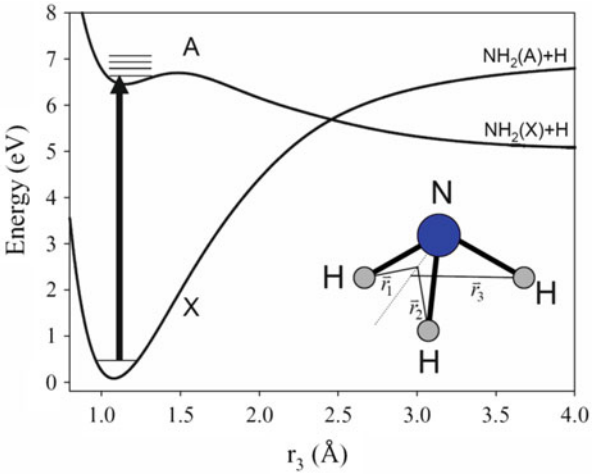

Fig. 3.1 Schematic $\tilde{X}/\tilde{A}$ potential energy surfaces for NH_3. Adapted from [38] with permission

To this end, Truhlar and coworkers have developed the first full-dimensional quasi-diabatic representation of the coupled $\tilde{X}/\tilde{A}$ PESs for NH_3 [35, 36]. More recently, Zhu, Ma, Guo, and Yarkony (ZMGY) presented a more accurate set of coupled quasi-diabatic PESs for this system [37]. These PESs allowed full-dimensional QM calculations of the absorption spectra, which yielded detailed information about the tunneling dynamics in this system [37–40].

Accurate knowledge of the PESs alone is of course insufficient to yield lifetimes. A QM treatment of the dissociation dynamics is required and full dimensionality is preferred as both tunneling and IVR are multidimensional in nature. To this end, we have developed such a wave packet-based method for the photodissociation of ammonia using an exact Hamiltonian ($J = 0$) for the nuclear motion [38]. The six-dimensional Hamiltonian and wavefunction in the Radau–Jacobi coordinates were discretized using a mixed representation [41]. Our approach relied on the Chebyshev propagation [42] of the excited state wave packet prepared by a vertical excitation from the ground electronic state, in the same spirit as the time-dependent approach to photodissociation [43]. The absorption spectrum can be readily obtained by a discrete Fourier transform of the Chebyshev autocorrelation function [44]. We note in passing that classical models have been employed for studying the photodissociation of ammonia [45, 46], but they are incapable of giving a good representation of the tunneling dynamics that dominates the absorption spectra.

The absorption spectra for both NH_3 and ND_3 were first calculated by our group [38] on the coupled full-dimensional PESs developed by Li, Valero, and Truhlar (LVT) [36]. Consistent with experiment, the absorption spectra are dominated by the predissociative umbrella (2^n) resonances. The calculated positions, widths, and intensities of these states are in qualitatively good agreement with the experimental

findings. For example, the ND_3 peaks have typically much narrower widths due to the larger reduced mass in the dissociation coordinate, consistent with the experimental observations [16, 17, 19]. Quantitatively, however, the line widths of the 2^n features in the absorption spectra, which underscore the state-specific tunneling rates, deviate significantly from the most reliable experimental values [34]. Specifically, the calculated widths of the low-lying states are generally three times too large, presumably because the classical barrier height of 1,750 cm^{-1} on the $\tilde{A}$-state PES [36] is too low compared with that estimated from experimental data ($\sim$2,100 cm^{-1}) [22]. Despite these large deviations, the 2^1 anomaly was reproduced. This anomaly is due apparently to the fact that the dissociation barrier rises quickly with the umbrella angle. Consequently, the 2^1 state, which has a node at planarity, is subjected to a larger effective barrier than the planar 2^0 state, thus possessing a longer lifetime [18]. For higher overtones, the predissociation is dominated by intermodel coupling, and as a result the dissociation rate increases with energy. Subsequent calculations by Giri et al. [39] using an approximate QM method yielded qualitatively similar results.

Since the nuclear dynamics was treated exactly, the errors in the absorption spectra can be attributed to inaccuracies in the PESs. Not surprisingly, the agreement with experiment is greatly improved when the more accurate ZMGY PESs were used [37]. In Fig. 3.2, the calculated absorption spectra of both NH_3 and ND_3 are compared with the experimental counterparts measured in a cold supersonic jet [19]. The nuclear spin statistics at the experimental temperature [26] has been included in the calculations. The agreement in both the positions and intensities is quite satisfactory. In addition, the calculated widths are also compared in Fig. 3.3 with experiment and previous theoretical results. The theory–experiment agreement in the absorption spectra is much better than that on the LVT PESs, and the agreement in the widths, including the 2^1 anomaly, is almost quantitative. The improvements can almost certainly be attributed to the higher level of the ab initio (multi-reference configuration interaction or MRCI using the aug-cc-pVTZ basis set with an extra 3 s Rydberg function for N) calculations and a better fitting scheme [47]. Indeed, the classical barrier height of the ZMGY $\tilde{A}$-state PES is, for example, 2,153 cm^{-1} [37], in much better agreement with the experimental estimation of $\sim$2,100 cm^{-1} [22].

It should be noted that the inclusion of the seam of conical intersections at larger N–H distances in latter dynamical calculations did not change the quantitative agreement in the absorption spectra [40], suggesting that the subsequent non-adiabatic dynamics has almost no impact on the initial tunneling dynamics. Interestingly, the ZMGY PESs have recently been shown to perform extremely well in reproducing the $NH_2(\tilde{A})/NH_2(\tilde{X})$ product branching ratio in the non-adiabatic dynamics of ammonia photodissociation [40], which further confirms the accuracy of the global PESs and their coupling.

One of the more intriguing questions concerning the tunneling dynamics in ammonia photodissociation is the impact of vibrational excitation prior to the electronic transition. Crim and coworkers have examined the action spectra of such vibrationally mediated photodissociation processes in NH_3 and found drastically

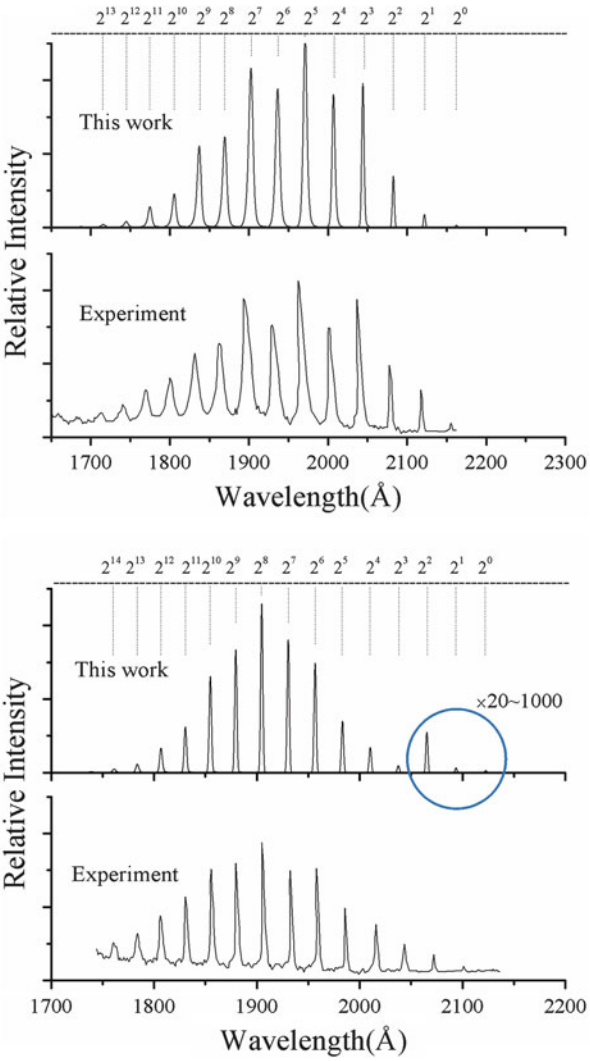

Fig. 3.2 Comparison of the calculated and measured [19] absorption spectra of NH_3 (*upper panel*) and ND_3 (*lower panel*). Adapted from [37] with permission

different line structures and widths from photodissociation of vibrationally unexcited NH_3 [34]. The changes in the absorption spectra can be qualitatively understood as different vibrational states on the ground electronic state have different Franck–Condon factors with those on the excited electronic $\tilde{A}$-state. More striking is the very unusual H translational energy distributions, which are interpreted as the result of changing product branching ratios resulted from different non-adiabatic transitions [48, 49]. Such problems can in principle be addressed using the same

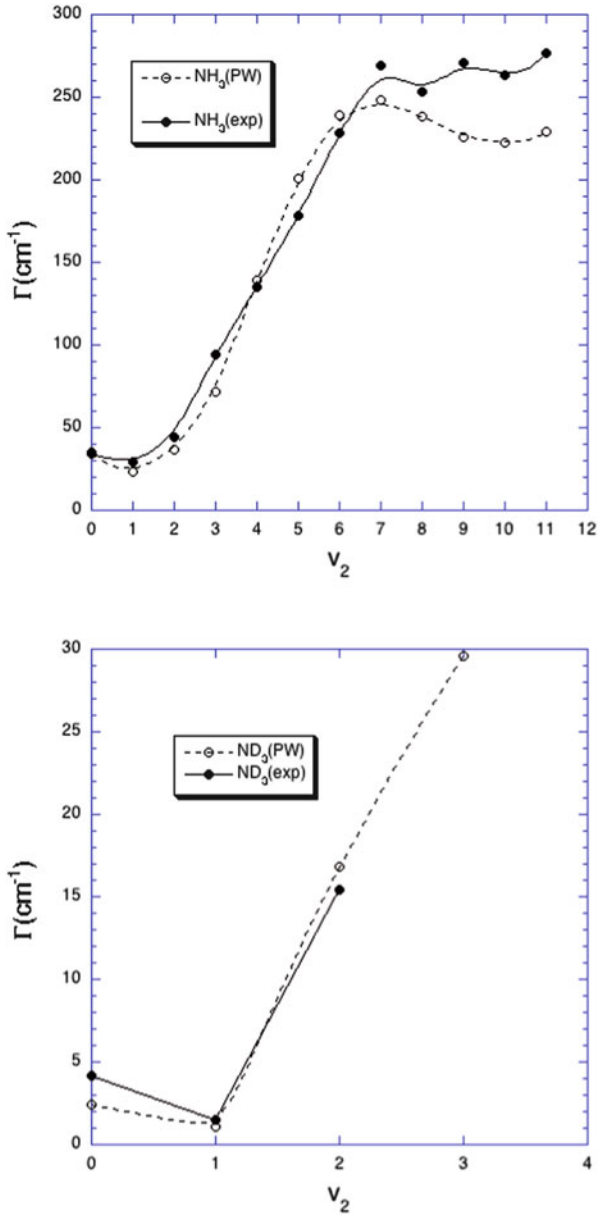

Fig. 3.3 Comparison of the calculated and measured [17, 19, 22] widths of the 2^n resonances of NH_3 (*upper panel*) and ND_3 (*lower panel*) in their absorption spectra. Adapted from [37] with permission

technique described above, which will provide additional information about the role of tunneling in this prototypical system.

3.3 $OH + CO \rightarrow H + CO_2$ Reaction

The exothermic OH + CO reaction plays an important role in combustion as the last step of hydrocarbon oxidation, which represents the main heat release step, and is considered to be the "second most important combustion reaction" [50]. It is also the main CO oxidation channel in the atmosphere and controls the atmospheric OH concentration [51]. Unlike many activated reactions, the PES of this reaction has a very small or null overall barrier. Instead, the association of HO and CO results in a relatively stable HOCO intermediate [52, 53], which has both *cis* and *trans* isomers. The kinetics of the reaction has been extensively studied and the rate constants have some very unusual characteristics [54–58]. For example, the reaction shows a strong pressure dependence, which was attributed to the complex-forming mechanism [54]. In addition, the rate constant is almost constant at low temperatures, but it increases sharply with temperature above 500 K. This non-Arrhenius behavior is indicative of tunneling along the reaction pathway. The importance of tunneling in the reaction dynamics is also supported by a strong H/D kinetic isotope effect [58–60], and rate enhancement *via* vibrational excitation of the OH reactant [59, 61, 62]. Indeed, tunneling has to be included in kinetic modeling of the reaction if a quantitative agreement with experiment is to be obtained [58, 63–65]. In particular, we note the recent semi-classical transition-state theory study of the reaction rate constant based on high-quality ab initio anharmonic force fields at transition states reproduced the experimental data, including the non-Arrhenius behaviors at low temperatures, almost perfectly [66], underscoring the importance of tunneling in the reaction.

This reaction and its reverse have become a prototype to understand complex-forming elementary reactions [9, 10, 67]. As illustrated in the previous section, the accuracy of the underlying PES is essential for quantitatively characterization of the reaction dynamics. For HOCO, several earlier global PESs, notably the ones by Schatz, Fitzcharles, and Harding (SFH) [68], by Yu, Muckerman, and Sears (YMS) [69], by Lakin, Troya, Schatz, and Harding (LTSH) [70], and by Valero, van Hemert, and Kroes (VvHK) [71], have been developed. These and other PESs have been used in numerous dynamical calculations, using both quasi-classical trajectory (QCT) [68, 70, 72–81] and QM methods [82–99]. Unfortunately, these PESs do not have the necessary accuracy, due primarily to the small number of ab initio points used in constructing these six-dimensional potential energy functions. To improve our understanding of this important reactive system, we have recently reported a new global PES for this system at the level of UCCSD(T)-F12/AVTZ [100–102]. This represents the most accurate level of theory affordable at present and the accuracy has recently been corroborated by MRCI + Q-F12 calculations [103]. Approximately ~50,000 points distributed in a large configuration space relevant to the reaction were fit with the permutation invariant polynomial method [104, 105]. The PES represents the stationary points

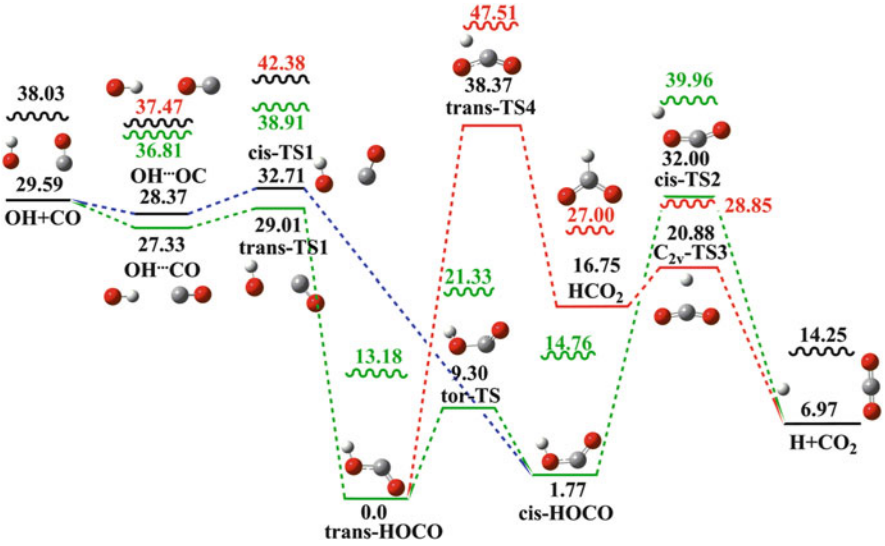

Fig. 3.4 Energetics of reaction pathways for the $HO + CO \rightarrow H + CO_2$ reaction. The ab initio energies (E_0) of the stationary points are given in kcal/mol relative to the *trans*-HOCO minimum. The wavy lines are for ZPE-corrected energies ($E_0 + ZPE$) of the relevant species. All species are planar, except tor-TS. Adapted with permission from [101]

quite well with a global fitting error of roughly 1.0 kcal/mol, indicating that the PES is sufficiently accurate for most dynamical calculations.

The ab initio-based energetics of the reaction pathway for this reaction is illustrated in Fig. 3.4. From the $HO + CO$ reactants, two pathways exist for the formation of the HOCO intermediate, each gated by a bottleneck (*trans* or *cis*-TS1). In the entrance channel, there also exist two collinear hydrogen-bonded van der Waals complexes, one of which has been detected experimentally [106]. Within the HOCO well, the *cis* and *trans*-HOCO species are separated by a relatively low isomerization barrier (tor-TS). On the other hand, the dissociation of the two HOCO isomers to the $H + CO_2$ products is controlled by two other transition states, namely TS2 and TS4, with the latter less relevant at low collision energies due to its higher energy. A key feature of the HOCO PES is that the lowest entrance and exit barriers are roughly isoenergetic, which give rise to the unusual kinetic behaviors of the reaction discussed above. In particular, the exit channel transition state (TS2) is much tighter and has a reaction coordinate dominated by the H–O stretching motion, which is amenable to tunneling dynamics.

This new PES was used in a recent full-dimensional QM calculations [107], which solves the nuclear Schrödinger equation with the Chebyshev propagator [42] in the OH–CO Jacobi coordinates. Such calculations are extremely challenging due to the three heavy atoms in the system and the large number of quantum states supported by the HOCO well. As a result, only the $J = 0$ partial wave was considered. The initial state in the reactant asymptote was represented by a

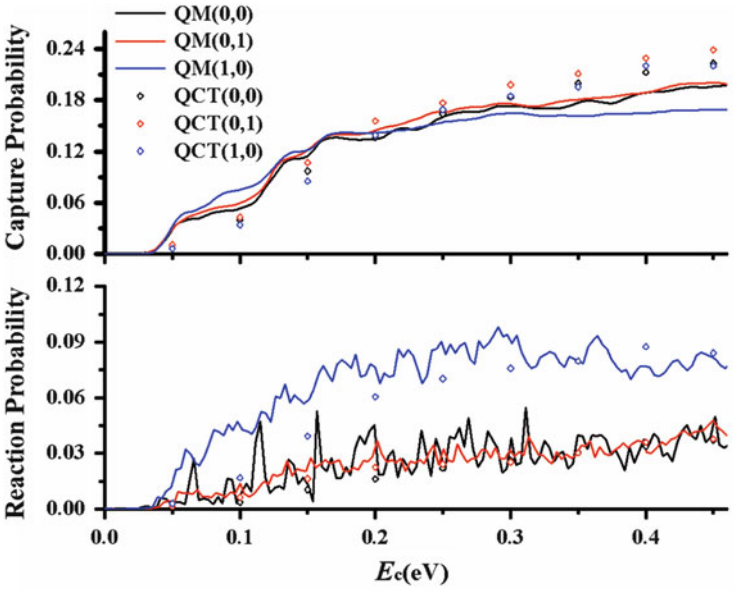

Fig. 3.5 Capture (*upper panel*) and reaction (*lower panel*) probabilities ($J = 0$) for (n_{OH}, n_{CO}) states of reactants as a function of collision energy (E_c). The quantum mechanical (QM) and QCT results ($b = 0$) are given in lines and symbols, respectively. Adapted with permission from [107]

Gaussian wave packet in the scattering coordinate multiplied by the internal state wave functions for OH and CO. A mixed grid/basis representation [41] was used to discretize the Hamiltonian and wave packet. The energy-dependent total reaction probability was calculated using a flux method [108] at a dividing surface placed in the product channel just beyond TS2. For capture calculations, on the other hand, the dividing surface was placed behind TS1, which saves a large number of grid points. The calculated $J = 0$ capture and reaction probabilities for a number of reactant internal states are shown in Fig. 3.5 as a function of the collision energy. As comparison, corresponding QCT results were also obtained with zero impact parameter ($b = 0$) and included in the same figure. It is clear from the figure that the reactivity is very low despite its near barrierless nature, in qualitative agreement with previous QM calculations on earlier PESs [93, 94, 98]. This is due to the fact that the reaction has to overcome two bottlenecks in both the entrance and exit channels, as shown by the substantially larger capture probabilities in Fig. 3.5. Both the capture and reaction probabilities tend to increase with the collision energy with a common reaction threshold of ~0.03 eV, which is primarily due to the entrance channel bottleneck. The oscillatory structures in the reaction probabilities are apparently due to numerous overlapping resonances, which have been noted in previous QM calculations [93, 94, 98].

As shown in Fig. 3.5, excitation in the vibration of the OH reactant ($v = 1$) significantly enhances the reactivity, while the effect in CO excitation is limited.

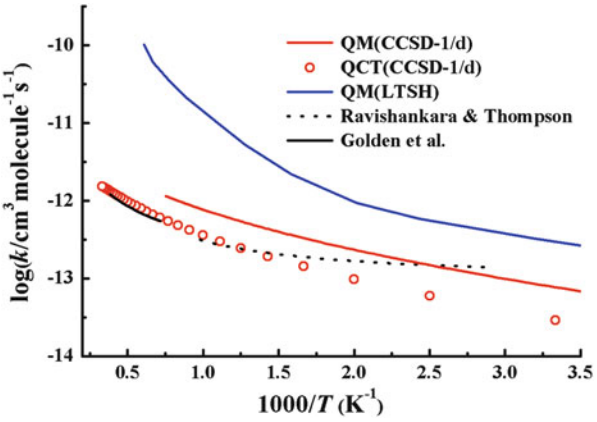

Fig. 3.6 Comparison of calculated quantum and QCT rate constants with experimental ones in the low pressure limit [55, 58]. The quantum rate constants reported by Liu et al. [98] on the LTSH PES are also included for comparison. Adapted with permission from [107]

This observation is consistent with experimental evidence for this reaction [59, 61], as well as our earlier QCT work [101] and previous QM calculations on the LTSH PES [98, 99]. Interestingly, the vibrational excitation in the reactant has little impact on the capture probabilities. This follows that the energy imparted in the OH vibration helps to surmount TS2 as the reaction coordinate at the saddle point is essentially the O–H stretch. However, this is possible only when the HOCO intermediate is relatively short-lived, rendering incomplete randomization of energy before surmounting TS2, which retains energy in the O–H bond. A short-lived HOCO intermediate is consistent with experimental observations [52, 53, 109, 110] and our QCT studies of this system on this new PES [101, 102].

It is also interesting to compare the $J = 0$ capture and reaction probabilities with the corresponding QCT results obtained with zero impact parameter. Although the QCT probabilities cannot account for quantum resonances, Fig. 3.5 suggests that the overall agreement with the corresponding QM results is quite reasonable. The QCT probabilities are typically smaller than their quantum counterparts at lower collision energy, particularly for the OH excited case, suggestive of tunneling. The importance of tunneling is expected to be even more pronounced as J increases, because the tight TS2 saddle point is raised by the centrifugal potential.

Figure 3.6 displays the comparison of the theoretically calculated thermal rate constants with the experimental data in the low pressure limit [55, 58]. The QM rate constants were estimated using the J-shifting method [111] with energy shifts determined at TS2, while the standard thermal sampling was used in the QCT calculations [100]. A caveat is in order concerning the validity of the J-shifting approximation in complex-forming reactions, since the reactivity in such a reaction is not completely determined by the saddle point [67]. For comparison, the J-shifted QM rate constants reported by Liu et al. [98], who used the earlier LTSH PES [98],

are also included in the same figure. The calculated QM rate constants on the new PES are in much better agreement with experimental data than that obtained on the LTSH PES, although there is still significant underestimation at low temperatures and overestimation at high temperatures. The discrepancies at low temperatures are partially due to tunneling that is not completely captured by the J-shifting model. Indeed, the centrifugal potential for $J > 0$ is expected to raise the thin barrier at the tight TS2 saddle point to energies significantly higher than the reactant asymptote, further accentuating the impact of tunneling. On the other hand, the errors at high temperatures may also be due to the over-simplification of the J-shifting model, but the precise origin has to await future explicit $J > 0$ calculations. Since the same QM method was used, the improvement in the theory–experiment agreement for thermal rate constants can be attributed to the improved accuracy in the new PES. On the other hand, the QCT rate constants also reproduced the high temperature data quite well, but underestimate at low temperatures, due almost certainly to the neglect of tunneling.

Despite the improvements in describing the reaction PES for the $HO + CO \rightarrow H + CO_2$ reaction, there is evidence indicating that the new PES is still not perfect. For example, our recent QCT studies [101, 112] failed to reproduce the experimental internal state distribution of the CO_2 product [109, 113, 114] and the corresponding angular distribution [80, 109, 114]. For the reverse $H + CO_2 \rightarrow HO + CO$ reaction, our QCT results [102] underestimate the CO rotational state distribution [115, 116], although in good agreement with the experimental rate constant [117], total integral cross sections [118, 119], and the HO rotational distribution [118, 119]. It is possible that these discrepancies are due to experimental errors, but it is more likely that subtle deficiencies in the PES are the culprit. Indeed, a more recent fit of the CCSD(T)-F12/AVTZ points for this system using neural network has uncovered several shortcoming of our PES, resulting in even lower reaction probabilities [120].

The most dramatic manifestation of tunneling was found in the photodetachment of the $HOCO^-$ anion, which produces the neutral HOCO species and its dissociation fragments. Photodetachment of negative ions has been widely used as a powerful way to probe dynamics of chemical reactions on the corresponding neutral PESs [121]. Since this approach sometimes affords a direct access to the transition-state region of the bimolecular reactions, this so-called transition-state spectroscopy by negative ion photodetachment has revealed intricate resonances near the reaction barrier [122], which control the reactivity. The photodetachment of $HOCO^-$ (and $DOCO^-$) has been extensively investigated by Continetti and coworkers [123–128]. The photo-ejection of an electron from the anion places the system on the neutral PES near the HOCO wells. Earlier photoelectron–photofragment coincidence (PPC) experiments revealed the formation of the HOCO, $HO + CO$, and $H + CO_2$ products [123, 124]. More recently, a new cryogenically cooled PPC apparatus was employed to achieve much higher resolution and to eliminate hot bands [126, 127]. One of the most striking observations is that nearly all photoelectrons in the $H + CO_2$ channel were found to have energies above the maximum limit predicted for TS2, suggesting the dissociation of HOCO into the $H + CO_2$ channel is mostly via tunneling through the barrier [126, 127]. In other words, the reaction is pure quantum in nature.

Interestingly, an earlier full-dimensional QM study of the photodetachment of $HOCO^-$ found no evidence of tunneling, although all three experimentally observed channels were identified [129]. There are several reasons for the discrepancy. The most likely is that the LTSH PES [70] used in the calculation was not sufficiently accurate, particularly with regard to the thickness of the barrier associated with TS2, as shown in our recent work [100, 101]. As a result, tunneling might be substantially underestimated. We have reinvestigated [130] the problem using our new HOCO PES [100, 101], which has a much thinner barrier leading to the $H + CO_2$ products than the LTSH PES. Both full-dimensional and reduced-dimensional QM models have been used. This is important because ample evidence suggests that tunneling is a multidimensional phenomenon [100, 127]. Due to the formidable computational costs, however, the former was restricted to the calculation of the low-resolution energy spectrum of the photodetachment, which is pertinent to the initial evolution of the wave packet on the neutral PES. In order to describe long time events due to tunneling, on the other hand, the dynamics was followed using a five-dimensional model with the non-reacting C–O bond fixed. While recent QM studies have shown that the non-reactive CO bond is not in the strict sense a spectator in the $HO + CO$ reaction [95, 98], this approximation is unlikely to qualitatively change the conclusion for photodetachment, especially concerning the tunneling over TS2. This is because the C–O bond length does not change significantly over the course of the dissociation.

The theoretical model for photodetachment is similar to that used to describe photodissociation outlined in the last section. As illustrated in Fig. 3.7, the initial wave packet on the neutral PES was chosen as the ground vibrational state of *cis*-$HOCO^-$, which has a lower energy than its *trans* counterpart. The anion vibrational eigenfunction was determined on a newly developed anion PES at the same CCSD(T)-F12/AVTZ level [130], as used to construct the neutral PES [100, 101]. The neutral wave packet was propagated to yield probabilities to both the $HO + CO$ and $H + CO_2$ asymptotes with a flux method [108] and the cosine Fourier transform of the Chebyshev autocorrelation function yielded the energy spectrum [44]. The discretization of the Hamiltonian and wavepacket, and the propagation were essentially the same as in our recent reaction dynamics study [107].

In Fig. 3.7, the low-resolution spectra were obtained from the Fourier transform of the corresponding Chebyshev autocorrelation functions after a short (100 steps) propagation of the initial wave packets on the neutral PES. In the same figure, we have also included the spectrum converted from the experimental electronic kinetic energy (eKE) distribution [126] via the following relation: $E = h\nu - \text{eKE}$, where the experimental photon energy is 3.21 eV (386 nm) [126]. The agreement between the experimental distribution and the full-dimensional spectrum is excellent, validating the PESs used in the calculations. The shift of the reduced-dimensional spectrum can presumably be attributed to the freezing of the non-reactive CO bond. It is interesting to note that the geometry of the anion is sufficiently similar to that of the corresponding neutral species, little amplitude was found outside the HOCO well on the neutral PES. This observation is important because it indicates that only a small

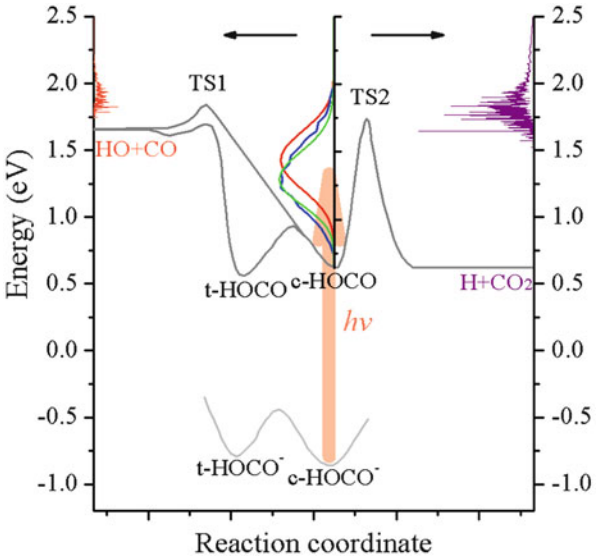

Fig. 3.7 Zero-point corrected energetics of the schematic HOCO/$HOCO^-$ PESs. The energy zero is placed at the global *trans*-HOCO minimum of the neutral PES. The calculated energy spectrum of the HOCO species prepared by photodetachment of the $HOCO^-$ anion is displayed in *green* (full-dimensional model) and *red* (five-dimensional model) with the experimentally derived spectrum in *blue*. In addition, the calculated dissociation probabilities for the HO + CO and $H + CO_2$ channels are also given in *orange* and *purple*. Note the substantial probabilities in the latter channel suggest tunneling. Adapted with permission from [130]

fraction of the neutral species will have the necessary energy to dissociate directly into both the HO + CO and $H + CO_2$ channels. On the other hand, the majority of the neutral species prepared by photodetachment is temporarily trapped in the HOCO well as metastable resonances. As shown in Fig. 3.4, the trapped HOCO species has no choice but to decay via tunneling through the barrier under TS2.

In Fig. 3.8, the high-resolution energy spectrum of HOCO prepared by photodetachment of *cis*-$HOCO^-$ is displayed. As expected, all HOCO species below the effective dissociation barriers exist as resonances, as illustrated by the sharp peaks in Fig. 3.8. There is no bound state because the lowest-lying vibrational state of *cis*-HOCO is above the $H + CO_2$ asymptote. Based on inspection of wave functions, these peaks can be assigned to bending (ν_5) progressions, due apparently to the fact that the bending angles of the anion differ significantly from those of the neutral species. Some excitation in the reactive C–O bond stretch (ν_4) is also present. On the other hand, the OH bond length in the negative ion and the neutral species is roughly the same, resulting in negligible excitation in ν_1 (O–H stretch). This assignment is in good agreement with the most recent photoelectron spectroscopic study of the cold $HOCO^-$ anion, in which bending progressions in ν_5 with some excitations in ν_4 and ν_3 (HOC bend) were found [128]. As discussed in our recent work [101], the vibrational frequencies of both *cis* and *trans*-HOCO species calculated on our PES

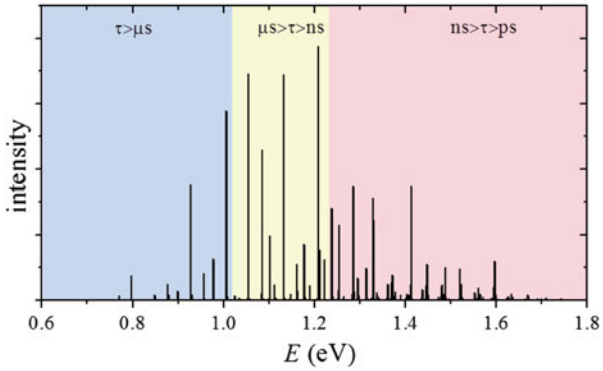

Fig. 3.8 High-resolution energy spectrum for HOCO prepared by photodetachment of the $HOCO^-$ anion. The energy is referenced to the *trans*-HOCO potential minimum and the approximate lifetime ranges of the resonances are color coded in *blue* for μs, *orange* for ns, and *red* for ps. Adapted with permission from [130]

are in good agreement with these experimental results as well as the benchmark ab initio data reported in the same publication [128].

The line widths of these resonances have been estimated and they are grouped in Fig. 3.8 based on their calculated lifetimes. It is clear that some of the resonances have exceedingly long lifetimes (>μs), which are comparable to the flight time in the experimental set up [127]. As a result, these resonances would have been classified as stable HOCO species in the experiment. Close to the energy of TS2, the lifetimes are on the order of ps, which can be readily captured in our flux calculations. The range of the lifetimes reported here is consistent with the estimates based on an earlier effective one-dimensional model [127]. Above the dissociation limit, there are still resonances superimposed on broad features, which correspond to direct dissociation.

The calculated dissociation probabilities to the HO + CO and H + CO_2 arrangement channels are shown in Fig. 3.7. In the HO + CO channel, the energy distribution centers at 1.82 eV relative to the *trans*-HOCO global minimum, in good agreement with the experimental distribution between 1.65 and 2.0 eV [126]. Comparing with the H + CO_2 channel, the HO + CO fraction is substantially smaller, again consistent with experiment [126]. On the other hand, the probability for the H + CO_2 channel has contributions from both above and under the TS2 barrier. The former converges quickly because of the relatively short time needed to dissociate. However, the tunneling contribution, which is apparent in the figure below the dissociation limit, is not quite converged in our calculation due to the extremely long lifetimes of the resonances at low energies. Nonetheless, it is clear that the tunneling channel makes up a large percentage of the total photodetachment.

In comparing with the experimental branching ratios, it is important to realize that the experimentally detected HOCO species are not strictly speaking stable because these resonances have energies higher than the H + CO_2 dissociation asymptote. However, lifetimes of these deep tunneling states are so long that the

7.8 μs flight time [127] might still be insufficient to observe their decomposition. As discussed above, it is impractical to expect wave packet propagations on such time scales either. Consequently, there is substantial uncertainty in the partition of the HOCO and $H + CO_2$ channels below the barrier. However, this uncertainty does not affect the overall agreement between theory and experiment. The calculation results presented here clearly demonstrated that photodetachment of $HOCO^-$ produces predominantly HOCO resonances that dissociate into $H + CO_2$, in agreement with the conclusion made by Continetti and coworkers [127].

Finally, it might be worthwhile to comment on the impact of tunneling facilitated HOCO decomposition in the bimolecular $HO + CO \rightarrow H + CO_2$ reaction kinetics. In the low pressure limit, the HOCO intermediate formed is largely above TS2 and as a result tunneling will be mostly through the centrifugal barrier near the exit bottleneck (TS2). In the high pressure limit, on the other hand, the reaction rate is dominated by the formation (capture) rate of the HOCO intermediate, as its overcome of the exit barrier is achieved by collisional excitations. The tunneling facilitated decomposition of thermalized HOCO is thus of less importance. As a result, the tunneling effect is expected to have an important, but not overwhelming, impact on kinetics of this bimolecular reaction and the impact will be limited to low temperatures.

3.4 Conclusions

In this chapter, we have shown through two examples the important role played by tunneling in reaction dynamics. In the unimolecular dissociation dynamics of ammonia photodissociation on its first excited electronic state, the lifetimes of the lowest-lying resonances are strongly affected by tunneling over a small barrier in the dissociation coordinate, which is responsible for a lifetime anomaly in the first overtone and for the large H/D isotope effect. Similarly, the tunneling in the bimolecular $HO + CO \rightarrow H + CO_2$ reaction has been shown to affect the rate constants at low temperatures as well as the H/D isotope effect. These two examples illustrate a typical scenario for the well-known quantum phenomenon in molecular systems, in which the dynamics is nominally perturbed by tunneling. On the other hand, chemical reactions dominated by deep tunneling are uncommon. In two systems found recently [131, 132], for example, the dominant products are produced via deep tunneling over a higher barrier even when another channel with a lower barrier is available. The photodetachment of $HOCO^-$ presents another interesting example, in which the decomposition of HOCO is almost exclusively due to tunneling. These unique reaction systems, suggest that quantum effects such as tunneling can in a few cases dominate, rather than merely influence, reactive systems.

Acknowledgments This work has been supported by the Department of Energy and National Science Foundation. We would also like to thank Joel Bowman, Fleming Crim, Richard Dawes, Evi Goldfield, Don Truhlar, Al Wagner, Daiqian Xie, David Yarkony, and Dong Hui Zhang for many stimulating discussions.

References

1. Schatz GC (1987) Tunneling in bimolecular collisions. Chem Rev 87:81
2. Schatz GC (1988) Quantum effects in gas phase bimolecular chemical reactions. Annu Rev Phys Chem 39:317
3. Aoiz FJ, Banares L, Herrero VJ (2005) The $H + H_2$ reactive system. Progress in the study of the simplest reaction. Int Rev Phys Chem 24:119
4. Mielke SL, Peterson KA, Schwenke DW, Garrett BC, Truhlar DG, Michael JV, Su M-C, Sutherland JW (2003) $H + H_2$ thermal reaction: a convergence of theory and experiment. Phys Rev Lett 91:063201
5. Fleming DG, Arseneau DJ, Sukhorukov O, Brewer JH, Mielke SL, Schatz GC, Garrett BC, Peterson KA, Truhlar DG (2011) Kinetic isotope effects for the reactions of muonic helium and muonium with H_2. Science 331:448
6. Suleimanov YV, Pérez de Tudela R, Jambrina PG, Castillo JF, Sáez-Rábanos V, Manolopoulos DE, Aoiz FJ (2013) A ring polymer molecular dynamics study of the isotopologues of the $H + H_2$ reaction. Phys Chem Chem Phys 15:3655
7. Guo H (2007) Recursive solutions to large eigenproblems in molecular spectroscopy and reaction dynamics. Rev Comput Chem 25:285
8. Bowman JM, Carrington T, Meyer H-D (2008) Variational quantum approaches for computing vibrational energies of polyatomic molecules. Mol Phys 106:2145
9. Bowman JM, Schatz GC (1995) Theoretical studies of polyatomic bimolecular reaction dynamics. Annu Rev Phys Chem 46:169
10. Althorpe SC, Clary DC (2003) Quantum scattering calculations on chemical reactions. Annu Rev Phys Chem 54:493
11. Nyman G, Yu H-G (2012) Quantum approaches to polyatomic reaction dynamics. Int Rev Phys Chem 32:39
12. Ashfold MNR, Bennett CL, Stickland RJ (1987) Rydberg states of ammonia. Comments At Mol Phys 19:181
13. Dixon RN (1994) Liversidge lecture. The dynamics of photodissociation. Chem Soc Rev 23:375
14. Leifson SW (1933) Astrophys J 63:73
15. Douglas AE (1963) Discuss Faraday Soc 35:158
16. Vaida V, Hess W, Roebber JL (1984) The direct ultraviolet absorption spectrum of the $A^1A_2'' \leftarrow X^1A_1$ transition of jet-cooled ammonia. J Phys Chem 88:3397
17. Ziegler LD (1985) Rovibrational absorption analysis of the A←X transition of ammonia. J Chem Phys 82:664
18. Ashfold MNR, Bennett CL, Dixon RN (1986) Dissociation dynamics of NH_3. Faraday Disc Chem Soc 82:163
19. Vaida V, McCarthy MI, Engelking PC, Rosmus P, Werner H-J, Botschwina P (1987) The ultraviolet absorption spectrum of the $A^1A_2'' \leftarrow X^1A_1'$ transition of jet-cooled ammonia. J Chem Phys 86:6669
20. Nakajima A, Fuke K, Tsukamoto K, Yoshida Y, Kaya K (1991) Photodissociation dynamics of NH_3, NH_2D, NHD_2, and ND_3: rovibronic absorption analysis of the A–X transition. J Phys Chem 95:571
21. Henck SA, Mason MA, Yan W-B, Lehmann KK, Coy SL (1995) Microwave detected, microwave-optical double resonance of NH_3, NH_2D, HND_2, and ND_3. I. Structure and force field of the A state. J Chem Phys 102:4772
22. Henck SA, Mason MA, Yan W-B, Lehmann KK, Coy SL (1995) Microwave detected, microwave-optical double resonance of NH_3, NH_2D, HND_2, and ND_3. II. Predissociation dynamics of the A state. J Chem Phys 102:4783
23. Baronavski AP, Owrutsky JC (1995) Lifetime of the $v_2' = 1$ A state of ND_3 measured by two color deep UV femtosecond multiphoton ionization spectroscopy. J Phys Chem 99:10077

24. Wells KL, Perriam G, Stavros VG (2009) Time-resolved velocity map ion imaging study of NH_3 photodissociation. J Chem Phys 130:074308
25. Runau R, Peyerimhoff SD, Buenker RJ (1977) Ab initio study of photodissociation of ammonia. J Mol Spectrosc 68:253
26. Rosmus P, Botschwina P, Werner H-J, Vaida V, Engelking PC, McCarthy MI (1987) Theoretical A–X absorption and emission spectrum of ammonia. J Chem Phys 86:6677
27. McCarthy MI, Rosmus P, Werner H-J, Botschwina P, Vaida V (1987) Dissociation of NH_3 to $NH_2 + H$. J Chem Phys 86:6693
28. Manz U, Reinsch E-A, Rosmus P, Werner H-J, O'Neil SV (1809) Dissociation of NH_3 to $NH + H_2$. J Chem Soc Faraday Trans 1991:87
29. Yarkony DR (2004) Exploring molecular complexity: conical intersections and NH_3 photodissociation. J Chem Phys 121:628
30. Dixon RN (1988) The stretching vibrations of ammonia in its A^1A'' excited state. Chem Phys Lett 147:377
31. Dixon RN (1996) Photodissociation dynamics of A state ammonia molecules. III. A three-dimensional time-dependent calculation using ab initio potential energy surfaces. Mol Phys 88:949
32. Tang SL, Imre DG (1988) Ammonia, the A<−X transition. Chem Phys Lett 144:6
33. Seideman T (1995) The predissociation dynamics of ammonia: a theoretical study. J Chem Phys 103:10556
34. Bach A, Hutchison JM, Holiday RJ, Crim FF (2002) Vibronic structure and photodissociation dynamics of the A state of jet-cooled ammonia. J Chem Phys 116:9315
35. Nangia S, Truhlar DG (2006) Direct calculation of coupled diabatic potential-energy surfaces for ammonia and mapping of a four-dimensional conical intersection seam. J Chem Phys 124:124309
36. Li ZH, Valero R, Truhlar DG (2007) Improved direct diabatization and coupled potential energy surfaces for the photodissociation of ammonia. Theor Chem Acc 118:9
37. Zhu X, Ma J, Yarkony DR, Guo H (2012) Computational determination of the A state absorption spectrum of NH_3 and of ND_3 using a new quasi-diabatic representation of the X and A states and full six-dimensional quantum dynamics. J Chem Phys 136:234301
38. Lai W, Lin SY, Xie D, Guo H (2008) Full-dimensional quantum dynamics of A-state photodissociation of ammonia. Absorption spectra. J Chem Phys 129:154311
39. Giri K, Chapman E, Sanz CS, Worth G (2011) A full-dimensional coupled-surface study of the photodissociation dynamics of ammonia using the multiconfiguration time-dependent Hartree method. J Chem Phys 135:044311
40. Ma J, Zhu X, Guo H, Yarkony DR (2012) First principles determination of the NH_2/ND_2(A/X) branching ratios for photodissociation of NH_3/ND_3 via full-dimensional quantum dynamics based on a new quasi-diabatic representation of coupled ab initio potential energy surface. J Chem Phys 137:22A541
41. Chen R, Ma G, Guo H (2001) Six-dimensional quantum calculation of highly excited vibrational energy levels of hydrogen peroxide and its deuterated isotopomers. J Chem Phys 114:4763
42. Chen R, Guo H (1996) Evolution of quantum system in order domain of Chebychev operator. J Chem Phys 105:3569
43. Balint-Kurti GG (2008) Time-dependent and time-independent wavepacket approaches to reactive scattering and photodissociation dynamics. Int Rev Phys Chem 27:507
44. Guo H (1998) A time-independent theory of photodissociation based on polynomial propagation. J Chem Phys 108:2466
45. Bonhommeau D, Truhlar DG (2008) Mixed quantum/classical investigation of the photodissociation of NH_3(A) and a practical method for maintaining zero-point energy in classical trajectories. J Chem Phys 129:014302
46. Bonhommeau D, Valero R, Truhlar DG, Jasper AW (2009) Coupled-surface investigation of the photodissociation of $NH_3(\tilde{A})$: effect of exciting the symmetric and antisymmetric stretching modes. J Chem Phys 130:234303

47. Zhu X, Yarkony DR (2012) On the representation of coupled adiabatic potential energy surfaces using quasi-diabatic Hamiltonians: a distributed origins expansion approach. J Chem Phys 136:174110
48. Bach A, Hutchison JM, Holiday RJ, Crim FF (2003) Competition between adiabatic and nonadiabatic pathways in the photodissociation of vibrationally excited ammonia. J Phys Chem A 107:10490
49. Hause ML, Yoon YH, Crim FF (2006) Vibrationally mediated photodissociation of ammonia: the influence of N–H stretching vibrations on passage through conical intersections. J Chem Phys 125:174309
50. Miller JA, Kee RJ, Westbrook CK (1990) Chemical-kinetics and combustion modeling. Annu Rev Phys Chem 41:345
51. Wayne RP (2000) Chemistry of atmospheres. Oxford University Press, Oxford
52. Scherer NF, Sipes C, Bernstein RB, Zewail AH (1990) Real-time clocking of bimolecular reactions: application to $H + CO_2$. J Chem Phys 92:5239
53. Ionov SI, Brucker GA, Jaques C, Valachovic L, Wittig C (1993) Subpicosecond resolution studies of the $H + CO_2 \rightarrow CO + OH$ reaction photoinitiated in CO_2–HI complexes. J Chem Phys 99:6553
54. Smith IWM, Zellner R (1973) Rate measurements of reactions of OH by resonance absorption. Part 2. Reaction of OH with CO, C_2H_4, and C_2H_2. J Chem Soc Faraday Trans II 69:1617
55. Ravishankara AR, Thompson RL (1983) Kinetic study of the reaction of OH with CO from 250 to 1040 K. Chem Phys Lett 99:377
56. Forster R, Frost M, Fulle D, Hamann HF, Schlepegrell A, Troe J (1995) High pressure range of the addition of HO to HO, NO, NO_2, and CO. I. Saturated laser induced fluorescence measurements at 298 K. J Chem Phys 103:2949
57. Fulle D, Hamann HF, Hippler H, Troe J (1996) High pressure range of addition reactions of HO. II. Temperature and pressure dependence of the reaction $HO + CO <=> HOCO <=> H + CO_2$. J Chem Phys 105:983
58. Golden DM, Smith GP, McEwen AB, Yu C-L, Eiteneer B, Frenklach M, Vaghjiani GL, Ravishankara AR, Tully FP (1998) OH(OD) + CO: measurements and an optimized RRKM fit. J Phys Chem A 102:8598
59. Brunning J, Derbyshire DW, Smith IWM, Williams MD (1988) Kinetics of OH(v = 0,1) and OD(v = 0,1) with CO and the mechanism of the OH + CO reaction. J Chem Soc Faraday Trans II 84:105
60. Frost MJ, Sharkey P, Smith IWM (1993) Reaction between hydroxyl (deuteroxyl) radicals and carbon monoxide at temperatures down to 80 K: experiment and theory. J Phys Chem 97:12254
61. Spencer JE, Glass GP (1977) Some reactions of OH(v = 1). Int J Chem Kinet 9:111
62. Kohno N, Izumi M, Kohguchi H, Yamasaki K (2011) Acceleration of the reaction $OH + CO \rightarrow H + CO_2$ by vibrational excitation of OH. J Phys Chem A 115:4867
63. Zhu RS, Diau EGW, Lin MC, Mebel AM (2001) A computational study of the OH(OD) + CO reactions: effects of pressure, temperature, and quantum-mechanical tunneling on product formation. J Phys Chem A 105:11249
64. Senosian JP, Klippenstein SJ, Miller JA (2005) A complete statistical analysis of the reaction between OH and CO. Proc Combus Inst 30:945
65. Chen W-C, Marcus RA (2005) On the theory of the CO + OH reaction, included H and C kinetic isotope effects. J Chem Phys 123:094307
66. Nguyen TL, Xue BC, Weston RE Jr, Barker JR, Stanton JF (2012) Reaction of HO with CO: tunneling Is Indeed Important. J Phys Chem Lett 3:1549
67. Guo H (2012) Quantum dynamics of complex-forming bimolecular reactions. Int Rev Phys Chem 31:1
68. Schatz GC, Fitzcharles MS, Harding LB (1987) State-to-state chemistry with fast hydrogen atoms. Faraday Disc Chem Soc 84:359

69. Yu H-G, Muckerman JT, Sears TJ (2001) A theoretical study of the potential energy surface for the reaction $OH + CO \rightarrow H + CO_2$. Chem Phys Lett 349:547
70. Lakin MJ, Troya D, Schatz GC, Harding LB (2003) A quasiclassical trajectory study of the reaction $OH + CO \rightarrow H + CO_2$. J Chem Phys 119:5848
71. Valero R, Van Hemert MC, Kroes G-J (2004) Classical trajectory study of the HOCO system using a new interpolated ab initio potential energy surface. Chem Phys Lett 393:236
72. Kudla K, Schatz GC (1991) A quasiclassical trajectory study of $H + CO_2 \rightarrow OH + CO$: bulk reaction dynamics and the effect of van der Waals precursor formation. J Phys Chem 95:8267
73. Kudla K, Schatz GC, Wagner AF (1991) A quasiclassical trajectory study of the $OH + CO$ reaction. J Chem Phys 95:1635
74. Kudla K, Koures A, Harding LB, Schatz GC (1992) A quasiclassical trajectory study of OH rotational excitation in $OH + CO$ collisions using ab initio potential surfaces. J Chem Phys 96:7465
75. Kudla K, Schatz GC (1995) Product state distributions in chemical reactions: the reaction $OH+CO \rightarrow H+CO_2$. In: Liu K, Wagner AF (eds) The chemical dynamics and kinetics of small radicals. World Scientific, Singapore, p 438
76. Bradley KS, Schatz GC (1997) A quasiclassical trajectory study of $H + CO_2$: angular and translational distributions and OH angular momentum alignment. J Chem Phys 106:8464
77. Troya D, Lakin MJ, Schatz GC, Harding LB, Gonzalez M (2002) Quasiclassical trajectory study of energy and angular distributions for the $H + CO_2 \rightarrow OH + CO$ reaction. J Phys Chem B 106:8148
78. Garcia E, Saracibar A, Zuazo L, Lagana A (2007) A detailed trajectory study of the $OH + CO \rightarrow H + CO_2$ reaction. Chem Phys 332:162
79. Garcia E, Corchado JC, Espinosa-García J (2012) A detailed product distribution analysis of some potential energy surfaces describing the $OH + CO \rightarrow H + CO_2$ reaction. Comput Theor Chem 990:47
80. Laganà A, Garcia E, Paladini A, Casavecchia P, Balucani N (2012) The last mile of molecular reaction dynamics virtual experiments: the case of the $OH(N = 1–10) + CO(j = 0–3)$ reaction. Faraday Disc 157:415
81. Valero R, Andersson S (2012) Quantitative integral cross sections for the $H + CO_2 \rightarrow OH + CO$ reaction from a density functional theory-based potential energy surface. Phys Chem Chem Phys 14:16699
82. Schatz GC, Dyck J (1992) A reduced dimension quantum reactive scattering study of $OH + CO \rightarrow H + CO_2$. Chem Phys Lett 188:11
83. Clary DC, Schatz GC (1993) Quantum and quasiclassical calculations on the $OH + CO \rightarrow CO_2 + H$ reaction. J Chem Phys 99:4578
84. Hernandez MI, Clary DC (1994) Study of HOCO resonances in the $OH–CO \rightarrow CO_2 + H$ reaction. J Chem Phys 101:2779
85. Zhang DH, Zhang JZH (1995) Quantum calculations of reaction probabilities for $HO + CO \rightarrow H + CO_2$ and bound states of HOCO. J Chem Phys 103:6512
86. Goldfield EM, Gray SK, Schatz GC (1995) Quantum dynamics of a planar model for the complex forming $OH + CO \rightarrow H + CO_2$ reaction. J Chem Phys 102:8807
87. Dzegilenko F, Bowman JM (1996) Recovering a full dimensional quantum rate constant from a reduced dimensionality calculation: application to the $OH + CO \rightarrow H + CO_2$ reaction. J Chem Phys 105:2280
88. Dzegilenko F, Bowman JM (1998) "Spectator" modes in resonance-driven reactions: three-dimensional quantum calculations of HOCO resonances. J Chem Phys 108:511
89. McCormack DA, Kroes G-J (2002) Converged five-dimensional quantum calculations for $OH + CO \rightarrow H + CO_2$. J Chem Phys 116:4184
90. McCormack DA, Kroes G-J (2002) Full-dimensional quantal initial state-selected reaction probabilities $(J = 0)$ for the reaction $OH(v = 0,\ j = 0) + CO(v = 0,\ j = 0) \rightarrow CO_2 + H$. Chem Phys Lett 352:281
91. Medvedev DM, Gray SK, Goldfield EM, Lakin MJ, Troya D, Schatz GC (2004) Quantum wave packet and quasiclassical trajectory studies of $OH + CO$: influence of the reactant channel well on thermal rate constants. J Chem Phys 120:1231

92. He Y, Goldfield EM, Gray SK (2004) Quantum dynamics of vibrationally activated OH–CO reactant complexes. J Chem Phys 121:823
93. Valero R, McCormack DA, Kroes G-J (2004) New results for the OH(v = 0, j = 0) + CO(v = 0, j = 0) → H + CO_2 reaction: five and full-dimensional quantum dynamical study on several potential energy surfaces. J Chem Phys 120:4263
94. Valero R, Kroes G-J (2004) Theoretical reaction dynamics study of the effect of vibrational excitation of CO on the OH + CO → H + CO_2 reaction. J Phys Chem A 108:8672
95. Valero R, Kroes G-J (2004) Role of CO vibration in the complex-forming OH + CO → H + CO_2 reaction. Phys Rev A 70:040701
96. Valero R, Kroes G-J (2006) Identifying spectator bonds in modeling reactions: OH + CO → H + CO_2. Chem Phys Lett 417:43
97. Liu S, Xu X, Zhang DH (2011) Communication: state-to-state quantum dynamics study of the OH + CO → H + CO_2 reaction in full dimensions (J = 0). J Chem Phys 135:141108
98. Liu S, Xu X, Zhang DH (2012) A full-dimensional time-dependent wave packet study of the OH + CO → H + CO_2 reaction. Theor Chem Acc 131:1068
99. Wang C, Liu S, Zhang DH (2012) Effects of reagent vibrational excitation on the state-to-state quantum dynamics of the OH + CO → H + CO_2 reaction in six dimensions (J = 0). Chem Phys Lett 537:16
100. Li J, Wang Y, Jiang B, Ma J, Dawes R, Xie D, Bowman JM, Guo H (2012) Communication: a chemically accurate global potential energy surface for the HO + CO → H + CO_2 reaction. J Chem Phys 136:041103
101. Li J, Xie C, Ma J, Wang Y, Dawes R, Xie D, Bowman JM, Guo H (2012) Quasi-classical dynamics of the HO + CO → H + CO_2 reaction on a new ab initio based potential energy surface. J Phys Chem A 116:5057
102. Xie C, Li J, Xie D, Guo H (2012) Quasi-classical trajectory study of the H + CO_2 → HO + CO reaction on a new ab initio based potential energy surface. J Chem Phys 127:024308
103. Shiozaki T, Werner H-J (2013) Multireference explicitly correlated F12 theories. Mol Phys 111:607
104. Braams BJ, Bowman JM (2009) Permutationally invariant potential energy surfaces in high dimensionality. Int Rev Phys Chem 28:577
105. Bowman JM, Czakó G, Fu B (2011) High-dimensional ab initio potential energy surfaces for reaction dynamics calculations. Phys Chem Chem Phys 13:8094
106. Lester MI, Pond BV, Anderson DT, Harding LB, Wagner AF (2000) Exploring the OH + CO reaction coordinate via infrared spectroscopy of the OH–CO reactant complex. J Chem Phys 113:9889
107. Ma J, Li J, Guo H (2012) Quantum dynamics of the HO + CO → H + CO_2 reaction on an accurate potential energy surface. J Phys Chem Lett 3:2482
108. Lin SY, Guo H (2003) Quantum wave packet study of reactive and inelastic scattering between C(^{1}D) and H_2. J Chem Phys 119:11602
109. Alagia M, Balucani N, Casavecchia P, Stranges D, Volpi GG (1993) Crossed beam studies of four-atom reactions: the dynamics of OH + CO. J Chem Phys 98:8341
110. Brouard M, Hughes DW, Kalogerakis KS, Simons JP (2000) The product rovibrational and spin–orbit state dependent dynamics of the complex reaction H + CO_2 → OH + CO: memories of a lifetime. J Chem Phys 112:4557
111. Bowman JM (1991) Reduced dimensionality theory of quantum reactive scattering. J Phys Chem 95:4960
112. Corchado JC, Espinosa-Garcia J, Li J, Guo H (2013) CO_2 vibrational state distributions from quasi-classical trajectory studies of the HO + CO → H + CO_2 reaction and H + CO_2 inelastic collision. J Phys Chem A 117:11648
113. Frost MJ, Salh JS, Smith IWM (1991) Vibrational-state distribution of CO_2 produced in the reaction between OH radicals and CO. J Chem Soc Faraday Trans 87:1037
114. Casavecchia P, Balucani N, Volpi GG (1995) Reactive scattering of O(^{3}P, ^{1}D), Cl(^{2}P) and OH radicals. In: Wagner AF, Liu K (eds) Chemical dynamics and kinetics of small free radicals, vol Part I. World Scientific, Singapore, p 365

115. Nickolaisen SL, Cartland HE, Wittig C (1992) CO internal excitation from the reaction: $H + CO_2 \rightarrow CO + OH$. J Chem Phys 96:4378
116. Rice JK, Baronavski AP (1991) Nonstatistical CO product distributions from the hot H-atom reaction, $H + CO_2 \rightarrow OH + CO$. J Chem Phys 94:1006
117. Baulch DL, Bowman CT, Cobos CJ, Cox RA, Just T, Kerr JA, Pilling MJ, Stocker D, Troe J, Tsang W et al (2005) Evaluated kinetic data for combustion modeling: supplement II. J Phys Chem Ref Data 34:757
118. Jacobs A, Wahl M, Weller R, Wolfrum J (1989) Absolute reactive cross section and oh product state distribution for the reaction H(1.86 eV) $+ CO_2 \rightarrow OH + CO$. Chem Phys Lett 158:161
119. Hoffmann G, Oh D, Chen Y, Engel YM, Wittig C (1990) Photoinitiated reactions of H atoms with CO_2: OH(v = 0) rotational excitation from the 239 nm photolysis of CO_2HI complexes. Israel J Chem 30:115
120. Chen J, Xu X, Xu X, Zhang DH (2013) Communication: an accurate global potential energy surface for the $OH + CO \rightarrow H + CO_2$ reaction using neural networks. J Chem Phys 138:221104
121. Neumark DM (2006) Probing chemical dynamics with negative ions. J Chem Phys 125:132303
122. Zhang DH, Yang M, Collins MA, Lee S-Y (2002) Probing the transition state via photoelectron and photodetachment spectroscopy of H_3O^-. Proc Natl Acad Sci U S A 99:11579
123. Clements TG, Continetti RE, Francisco JS (2002) Exploring the $OH + CO \rightarrow H + CO_2$ potential surface via dissociative photodetachment of $(HOCO)^-$. J Chem Phys 117:6478
124. Lu Z, Hu Q, Oakman JE, Continetti RE (2007) Dynamics on the HOCO potential energy surface studied by dissociative photodetachment of $HOCO^-$ and $DOCO^-$. J Chem Phys 126:194305
125. Lu Z, Oakman JE, Hu Q, Continetti RE (2008) Photoelectron–photofragment angular correlations in the dissociative photodetachment of $HOCO^-$. Mol Phys 106:595
126. Johnson CJ, Continetti RE (1895) Dissociative photodetachment studies of the cooled $HOCO^-$ anions revealing dissociation below the barrier to $H + CO_2$. J Phys Chem Lett 2010:1
127. Johnson CJ, Poad BLJ, Shen BB, Continetti RE (2011) Communication: new insight into the barrier governing CO_2 formation from OH + CO. J Chem Phys 134:171106
128. Johnson CJ, Harding ME, Poad BLJ, Stanton JF, Continetti RE (2011) Electron affinities, well depths, and vibrational spectroscopy of cis- and trans-HOCO. J Am Chem Soc 133:19606
129. Zhang S, Medvedev DM, Goldfield EM, Gray SK (2006) Quantum dynamics study of the dissociative photodetachment of $HOCO^-$. J Chem Phys 125:164312
130. Ma J, Li J, Guo H (2012) Tunneling facilitated dissociation to $H + CO_2$ in $HOCO^-$ photodetachment. Phys Rev Lett 109:063202
131. Schreiner PR, Reisenauer HP, Pickard F IV, Simmonett AC, Allen WD, Matyus E, Csaszar AG (2008) Capture of hydroxymethylene and its fast disappearance through tunneling. Nature 453:906
132. Schreiner PR, Reisenauer HP, Ley D, Gerbig D, Wu C-H, Allen WD (2011) Methylhydroxycarbene: tunneling control of a chemical reaction. Science 332:1300

Reactive Scattering and Resonance

4

Zhigang Sun, Bin Zhao, Shu Liu, and Dong-H. Zhang

Abstract

In this chapter, recent developments of the quantum wave packet methods for calculating differential cross sections (DCSs) of tetra-atomic reaction, for calculating DCSs of triatomic reaction using wave packet method only with reactant Jacobi coordinates, for calculating and analyzing the reactive resonance wave functions, and for simulating and explaining experimental observables of a reactive scattering, are given. Applications to the $F + H_2$ reaction, especially some fundamental understandings of its short-lived reactive resonances, the $H + O_2$ reaction, the $H_2 + OH \rightarrow H + H_2O$ reaction, and the $OH + CO \rightarrow H + CO_2$ reaction are presented for illustration.

4.1 Introduction

For decades it has been witnessed the persistent endeavors from both experimental and theoretical sides in the attempts to reveal the ever detailed minutes of how the reactants evolve to products during a chemical reaction process in various conditions. A chemical reaction may be envisioned as a scattering collision in which the original chemical bonds are cleaved and new ones are formed. Considering the large mass difference between electrons and nuclei, it is advantageous to separate the treatment of a reaction into solutions of two Schrödinger equations: first for the electrons at fixed nuclear positions, and then for the nuclei. This is the Born–Oppenheimer (BO) approximation, and it is valid for many chemical reactions. The treatment of the motions of electrons allows the definition of potential energy

Z. Sun (✉) • B. Zhao • S. Liu • D.-H. Zhang (✉)
State Key Laboratory of Molecular Reaction Dynamics and Center for Theoretical and Computational Chemistry, Dalian Institute of Chemical Physics, Chinese Academy of Sciences, Dalian 116023, China
e-mail: zsun@dicp.ac.cn; zhangdh@dicp.ac.cn

F. Gatti (ed.), *Molecular Quantum Dynamics*, Physical Chemistry in Action,
DOI 10.1007/978-3-642-45290-1_4,

surface (PES) as a function of all nuclear coordinates, and then the dynamic motions of nuclei during a reaction are governed by the PES, which provides the force acting on each nuclei in the system. A chemical reaction takes place on the PES along a minimum energy path connecting the reactant region to the product region, and it is called the reaction coordinate for the chemical reaction. In a typical chemical reaction, the path traverses a reaction intermediate region, which is defined as the transition state [34, 35].

Theoretically, the very early theory was pioneered by Hirschfelder and his coworkers dated back to the later 1930s and early 1940s [49, 52], but it takes more than 30 years to see the report of the fully quantum mechanical method on the simplest three-dimensional $H + H_2$ exchange reaction [110, 111], even though various model calculations were implemented on $H + H_2$ [62,108,109,133,134,143] and $F + H_2$ [106, 112, 144]. With the tremendous progress of various theoretical and numerical methods to deal with the partial differential equations and associated boundary conditions in the field of quantum reaction dynamics [4,15,50,90,96,107], it has now become just a routine to perform full-dimensional quantum scattering calculations for atom–diatom systems with both accurate ICS and DCS at the state-to-state level [3, 100, 119, 124, 140], especially after the introduction of reactant coordinate-based method [43, 126, 127]. Previously one had to transform the wave function between the reactant Jacobi coordinates and the product Jacobi coordinates (Jacobi coordinate is defined in Sect. 4.3), in order to efficiently express the reactant ro-vibrational states and the product ro-vibrational states and further obtain the state-to-state information. This leads to the well-known coordinate problem in time-dependent quantum wave packet calculation for extracting state-to-state reactive scattering information. Therefore quantum wave packet method had only been considered as a convenient method for calculating initial state-specific total reaction probabilities. Nowadays the quantumwave packet method has also been proved an effectivemethod for extracting state-to-state information.

Once the atom–diatom reactive scattering problem had essentially been solved, attention naturally turned to more complicated reactions involving more than three atoms—as the first step, to systems involving four atoms. Unfortunately, this is not a trivial task, as the number of degrees of freedom increases from three for a three-atom system to six for a four-atom system. In the past decades, significant progress has been made on accurate quantum reactive scattering studies of four-atom chemical reactions. Starting from time-independent (TI) reduced dimensionality approaches [15, 26], it is now possible to calculate fully converged integral cross sections [42, 155, 164], and state-to-state dynamical quantities for the total angular momentum $J = 0$ [29, 156, 165] without any dynamical approximation for some four-atom reactions, mainly through the development of the initial state selected wave packet method. Other quantum dynamical approaches have also received great success in four-atom reactions, such as the Multi-configurational Time-Dependent (TD) Hartree (MCTDH) approach for thermal rate constant calculations [72]. Various TID and TD reduced dimensionality calculations were also reported on different systems [118, 149, 154, 163, 166]. Recently, time-dependent wave packet (TDWP) method was developed to compute differential cross sections (DCSs) for

four-atom reactions and applied to the prototypical HD + OH → H_2O + D [70,145] and D_2 + OH → HOD + D reactions [69]. Excellent agreements were achieved for the first time for a four-atom reaction between the full-dimensional DCS and high-resolution crossed-molecular beam experimental results. Because it only takes a relatively short time to obtain fully converged DCS for the reaction, it is conceivable that the wave packet-based quantum scattering method has matured to the stage where it can afford yielding complete dynamical information for many four-atom reactions, as have been done for three-atom reactions in the past decades.

While fully quantum mechanical calculations on larger reactive system are always limited by the current computational power, the quasi-classical trajectory (QCT) method provides a feasible alternative by describing the scattering collisions with classical equations of motion [54, 99]. However, despite its high efficiency and intuitive nature, QCT is not a rigorous method to deal with quantum dynamics in reactive scattering, such as reactive resonance, zero-point energy, quantum tunneling, and interference. Even atoms other than hydrogen and its isotopes usually are not believed to have strong tunneling effect at room temperature, it is not clear what is exact the role of the zero-point energy in a molecular dynamics process.

In this chapter, we aim to provide quantum mechanical methods to simulate and explain some interesting experimental observables of reactive scatterings, especially some fundamental understandings of the short-lived reactive resonances.

4.2 Resonance in a Reactive Scattering

For a reactive scattering, the properties of the reaction system near the transient region have the dominant role that determines various details of reactive collisions including the nature of potential surfaces, nonadiabaticity, direct and complex-forming collision dynamics, energy partitioning, product state and angular distributions, quantum tunneling and resonances in the transient region, and other interference effects.

The literature has seen several comprehensive reviews that summarized the recent advances in the understanding of reactive resonance [22, 37, 66, 67, 148], and for the consideration of integrity, here we shall only briefly explain the basic concepts.

The properties of the reaction system near the transient region determine how the reactant evolves to the product side, and in a typical chemical reaction, reactions form short-lived intermediate reactive complex at the transition state region and finally decay into the final reaction products. The transition state region can be an energetic barrier, which separates the reactants from products, and in some cases after this barrier the reaction coordinate shows itself with a deep potential well, shown in Fig. 4.1a, which attracts the intermediate complex for a long time before it decays into the final products. The latter is always named as complex-forming reaction, and we shall not go into too much details in this kind of resonance, as recently it has been intensely reviewed by an elegant article [46]. We shall from now on only focus on the reactive resonance in direct reactions.

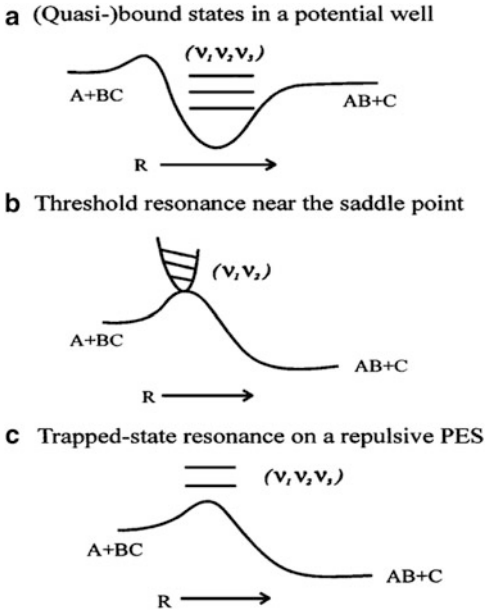

Fig. 4.1 Three types of reactive resonances near the transition state region in chemical reactions, adapted from [66]. Panel (**a**) illustrates the case associated with a deep potential well along the reaction coordinate. The resulting bound and pre-dissociative quasi-bound states can be characterized, for a three-atom system, by three vibrational modes. (**b**) Threshold resonance for which only the two motions orthogonal to the unbound reaction coordinate are quantized and thus assignable by vibrational quantum numbers. The dynamical trapped-state resonance is schematically shown in panel (**c**). Despite the repulsive potential energy surface along the reaction coordinate, this metastable state can be assigned by three vibrational quantum numbers

In a direct reaction, the minimum energy path along the reaction coordinate shows itself with repulsive feature on the PES, and no discrete quantum state exists in the transition state region along the reaction coordinate R, shown in Fig. 4.1b, c. The directions perpendicular to R are the internal coordinates $\mathbf{u}$ of the reaction system, and the motions along $\mathbf{u}$ are quasi-bound, which is the character of the saddle-point nature in the transition state region, shown in Fig. 4.1b. In a typical atom–diatom reaction, A + BC, the reaction coordinate approaches the asymmetric stretch motion of the ABC complex in the transition state region, and the two quasi-bound states are the symmetric stretching and bending modes. Due to the discrete nature of the two quasi-bound states, they would serve as a bottleneck to gate the flux going from the reactant region to product side. This is named as the threshold resonance or barrier resonance, and the discrete quasi-bound states are the quantized bottleneck states. As a result, stair-like feature is observed in the reaction probability $P_J(E_c)$ from a single partial wave J as a function of the collision energy, as shown in Fig. 4.2a (middle). The effect of zero-point energy manifests itself in the reaction probability as the smaller reaction threshold energy than the height of the barrier.

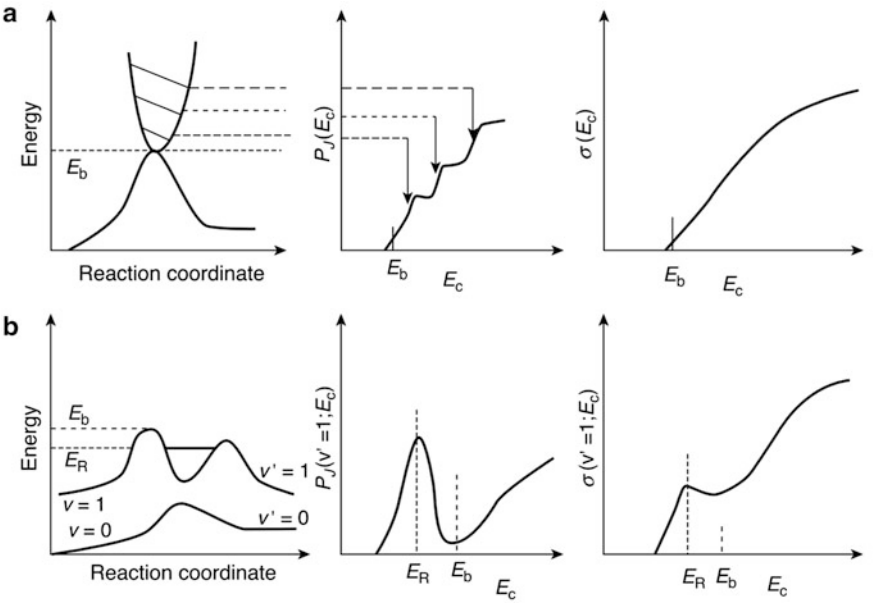

Fig. 4.2 Schematic illustration of the threshold resonances (**a**) and quantum dynamical resonance (**b**), adapted from [67]. In each panel, the *left figure* illustrates the effective dynamical potential along the reaction coordinate R, and the *middle* and the *right* ones are the E_c-dependence of the reaction probability $P_J(E_c)$ and the reaction cross section $\sigma(E_c)$. In the case of threshold resonance, the non-zero values of the reaction probability and cross section start at a smaller collision energy than the height of the barrier, which manifests the effect of zero-point energy

The other reactive resonance is called the trapped-state resonance or Feshbach resonance, shown in Fig. 4.1c. In this case, the ABC complex is dynamically trapped along the reaction coordinate, even the minimum energy path on the BO PES is totally repulsive. The trapping of the short-lived ABC complex is caused by the vibrationally adiabatic potential, which is based on the concept of vibrational adiabaticity [23, 75, 76, 120]. As the vibrational motions along the directions perpendicular to R are fast compared with the motion along R, the vibrational modes should approximately conserve the quantum number $\mathbf{n}$, which is in the spirit of BO separation of motions with different time scale. A typical vibrationally adiabatic potential along the reaction coordinate R is shown in Fig. 4.2b (left), and it can be constructed as

$$V_{\mathrm{VAP}}(R) = V_{\mathrm{MEP}}(R) + \varepsilon_{\mathbf{n}}(R) \tag{4.1}$$

in which $V_{\mathrm{MEP}}(R)$ is the minimum energy path along the reaction coordinate, and $\varepsilon_{\mathbf{n}}(R)$ is the quantized vibrational energy of the orthogonal motions. In the vicinity of the transition state region, the strong couplings between the vibrational motions and the reaction coordinate lead to the dramatic vibrational frequency

decrease due to the weakening of the bonds, and consequently dynamic potential well would appear along the reaction coordinate, especially for high vibrational quantum numbers. If the well is deep enough to support discrete resonance quantum state along the reaction coordinate, an isolated sharp peak should be observed in the reaction probability $P_J(E_c)$, as shown in Fig. 4.2b (middle) for $P_J(v' = 1; E_c)$ of the $v' = 1$ product state from a single partial wave J. The appearance of the isolated sharp peak before the reaction threshold energy is due to the resonant tunneling process through the barrier, which enhances the formation of the resonance complex state, and at higher collision energy, the direct reaction of the broad over-the-barrier probability dominates the process. In a one-dimensional model, the resonance produced by a potential like in Fig. 4.2b (left) is called as shape resonance [37]. While in multi-dimensional case, energy exchange occurs between various collective modes of the compound molecule, and it is named as the Feshbach resonace.

Even though the reaction probability provides distinctly different characteristics for the above two types of reactive resonance, the experimental observables of the reaction cross sections are often smeared out due to the summation of all possible $P_J(E_c)$, which is inevitable because of the existence of many partial. The interpretation of the experimental observables and further understanding of the effects of reactive resonance require the intense interplay between theory and experiment. For example, the transition state region is often tight, and only a small range of partial waves contributing to the DCS in certain direction, which is amenable to quantum mechanical calculations. We shall be able to focus on reaction probabilities of a certain range of partial waves, from which the different kinds of reactive resonance manifest themselves with distinct features.

In the following part, we will review the current quantum wave packet method for simulating reactive scattering processes and its applications, especially on understandings of reactive resonances. The quantum dynamical studies have greatly deepened our understandings of the reaction dynamics in some prototypical systems. The following part is full of technical details and one may skip it for a general interest.

4.3 Theory by Quantum Wave Packet Method

4.3.1 Overall Theory

In a reactive scattering, the full Hamiltonian H needs to be partitioned in different arrangement channels ν,

$$H = H_0^\nu + V^\nu \tag{4.2}$$

in which $H_0^\nu = T^\nu(R) + h^\nu(\boldsymbol{q})$ is the asymptotic Hamiltonian, V^ν is the interaction potential, and $T^\nu(R)$ is the kinetic energy operator in the translational degree of

freedom, R, $h^{\nu}(\boldsymbol{q})$ is the internal Hamiltonian in the internal degrees of freedom, $\boldsymbol{q}$. In the limit that the separation of the two fragments R goes to infinity, the interaction potential would be vanished, and the eigenfunction of the system is simply the product of a plane wave and the eigenfunction $\chi_n(\boldsymbol{q})$ of the internal Hamiltonian $h^{\nu}(\boldsymbol{q})$,

$$\psi^{\nu}_{n,E}(R,\boldsymbol{q}) = u^{\nu}_{k}(R)\chi^{\nu}_{n}(\boldsymbol{q}) \tag{4.3}$$

in which $\chi^{\nu}_{n}(\boldsymbol{q})$ is related to E_n by

$$h^{\nu}(\boldsymbol{q})\chi^{\nu}_{n}(\boldsymbol{q}) = E_n\chi^{\nu}_{n}(\boldsymbol{q}) \tag{4.4}$$

and the translational plan wave is directly written as

$$u^{\nu}_{k}(R) = \frac{e^{ikR}}{\sqrt{2\pi}} \tag{4.5}$$

where $k = \sqrt{2\mu(E-E_n)/\hbar^2}$, μ is the reduced mass of the translational motion. The eigenfunction $\psi^{\nu,\pm}_{n,E}$ of the full Hamiltonian H is related to the asymptotic wave function through the Møller operator, $\Omega_{\pm}$ [153],

$$\psi^{\nu,\pm}_{n,E} = \Omega_{\pm}\psi^{\nu}_{n,E} \tag{4.6}$$

Given the definition of S matrix operator, $S = \Omega^{\dagger}_{-}\Omega_{+}$, the probability amplitude to scatter from an initial state i of the reactant arrangement α to a final state f of the product arrangement β is written as the matrix element of the S operator [153],

$$S_{\beta f,\alpha i} = \langle\psi^{\beta}_{f,E}|S|\psi^{\alpha}_{i,E}\rangle = \langle\psi^{\beta}_{f,E}|\Omega^{\dagger}_{-}\Omega_{+}|\psi^{\alpha}_{i,E}\rangle = \langle\psi^{\beta,-}_{f,E}|\psi^{\alpha,+}_{i,E}\rangle \tag{4.7}$$

There are generally two methods to calculate the S matrix element. The first one is the time-independent (TI) method, which solves the eigenvalues of the full Hamiltonian H to obtain the scattering matrix $\psi^{\beta,-}_{f,E'}$ and $\psi^{\alpha,+}_{i,E}$. In a single run of the TI method, the entire S-matrix is obtained at a particular energy E. TI method is especially suitable for the case with low energy, such as cold collision problem. However, the TI method is notorious for its bad scaling relation N^3, with respect to the number of basis functions, N. Alternatively, the time-dependent (TD) method or wave packet method has a better scaling of N^2, and it is carried out by solving the TD Schrödinger equation of a first-order differential equation.

In a typical wave packet method, three steps are involved to calculate the S matrix. First, an initial wave packet Ψ_i of definite internal quantum states is launched in the reactant region with normally a Gaussian shape wave packet in the scattering coordinate, and this determines the range of collision energy. Then the wave packet is propagated for a sufficient length of time until the reaction is finished. Finally, the state-to-state S-matrix element is obtained for the reactive scattering. In the TD

method, the S-matrix element is reformulated by wave packet correlation function [132],

$$S_{\beta f,\alpha i} = \frac{(2\pi\hbar)^{-1}}{a_f^*(E)a_i(E)} \int_0^\infty e^{iEt/\hbar} \langle \Psi_f | e^{-iHt/\hbar} | \Psi_i \rangle dt \tag{4.8}$$

where Ψ_f is the final wave packet, $a_i(E)$ and $a_f(E)$ are the energy amplitudes of the energy normalized eigenfunctions contained in the initial and final wave packets. It can be seen that the S matrix element is obtained by the Fourier transform of the time correlation function $C_{fi}(t)$ between the final wave packet and the propagated initial wave packet, $C_{fi}(t) = \langle \Psi_f | \Psi_i(t) \rangle$.

It should be noted that the initial and final wave packets are usually expressed in the Jacobi coordinates of their own arrangements, which results in the difficult coordinate problem in state-to-state reactive scattering as we mentioned previously. One may either choose the product Jacobi coordinate [47, 53, 65, 151], or reactant Jacobi coordinate to propagate the initial wave packet, and there also exist two other methodologies but may be both named as reactant coordinate-based (RCB) method: the first one is to employ interpolation schemes for the coordinate transformation [41, 89, 126, 127, 156], and the second one is realized by projection of both reactant and product wave packets to an intermediate coordinate [43, 127], Alternatively, in the reactant–product decoupling (RPD) method [6, 7, 96], both the reactant and product coordinates are used, and they are divided and combined by a complex absorbing potential.

4.3.2 Quantum Wave Packet Method

The ever increasing popularity of the wave packet approach to reactive scattering is attributed largely to its intuitive time dependence and better scaling laws [87]. However, the concept of wave packet was originally postulated long time ago by Schrödinger in 1926 [115] as a coherent superposition of states, with localization in its position representation. The states can be electronic states, vibrational states, or rotational states, but in molecular wave packet method, the wave packet represents the coherent nuclei motion on certain electronic PES under Born–Oppenheimer approximation. Since the formulation of these original works, molecular wave packet theory has undergone a huge development, as reviewed by Manz in his comprehensive historical survey of molecular wave packet theory in the period of 1926–1996 [74].

Since the numerical details for a triatomic reactive scattering can be directly extended to more complicated systems and are very typical, we will focus on the triatomic reactions in this part.

4.3.2.1 Hamiltonian and Discretization

To study the atom–diatom reactive scattering, $\mathrm{A} + \mathrm{BC}(v_i, j_i) \rightarrow \mathrm{AB}(v_f, j_f) + \mathrm{C/AC}(v_f, j_f) + \mathrm{B}$ at a state-to-state level, body-fixed (BF) frame Jacobi coordinates are

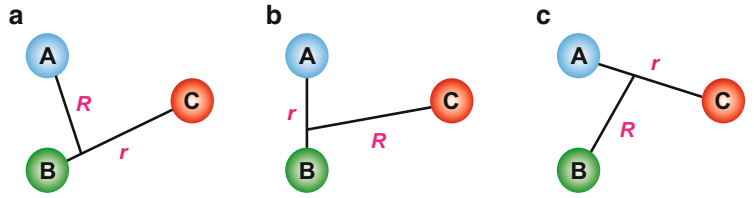

Fig. 4.3 The Jacobi coordinates for the reactant A + BC (**a**), and product AB + C (**b**) and AC + B (**c**)

used to represent the corresponding wave packets in their arrangements: normally the reactants A + BC is for the α arrangement, and the two product channels AB + C and AC + B are for the β and γ arrangements, respectively. The Jacobi coordinates for the three arrangements are shown in Fig. 4.3. In each arrangement, the coordinate is denoted as $(R_v, r_v, \theta_v; \boldsymbol{\Omega_v})$, where v represents any one of the above arrangements. For example, when v represents the reactant arrangement, R_v is the length of vector $\boldsymbol{R}_v$ pointing from the BC center of mass to A, r_v the BC bond length, and θ_v the angle between BC bond and $\boldsymbol{R}_v$; $\boldsymbol{\Omega_v}$ denotes the Euler angles orienting $\boldsymbol{R}_v$ in the space-fixed (SF) frame.

Considering the reaction scattering as an isolated system, the calculation is always carried out using a partial wave representation, in which the total angular momentum J is a good quantum number and one can take advantage of the conservation of the total angular momentum to break the problem into separate calculations for each value of the total angular momentum quantum number J. The Hamiltonian for a given total angular momentum $\boldsymbol{J}$ is given in the reactant Jacobi coordinate as

$$\hat{H} = -\frac{\hbar^2}{2\mu_R}\frac{\partial^2}{\partial^2 R} - \frac{\hbar^2}{2\mu_r}\frac{\partial^2}{\partial^2 r} + \frac{\hat{l}^2}{2\mu_R R^2} + \frac{\hat{j}^2}{2\mu_r r^2} + V(R, r, \theta) \tag{4.9}$$

where the arrangement label α is removed for clarity consideration, μ_R and μ_r are the corresponding reduced mass for R and r, respectively. The squared orbital angular momentum operator is responsible for the centrifugal potential and expressed as

$$\hat{l}^2 \equiv (\hat{\boldsymbol{J}} - \hat{j})^2 = \hat{\boldsymbol{J}}^2 + \hat{j}^2 - 2\hat{\boldsymbol{J}}_z\hat{j}_z - \hat{\boldsymbol{J}}_+\hat{j}_- - \hat{\boldsymbol{J}}_-\hat{j}_+ \tag{4.10}$$

where $\hat{\boldsymbol{J}}$ and $\hat{j}$ are the total and BC diatomic rotational angular momentum operators, with $\hat{\boldsymbol{J}}_z$ and $\hat{j}_z$ as their corresponding projections onto the BF z-axis, which coincides with the vector $\mathbf{R}$. The raising/lowering operators in the last two terms, $\hat{\boldsymbol{J}}_\pm$ and $\hat{j}_\pm$, represent the Coriolis coupling, which couples the adjacent helicity quantum number K. K is the projection of both J and j onto the BF z-axis, and it is a good quantum number in the BF frame.

For each partial wave J and parity ϵ, the Hamiltonian and wave packet are discretized in the BF frame in mixed representation [21, 64, 80, 89, 160]: discrete variable representation (DVR) is employed for the two radial degrees of freedom and finite basis representation (FBR) of normalized associated Legendre function $\mathscr{Y}_{jK}(\theta)$ for the angular degree of freedom. Thus the wave packet in the BF frame is written as

$$\Psi^{JM\epsilon}(\boldsymbol{R}, \boldsymbol{r}) = \sum_{K} \mathscr{D}^{J\epsilon *}_{MK}(\boldsymbol{\Omega}) \psi(t, R, r, \theta^K; K) \tag{4.11}$$

where $\mathscr{D}^{J\epsilon *}_{MK}(\boldsymbol{\Omega})$ is the parity-adapted normalized rotation matrix, depending only on the Euler angles $\boldsymbol{\Omega}$,

$$\mathscr{D}^{J\epsilon *}_{MK}(\boldsymbol{\Omega}) = (1 + \delta_{K,0})^{-1/2} \sqrt{\frac{2J+1}{8\pi}} [D^{J*}_{MK}(\boldsymbol{\Omega}) + \epsilon(-1)^{J+K} D^{J*}_{M-K}(\boldsymbol{\Omega})], \tag{4.12}$$

where ϵ is the parity of the system defined as $\epsilon = (-1)^{j+l}$ with l being the orbital angular momentum quantum number, and $D^{J*}_{MK}(\boldsymbol{\Omega})$ is Wigner rotation matrix [16, 152]. The usage of the parity-adapted normalized rotation matrix restricts the K to be nonnegative and the basis size is reduced almost by half. $\psi(t, R, r, \theta^K; K)$ only depends on three internal coordinates and K, and it is expanded as

$$\psi(t, R, r, \theta^K; K) = \sum_{n,m,j} F^K_{nmj}(t) u_n(R) \phi_m(r) \mathscr{Y}_{jK}(\theta) \tag{4.13}$$

where n and m are the radial basis labels, $u_n(R)$ and $\phi_m(r)$ are the corresponding basis functions, respectively, and $\mathscr{Y}_{jK}(\theta)$ is the normalized associated Legendre function.

4.3.2.2 Construction of the Initial Wave Packet

As has been mentioned above, the first step of the wave packet method is to set up the initial wave packet. The initial wave packet is advantageous to be defined in the SF frame, because the Coriolis couplings in the BF frame are long ranged and it requires to define the initial wave packet at rather large position of R. There are not many ways to account for them in a reasonable grid. On the other hand, in the SF frame, the asymptotic form of the scattering wave function can be described by the Riccati–Hankel function, and the long-range centrifugal term is diagonal, $l(l+1)/2\mu_R R^2$ [3, 30]. Consequently, the initial wave packet can be placed as close as the interaction potential is negligible. In such a manner, the initial wave packet is defined as the product of the diatomic ro-vibrational eigenstate $\phi_{v_0 j_0}(r)$ of BC and a Gaussian wave packet $G(R)$ in the translational coordinate [3, 65, 126],

$$\Psi^{JM\epsilon}_{v_0 j_0 l_0}(\boldsymbol{R}, \boldsymbol{r}) = G(R) \phi_{v_0 j_0}(r) |JMj_0 l_0 \epsilon\rangle, \tag{4.14}$$

where $|JMj_0l_0\epsilon\rangle$ is the eigenfunction of the total angular momentum operator in the coupled representation of the SF frame with parity of system $\epsilon = (-1)^{j_0+l_0}$, and the Gaussian wave packet $G(R)$ in the translational coordinate is given as

$$G(R) = \left(\frac{2}{\pi\delta^2}\right)^{1/4} e^{-(R-R_0)^2/\delta^2} e^{-ik_0R}, \tag{4.15}$$

in which δ, R_0, and k_0 are the width, mean position, and mean momentum of the translational wave packet, respectively, and they determine the range of collision energy.

Wave packet is always propagated in the BF frame, and the initial wave packet needs to be transformed from the SF to the BF frames before the propagation, which is to transform the SF eigenfunction $|JMj_0l_0\epsilon\rangle$ of the total angular momentum operator in the coupled representation to the BF frame,

$$\begin{aligned} |JMj_0l_0\epsilon\rangle &= \sum_{K\geq 0} \boldsymbol{C}_{l_0K}^{Jj_0\epsilon} |JMj_0K\epsilon\rangle \\ &= \sum_{K\geq 0} \boldsymbol{C}_{l_0K}^{Jj_0\epsilon} D_{MK}^{J\epsilon *}(\boldsymbol{\Omega}) \mathscr{Y}_{j_0K}(\theta), \end{aligned} \tag{4.16}$$

where $\boldsymbol{C}_{l_0K}^{Jj_0\epsilon}$ is the parity-adapted orthogonal transform matrix between the SF and BF frames [65, 101, 153, 157] and given as

$$\boldsymbol{C}_{l_0K}^{Jj_0\epsilon} = \sqrt{\frac{2l+1}{2J+1}} \sqrt{2-\delta_{K,0}} \langle jKl0|JK\rangle, \tag{4.17}$$

where $\langle jKl0|JK\rangle$ is the Clebsch–Gordan coefficient.

4.3.2.3 Propagation of the Wave Packet

After the preparation of the initial wave packet, it is then propagated under the operation of system Hamiltonian by the unitary propagator $U(t, t_0) = e^{-\frac{i}{\hbar}H(t-t_0)}$.

Usually, the propagator $U(t, t_0)$ is approximated by various schemes [55,60,137], and there are plenty of wonderful articles that have explained each in detail, such as the split operator method and higher order split operator methods [11, 36, 130], Chebyshev polynomial expansion [131], Faber polynomial expansion [51, 146], short iterative Lanczos propagation method [95], Crank–Nicholson second-order differencing [10, 56, 57], symplectic method [14, 45], recently proposed real Chebyshev method [24, 44, 125], and Multi-configuration Time-Dependent Hartree (MCTDH) Method [12, 73, 81–83]. For details, one may refer to the corresponding references.

4.3.3 State-to-State Method: The RPD Approach

It has been a long time that only the product Jacobi coordinates were used in the propagation for extracting state-to-state information: the initial wave function, which is constructed in reactant Jacobi coordinate, is first transformed into product Jacobi coordinate, directly or after some propagation time to focus the initial wave packet in interaction region. Then the wave function propagation and product state-resolved information is calculated. Later, RPD method was proposed [96], particularly for direct reactive scattering process where it has been proved being very efficient. Recently, efficient RCB method was put forward by Sun et al. and Roncero et al. [43, 126, 127], particularly for reactive scattering process involving intermediate complex. The RCB method has been applied with $H + O_2$ [124], $O + O_2$ [128], $N + NO \rightarrow N_2 + O$ etc., which clearly demonstrated its efficiency and convenience for usage. In this part we only briefly introduce the RPD method, which is the only technique capable of extracting state-to-state DCS of tetra-atomic molecules currently.

The RPD method, originally introduced by Peng and Zhang [96] in order to extract the state-to-state information efficiently, transforms no-return part of reacted wave packet continuously in time from reactant to product coordinates with the help of absorption potentials. It divides the full time-dependent wave function into the reactant and product components and the calculation of each component can be carried out using the Jacobi coordinates of the corresponding arrangement channel separately. The RPD method solves, to a large extent, the problem of the choice of coordinates in quantum reactive scattering.

In the time domain, the RPD scheme partitions the full time-dependent (TD) wave function into a sum of reactant component (Ψ_r) and all product components (Ψ_p, $p = 1, 2, 3, \ldots$) that satisfy the following decoupled equations:

$$
\begin{aligned}
i\hbar\frac{\partial}{\partial t}|\Psi_r(t)\rangle &= H|\Psi_r(t)\rangle - i\sum_p V_p|\Psi_r(t)\rangle \\
i\hbar\frac{\partial}{\partial t}|\Psi_p(t)\rangle &= H|\Psi_p(t)\rangle + iV_p|\Psi_r(t)\rangle,
\end{aligned}
\tag{4.18}
$$

where $-iV_p$ is the negative imaginary potential (absorption potential) used to prevent the wave function $\Psi_r(t)$ from entering the pth product arrangement. The solution for $\Psi_r(t)$ is independent of those for $\Psi_p(t)$ and the latter are independent of each other. Therefore, $\Psi_r(t)$ can be propagated in the reactant Jacobi coordinates just as for total reaction probability calculations,

$$
\Psi_r(t + \Delta) = e^{-V_p\Delta/\hbar}e^{-(i/\hbar)H\Delta}\Psi_r(t). \tag{4.19}
$$

Every product wave function, Ψ_p, can be propagated in its own coordinates as in a normal wave packet propagation except with a source term, ξ_p, provided by Eq. (4.19),

$$\Psi_p(t+\Delta) = e^{-(i/\hbar)H\Delta}\Psi_p(t) + \xi_p(t) = e^{-(i/\hbar)H\Delta}\Psi_p(t) + (1 - e^{-V_p\Delta/\hbar})\Psi_r(t+\Delta). \tag{4.20}$$

Finally, one can extract the final state information, such as state-to-state S matrix elements or reaction probabilities, from the Fourier transformation of $\Psi_p(t)$.

The RPD approach is very efficient on dealing with direct reactants with barriers as demonstrated by Althorpe and coworkers [3, 8], because in this case the absorption potential can be applied right after the barrier as in initial selected total reaction probability calculations and it is also rather cheap to carry out the continuous propagation for the absorbed wave packet in a product channel. In particular, Althorpe and coworkers have realized that the absorption of reacted wave packet can be performed after multiple propagation steps [5, 29].

In the original RPD approach, the source term $\xi_p(t) = (1 - e^{-V_p\Delta/\hbar})\Psi_r(t)$ is saved and transformed from reactant to product Jacobi coordinates at every propagation time step. By using the multiple-step reactant–product decoupling (MRPD) scheme, one can be saving and transforming the source term at every M time [68, 70, 71].

$$\begin{aligned}
&\Psi_r(t+\Delta) = e^{-V_pM\Delta/\hbar}e^{-(i/\hbar)H\Delta}\Psi_r(t), \text{ when } \mathrm{mod}((t+\Delta) - t_0, M\Delta) = 0,\\
&\Psi_p(t+\Delta) = e^{-(i/\hbar)H\Delta}\Psi_p(t) + (1 - e^{-V_pM\Delta/\hbar})\Psi_r(t+\Delta),
\end{aligned} \tag{4.21}$$

where t_0 is the starting point for performing wave function transformation. At other time steps, we carried out the standard split-operator propagation for $\Psi_r(t)$ and $\Psi_p(t)$ without the absorption potential, V_p, related terms. In this way, we can cut the computational time for wave function transformation from reactant coordinates to product coordinates by a factor of M.

Since the efficiency of RPD method for a state-to-state calculation of a direct reactive scattering process, it is crucial for extracting product state-resolved information of tetra-atomic reaction limited by current computer resource. The applications below of tetra-atomic reaction are accomplished by using the RPD method.

4.3.4 Calculation of the Experimental Observations

4.3.4.1 Calculation of S-Matrix of Triatomic Reaction Using the RCB Method

To calculate the state-to-state S-matrix in Eq. (4.8), the time correlation function $C_{fi}(t) = \langle\Psi_f|\Psi_i(t)\rangle$ needs to be calculated at each time step during the propagation. A projection plane is often defined as $R_\nu = R_{\nu 0}$ for the νth ($\nu = \beta$ or γ) arrangement using the corresponding product Jacobi coordinate, and the time correlation function is always carried out on this projection plane but the projection action can be carried out in either reactant or product Jacobi coordinate. The final product wave packet $\Psi_f(R_\nu)$ is also defined in the SF frame due to the merits already mentioned above,

$$\begin{aligned}\Psi_f^{JM\epsilon}(R_{v0}) &\equiv \Psi_{v_v j_v l_v}^{JM\epsilon}(\boldsymbol{R}', \boldsymbol{r}') \\ &= \delta(R' - R_{v0})\phi_{v_v j_v}(r')|JMj_v l_v \epsilon\rangle \\ &= \delta(R' - R_{v0})\phi_{v_v j_v}(r') \sum_{K' \geq 0} \boldsymbol{C}_{l_v K'}^{J j_v \epsilon} D_{MK'}^{J\epsilon *}(\boldsymbol{\Omega}') \mathscr{Y}_{j_v K'}(\theta') \end{aligned} \tag{4.22}$$

in which R', r', and θ' describe the product Jacobi coordinate, and $\boldsymbol{\Omega}'$ are the Euler angles for $\boldsymbol{R}'$ in the SF frame. In practice, one often calculates the scattering wave function in the energy domain before taking overlap with the final product state, and it is obtained by a time-energy Fourier transform from the propagated wave packet,

$$\Phi_i^{JM\epsilon}(E; R_{v0}) = \int_0^\infty e^{iEt/\hbar} \Psi_i^{JM\epsilon}(t; R_{v0}) dt, \tag{4.23}$$

With the strategy to deal with the coordinate problem as mentioned in Sect. 4.3.1, the state-to-state S-matrix can be readily evaluated,

$$S_{v_v j_v l_v \leftarrow v_0 j_0 l_0}^{J\epsilon}(E) = \frac{(2\pi\hbar)^{-1}}{a_f^*(E) a_i(E)} \langle \Psi_f(R_{v0}) | \Phi_i^{JM\epsilon}(E; R_{v0}) \rangle \tag{4.24}$$

where $a_i(E)$ and $a_f(E)$ are given by

$$a_i(E) = \left(\frac{\mu_R}{2\pi\hbar^2 k_{v_0 j_0}} \right)^{1/2} \int \mathscr{H}_{l_0}(k_{v_0 j_0} R) G(R) dR \tag{4.25}$$

$$a_f(E) = \left(\frac{\mu_{R'}}{2\pi\hbar^2 k_{v_v j_v}} \right)^{1/2} \mathscr{H}_{l_v}(k_{v_v j_v} R_{v0}) \tag{4.26}$$

in which $\mu_{R'}$ is the reduced mass for the product translational degree of freedom, $\mathscr{H}_l$ is the outgoing Riccati–Hankel function.

Finally, the S-matrix needs to be transformed from the SF frame to the helicity representation by the standard transformation,

$$S_{v'j'K' \leftarrow vjK}^{J} = \sum_{l'l} i^{l-l'} \sqrt{\frac{2l'+1}{2J+1}} \langle j'K'l'0|JK' \rangle S_{v'j'l' \leftarrow vjl}^{J} \sqrt{\frac{2l+1}{2J+1}} \langle jKl0|JK \rangle. \tag{4.27}$$

4.3.4.2 Calculation of ICS and DCS

By substituting the S-matrix $S_{v'j'K' \leftarrow vjK}^{J}(E)$ in the helicity representation into the standard formulas, the state-to-state ICS can be obtained by summing over the contributions from all partial waves [157],

$$\sigma_{v_v j_v \leftarrow v_0 j_0}(E) = \frac{\pi}{(2j_0+1)k^2_{v_0 j_0}} \sum_{K_v} \sum_{K_0} \sum_{J} (2J+1) |S^{J\epsilon}_{v_v j_v K_v \leftarrow v_0 j_0 K_0}(E)|^2 \tag{4.28}$$

and the state-to-state DCS [157],

$$\frac{d\sigma_{v_v j_v \leftarrow v_0 j_0}(\vartheta, E)}{d\Omega} = \frac{1}{(2j_0+1)} \sum_{K_v} \sum_{K_0} \left| \frac{1}{2ik^2_{v_0 j_0}} \sum_{J} (2J+1) d^J_{K_v K_0}(\vartheta) S^{J\epsilon}_{v_v j_v K_v \leftarrow v_0 j_0 K_0}(E) \right|^2, \tag{4.29}$$

in which ϑ is the scattering angle between the direction of incoming reactant A and outgoing product AB/AC in the center of mass frame, and $d^J_{K_v K_0}(\vartheta)$ is the reduced rotational matrix [16, 152].

4.3.4.3 Calculation of Reaction Rate

With the calculated initial state-specific ICS, the initial state-specific temperature-dependent reaction rate constant can be expressed as

$$k(T|v_0 j_0) = \left(\frac{8K_b T}{\pi \mu_R}\right)^{1/2} (k_b T)^{-2} \int_0^\infty dE \exp\left(\frac{E_t}{k_b T}\right) \sigma_{v_v j_v \leftarrow v_0 j_0}(E) \tag{4.30}$$

where k_b is Boltzmann's constant. The thermal rate constant can be calculated from the Boltzmann averaging of the initial state-specific reaction rate constants as

$$k(T) = Z_{\text{elec}}(T) \frac{\sum_{v_0 j_0} (2j_0+1) k(T|v_0 j_0) \exp(-E_{v_0 j_0}/(k_b T))}{\sum_{v_0 j_0} (2j_0+1) \exp(-E_{v_0 j_0}/(k_b T))} \tag{4.31}$$

where $E_{v_0 j_0}$ is the ro-vibrational energy of the reactant diatomic molecule, and $Z_{\text{elec}}(T)$ is the possible electronic partition function for the system.

For a reaction with a defined transition state and without recrossing, reaction rate can be well approximated by many methods. For such reaction, we can assume that there is a dynamics bottleneck located at the transition state (conventional transition state theory, TST) or at a generalized transition state obtained by a canonical (CTV) or microcanonical (μVT) criterion. In the later cases, the dividing surface is optimized variationally to minimize the recrossing. Evans first proposed to place the transition state at the location that maximizes the free energy of activation which provides a key conceptual framework for modern variational transition state theory [33]. However, recrossing always possibly exists and only a full-dimensional reactive scattering dynamics calculations are able to provide us the exact rate constant on a defined PES. For a detailed discussion, one may refer to the reviews by Truhlar et al. [38, 136].

4.3.4.4 Calculation and Characterization of the Reactive Resonance Wavefunction

It is crucial to characterize the features of the reactive resonance wave function, in order to understand the nature and role of a particular reactive resonance state in the reaction.

The nomenclature "resonance" refers to a transient metastable species produced in the reaction scattering processes, and it results in peaks in the plots of reaction probabilities as a function of collision energy. Although its observation and assignment in scattering experiments usually is difficult because the coherent summation of many partial waves tends to wash out most of the resonance structures, numerically the quantum calculation is carried out with a specified partial wave and the resonance is much easier to pick out. The existence signature of a dynamical resonance is the arising of a peak in the collision energy-dependent reaction probability enhanced by the metastable transient state with long enough lifetime. Thus, such dynamical resonance wavefunctions can be figured out by using the so-called spectral quantization method. The bottleneck state in the $H + H_2$ and its isotopes reactions scattering processes [104] and the reactive resonance state in the $F + HD$ reaction processes [116] have been investigated using the spectral quantization method. In that method a carefully designed initial wave function was applied to obtain the time-independent wave function at the peak energies in the reaction probabilities by Fourier transform of the time-propagated wave packet. The reactive resonance wave function calculated in this way strongly depends on the initial wave function, and one must be careful for further studying with it.

Instead, a rigorous, robust, and convenient method to calculate the dynamical resonance wave functions in a reactive process may be applied, which is a direct extension of the standard TDWP method for describing a reaction scattering process. For a reactive scattering of a triatomic $A + BC$ reaction with the initial incoming wave function $\Psi^{JM\epsilon}_{v_0 j_0 l_0}(t=0)$ for an initial state (v_0, j_0, l_0), the dynamical resonance wave function at certain collision energy E_n can be obtained with a Fourier transform of the time evolved incoming wave function as

$$\Phi(E_n) = \sum_{l_0,\epsilon} \int_{-\infty}^{+\infty} \Psi^{JM\epsilon}_{v_0 j_0 l_0}(t) \exp(iE_n t) dt \equiv \sum_{l_0,\epsilon} \int_{0}^{+\infty} \Psi^{JM\epsilon}_{v_0 j_0 l_0}(t) \exp(iE_n t) dt \tag{4.32}$$

The last step is reached by using the fact that before time zero the incoming wave contributes nothing to the interaction region. Thus the calculated resonance wave function is rigorous in the whole grid region and can be safely used to analyze the reactive process. The dynamical resonance wave function must have relatively large amplitude in the interaction region and pure incoming and outgoing tails with relatively small amplitude, and exhibits features of a quasi-bound state. And we can use this evidence to justify if the calculated wave function at specified collision energies corresponds to a dynamic resonance state. In contrast to the spectral

quantization method, the wave function in resonance region may not be so clear since it is not overemphasized.

After the extraction of the reactive resonance wave function in certain convenient coordinates used in the propagation, one may need to transform it into another optimal coordinates to facilitate the observation of its resonance quantization structure, such as normal mode near the transition state region or product/reactant Jacobi coordinates or hyperspherical coordinates. In this way, the dynamics origin of the reactive resonance wave functions may be clarified to us.

4.4 Applications

4.4.1 Resonances in F Plus H_2 and Its Isotopes

The reactive resonances reveal the quasi-bound levels of the reaction complex with unique clarity and they do exist. Identification of the reactive resonances can help us with understanding how elementary chemical processes take place at a single quantum state level. $F + H_2$ and its isotopic analogs are the most beautiful examples.

Interest in the $F + H_2$ reaction was largely due to Lee's benchmark molecular beam studies [105] and early chemiluminescence and chemical laser work [98]. This work led to the early QCT studies of Muckerman [88], Blais and Truhlar [13], and Polanyi and Schreiber [97], using the PES but with serious flaws. A series of surface by Truhlar and his coworkers [17, 84, 122, 135] led to gradual improvement, and then Stark and Werner developed surfaces (SW PES) [121] from multireference configuration interaction calculations that resolved many of the earlier issues, even some problems remain. Very recently, Zhang and his coworkers developed several versions of the PES for the $F + H_2$ reaction using icMRCI [100] and CCSDT method [40, 102], whose ultimate version has been proved to be of spectroscopy accuracy.

Early the QCT [106] and collinear quantum reactive scattering studies [113] revealed their distinct difference for predicting the $F + H_2$ reaction, especially for the F + HD reaction where reactive resonances played a big role. Subsequent 3D quantum scattering calculations by Wyatt and coworkers [77, 78] and a variety of 3D quantum models confirmed the existence of the resonance, thereby stimulating further experiments on $F + H_2$ and its isotopic analogs and finally leading to the molecular beam studies of Neumark and coworkers [91–94] which proved important hints that resonances play a role in this reaction.

However, the following theoretical work on the SW PES argued that the forward scattering of the $F + H_2$ reaction results from the tunneling-induced reactivity at high impact parameters which do not need the formation of resonance [20]. And the QCT work by Aoiz et al. [9] yielded angular distributions with forward components that were consistent with the experiments, suggesting that the quantum effects, especially resonance effects, are relatively unimportant.

In 2000, the work on the F + HD reaction of Dong et al. [31] discovered the existence of reactive resonances in crossed beam experiments, where a

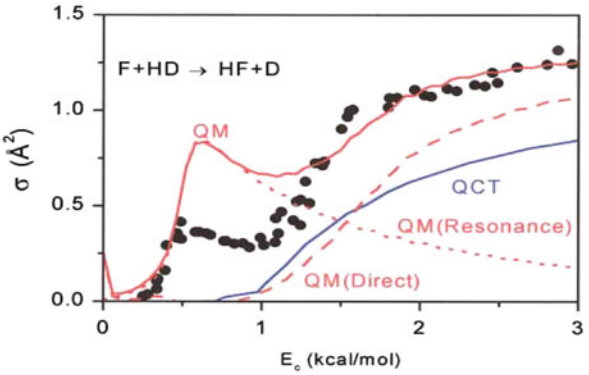

Fig. 4.4 The excitation functions for $F + HD \rightarrow HF + D$. The experimental results are shown with *solid dots*, the QCT simulations with a *blue line*, and the QM results with a *red line*. The resonance contribution is depicted with a *dotted red line*, and the direct reaction contribution with a *dashed red line*. A multisurface factor of 1/2 has been used to scale the ICS

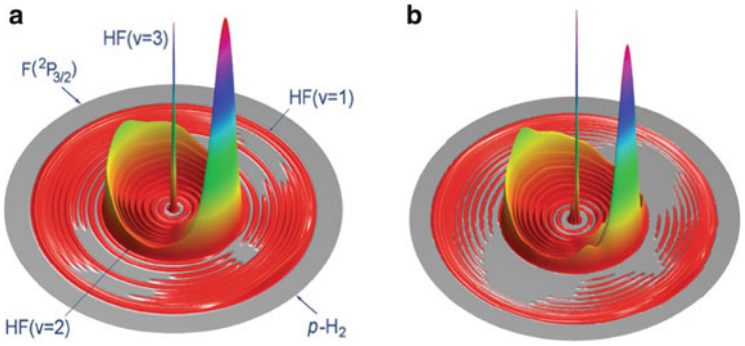

Fig. 4.5 Experimental (**a**) and theoretical (**b**) 3D contour plots for the product translational energy and angle distributions for the $F(^2P_{3/2}) + H_2(j_0 = 0)$ reaction at the collision energy of 0.52 kcal/mol. The *different circles* represent different HF product ro-vibrational states. The forward-scattering direction for HF is defined along the F atom beam direction

resonance-enhanced step in the excitation function was observed, as shown in Fig. 4.4. Subsequent IR work by Nesbitt [48] confirmed this results and theoretical calculations have been presented to interpret the dynamics using SW PES [116,117].

In 2006, the work of Qiu et al. [100] presented the evidence for the resonances in the $F + H_2$ reaction, with both theory and experiment exhibiting consistent behavior on XXZ PES, as shown in Fig. 4.5. The appearance of this report is catalyzed by the developments on quantum scattering method development, ab initio method and crossed-molecular beam combined with high resolution H-Rydberg state tagging technique [147]. The sharp forward peak at collision energy of 0.52 kcal/mol actually results from the interference between the first two Feshbach resonances. For total angular momentum $J = 0$, there are two resonance states at collision

energy of 0.26 and 0.46 kcal/mol. With increasing J, the resonance energy will shift to higher collision energy. The three-dimensional (3D) scattering wave function at the collision energy of 0.26 kcal/mol shows the existence of three nodes along the H-F coordinate (correlating to the HF product) in the HF-H′ complex with no node along the reaction coordinate. The projection of the $J = 0$ scattering wave function at 0.26 kcal/mol to the HF vibrational states shows that the main character in this wave function is HF($v' = 3$) with the outgoing waves mostly on HF($v' = 2$). This implies that the resonance state at 0.26 kcal/mol is the ground resonance state, (003), trapped in the HF($v' = 3$)-H′ vibrational adiabatic potential (VAP) well. The 3D scattering wave function for $J = 0$ at the collision energy of 0.46 kcal/mol shows the existence of three nodes along the HF coordinate (correlating to the HF product) in the HF-H′ complex with one node along the reaction coordinate. The projection of the $J = 0$ scattering wave function at 0.46 kcal/mol to the HF vibrational states shows the main character in this wave function is predominantly HF($v' = 3$) with the outgoing waves also mostly on HF($v' = 2$). This suggests that the resonance state at 0.46 kcal/mol is the excited reaction resonance state trapped in the HF($v' = 3$)-H′ VAP well. This resonance state can be assigned to the (103) resonance state with one-quantum vibration along the reaction coordinate, zero-quantum vibration on the bending motion (or hindered rotation), and three-quanta vibration along the HF stretching. The resonance schemes were shown in Fig. 4.6.

Their subsequent work at higher collision energy (0.94 kcal/mol) demonstrated the tunneling and shape resonance effects [139], other than Feschbash resonance for arising the forward scattering in the reaction of $F + H_2$, which suggested that the reactive resonances played quite different roles in the same reaction but at different collision energies [139].

In 2008, Ren et al. [102] measured the DCSs at several collision energies, which showed strong variation as a function of collision energies, as shown in Fig. 4.7, due to the existence of strong reactive resonance state. The theoretical DCSs on the new version PES by Zhang and his coworkers (FXZ PES) agree with the experimental observation very well, as shown in Fig. 4.8 which demonstrated that the $F + H_2$ reaction is the first reaction which can be studied at spectroscopy accuracy, besides the $H + H_2$ reaction.

To have a better feeling about the resonance state, the ground reactive resonance state wave function of the $F + HD \rightarrow HF + D$, along with the 2D minimal potential, which is optimized along the angle degree of freedom, is given in Fig. 4.9. It is observed there that the wave function exhibits well features of a semi-bound state. The outgoing part, which corresponds to the HF ($v' = 2$) product, has two nodes of structure but the inside peak has three nodes, which corresponds to an excited vibrational state of $v' = 3$.

The most exciting chapter on detecting the reactive resonances in the $F + H_2$ reaction and its isotopic analogs is the observation of the partial wave resonance in the F + HD by Dong et al. in 2010 [32]. The reactive resonance, as we know, which commonly is considered as being elusive and smeared by summation of many partial waves, was observed individually by Dong et al. at three different rotational quantum states of the temporarily trapped FHD complex, as shown in Fig. 4.10.

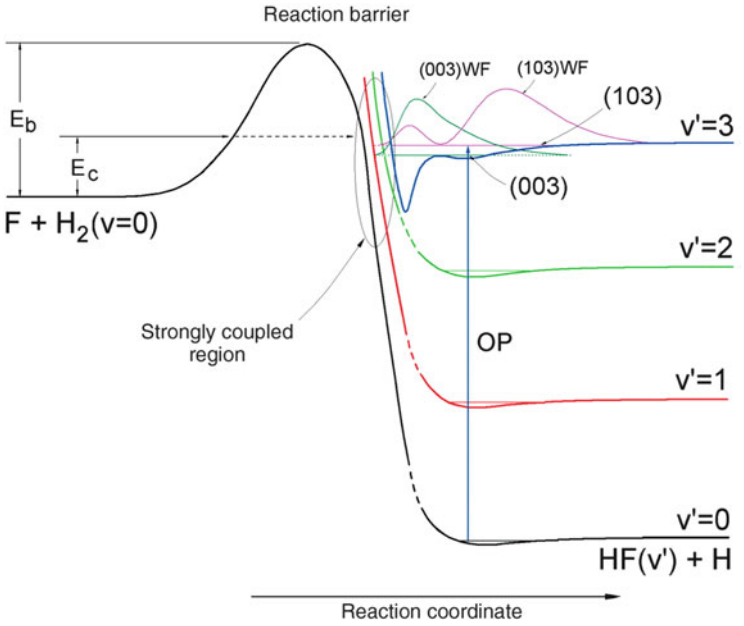

Fig. 4.6 Schematic diagram showing the resonance-mediated reaction mechanism for the $F + H_2$ reaction with two resonance states trapped in the peculiar HF($v' = 3$)-H′ VAP well. The 1D wave functions of the two resonance states are also shown. The (003) state is the ground resonance state; the (103) resonance is the first excited resonance state. Calculated van der Waals states for the lower VAPs are also shown. OP, overtone pumping; E_b, barrier height; E_c, collision energy

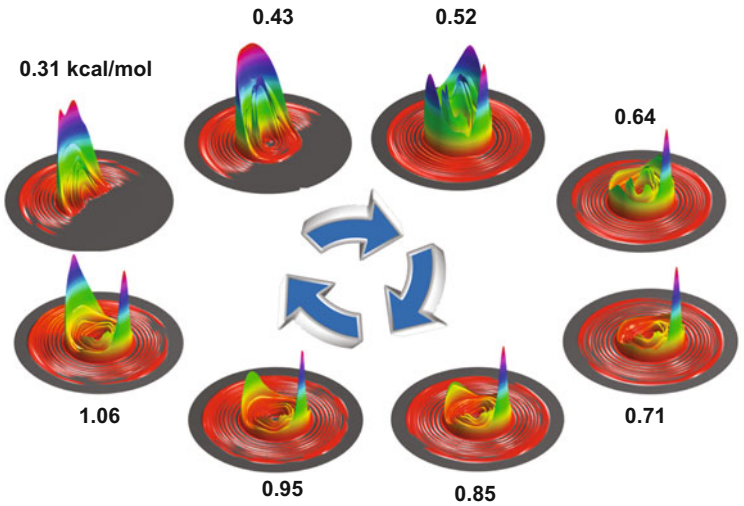

Fig. 4.7 The experimental 3D contour plots for the product translational energy and angular distributions for the $F(^2P_{3/2}) + HD(j_0 = 0)$ reaction at various collision energies: 0.31, 0.43, 0.52, 0.64, 0.71, 0.85, 0.95, and 1.06 kcal/mol

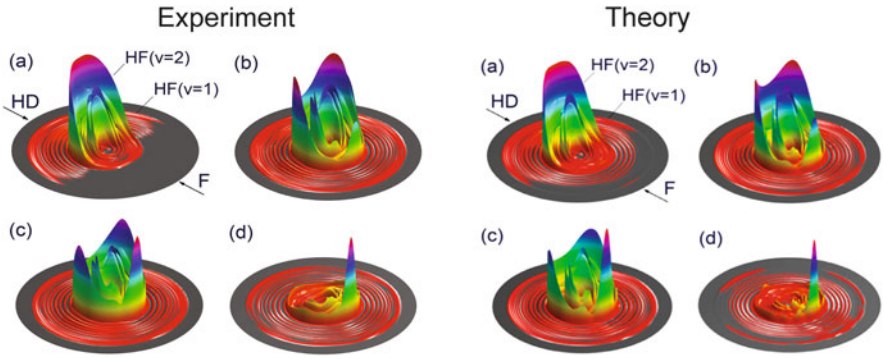

Fig. 4.8 The experimental and theoretical 3D contour plots for the product translational energy and angular distributions for the $F(^2P_{3/2}) + HD(j_0 = 0)$ reaction at various collision energies: 0.43 kcal/mol (**a**); 0.48 kcal/mol (**b**); 0.52 kcal/mol (**c**); and 0.71 kcal/mol (**d**)

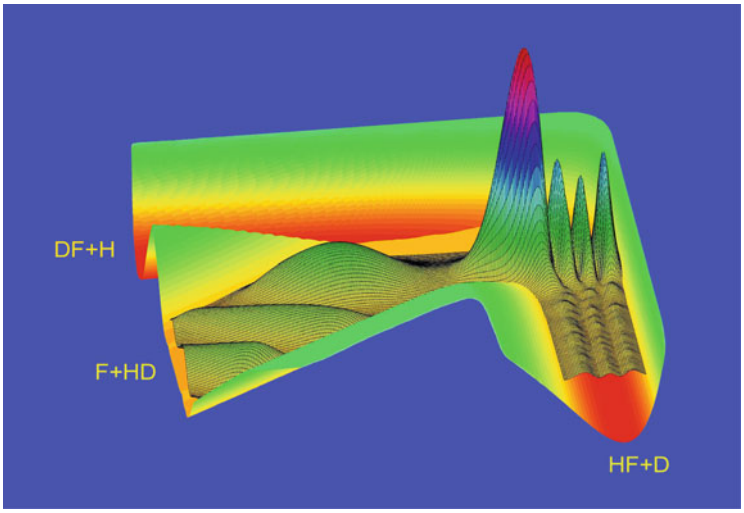

Fig. 4.9 3D ground reactive resonance wave function of the $F + HD$ ($v_0 = 0$, $j_0 = 0$) $\rightarrow HF + D$ reaction, along with the potential which is optimized along angle degree of freedom

This is different from the work in 2000 by Dong et al. [31] where the resonance in $F + HD$ was identified by observing the averaged contribution from a sequence of the resonances in the cross sections. Dong et al. are, however, in 2010 the first to pick out individual resonances from this series [32].

Recent quantum reactive scattering studies of $F + H_2$ and $Cl + H_2$ have included spin-orbit effects and multiple surfaces within both the framework of hyperspherical coordinate coupled channel and TDWP calculations [2, 129, 140]. These works help us with better understanding the role of the spin-orbit effects in reactions.

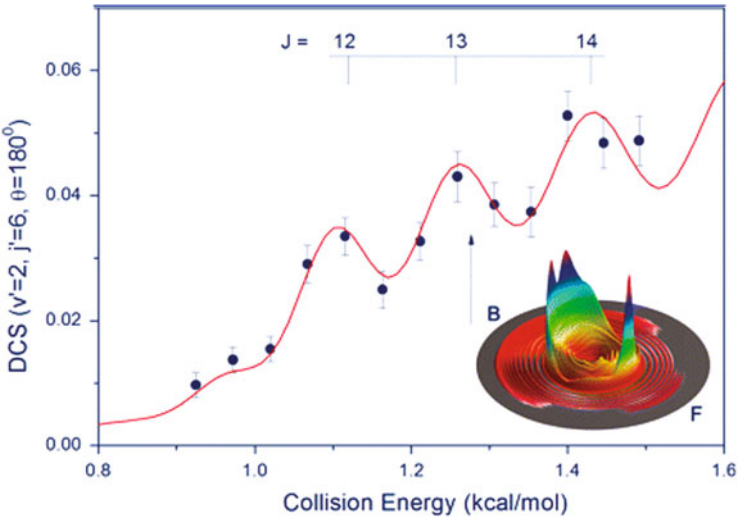

Fig. 4.10 Experimental and theoretical DCS of the HF($v = 2$, $j = 6$) product of the $F(^2P_{3/2}) + HD(j_0 = 0)$ reaction in the backward scattering direction. The *solid circles* are experimental data; the *red curve*, the result of full quantum dynamics calculations convoluted with the experimental resolution and shifted 0.03 kcal/mol lower in energy. The error bars in the experimental data are the estimated measurement errors (1σ) for the HF($v = 2$, $j = 6$) product peak intensity in the collision energy scan. The three peaks are assigned to the partial wave Feshbach resonances of $J = 12$, 13, and 14 in the $F + HD \rightarrow HF + D$ reaction, as explained in the text. The three-dimensional DCS shown was measured at 1.285 kcal/mol, with F and B indicating the forward- and backward-scattering, respectively, directions for HF with respect to the F-atom beam direction

From above discussion, we have seen a close interplay between theory and experiment which is extremely helpful with revealing the reaction dynamics mechanism. Theory and experiment verify and reinforce each other, develop side by side through mutual cross-fertilization. We can expect even more success through a close interplay between them.

4.4.2 Non-statistical Effects in $H + O_2$ Reaction

The $H + O_2 \rightarrow HO + O$ reaction and its reverse are of fundamental importance to combustion chemistry. This reaction proceeds via the formation of an intermediate complex in a deep well of 2.4 eV which is relatively stable with no barrier to dissociation. There have been many theoretical and experimental studies on this reaction, particularly on the concern about the non-statistical effects. Statistical modeling based on the statistical adiabatic channel model (SCAM) is able to account for the observed forward and reverse thermal rate constants overall a wide range of temperature, implying that the reaction is statistical. However, QCT studies find

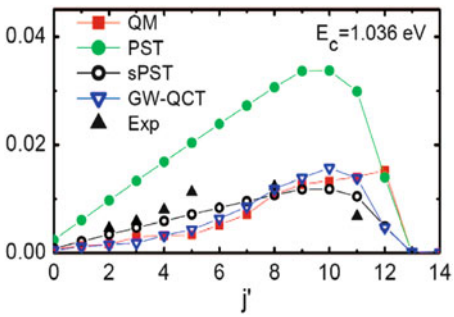

Fig. 4.11 Comparison of the QM rotational state distribution of OH (*filled square*) with the PST results (*filled circle*), GW-QCT results (*filled inverted triangle*), and available experimental data (*filled triangle*). The PST result normalized to the QM distribution (sPST) is also presented (*open circle*)

that there is significant recrossing of reasonably chosen dividing surfaces after the HO_2 complex is formed in the $HO + O$ reaction, suggesting the existence of the important non-statistical effects in this reaction. Rigorous quantum reactive scattering calculations and more accurate potentials are required to settle down this issue. However, this reaction presents obvious challenges for quantum scattering calculations, on account of the heavy masses and the deep HO_2 well.

Using DMBE IV potential, Meijer and coworkers carried out wavepacket calculations of the initial state selected total cross sections for the $H + O_2$, including partial waves up to $J = 35$. All of the projections of J onto the intermolecular axis have been incorporated in the calculations. They found that the calculated cross sections are lower than the experiment, which indicated the deficiencies in the DMBE IV potentials. In 2005, Xu et al. constructed a new potential (XXZLG PES) for this reaction at the internally contracted multireference configuration interaction plus the Davidson correction level with the augmented correlation consistent polarized valence quadruple zeta (aug-cc-pVQZ) basis set. It has been shown that there is remarkable improvement over the previous DMBE IV potential. Based upon this new potential and using the recent developed RCB quantum wave packet method, Sun et al. calculated state-to-state DCS and ICS of the $H + O_2$ reaction up to 1.5 eV.

By comparing the QM rotational state distribution with the statistical limit represented by the phase space theory (PST), which assumes that the formation and decay of the reaction intermediate are separate events and the decay probability is proportional to the number of open channels. As shown in Fig. 4.11, the shape of the PST distribution is similar to that of the QM counterpart; namely, it increases with j until the highest accessible rotational state. However, the statistical model severely overestimates the QM distribution. Even when comparing with the normalized PST distribution, as shown in the same figure, the QM distribution typically overpopulates at large j values and underpopulates at small j values. Similar differences exist in other collision energies.

The deviation of the QM rotational state distribution from the statistical limit is a convincing piece of evidence in support of the argument that the title reaction has a significant non-statistical component despite its complex-forming nature. In other words, the dynamics plays a non-negligible role in the reaction. This is contrast with

the conventional wisdom: usually it is assumed that the deep well in the PES which creates the long-lifetime intermediate complex will smear out all of the dynamics effect thus leads to statistical limit. This conclusion is consistent with the slight forward–backward asymmetry of the calculated DCSs reported here and the non-statistical decay of the HO_2 complex observed in QCT studies. The origin of the non-statistical behavior can presumably be attributed to the relatively short lifetime of the HO_2 intermediate which has not enough time to fully relax the internal energy into all degrees of the freedom in a statistical way.

The atmospherically important reaction $O + O_2$ with three heavy atoms and deep potential well has also been studied at the state-to-state DCS level by quantum wave packet method. It reveals the failure of the statisical model from the calculated strong non-statistical effects and some quantum effects in the reaction [128].

4.4.3 $H_2 + OH$

The $H_2 + OH \rightarrow H + H_2O$ reaction is a prototype reaction for H atom abstraction by an OH radical to form water as a product. Moreover, it is important in combustion chemistry and interstellar chemistry [85, 142]. Consequently, it has attracted extensive experimental and theoretical studies. Crossed-molecular beam experiments on the isotopically substituted $D_2 + OH \rightarrow D + HOD$ reaction revealed that the product was strongly backward-scattered, with the majority of the available energy channeled into HOD internal excitation and the newly formed OD bond in the HOD molecule preferentially excited to the $v = 2$ state [123]. The reverse reaction has also been studied widely as a prototype system for mode specific chemistry, in which different vibrational modes in the reactants can play an important role in the reaction dynamic. As three of the four atoms in this system are hydrogen isotopes, it has been straightforward to pursue both high-quality ab initio calculation of a PES and accurate quantum dynamics calculations. As a result, this reaction has become a benchmark system for four-atom reactions, in much the same role that the $H + H_2$ reaction played for three-atom reactions.

In 1993, the first TDWP calculation was reported for the $H_2 + OH \rightarrow H_2O + H$ reaction with the total angular momentum $J = 0$ by using diatom–diatom Jacobi coordinates with only the spectator OH bond length frozen [158]. It was quickly extended to include all degrees of freedom for a four-atom reaction without any dynamical approximate on the same reaction system [159]. In 1996, the TDWP method was applied to study the $H + H_2O \rightarrow H_2 + OH$ reaction in full dimensions on the atom–triatom Jacobi coordinates [161]. Then, the method was extended to study four-atom reactions for the total angular momentum $J > 0$ in one set of Jacobi coordinates, with the full converged integral cross sections reported for the $H_2 + OH \rightarrow H_2O + H$ reaction [155] in 1999, for the $H + D_2O \rightarrow D + HOD$ and $H_2O + H \rightarrow H_2 + OH$ reactions in 2000 [162, 164].

Figure 4.12 compares theoretical integral cross sections for the $H + D_2O \rightarrow D + HOD$ exchange reaction with the experimental results [18,19,162]: the absolute cross sections at a relative translational energy of 1.5 and 2.2 eV and the excitation

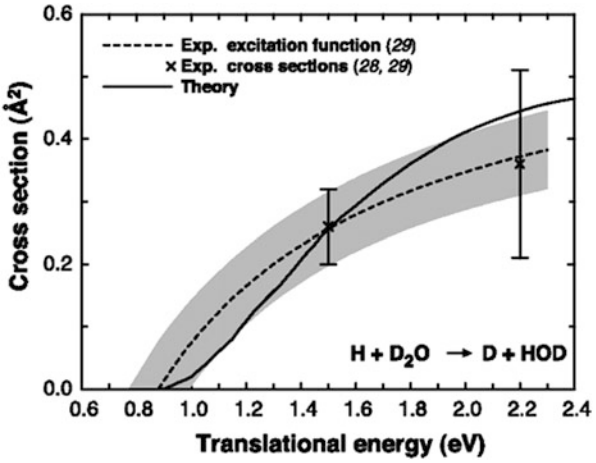

Fig. 4.12 Comparison between the experimental and theoretical integral cross sections for the $H + D_2O \rightarrow D + HOD$ reaction. The *dashed line* is the experimental excitation function. The *shaded area* reflects the statistical uncertainty (1σ) of the global least squares fit procedure used to determine the optimum excitation function

function of the reaction in the line-of-center functional model. The first-principles theoretical results agree excellently with the experiments in all respects. We note that the experimental result is thermally averaged over the initial rotation of D_2O, whereas the theoretical result is for initial non-rotating D_2O (preliminary calculations showed that rotational excitation of the triatomic reactant has no substantial effect on the integral cross section).

Despite the significant progress in initial state selected level, the accurate quantum calculation of the state-to-state DCSs for four-atom reactions remained a challenge for many years. State-to-state reaction probabilities for the total angular momentum $J = 0$ were reported for the $H_2 + OH \rightarrow H_2O + H$ reaction by using both the diatom–diatom and atom–triatom Jacobi coordinates [165]. Following that, the state-to-state integral and DCSs were reported for the $H + H_2O \rightarrow H_2 + OH$ reaction in five dimensions with the spectator OH bond length fixed, in 2002 [163] and 2005 [154], respectively. In the past few years, Althorpe and coworkers used quantum wave packet method to obtain the state-to-state reaction probability for the $H_2 + OH \rightarrow H_2O + H$ reaction in five and fully six dimensions [27–29]. All of these state-to-state calculations were using the reduced dimensionality method or limited to total angular momentum $J = 0$.

Recently, TDWP method was developed to compute DCSs for four-atom reactions and applied to the prototypical $HD + OH \rightarrow H_2O + D$ [70, 145] and $D_2 + OH \rightarrow HOD + D$ reactions [69]. Excellent agreements were achieved for the first time for a four-atom reaction between the full-dimensional DCS and high-resolution crossed-molecular beam experimental results on the $HD + OH \rightarrow H_2O + D$ reaction [145]. Figure 4.13 compares the theoretical energy

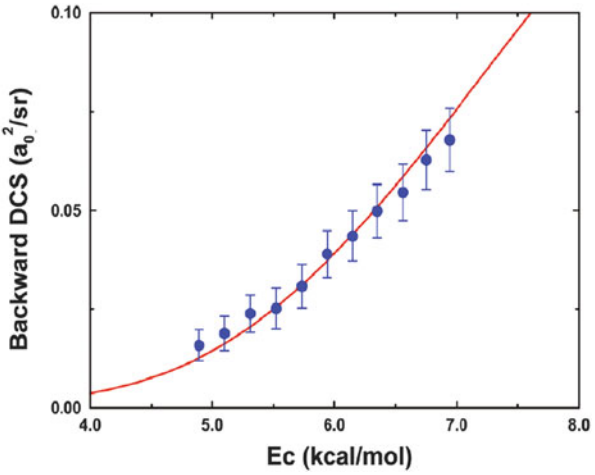

Fig. 4.13 Experimental and theoretical DCSs of the $HD + OH \rightarrow H_2O + D$ reaction in the backward scattering direction. The experimental data, measured in relative values, are scaled to the theoretical DCS value at the collision energy (E_c) of 6.15 kcal/mol. In the experiment, the DCSs at the backward scattering direction were measured by scanning the collision energy back and forth 15 times. Error bars in the experimental data indicate the estimated errors ($\pm 1\sigma$) for the DCS signal at the backward direction from the 15 scans of the collision energy

dependence of DCSs in the backward direction with the experimental result. The agreement between theory and experiment is remarkable. It also reveals that the theoretical reaction barrier of 5.4 kcal/mol on the PES they used is very accurate, and the quantum tunneling effect for the hydrogen transfer reaction is quite strong, since the reaction threshold is apparently much lower than the barrier height 5.4 kcal/mol.

4.4.4 OH + CO

After simple four-atom reactions have been solved, however, huge challenges still persist in rigorous quantum scattering studies of complex-forming four-atom reactions with more than one heavy atoms, such as the $OH + CO \rightarrow H + CO_2$. Because of its crucial role in the conversion of CO to CO_2, the $OH + CO \rightarrow H + CO_2$ reaction is important to both atmospheric [39] and combustion chemistry [86]. Due to the presence of two deep wells along the reaction path which support long-lived collision complex HOCO in both *trans* and *cis* configurations, the reaction dominated by pronounced resonances has become a prototype recently for complex-forming four-atom reactions, just as $H_2 + OH \rightarrow H + H_2O$ is for direct four-atom reactions.

Considerable experimental studies have been carried out on this reaction and its reverse [1, 61, 103]. Theoretically, in 1987 the first global analytic PES was constructed by Schatz, Fitzcharles, and Harding (denoted as SFH) based on the

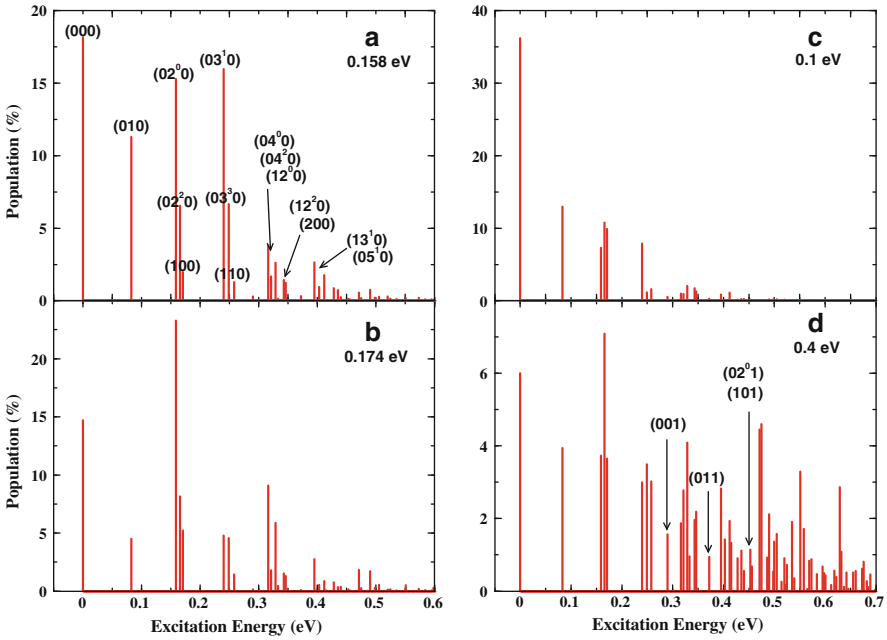

Fig. 4.14 Product vibrational state distributions of CO_2 for the $OH + CO \rightarrow H + CO_2$ reaction with total angular momentum $J = 0$ at reactant translational energy of (**a**) 0.158 eV, (**b**) 0.174 eV, (**c**) 0.1 eV, and (**d**) 0.4 eV

many-body expansion approach [114]. Following that, a number of global analytic [58,59,150] and numerical [25,63] PES have been constructed to study the reaction more accurately, and many dynamics calculations have been performed by using quasiclassical trajectory method [59, 79]. We would like to note here that there is more detailed discussion about this reaction in the chapter by Guo et al. in this book.

The $OH + CO$ reaction presents a huge challenge to quantum dynamics. The combination of a relatively long-lived collision complex and three heavy atoms in this reaction makes the rigorous quantum scattering calculations difficult. Kroes and coworkers obtained the first 6D total reaction probabilities for this reaction. Very large basis sets had to be used to ensure converged results [138]. Recently, Zhang and coworkers gave some preliminary full-dimensional (6D) quantum state-to-state results for this reaction on the LTSH PES. It is the first such a calculation for a four-atom reaction other than the $H_2 + OH \leftrightarrow H_2O + H$ and its isotopically substituted reactions. The calculation is carried out by the RPD method. The results presented are limited to total angular momentum $J = 0$ for the ground initial ro-vibrational state. Advancing from $J = 0$ to $J > 0$ is extremely difficult due to the rapid increase of the rotational basis functions needed in calculation [68].

Figure 4.14 shows the CO_2 product vibrational state distributions at four collision energies. For CO_2, because the symmetric stretching vibrational frequency ν_1 is

very close to the double of the bending frequency ν_2, it is extremely hard to make a complete assignment of all the vibrational states, and they only managed to assign some of the vibrational states with low excitation energies. The total reaction probability exhibits a pronounced peak at $E_c = 0.158\,\text{eV}$ and a dip at $E_c = 0.174\,\text{eV}$. Although the total and, therefore the CO_2 vibrational state-specific reaction probabilities at 0.158 eV are much larger than at 0.174 eV, the population structures for the two collision energies are quite similar. The (000) state has large population, but the majority of the population are contributed by the bending excited states. Figure 4.3c, d present the CO_2 vibrational population at $E_c = 0.1$ and 0.4 eV, to show the effect of collision energy on product vibrational state distribution.

4.5 Conclusion

After persistent endeavors of decades, the quantum wave packet method has been well developed and currently it is quite mature for calculating product state-resolved different cross sections of triatomic and tetra-atomic reactive scatterings. However, due to numerical scaling of a quantum calculation, in order to study more complicated systems, developments of more efficient numerical methods are still very important in the future, such as the search and develop more efficient grid representation for angular degree of freedom and more compact Hamiltonian forms etc.

MCTDH method has been proven being efficient and memory-saving for dealing with polyatomic molecular dynamics. Theoretical methods for approximately extracting state-to-state differential cross section using MCTDH method would be worth more investigating, particularly for the reaction $H + CH_4$ and its isotopic analogs.

Resonances in triatomic reactive scattering from the reactants in ground vibrational state have been identified and characterized, which help us to deepen the understanding of the chemical reaction dynamics at a single quantum state level. Reactive resonances in a polyatomic reaction and reaction starting with initial states other than ground vibrational states will receive more interest, along with the experimental techniques development [141]. This in turn stimulates the theoretical endeavors for more efficient theoretical methods. In a cold chemical reaction, similar resonance would, in principle, easier to be experimentally observed since there are only very limited partial waves involved. The techniques developed in this chapter can be applied to study the resonance in a cold chemical reaction straightforward.

Acknowledgments We acknowledge X.M. Yang (DICP), H. Guo (UNM), D.Q. Xie (NJU), M. Alexander (UM), Soo-Y. Lee for helpful discussion and cooperated work. Funding supports from Chinese Academy of Sciences and NSFS (Grant No. 21222308, 21103187, 21133006) are acknowledged.

References

1. Alagia M, Casavecchia P, Stranges D (1993) Crossed beam studies of four-atom reactions: the dynamics of OH + CO. J Chem Phys 98:8341
2. Alexander MH, Manolopoulos DE, Werner HJ (2000) An investigation of the F + H_2 reaction based on a full ab initio description of the open-shell character of the F(^2P) atom. J Chem Phys 113(24):11084
3. Althorpe SC (2001) Quantum wavepacket method for state-to-state reactive cross sections. J Chem Phys 114(4):1601
4. Althorpe SC, Clary DC (2003) Quantum scattering calculations on chemical reactions. Annu Rev Phys Chem 54:493
5. Althorpe S, Kouri D, Hoffman D (1997) A chebyshev method for calculating state-to-state reaction probabilities from the time-independent wavepacket reactant-product decoupling equations. J Chem Phys 106:7629
6. Althorpe SC, Kouri DJ, Hoffman DK (1997) Further partitioning of the reactant-product decoupling equations of state-to-state reactive scattering and their solution by the time-independent wave-packet method. J Chem Phys 107(19):7816
7. Althorpe SC, Kouri DJ, Hoffman DK, Zhang JZH (1997) Reactantproduct decoupling approach to state-resolved reactive scattering time-independent wavepacket formulation. J Chem Soc Faraday Trans 93(5):703
8. Althorpe S, Fernández-Alonso F, Bean B, Ayers J, Pomerantz A, Zare R, Wrede E (2002) Observation and interpretation of a time-delayed mechanism in the hydrogen exchange reaction. Nature 416:67
9. Aoiz FJ, Bañares L, Martinez-Haya B, Castillo JF, Manolopoulos DE, Stark K, Werner HJ (1997) Ab initio simulation of molecular beam experiments for the F + H_2 → HF + H reaction. J Phys Chem A 101(36):6403
10. Askar A, Cakmak AS (1978) Explicit integration method for the time-dependent Schrödinger equation for collision problems. J Chem Phys 68:2794
11. Bandrauk AD, Shen H (1991) Improved exponential split operator method for solving the time-dependent Schrödinger equation. Chem Phys Lett 176:428
12. Beck MH, Jäckle A, Worth GA, Meyer HD (2000) The multiconfiguration time-dependent Hartree method: a highly efficient algorithm for propagating wavepackets. Phys Rep 324:1
13. Blais NC, Truhlar DG (1973) Monte carlo trajectories: dynamics of the reaction F + D_2 on a semiempirical valencebond potential energy surface. J Chem Phys 58(3):1090
14. Blanes S, Casas F, Murua A (2006) Symplectic splitting operator methods for the time-dependent Schrödinger equation. J Chem Phys 124:234105
15. Bowman JM, Schatz GC (1995) Theoretical studies of polyatomic bimolecular reaction dynamics. Annu Rev Phys Chem 46(1):169
16. Brink DM, Satchler GR (1968) Angular momentum. Clarendon, Oxford
17. Brown FB, Steckler R, Schwenke DW, Truhlar DG, Garrett BC (1985) An improved potential energy surface for F + H_2 → HF + H and H + HFHF + H. J Chem Phys 82(1):188
18. Brownsword R, Hillenkamp M, Laurent T, Vatsa RK, Volpp HR, Wolfrum J (1996) Dynamics of the H + D_2O → D + HOD hydrogen exchange reaction. Chem Phys Lett 259:375
19. Brownsword R, Hillenkamp M, Laurent T, Vatsa RK, Volpp HR, Wolfrum J (1997) Excitation function and reaction threshold studies of isotope exchange reactions: H + D_2 → D + HD and H + D_2O → D + HOD. J Phys Chem A 101:6448
20. Castillo JF, Manolopoulos DE, Stark K, Werner HJ (1996) Quantum mechanical angular distributions for the F + H_2 reaction. J Chem Phys 104(17):6531
21. Cerjan C (ed) (1993) Numerical grid methods and their application to Schrödinger's equation. Springer, New York
22. Chao SD, Skodje RT (2002) Signatures of reactive resonance: three case studies. Theor Chem Acc 108(5):273

23. Chatfield DC, Friedman RS, Schwenke DW, Truhlar DG (1992) Control of chemical reactivity by quantized transition states. J Phys Chem 96(6):2414
24. Chen R, Guo H (1999) The chebyshev propagator for quantum systems. Comput Phys Commun 119(1):19
25. Chen J, Xu X, Zhang D (2013) An accurate global potential energy surface for the OH + CO → H + CO_2 reaction using neural networks. J Chem Phys 138:221104
26. Clary DC (1994) 4-Atom reaction dynamics. J Phys Chem 98:10678
27. Cvitas M, Althorpe S (2009) Quantum wave packet method for state-to-state reactive scattering calculations on AB + CD → ABC + D reactions. J Chem Phys 113:4557
28. Cvitas M, Althorpe S (2009) State-to-state reactive scattering using reactant-product decoupling. Phys Scr 80:048115
29. Cvitas M, Althorpe S (2011) State-to-state reactive scattering in six dimensions using reactant-product decoupling: OH + H_2 → H_2O + H ($J = 0$). J Chem Phys 134:024309
30. Dai J, Zhang JZH (1996) Time-dependent wave packet approach to state-to-state reactive scattering and application to h + o2reaction. J Phys Chem 100(17):6898
31. Dong F, Lee SH, Liu K (2000) Reactive excitation functions for F + p-H_2/n-H_2/D_2 and the vibrational branching for F + HD. J Chem Phys 112(9):3633
32. Dong W, Xiao C, Wang T, Dai D, Yang X, Zhang DH (2010) Transition-state spectroscopy of partial wave resonances in the f + hd reaction. Science 327(5972):1501
33. Evans MG (1938) Thermodynamical treatment of transition state. Trans Faraday Soc 34:49
34. Evans MG, Polanyi M (1935) Some applications of the transition state method to the calculation of reaction velocities, especially in solution. Trans Faraday Soc 31(1):0875
35. Eyring H (1935) The activated complex in chemical reactions. J Chem Phys 3(2):107
36. Feit MD, Fleck JA Jr, Steiger A (1982) Solution of the Schrödinger-equation by a spectral method. J Comput Phys 47:412
37. Fernandez-Alonso F, Zare RN (2002) Scattering resonances in the simplest chemical reaction. Annu Rev Phys Chem 53:67
38. Fernández-Ramos A, Miller JA, Klippenstein SJ, Truhlar GD (2006) Modeling the kinetics of bimolecular reactions. Chem Rev 106:4518
39. Finlayson-Pitts B, Pitts J (2000) Chemistry of the upper and lower atmosphere. Academic, London
40. Fu B, Xu X, Zhang DH (2008) A hierarchical construction scheme for accurate potential energy surface generation: an application to the F + H_2 reaction. J Chem Phys 129(1):011103
41. Gogtas F, Balint-Kurti GG, Offer AR (1996) Quantum mechanical three-dimensional wavepacket study of the Li + HFLiF + H reaction. J Chem Phys 104(20):7927
42. Goldfield E, Gray S (2002) A quantum dynamics study of H_2 + OH → H_2O + H employing the Wu–Schatz–Lendvay–Fang–Harding potential function and a four-atom implementation of the real wave packet method. J Chem Phys 117:1604
43. Gomez-Carrasco S, Roncero O (2006) Coordinate transformation methods to calculate state-to-state reaction probabilities with wave packet treatments. J Chem Phys 125(5):054102
44. Gray SK, Balint-Kurti GG (1998) Quantum dynamics with real wave packets, including application to three-dimensional (j = 0)d + h[sub 2]hd + h reactive scattering. J Chem Phys 108(3):950
45. Gray SK, Manolopoulos DE (1996) Symplectic integrators tailored to the time-dependent Schrödinger equation. J Chem Phys 104:7099
46. Guo H (2012) Quantum dynamics of complex-forming bimolecular reactions. Int Rev Phys Chem 31(1):1
47. Hankel M, Balint-Kurti GG, Gray SK (2000) Quantum mechanical calculation of product state distributions for the o([sup 1]d) + h[sub 2]oh + h reaction on the ground electronic state surface. J Chem Phys 113(21):9658
48. Harper WW, Nizkorodov SA, Nesbitt DJ (2002) Reactive scattering of F + HD → HF(v, J) + D:HF(v, J) nascent product state distributions and evidence for quantum transition state resonances. J Chem Phys 116(13):5622

49. Hirschfelder J, Eyring H, Topley B (1936) Reactions involving hydrogen molecules and atoms. J Chem Phys 4(3):170
50. Hu W, Schatz GC (2006) Theories of reactive scattering. J Chem Phys 125(13):132301
51. Huang Y, Kouri DJ, Hoffman DK (1994) General, energy-separable Faber polynomial representation of operator functions: theory and application in quantum scattering. J Chem Phys 101:10493
52. Hulburt HM, Hirschfelder JO (1943) The transmission coefficient in the theory of absolute reaction rates. J Chem Phys 11(6):276
53. Judson R, Kouri D, Neuhauser D, Baer M (1990) Time-dependent wave-packet method for the complete determination of s-matrix elements for reactive molecular collisions in three dimensions. Phys Rev A 42(1):351
54. Karplus M, Porter RN, Sharma RD (1965) Exchange reactions with activation energy. i. simple barrier potential for (h, h2). J Chem Phys 43(9):3259
55. Kosloff R (1994) Propagation methods for quantum molecular dynamics. Ann Rev Phys Chem 45:145
56. Kosloff D, Kosloff R (1983) A Fourier method solution for the time dependent Schrödinger equation: a study of the reaction $H^+ + H_2$, $D^+ + HD$, and $D^+ + H_2$. J Chem Phys 79:1823
57. Kosloff D, Kosloff R (1983) A Fourier method solution for the time dependent Schrödinger equation as a tool in molecular dynamics. J Comput Phys 52:35
58. Kudla K, Schatz G, Wagner A, Harding L (1991) A quasiclassical trajectory study of the OH + CO reaction. J Chem Phys 95:1635
59. Lakin M, Troya D, Schatz G, Harding L (2003) A quasiclassical trajectory study of the reaction $OH + CO \rightarrow H + CO_2$. J Chem Phys 119:5848
60. Leforestier C, Bisseling RH, Cerjan C, Feit MD, Friesner R, Guldenberg A, Hammerich A, Jolicard G, Karrlein W, Meyer HD, Lipkin N, Roncero O, Kosloff R (1991) A comparison of different propagation schemes for the time dependent Schrödinger equation. J Comput Phys 94:59
61. Lester M, Pond B, Anderson D (2000) Exploring the oh + co reaction coordinate via infrared spectroscopy of the OH–CO reactant complex. J Chem Phys 113:9889
62. Levine RD, Wu SF (1971) Resonances in reactive collisions: computational study of the h + h2 collision. Chem Phys Lett 11(5):557
63. Li J, Wang Y, Jiang B, Ma J, Dawes R, Xie D, Bowman J, Guo H (2012) A chemically accurate global potential energy surface for the ho + co $\rightarrow$ h + co_2 reaction. J Chem Phys 136:041103
64. Light JC, Carrington T (2000) Discrete-variable representations and their utilization. Adv Chem Phys 114:263
65. Lin S, Guo H (2006) Quantum state-to-state cross sections for atom-diatom reactions: a chebyshev real wave-packet approach. Phys Rev A 74(2):022703
66. Liu K (2001) Crossed-beam studies of neutral reactions: state-specific differential cross sections. Annu Rev Phys Chem 52:139
67. Liu K (2012) Quantum dynamical resonances in chemical reactions: from a + bc to polyatomic systems. Adv Chem Phys 149:1
68. Liu S, Xu X, Zhang D (2011) State-to-state quantum dynamics study of the $OH + CO \rightarrow H + CO_2$ reaction in full dimensions ($J = 0$). J Chem Phys 135:141108
69. Liu S, Xiao C, Wang T, Xu X, Zhang D, Yang X (2012) The dynamics of the $D_2 + OH \rightarrow HOD + D$ reaction: a combined theoretical and experiment study. Faraday Discuss 157:101
70. Liu S, Xu X, Zhang D (2012) Time-dependent wave packet theory for state-to-state differential cross sections of four-atom reactions in full dimensions: application to the $HD + OH \rightarrow H_2O + D$ reaction. J Chem Phys 136:144302
71. Liu S, Chen J, Zhang Z, Zhang D (2013) A six-dimensional state-to-state quantum dynamics study of the $H + CH_4 \rightarrow H_2 + CH_3$ reaction ($j = 0$). J Chem Phys 138:011101
72. Manthe U, Matzkies F (2000) Rotational effects in the $H_2 + OH \rightarrow H_2O + H$ reaction rate: full-dimensional close-coupling results. J Chem Phys 113:5725

73. Manthe U, Meyer HD, Cederbaum LS (1992) Wave-packet dynamics within the multiconfiguration Hartree framework: general aspects and application to NOCl. J Chem Phys 97:3199–3213
74. Manz J (1996) Molecular wavepacket dynamics: thoery for experiments 1926–1996. In: Nobel symposium book: femtochemistry and femtobiology. Imperial College Press, London
75. Marcus RA (1966) On the analytical mechanics of chemical reactions. Classical mechanics of linear collisions. J Chem Phys 45(12):4500
76. Marcus RA (1966) On the analytical mechanics of chemical reactions. Quantum mechanics of linear collisions. J Chem Phys 45(12):4493
77. McNutt JF, Wyatt RE, Redmon MJ (1984) Quantum dynamics of the threedimensional $F + H_2$ reaction. I. Energy partitioning and entropy analysis in the collision complex. J Chem Phys 81(4):1692
78. McNutt JF, Wyatt RE, Redmon MJ (1984) Quantum dynamics of the threedimensional $F + H_2$ reaction. II. Scattering wave function density and flux analysis. J Chem Phys 81(4):1704
79. Medvedev D, Gray S, Goldfield E, Lakin M, Troya D, Schatz G (2004) Quantum wave packe and quasiclassical trajectory studies of OH + CO: influence of the reactant channel well on thermal rate constants. J Chem Phys 120:1231
80. Meijer AJHM, Goldfield EM (1998) Time-dependent quantum mechanical calculations on h + o[sub 2] for total angular momentum j>0. J Chem Phys 108(13):5404
81. Meyer HD, Worth GA (2003) Quantum molecular dynamics: propagating wavepackets and density operators using the multiconfiguration time-dependent Hartree (MCTDH) method. Theor Chem Acc 109:251–267
82. Meyer HD, Manthe U, Cederbaum LS (1990) The multi-configurational time-dependent Hartree approach. Chem Phys Lett 165:73–78
83. Meyer HD, Gatti F, Worth GA (eds) (2009) Multidimensional quantum dynamics, 1st edn. Wiley, London
84. Mielke SL, Lynch GC, Truhlar DG, Schwenke DW (1993) A more accurate potential energy surface and quantum mechanical cross section calculations for the $F + H_2$ reaction. Chem Phys Lett 213(1):10
85. Millar T, Williams D (1988) Rate coefficients in atmospheric chemistry. Kluwer, Dordrecht
86. Miller J, Kee R, Westbrook C (1990) Chemical kinetics and combustion modeling. Annu Rev Phys Chem 41:345
87. Mowrey RC, Kouri DJ (1986) Closecoupling wave packet approach to numerically exact moleculesurface scattering calculations. J Chem Phys 84:6466
88. Muckerman JT (1971) Monte carlo calculations of energy partitioning and isotope effects in reactions of fluorine atoms with H_2, HD, and D_2. J Chem Phys 54(3):1155
89. Neuhauser D, Baer M, Judson RS, Kouri DJ (1990) A time-dependent wave packet approach to atomdiatom reactive collision probabilities: theory and application to the $H + H_2$ ($J = 0$) system. J Chem Phys 93(1):312
90. Neuhauser D, Baer M, Judson RS, Kouri DJ (1991) The application of time-dependent wavepacket methods to reactive scattering. Comput Phys Commun 63(13):460
91. Neumark D, Wodtke A, Robinson G, Hayden C, Lee Y (1984) Experimental investigation of resonances in reactive scattering: the $F + H_2$ reaction. Phys Rev Lett 53(3):226
92. Neumark DE, Wodtke AM, Robinson GN, Hayden CC, Lee YT (1984) Dynamic resonances in the reaction of fluorine atoms with hydrogen molecules. ACS Symp Ser 263:479
93. Neumark DM, Wodtke AM, Robinson GN, Hayden CC, Lee YT (1985) Molecular beam studies of the $F + H_2$ reaction. J Chem Phys 82(7):3045
94. Neumark DM, Wodtke AM, Robinson GN, Hayden CC, Shobatake K, Sparks RK, Schafer TP, Lee YT (1985) Molecular beam studies of the $F + D_2$ and F + HD reactions. J Chem Phys 82(7):3067
95. Park TJ, Light JC (1986) Unitary quantum time evolution by iterative Lanczos reduction. J Chem Phys 85:5870

96. Peng T, Zhang JZH (1996) A reactant-product decoupling method for state-to-state reactive scattering. J Chem Phys 105(14):6072
97. Polanyi JC, Schreiber JL (1974) Distribution of reaction products (theory). Investigation of an ab initio energy-surface for $F + H_2 \rightarrow HF + H$. Chem Phys Lett 29:319
98. Polanyi JC, Schreiber JL (1977) The reaction of $F + H_2 \rightarrow HF + H$. A case study in reaction dynamics. Faraday Discuss Chem Soc 62:267
99. Porter RN (1974) Molecular trajectory calculations. Annu Rev Phys Chem 25(1):317
100. Qiu M, Ren Z, Che L, Dai D, Harich SA, Wang X, Yang X, Xu C, Xie D, Gustafsson M, Skodje RT, Sun Z, Zhang DH (2006) Observation of feshbach resonances in the $F + H_2 \rightarrow HF + H$ reaction. Science 311(5766):1440
101. Rackham EJ, Gonzalez-Lezana T, Manolopoulos DE (2003) A rigorous test of the statistical model for atomdiatom insertion reactions. J Chem Phys 119(24):12895
102. Ren ZF, Che L, Qiu MH, Wang XA, Dong WR, Dai DX, Wang XY, Yang XM, Sun ZG, Fu B, Lee SY, Xu X, Zhang DH (2008) Probing the resonance potential in the f atom reaction with hydrogen deuteride with spectroscopic accuracy. Proc Natl Acad Sci USA 105(35):12662
103. Rice J, Baronavski A (1991) Nonstatistical CO product distributions from the hot H-atom reaction, $H + CO_2 \rightarrow OH + CO$. J Chem Phys 94:1006
104. Sadeghi R, Skodje RT (1994) Barriers, thresholds, and resonances: spectral quantization of the transition state for the collinear $D + H_2$ reaction. J Chem Phys 102(1):193
105. Schaefer TP, Siska PE, Parson JM, Tully FP, Wong YC, Lee Y (1970) Crossed molecular beam study of $F + D_2$. J Chem Phys 53(8):3385
106. Schatz GC (1973) Large quantum effects in the collinear $F + H_2 \rightarrow FH + H$ reaction. J Chem Phys 58(9):4023
107. Schatz GC (1996) Scattering theory and dynamics: time-dependent and time-independent methods. J Phys Chem 100:12839
108. Schatz GC, Kuppermann A (1973) Role of direct and resonant (compound state) processes and of their interferences in the quantum dynamics of the collinear $H + H_2$ exchange reaction. J Chem Phys 59(2):964
109. Schatz G, Kuppermann A (1975) Dynamical resonances in collinear, coplanar, and three-dimensional quantum mechanical reactive scattering. Phys Rev Lett 35(19):1266
110. Schatz GC, Kuppermann A (1976) Quantum mechanical reactive scattering for three-dimensional atom plus diatom systems. I. Theory. J Chem Phys 65(11):4642
111. Schatz GC, Kuppermann A (1976) Quantum mechanical reactive scattering for three-dimensional atom plus diatom systems. II. Accurate cross sections for $H + H_2$. J Chem Phys 65(11):4668
112. Schatz GC, Bowman JM, Kuppermann A (1975) Exact quantum, quasiclassical, and semiclassical reaction probabilities for the collinear $F + H_2 \rightarrow FH + H$ reaction. J Chem Phys 63(2):674
113. Schatz GC, Bowman JM, Kuppermann A (1975) Exact quantum, quasiclassical, and semiclassical reaction probabilities for the collinear $F + D_2 \rightarrow FD + D$ reaction. J Chem Phys 63(2):685
114. Schatz G, Fitzcharles M, Harding L (1987) State-to-state chemistry with fast hydrogen atoms. Faraday Discuss 84:359
115. Schrödinger E (1926) Quantisierung als eigenwert problem. Ann Phys 79:361
116. Skodje RT, Skouteris D, Manolopoulos DE, Lee SH, Dong F, Liu K (2000) Observation of a transition state resonance in the integral cross section of the $F + HD$ reaction. J Chem Phys 112(10):4536
117. Skodje R, Skouteris D, Manolopoulos D, Lee SH, Dong F, Liu K (2000) Resonance-mediated chemical reaction: $F + HD \rightarrow HF + D$. Phys Rev Lett 85(6):1206
118. Skokov S, Bowman J (2001) State-to-state reactive scattering via real l^2 wave packet propagation for reduced dimensionality $AB + CD$ reactions. J Phys Chem A 105:2502–2508
119. Skouteris D, Castillo JF, Manolopoulos DE (2000) Abc: a quantum reactive scattering program. Comput Phys Commun 133(1):128–135

120. Smith IWM (1990) Vibrational adiabaticity in chemical reactions. Acc Chem Res 23(4):101
121. Stark K, Werner HJ (1996) An accurate multireference configuration interaction calculation of the potential energy surface for the $F + H_2 \rightarrow HF + H$ reaction. J Chem Phys 104(17):6515
122. Steckler R, Truhlar DG, Garrett BC (1985) A highbarrier potential energy surface for $F + H_2 \rightarrow HF + H$. J Chem Phys 83(6):2870
123. Strazisar B, Lin C, Davis H (2000) Mode-specific energy disposal in the four-atom reaction $OH + D_2 \rightarrow HOD + D$. Science 290:958
124. Sun Z, Zhang DH, Xu C, Zhou S, Xie D, Lendvay G, Lee SY, Lin SY, Guo H (2008) State-to-state dynamics of $H + O_2$ reaction, evidence for nonstatistical behavior. J Am Chem Soc 130(45):14962
125. Sun Z, Lee SY, Guo H, Zhang DH (2009) Comparison of second-order split operator and chebyshev propagator in wave packet based state-to-state reactive scattering calculations. J Chem Phys 130(17):174102
126. Sun Z, Lin X, Lee SY, Zhang DH (2009) A reactant-coordinate-based time-dependent wave packet method for triatomic state-to-state reaction dynamics: application to the $H + O_2$ reaction. J Phys Chem A 113(16):4145
127. Sun Z, Guo H, Zhang DH (2010) Extraction of state-to-state reactive scattering attributes from wave packet in reactant jacobi coordinates. J Chem Phys 132(8):084112
128. Sun Z, Liu L, Lin SY, Schinke R, Guo H, Zhang DH (2010) State-to-state quantum dynamics of $O + O_2$ isotope exchange reactions reveals nonstatistical behavior at atmospheric conditions. Proc Natl Acad Sci USA 107(2):555
129. Sun ZG, Zhang DH, Alexander MH (2010) Time-dependent wavepacket investigation of state-to-state reactive scattering of Cl with $para$-H_2 including the open-shell character of the cl atom. J Chem Phys 132(3):034308
130. Sun Z, Yang W, Zhang DH (2012) Higher-order split operator schemes for solving the Schrödinger equation in the time-dependent wave packet method: applications to triatomic reactive scattering calculations. Phys Chem Chem Phys 14:1827
131. Tal-Ezer H, Kosloff R (1984) An accurate and efficient scheme for propagating the time dependent Schrödinger equation. J Chem Phys 81:3967
132. Tannor DJ, Weeks DE (1993) Wave packet correlation function formulation of scattering theory: the quantum analog of classical s-matrix theory. J Chem Phys 98(5):3884
133. Truhlar DG (1972) Exact and approximate quantum mechanical reaction probabilities and rate constants for the collinear $H + H_2$ reaction. J Chem Phys 56(5):2232
134. Truhlar DG, Kuppermann A (1970) Quantum mechanics of the $h + h_2$ reaction: exact scattering probabilities for collinear collisions. J Chem Phys 52(7):3841
135. Truhlar DG, Garrett BC, Blais NC (1984) Two new potential energy surfaces for the $F + H_2$ reaction. J Chem Phys 80(1):232
136. Truhlar DG, Garrett BC, Klippenstein SJ (1996) Current status of transition-state theory. J Phys Chem 100(31):12771
137. Truong TN, Tanner JJ, Bala P, McCammon JA, Kouri DJ, Lesyng B, Hoffman DK (1991) A comparative study of time dependent quantum mechanical wave packet evolution methods. J Chem Phys 96:2077
138. Valero R, McCormack D, Kroes G (2004) New results for the $OH(v = 0, j = 0) + CO(v = 0, j = 0) \rightarrow H + CO_2$ reaction: five-and full-dimensional quantum dynamical study on several potential energy surfaces. J Chem Phys 120:4263
139. Wang XA, Dong WR, Qiu MH, Ren ZF, Che L, Dai DX, Wang XY, Yang XM, Sun ZG, Fu B, Lee SY, Xu X, Zhang DH (2008) Hf(v = 3) forward scattering in the $F + H_2$ reaction: shape resonance and slow-down mechanism. Proc Natl Acad Sci USA 105(17):6227
140. Wang XG, Dong WR, Xiao CL, Che L, Ren ZF, Dai DX, Wang XY, Casavecchia P, Yang XM, Jiang B, Xie DQ, Sun ZG, Lee SY, Zhang DH, Werner HJ, Alexander MH (2008) The extent of non-born-oppenheimer coupling in the reaction of $Cl(P_2)$ with $para$-H_2. Science 322(5901):573

141. Wang T, Yang TG, Xiao CL, Dai DX, Yang XM (2013) Highly efficient pumping of vibrationally excited HD molecules via stark-induced adiabatic Raman passage. J Phys Chem Lett 4:368
142. Warnatz J (1984) Combustion chemistry. Springer, New York
143. Wu SF, Levine RD (1971) Quantum mechanical computational studies of chemical reactions: I. Close-coupling method for the collinear $H + H_2$ reaction. Mol Phys 22(5):881
144. Wu SF, Johnson BR, Levine RD (1973) Quantum mechanical computational studies of chemical reactions: III. Collinear a + bc reaction with some model potential energy surfaces. Mol Phys 25(4):839
145. Xiao CL, Xu X, Liu S, Wang T, Dong WR, Yang TG, Sun ZG, Dai DX, Xu X, Zhang DH, Yang XM (2011) Experimental and theoretical differential cross sections for a four-atom reaction: $HD + OH \rightarrow H_2O + D$. Science 333(6041):440
146. Xie D, Chen R, Guo H (2000) Comparison of Chebyshev, Faber, and Lanczos propagation-based methods for calculating resonances. J Chem Phys 112:5263
147. Yang X (2005) State-to-state dynamics of elementary chemical reactions using rydberg h-atom translational spectroscopy. Int Rev Phys Chem 24(1):37
148. Yang X, Zhang DH (2008) Dynamical resonances in the fluorine atom reaction with the hydrogen molecule. Acc Chem Res 41(8):981
149. Yu H, Nyman G (2000) Interpolated ab initio quantum scattering for the reaction of oh with hcl. J Chem Phys 113:8936
150. Yu H, Muckerman J, Sears T (2001) A theoretical study of the potential energy surface for the reaction OH + CO. Chem Phys Lett 349:547
151. Yuan K, Cheng Y, Liu X, Harich S, Yang X, Zhang D (2006) Experimental and quantum dynamical study on an asymmetric insertion reaction: state-to-state dynamics of $O(^1D) + HD(^1\Sigma_g^+, v = 0, j = 0) \rightarrow OH(^2\Pi, v, N) + D(^2S)$. Phys Rev Lett 96(10):103202
152. Zare RN (1988) Angular momentum: understanding spatial aspects in chemistry and physics. Wiley, New York
153. Zhang JZH (1999) Theory and application of quantum molecular dynamics. World Scientific, River Edge
154. Zhang D (2006) State-to-state quantum reactive scattering for four-atom chemical reactions: differential cross section for the $H + H_2O \rightarrow H_2 + OH$ abstraction reaction. J Chem Phys 125:133102
155. Zhang D, Lee S (1999) Fully converged integral cross sections of diatom-diatom reactions and the accuracy of the centrifugal sudden approximation in the $H_2 + OH$ reaction. J Chem Phys 110:4435
156. Zhang DH, Light JC (1996) Quantum state-to-state reaction probabilities for the $H + H_2O \rightarrow H_2 + OH$ reaction in six dimensions. J Chem Phys 105(3):1291
157. Zhang JZH, Miller WH (1989) Quantum reactive scattering via the s-matrix version of the kohn variational principle: differential and integral cross sections for $D + H_2 \rightarrow HD + H$. J Chem Phys 91(3):1528
158. Zhang D, Zhang J (1993) Accurate quantum calculation for the benchmark reaction $H_2 + OH \rightarrow H_2O + H$ in five-dimensional space: reaction probabilities for $J = 0$. J Chem Phys 99:5615
159. Zhang D, Zhang J (1994) Full-dimensional time-dependent treatment for diatom-diatom reactions: the $H_2 + OH$ reaction. J Chem Phys 101:1146
160. Zhang DH, Zhang JZH (1994) Quantum reactive scattering with a deep well: time-dependent calculation for $H + O_2$ reaction and bound state characterization for HO_2. J Chem Phys 101(5):3671
161. Zhang D, Zhang J, Light J (1996) A six dimensional quantum study for atom-triatom reactions: the $H + H_2O \rightarrow H_2 + OH$ reaction. J Chem Phys 104:4544
162. Zhang D, Collins M, Lee S (2000) First-principles theory for the $H + H_2O$, D_2O reactions. Science 290:961
163. Zhang D, Xie D, Yang M, Lee S (2002) State-to-state integral cross section for the $H + H_2O \rightarrow H_2 + OH$ abstraction reaction. Phys Rev Lett 89:283203

164. Zhang D, Yang M, Lee S (2003) Accuracy of the centrifugal sudden approximation in the $H + H_2O$ reaction and accurate integral cross sections for the $H + H_2O \rightarrow H_2 + OH$ abstraction reaction. J Chem Phys 117:10067
165. Zhu W, Dai J, Zhang J, Zhang D (1996) State-to-state time-dependent quantum calculation for reaction $H_2 + OH \rightarrow H_2O + H$ in six dimensions. J Chem Phys 105:4881
166. Zhu W, Zhang JZH, Zhang YC, Zhang YB, Zhan LX, Zhang SL, Zhang DH (1998) Quantum dynamics study of $H_2 + CN \rightarrow HCN + H$ reaction in full dimensions. J Chem Phys 108:3509

Vibrational Spectroscopy and Molecular Dynamics

5

Oriol Vendrell, Markus Schröder, and Hans-Dieter Meyer

Abstract

Quantum dynamical simulations in full dimensionality play an essential role in the field of molecular dynamics. This is shown with the help of two examples: (1) the simulation of the infrared spectrum of the Zundel cation ($H_5O_2^+$) and (2) the investigation of the tunneling splitting in malonaldehyde ($C_3H_4O_2$). For the Zundel cation, full, 15-dimensional dynamics calculations are presented for different isotopomers and experimental spectra are assigned to vibrational transitions. Furthermore, the internal proton transfer process within the Zundel cation is discussed. For malonaldehyde, full, 21-dimensional calculations of the ground state, the four lowest fundamentals, and their tunneling splittings are presented. The results are, along with assignments, compared to experimental data and findings of other researchers.

5.1 Introduction

In a classical picture, a molecule is often seen as collection of N atoms, connected by chemical bonds that are formed by light electrons orbiting the heavy atomic nuclei. The particular geometrical configuration of the molecule is determined by type and character of the chemical bonds, which are seen as spring-like elastic connections between the atoms, and the kind of atoms involved. As a consequence of the elasticity of the inter-atomic bonds, the molecule can vibrate, i.e., the atoms can perform periodic motions relative to each other. Within a harmonic approximation, these vibrations can be expressed as superpositions of $N - 6$ ($N - 5$ for linear

O. Vendrell
Center for Free-Electron Laser Science, DESY, Notkestr. 85, 22607 Hamburg, Germany

M. Schröder • H.-D. Meyer (✉)
Theoretische Chemie, PCI, Universität Heidelberg, INF 229, 69120 Heidelberg, Germany
e-mail: Hans-Dieter.Meyer@pci.uni-heidelberg.de

F. Gatti (ed.), *Molecular Quantum Dynamics*, Physical Chemistry in Action,
DOI 10.1007/978-3-642-45290-1_5,

molecules) so-called normal mode vibrations, i.e., global vibrations of the molecule where all atoms vibrate with the same phase and the same *normal mode frequency*. Most of those normal mode vibrations involve a large number of the atoms of the molecule, but, depending on the particular structure, some of the normal mode vibrations can be quite localized and the corresponding frequency can be very typical for a certain chemical bond or groups of involved atoms.

In a quantum mechanical description, the simple spring-like picture of chemical bonds, of course, breaks down and the molecule has to be described as a many-body system of interacting particles including electrons and nuclei. Nevertheless, the normal mode vibrations have their counterpart in the fundamental excitations of the nuclear vibrational degrees of freedom (DOF) of the molecule. The fundamentals can be excited by infrared radiation (IR) and characteristic absorption bands in the IR spectra immediately point to the existence of certain chemical bonds or to functional groups and hence IR (and Raman) spectroscopy are powerful tools to investigate and study the chemical structure of molecules.

However, not all of the experimentally observed absorption bands can be assigned to characteristic bonds or groups. Here, model calculations can be a useful tool to assign transitions to the involved vibrational states and may help to identify a variety of properties such as the molecular structure itself, the determination of reaction mechanisms, characterization of transition states, etc. The advantage of model calculations is that the quantum mechanical wavefunction can be inspected in detail and to arbitrary precision, only limited, of course, by the available computational capacities.

For the theoretical modeling of IR absorption spectra there exist in essence two strategies which are commonly used, both based on the semi-classical dipole approximation for light–matter interaction: a time-independent one where eigenstates and energies of the molecular Hamiltonian are obtained by solving the time-independent Schrödinger equation and, hence, giving direct access to transition frequencies and dipole matrix elements. The second ansatz is based on a perturbative approach within a time-dependent framework. It aims for the calculation of the linear response[1] of the molecule upon IR irradiation. The latter method requires solving the time-dependent Schrödinger equation for a dipole operated initial system state and subsequently obtaining the absorption spectrum as the frequency components of the linear response function. The advantage of the time-dependent approach is that multiple spectral lines and their intensities are obtained within a single calculation, while, on the other hand, it lacks the possibility to inspect particular eigenstates. A characterization of the eigenstates, i.e., an assignment of the spectral lines, however, can be performed in the time-dependent picture as well.

The key ingredient for both approaches is solving the molecular Schrödinger equation and a large variety of methods are known to accomplish this task, both within the time-dependent and a time-independent framework. However, most of these methods can only be applied to very small and rather rigid molecules, containing three to four atoms with limited flexibility. The challenges of today lie in the accurate modeling of larger and flexible molecules beyond the limit of so few atoms. Large and flexible molecules, especially those exhibiting large amplitude

motions and reorganization processes, usually need to be described by highly correlated multi-dimensional wavefunctions which makes these systems difficult to treat numerically. However, it is also in particular these problems which are stimulating the exploration of new methodologies in the field of quantum dynamics.

One such approach is the multi-configuration time-dependent Hartree (MCTDH) method [2–5] which first emerged in 1990 and since then has been further developed and applied to a large variety of problems. With MCTDH two major breakthroughs could be achieved, one of which we are presenting in the present contribution. The first one was the calculation of the absorption spectrum of pyrazine[6, 7] using a realistic 24-mode model Hamiltonian. The second one was the calculation of IR spectra and assignment of states[8–12] of the Zundel cation, a system with 15 internal DOF. The latter is discussed in detail in Sect. 5.3. We also present recent calculations of state energies and tunneling splittings of malonaldehyde (21 DOF) in Sect. 5.4 in comparison with experimental results, recently published by Lüttschwager et al. [13].

The present chapter is organized as follows: in Sect. 5.2 we briefly review present limitations and current challenges for solving the time-dependent and time-independent Schrödinger equation in multiple dimensions and outline the MCTDH approach in contrast to "standard" methods. In Sect. 5.3 we present full-dimensional calculations on the protonated water dimer, also called the Zundel cation, including the assignment of recorded spectral lines. In Sect. 5.4 we present calculations on the proton tunneling splittings of malonaldehyde in comparison with experimental data. We finally summarize in Sect. 5.5.

5.2 High-Dimensional Quantum Dynamics

An accurate numerical description of molecular vibrations in the field of physical chemistry often requires explicit solutions of the time-dependent or time-independent Schrödinger equation. A full quantum mechanical treatment of all involved particles, i.e., all electrons and nuclei, however, is only possible for very small and rather simple systems such as H_2^+. For larger systems one must rely an approximations, because the demands on CPU time and memory of a numerically exact treatment quickly exceed today's numerical capacities.

The most powerful approximation for treating molecular systems even today was already published in 1927, almost a 100 years ago: the famous Born–Oppenheimer approximation [14]. The key ingredient to this approximation is the separation of the electronic and the nuclear motions, motivated by the different masses of the two types of particles. The electronic wavefunction is treated as being parametrically dependent on the nuclear DOFs while the nuclei evolve within a set of PESs which reflect the energies of the electronic eigenstates.

This separation into subsystems is even today indispensable. It reduces the number of particles in each of the two problems, and, most importantly, it also enables the use of specialized methods and algorithms which take into account the different nature of the involved particles: indistinguishable Fermions within

the electronic system and (in most cases) distinguishable nuclei. Especially for the calculation of the electronic states a large variety of quantum chemistry methods and programs on different levels of theory exist. Nevertheless, the calculation of full-dimensional PESs on which the nuclei of a molecule evolve is even for small molecules a formidable task. Many research groups spend much effort in calculating and fitting these PESs and make them available as numerical subroutines that can be integrated in other program codes which then may use them as a kind of "black box" routines that allow to calculate the potential at any given configuration of the nuclei.

In this spirit we will consider the problem of obtaining the potential as solved for our purposes and focus on the description of the nuclear DOF. Here one usually concentrates on the internal DOFs and chooses a well-suited set of coordinates $\mathbf{q} = \{q_\kappa\}$ to describe the system. Once having defined this set of coordinates one usually represents the nuclear wavefunction Ψ in terms of basis functions on a product grid, that is, for each DOF one chooses a set of basis functions $\chi_{i_\kappa}(q_\kappa)$, in practice often grid points in coordinate representation, on which the wavefunction is sampled such that it can be written as

$$\Psi(\mathbf{q},\mathbf{t}) = \sum_{i_1}^{N_1} \cdots \sum_{i_f}^{N_f} C_{i_1 \cdots i_f} \chi_{i_1}^{(\kappa)}(q_1) \cdots \chi_{i_f}^{(\kappa)}(q_f), \tag{5.1}$$

where the coefficients $C_{i_1 \cdots i_f}$ take the form of a complex valued f-way tensor and are the quantities that need to be stored in a computer to describe the systems state.

The representation Eq. (5.1) is sometimes also called the *standard form* of the wavefunction. Given that on average N basis functions per DOF are sufficient for an accurate description of Ψ the amount of information that needs to be stored and processed scales exponentially with N^f, where N is usually of the order of 10. The standard form therefore de facto limits the size of the molecules that can be treated to about 4 atoms, i.e., 6 internal DOF.

MCTDH therefore takes a different route. The basis functions that are used to represent the wavefunction are chosen variationally optimal and typically span a few (one to four) physical DOF. Numerically, this corresponds to combining a subset of the indices in Eq. (5.1) into one single index and subsequently finding an optimal basis to describe this subset of DOF. In this way only a few most important basis functions and their expansion coefficients on the primitive grid as well as the expansion coefficients of the wavefunction in this optimal basis have to be stored. This leads to an enormous reduction of data.

The MCTDH ansatz of the wavefunction reads

$$\begin{aligned} \Psi(q_1,\ldots,q_f,t) &\equiv \Psi(Q_1,\ldots,Q_p,t) \\ &= \sum_{j_1}^{n_1} \cdots \sum_{j_p}^{n_p} A_{j_1,\ldots,j_p}(t) \prod_{\kappa=1}^{p} \varphi_{j_\kappa}^{(\kappa)}(Q_\kappa,t) \\ &= \sum_J A_J \, \Phi_J \ . \end{aligned} \tag{5.2}$$

Here $A_{j_1,\ldots,j_p}$ are the MCTDH expansion coefficients and φ are optimal basis functions for this particular wavefunction, also called single particle functions (SPF), that are (exclusively) defined on one combined coordinate Q_κ, the latter comprising the aforementioned d (one to four) physical DOF. Note that the ansatz Eq. (5.2) is a generalized form of the standard Hartree ansatz and reduces to the very same if one sets $n_i = 1$.

As mentioned before, the SPF are expanded on the primitive grid such that

$$\varphi_{j_\kappa}^{(\kappa)}(Q_\kappa, t) = \sum_{l_1=1}^{N_{1,\kappa}} \cdots \sum_{l_d=1}^{N_{d,\kappa}} c_{j_\kappa l_1 \cdots l_d}^{(\kappa)}(t)\ \chi_{l_1}^{(\kappa,1)}(q_{1,\kappa}) \cdots \chi_{l_d}^{(\kappa,d)}(q_{d,\kappa}), \tag{5.3}$$

where the χ represent the primitive basis functions as in Eq. (5.1), usually grid points within a discrete-variable representation (DVR), and the c are again expansion coefficients.

Note, that other than in the standard form Eq. (5.1) not only the coefficients, but both the basis functions (SPFs) and the MCTDH expansion coefficients, are taken to be time-dependent in Eq. (5.2). Inserting this ansatz in the Dirac–Frenkel variational principle leads to equations of motion (EOM) for the SPF and the coefficients ($\hbar = 1$),

$$i\frac{\partial}{\partial t} A_J = \sum_L \langle \Phi_J | \hat{H} | \Phi_L \rangle A_L, \tag{5.4}$$

and

$$i\frac{\partial}{\partial t} \varphi_j^{(\kappa)} = \left(1 - P^{(\kappa)}\right) \sum_{k,l=1}^{n_\kappa} \left(\rho^{(\kappa)}\right)_{j,k}^{-1} \left\langle \hat{H} \right\rangle_{k,l}^{(\kappa)} \varphi_l^{(\kappa)}, \tag{5.5}$$

where $\hat{H}$ is the system Hamiltonian, $\left\langle \hat{H} \right\rangle_{k,l}^{(\kappa)}$ are the so-called mean fields, $\rho^{(\kappa)}$ is the reduced system density matrix for the κth coordinate, and $(1 - P^{(\kappa)})$ projects outside the space currently spanned by the SPF of DOF κ. Like for the standard form Eq. (5.4) resembles the matrix form of the time-dependent Schrödinger equation and Eq. (5.5) ensures that the basis set follows the motion of the wavefunction as it evolves in time.

Note that Eqs. (5.4) and (5.5) are coupled via the mean fields and the matrix elements. In practice, the EOMs are decoupled during an update time step, by the so called constant mean-field approach. Nevertheless, the evaluation of the EOMs (5.4) and (5.5) is rather costly as the calculation of the mean fields and matrix elements involves multi-dimensional integrals over all physical DOF. A key ingredient of the MCTDH algorithm therefore is that the Hamiltonian operator can be expressed in terms of products of low-dimensional terms $\hat{h}_r^{(\kappa)}$ such that

$$\hat{H} = \sum_{r=1}^{s} c_r \prod_{\kappa=1}^{p} \hat{h}_r^{(\kappa)}, \tag{5.6}$$

where the $\hat{h}_r^{(\kappa)}$ operate only on the κth composite coordinate. With this ansatz the multi-dimensional integrals reduce to sums of products of low-dimensional integrals:

$$\langle \Phi_J | \hat{H} | \Phi_L \rangle = \sum_{r=1}^{s} c_r \prod_{\kappa=1}^{p} \langle \varphi_{j_\kappa}^{(\kappa)} | \hat{h}_r^{(\kappa)} | \varphi_{l_\kappa}^{(\kappa)} \rangle \ . \tag{5.7}$$

In this form the evaluation of the right-hand sides of the EOMs can be effectively performed. (An alternative to the product form discussed here is the correlated DVR (CDVR) method of Manthe [15].)

The MCTDH ansatz Eq. (5.2) is also suitable for the calculation of eigenstates in which case the expectation value of the Hamiltonian is minimized. This leads to an eigenvalue problem for the A-vector

$$\sum_{L} \langle \Phi_J | \hat{H} | \Phi_L \rangle \, A_L = E \, A_J, \tag{5.8}$$

which constitutes an ordinary eigenvalue equation that can be solved using a Krylow subspace method, and a propagation of the SPF in negative imaginary time $\tau = -it$, i.e., a relaxation, with the EOM

$$\frac{\partial}{\partial \tau} \varphi_j^{(\kappa)} := -\left(1 - P^{(\kappa)}\right) \sum_{k,l=1}^{n_\kappa} \left(\rho^{(\kappa)}\right)_{jk}^{-1} \left\langle \hat{H} \right\rangle_{kl}^{(\kappa)} \varphi_l^{(\kappa)} \to 0. \tag{5.9}$$

Since both equations have to be fulfilled simultaneously, one again uses the constant mean-field approach to iteratively solve both equations until convergence is achieved.

One of the main challenges at the present time, however, is not so much the compact representation of the wavefunction but of the Hamiltonian. While the kinetic energy operator is in most cases known analytically and of the form Eq. (5.6) this is not the case for the PES. As stated above, accurate PES are often available only as intricate numerical subroutines resulting from previous quantum chemistry calculations. The sheer size of the primitive basis prohibits sampling of the PES or calculating the potential points on the fly for larger systems.

For smaller systems (six to eight DOF) one can use a similar ansatz for the potential as for the wavefunction Eq. (5.2) and use the so-called POTFIT algorithm[3, 16–19] or its multi-grid extension[20], to transform the PES into product form. This, however, requires multiple integrals over the complete grid such that POTFIT can only be used up to a certain number of DOF. For larger systems, one needs to use alternative techniques.

Within the present contribution we resorted to the so-called cluster expansion (CE)[10], a variant of the n-mode representation[21, 22], also called high-dimensional model representation or cut-high dimensional model representation (cut-HDMR)[23–26]. Within the CE the potential is approximated by n-particle interaction terms. These terms are called clusters. Again the Q_α refer to the composite coordinates as detailed above. The PES is approximated by the expansion

$$\begin{aligned} V(\mathbf{Q}) = v^{(0)}_{\text{ref}}(Q_{\text{ref}}) + \sum_{\alpha=1} v^{(1)}_{\alpha,\text{ref}}(Q_\alpha, Q_{\text{ref}}) + \sum_{\alpha<\beta} v^{(3)}_{\alpha,\beta,\text{ref}}(Q_\alpha, Q_\beta, Q_{\text{ref}}) \\ + \sum_{\alpha<\beta<\gamma} v^{(3)}_{\alpha,\beta,\gamma,\text{ref}}(Q_\alpha, Q_\beta, Q_\gamma, Q_{\text{ref}}) + \cdots \end{aligned} \tag{5.10}$$

with

$$\begin{aligned} v^{(0)}_{\text{ref}}(Q_{\text{ref}}) &= V(0, \ldots, Q_{\text{ref}}) \\ v^{(1)}_{\alpha,\text{ref}}(Q_\alpha, Q_{\text{ref}}) &= V(0, \ldots, Q_\alpha, 0, \ldots, Q_{\text{ref}}) - v^{(0)}_{\text{ref}}(Q_{\text{ref}}), \end{aligned} \tag{5.11}$$

etc. Q_{ref} here may either be a reference configuration or contain reference coordinate which is present in all clusters. The main advantage of this technique is that the series can often be truncated at low orders n and that the n-particle interaction terms $v^{(n)}$ only depend on a few (composite) coordinates such that POTFIT can be used to transform these low-dimensional terms into product form. The main disadvantage, on the other hand, is that this method is not variational and hence additional terms are not always guaranteed to improve the global accuracy of the expansion. It is also unknown which terms are significant and which ones can be neglected prior to their actual calculation, however, it can be estimated using statistical methods. Moreover, especially in the edges of the primitive grid the error of the expansion Eq. (5.10) is known to be rather uncontrollable. The CE often leads to numerical instabilities due to unphysically and strongly negative parts of the approximated potential which need to be “repaired" by adding either additional higher order terms of the CE or artificial external potentials. But even with these limitations, the CE is a powerful tool to represent potentials with a large number of DOF and hence this method is used for all calculations presented in this chapter.

5.3 Infrared Spectroscopy and Dynamics of the Protonated Water Dimer

Protonated water clusters ($H(H_2O)_n^+$) of various sizes and geometries have captured the attention of many researchers in recent years due to their importance to many areas of chemistry and biology. Advancements in understanding the dynamics and spectroscopy of this kind of systems were made possible owing to important improvements in the measurements of IR action spectra in the gas phase [27–32]. In order to assign the recorded spectra and extract meaningful structural and dynamical information, computational simulations are needed in conjunction with experiments.

However, we are still far from accurate and reliable simulations of the IR spectra of all but the smallest clusters. This is caused by the coupled, anharmonic interatomic potential governing the motion of these systems, featuring many accessible minima connected through shallow barriers, and the need of a quantum dynamical treatment of the system to obtain accurate vibrational eigenstate energies and absorption cross-sections. Among the various clusters, the protonated water dimer ($H(H_2O)_2^+$), also known as Zundel cation, has been the subject of intense research efforts, both from the experimental [28–32] and from the theoretical [8, 10, 11, 31–38] perspectives. The cleanest experimental IR spectra for the Zundel cation could be obtained by messenger atom tagging techniques using Ar [30–32] and Ne [31, 32] as the tagging agents. Previous multiphoton spectra measured by IR free electron lasers had presented substantially different features to the linear spectra measured at lower light intensities and had been very difficult to interpret [28, 29]. The spectrum obtained with Ne-tagging could be shown to be very close to the linear absorption spectrum of the bare cation. This spectrum could be assigned and fully understood *only* after full-dimensional quantum-dynamical simulation [8–10]. IR spectra of various isotopically substituted forms of the Zundel cation were also reported using the messenger predissociation technique with Ar-tagging in the range 600–4,000 cm^{-1} [32]. The large observed variation in the spectral features of the different isotopomers clearly pinpoints the complex nature of the cluster dynamics, dominated by anharmonicities and Fermi resonances.

5.3.1 Infrared Spectroscopy

The infrared spectra are calculated in the time-dependent representation of quantum mechanics by Fourier transformation of the auto-correlation of the dipole-operated initial state [1]:

$$I(E) = \frac{E}{3\,c\,\epsilon_0\,\hbar^2}\mathrm{Re}\int_0^\infty \exp(i\,(E+E_0)\,t/\hbar) \times\langle\Psi_{\mu,0}|\exp(-i\,\hat{H}\,t/\hbar)|\Psi_{\mu,0}\rangle\;\;dt \tag{5.12}$$

where E_0 is the ground-state energy and $|\Psi_{\mu,0}\rangle \equiv \hat{\mu}\,|\Psi_0\rangle$. This corresponds to the first order time-dependent perturbation theory result for absorption spectroscopy. The great advantage of the time-dependent approach is that no full Hamiltonian diagonalization is required in order to obtain the vibrational eigenstates from which later transition dipole matrix elements would be computed. The latter becomes simply impracticable in systems of just moderate dimensionality due to the large number and density of states. Instead, the application of Eq. (5.12) requires an efficient wavepacket propagation method. As outlined in Sect. 5.2 an efficient propagation method for the time-dependent Schrödinger equation is given by MCTDH [2–5]. The choice of coordinates is crucial in quantum dynamics

calculations of large molecules. The coordinates should correspond as much as possible to what could be called "natural motions" of the system. In rigid and weakly coupled systems these correspond to normal modes of vibration calculated from second order expansion of the PES around a suitable stationary point. In molecules and clusters featuring large amplitude motions and with strong mode couplings the best choice is usually to use internal coordinates consisting of, e.g., bond distances, bond angles or dihedral angles. Internal coordinates of this kind lead usually to complicated kinetic energy operators (KEO), and this is discussed elsewhere. Once the coordinates are fixed and the KEO has been obtained, the potential energy operator (PEO) part of the Hamiltonian has to be expressed in such coordinates in a form that makes the subsequent quantum dynamics calculations as efficient as possible. Various possibilities to attack this question are also discussed elsewhere. All details on the setup of the vibrational Hamiltonian of the Zundel cation can be found in [9, 39]. For the sake of completeness we mention that a set of curvilinear coordinates was used to describe the configuration of the system and that the exact KEO in this set of coordinates was employed. The 15 internal coordinates describing the system are: the distance between the oxygen atoms of both water molecules (R), the position of the central proton with respect to the center of mass of both oxygen atoms (x,y,z), the Euler angles defining the relative orientation between the two water molecules (waggings: γ_A, γ_B; rockings: β_A, β_B; internal relative rotation: α) and the Jacobi coordinates which account for the particular configuration of each water molecule ($R_{1(A,B)}$, $R_{2(A,B)}$, $\theta_{(A,B)}$)) where R_{1x} is the distance between the oxygen atom and the center of mass of the corresponding H_2 fragment, R_{2x} is the H–H distance and θ_x is the angle between these two vectors. Figure 5.1 presents a scheme of the 15 coordinates that describe the configuration of the system. To account for the interatomic potential we made use of the PES of Bowman and coworkers, which constitutes the most accurate ab initio surface available to date for this system [34]. The PEO was constructed as a CE or n-mode representation [21] as outlined in Sect. 5.2.

We will now discuss the accurate calculation and assignment of the IR spectra of the isotopically substituted forms of the Zundel cation $D(D_2O)_2^+$, $H(D_2O)_2^+$, and $D(H_2O)_2^+$ [12]. These spectra are compared to the non-deuterated $H(H_2O)_2^+$ cation, whose main features are extensively discussed in [8, 10]. Figure 5.2a presents the computed MCTDH spectrum for $H(H_2O)_2^+$ in comparison with spectra from [32] measured using Ne and Ar as tagging agents. The agreement of the computed IR linear absorption spectrum with the Ne-tagging spectrum is excellent. The Ar-tagging spectrum presents splitting and broadening of its features due to the stronger interaction of Ar with the cation. For the deuterated species only Ar-tagged spectra have been reported to date [32]. Figure 5.2b presents the comparison of the computed $D(D_2O)_2^+$ spectrum with the one obtained with Ar-tagging. The last presents relatively broad features, but the agreement in the positions of the main absorptions with theory is good. Therefore we can conclude that the spectra of the various Zundel forms computed with MCTDH will display a very good agreement with messenger predissociation spectra whenever the perturbation due to the tagging agent is small. This is in itself an important result that could only be established

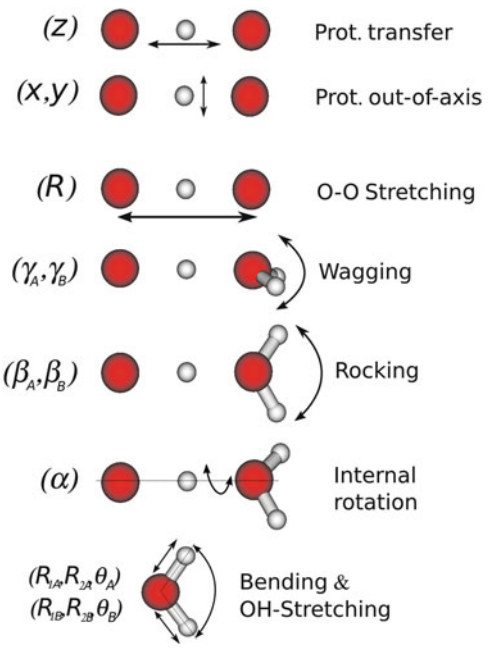

Fig. 5.1 Diagram of the 15 internal coordinates describing the configuration of the Zundel cation. The internal coordinates of the water molecules $(R_{1X}, R_{2X}, \theta_X)$ correspond to the Jacobi vectors connecting the oxygen atom to the center of the H–H fragment, the vector joining both hydrogen atoms and the angle between both vectors, respectively. The bending mode of a monomer is well described by the R_{2X} coordinate in the absence of large oscillations in the OH-stretching modes

after comparison of the messenger tagging spectra with spectra calculated by a full-dimensional quantum mechanical treatment using MCTDH.

The interpretation of the IR spectra requires definite assignments of the spectral lines and an understanding of their origin. Zeroth-order states are used as a tool to perform such assignments. They correspond to well-defined local excitations of the system, e.g. the bending mode of the water molecules or the one-quantum excitation of the proton-transfer mode, and they are constructed as products of eigenfunctions of low-dimensional Hamiltonians. A more specific definition and procedures to obtain them in the context of MCTDH was presented elsewhere [10]. In the following, $|\Phi_l\rangle$ refers to the vibrational wavefunction of a zeroth-order state while $|\Psi_m\rangle$ corresponds to a vibrational eigenstate. The quantities used for assignments are the $|\langle\Phi_l|\Psi_m\rangle|^2$ products, which tell us to which extent a particular and well-defined zeroth-order vibration participates in a certain spectral line. Even though each line contains contributions from all or some of the considered zeroth-order states (non-vanishing $|\langle\Phi_l|\Psi_m\rangle|^2$ elements), there is usually a zeroth-order state that contributes to a specific transition appreciably more than the others. Thus, when we refer to a certain spectral line as the (X) transition or to the corresponding eigenstate as $|\Psi_X\rangle$, it is because it is possible to identify the zeroth-order state $|\Phi_X\rangle$ as the *leading* contribution to $|\Psi_X\rangle$. In the case of very large coupling it may not be possible to cleanly disentangle the spectrum into one-to-one assignments of spectral peaks to zeroth-order states, since a given transition may present similar contributions from two or more zeroth-order states. Tables containing the most

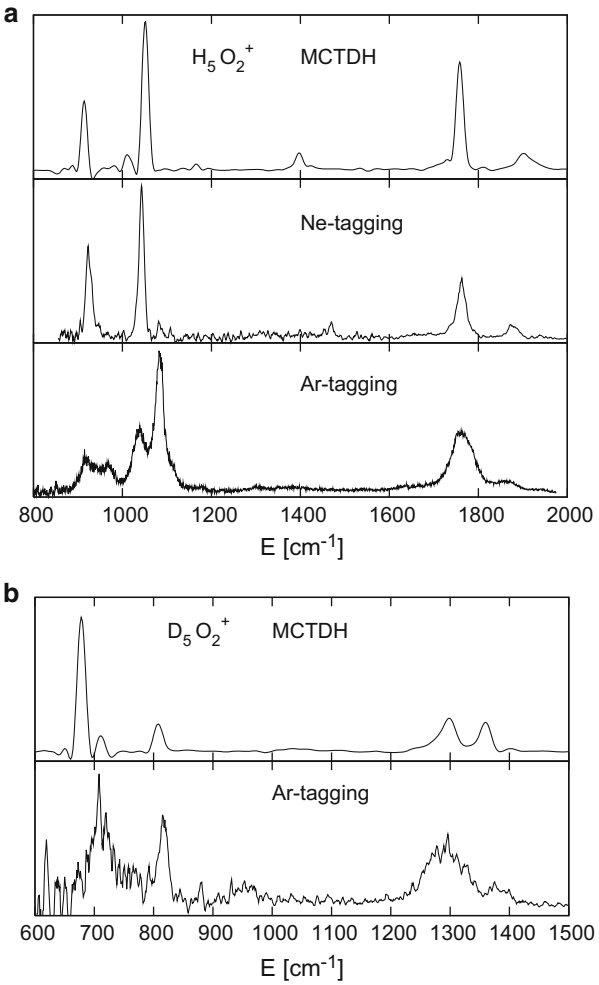

Fig. 5.2 Comparison of MCTDH spectra with available experimental measurements from [32] for (**a**) $H(H_2O)_2^+$ and (**b**) $D(D_2O)_2^+$

important $|\langle \Phi_l | \Psi_i \rangle|^2$ elements for the four considered isotopologues are provided in [40].

Figure 5.3 presents the IR spectra of $H(H_2O)_2^+$, $D(D_2O)_2^+$, $H(D_2O)_2^+$ and $D(H_2O)_2^+$. The lowest frequency parts of the four spectra are composed of two lines related to the one-quantum wagging motions and its combination with the internal rotation motion of one of the monomers with respect to the other. The highest frequency parts of the spectra are composed of two bright lines related to the terminal O–H(D) vibrations of the water molecules. Neither the assignment of the just discussed peaks in the lowest and highest energy domain nor the relative

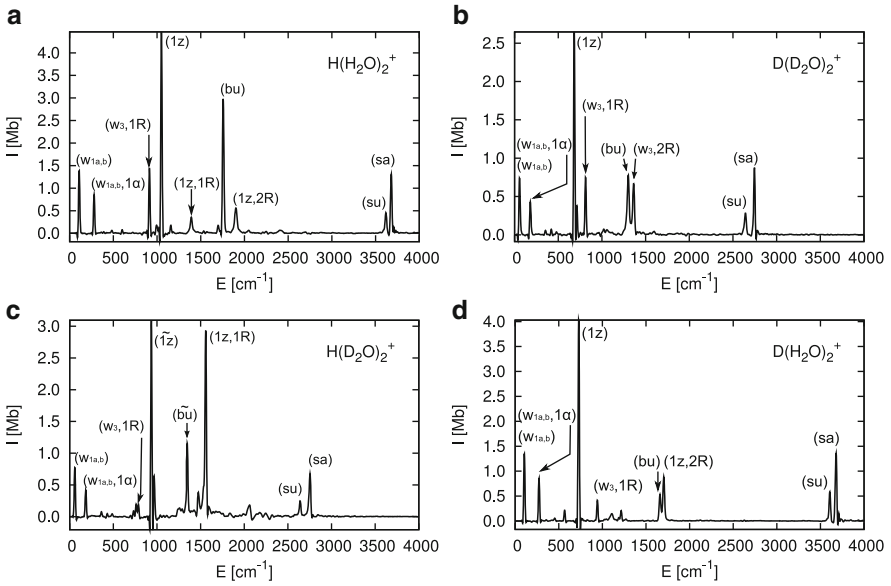

Fig. 5.3 Computed IR spectra of the (**a**) $H(H_2O)_2^+$, (**b**) $D(D_2O)_2^+$, (**c**) $H(D_2O)_2^+$, and (**d**) $D(H_2O)_2^+$ isotopologues of the Zundel cation with assignments of the most important peaks

positions between each other change after deuteration. Only the expected red-shifts take place for $D(D_2O)_2^+$ and $H(D_2O)_2^+$, i.e. when the terminal hydrogens are substituted by deuterium atoms.

The situation turns out to be much more complex in the spectral region between 600 and 2,000 cm^{-1}. The middle range spectrum of the $H(H_2O)_2^+$ cation in Fig. 5.3a features five clearly visible absorptions in the range between 900 and 1,900 cm^{-1}. They could be assigned and explained as arising from a set of five coupled zeroth-order states composed of [8, 10]: $|\Phi_{1R,w_3}\rangle$, a combination of two modes, a two-quanta asymmetric wagging (w_3) mode and the one-quantum ($1R$) mode, where R is the O–O stretching coordinate; $|\Phi_{1z}\rangle$, the one-quantum asymmetric proton stretch along the central O–O axis (z refers to the proton position along the O–O axis); $|\Phi_{1z,1R}\rangle$, the combination of the $1z$ and $1R$ excitations; $|\Phi_{1z,2R}\rangle$, the combination of the $1z$ and two-quanta O–O excitations; $|\Phi_{bu}\rangle$, the *ungerade* water-bending mode.

The most intense line of the $H(H_2O)_2^+$ spectrum centered at 1,040 cm^{-1} is related to the ($1z$) transition since the displacement of the central proton along the O–O axis causes the largest variation of the dipole moment. Thus the $|\Phi_{1z}\rangle$ zeroth-order state has a large contribution to this eigenstate, but the second most important contribution to this line arises from the $|\Phi_{1R,w_3}\rangle$ zeroth-order state. The situation is reversed for the transition centered at 915 cm^{-1}, whose leading contribution is $|\Phi_{1R,w_3}\rangle$ and the second most important one is $|\Phi_{1z}\rangle$. Therefore the doublet of peaks centered at about 1,000 cm^{-1} in the $H(H_2O)_2^+$ arises from a Fermi resonance between the strongly coupled, zeroth-order states $|\Phi_{1z}\rangle$ and $|\Phi_{1R,w_3}\rangle$ [8, 10, 11]. The

next three lines of the spectrum correspond to the 1,415 cm^{-1} ($1z, 1R$), 1,750 cm^{-1} (bu) and 1,905 cm^{-1} ($1z, 2R$) transitions, respectively. All three transitions, and specially (bu), have a non-negligible contribution from the $|\Phi_{1z}\rangle$ zeroth-order state, from which they obtain a large part of their spectral intensity [10]. Moreover, the strong coupling between the $|\Phi_{1z}\rangle$ and $|\Phi_{bu}\rangle$ modes is responsible for shifting the ($1z$) and (bu) lines about 150 cm^{-1} down and up, respectively, with respect to their estimated uncoupled positions [10, 11].

The IR spectrum of $D(D_2O)_2^+$ is shown in Fig. 5.3b. The ($1z$) peak is found here at 678 cm^{-1} and is, as in $H(H_2O)_2^+$, the most intense IR absorption. The ($1R, w_3$) peak is found at 807 cm^{-1}. Therefore the characteristic doublet at about 1,000 cm^{-1} in $H(H_2O)_2^+$ is also found in $D(D_2O)_2^+$, but with its constituent peaks in reverse order [12]. The (bu) peak is found at 1,298 cm^{-1}, about 450 cm^{-1} below its position in $H(H_2O)_2^+$. Neither ($1z, 1R$) nor ($1z, 2R$) peaks appear in the spectrum of $D(D_2O)_2^+$. The position of these two eigenstates has been computed to be 1,150 and 1,600 cm^{-1}, respectively. Therefore they are located far from absorptions from which they could borrow intensity. Moreover, after deuteration the coupling between z (proton position) and R (O–O distance) is reduced since the system remains in deeper, less anharmonic regions of the potential, thus reducing even more the possibility for direct absorption of the ($1z, 1R$) and ($1z, 2R$) combinations [12]. Immediately above the (bu) peak a line is found, which can be assigned to ($w_3, 2R$) [40]. This peak therefore borrows some intensity from (bu) in order to become bright in $D(D_2O)_2^+$ via a similar mechanism that gives rise to the main doublet in $H(H_2O)_2^+$. This absorption is seen as a shoulder to the (bu) peak in experimental spectra in this region [32].

The most complex of all considered spectra is $H(D_2O)_2^+$, shown in Fig. 5.3c. Here the deuteration of the external positions brings the position of the zeroth-order state $|\Phi_{bu}\rangle$ down to lower frequencies by about 300 cm^{-1}, while the zeroth-order states $|\Phi_{1z}\rangle$ and $|\Phi_{1z,1R}\rangle$ remain almost unaffected. This results in a situation in which the zeroth-order $|\Phi_{bu}\rangle$ is found between $|\Phi_{1z}\rangle$ and $|\Phi_{1z,1R}\rangle$. These three zeroth-order states strongly couple to each other and are responsible for the triplet absorption with peaks at 938, 1,355, and 1,564 cm^{-1} [12, 40]. The peak at 938 cm^{-1} has almost equal relative contribution from $|\Phi_{1z}\rangle$ and $|\Phi_{bu}\rangle$. The central peak at 1,355 cm^{-1} has almost equal participation from $|\Phi_{1z}\rangle$, $|\Phi_{bu}\rangle$, and $|\Phi_{1z,1R}\rangle$, while the peak at 1,564 cm^{-1} is a mixture of $|\Phi_{bu}\rangle$ and $|\Phi_{1z,1R}\rangle$ with a slightly larger participation of the latest. The strong couplings shaping the middle region of the spectrum are reflected in the loss of diagonal dominance of the matrix composed of the $|\langle\Phi_l|\Psi_m\rangle|^2$ elements (see table in [40]) for $H(D_2O)_2^+$. The use of a tilde in these three assignments in Fig. 5.3c indicates that the tag assignments are a bit arbitrary because of the strong mixing of underlying zeroth-order states, in contrast to other assignments in which one zeroth-order state is mainly responsible for a given peak. The ($1R, w_3$) peak is of reduced intensity due to its red shift and consequent decoupling from the zeroth-order ($1z$). The ($1z, 2R$) state is located far from peaks from which it can borrow intensity and shows no IR absorption.

In contrast to $H(D_2O)_2^+$, deuteration of the central position alone in $D(H_2O)_2^+$ leads to the simplest and most diagonally dominant IR spectrum of this series. Here the zeroth-order $(1z)$ shifts to lower frequencies and decouples from $(1R, w_3)$. The peak at 785 cm^{-1} is cleanly assigned to $(1z)$. $(1z)$ decouples as well from (bu). This brings the position of the (bu) peak down to 1,662 cm^{-1}, closer to the bending frequency of an isolated water molecule and explains the reduced intensity [12, 40]. Note that the position of (bu) at 1,758 cm^{-1} in $H(H_2O)_2^+$ was due to strong coupling with the central proton $(1z)$ mode. Due to the isotopic substitution the $(1z, 2R)$ peak is shifted down, ending relatively close to (bu). The doublet formed by (bu) and $(1z, 2R)$ is the only structure related to a resonance in $D(H_2O)_2^+$. However, both lines can be cleanly assigned, as seen by inspecting the contribution of the corresponding zeroth-order states [12, 40].

We have seen that the effect of a full or partial deuteration of the cation not only leads to line shifts but also significantly changes the intensities and modifies the assignment of the infrared signatures of the different isotopologues. This is due to the soft, anharmonic, and coupled potential of the Zundel cation, where the dynamics and spectroscopy are strongly dominated by Fermi resonances between various coupled zeroth-order vibrations. The discussed quantum dynamical calculations represent an important milestone in our understanding of the spectroscopy and dynamics of protonated water clusters and on their dramatic isotope effects [41], and could only be achieved after a full-dimensional quantum dynamical treatment of the clusters.

5.3.2 Dynamics of the Excess Proton

We are now in a position to further explore the dynamics of the protonated water dimer and attempt to learn about the details of proton transfer dynamics in acidic water. These issues can be naturally addressed within the same methodological framework presented above to calculate the IR spectrum. The first proposal of a plausible mechanism for charge migration in water dates from two centuries ago and depicts the excess charge as hoping between neighboring waters [42]. In more recent times two limiting structures were proposed, namely the Zundel [43] ($H_5O_2^+$) and Eigen [44] ($H_9O_4^+$) cations, which represented excluding views of the hydrated proton in water. With the advent of sophisticated experimental and computational techniques during recent years a concordant view emerged for the transfer of an excess proton between two hydrogen-bonded water molecules [38, 45–47]. Both the Eigen and Zundel structures play a role as limiting ideal configurations in such mechanism. Basically, the breakage of a hydrogen bond in the second solvation shell of the Eigen cation allows for the excess proton to advance towards a neighboring water molecule while forming a Zundel-like transient structure. Based on the analysis of classical trajectories of an excess proton in bulk water two different time regimes were identified. On the one hand, the rate-limiting hydrogen bond breakage occurs in the time-scale of 1–2 ps. On the other hand, the ultra-fast rattling

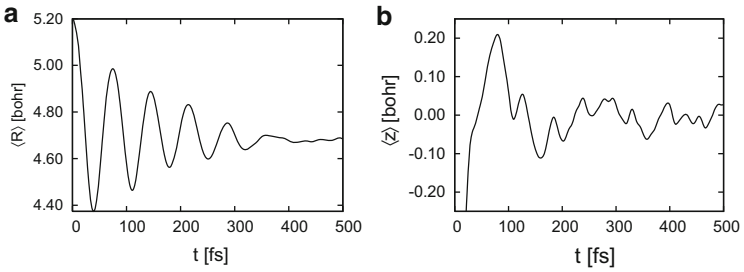

Fig. 5.4 (**a**) Expectation value $\langle R \rangle$ and (**b**) expectation value $\langle z \rangle$. The vibrational energy of the system is 2,575 cm^{-1} (7.36 kcal/mol) above the ZPE. The expectation value $\langle z \rangle$ at $t = 0$ is −0.61 Bohr

of the transferring proton between water molecules before the transfer is complete occurs in the time-scale of 100–200 fs or even less [48, 49]. Femtosecond pump-probe experiments in the infrared domain were able to access such ultra-fast proton oscillations between neighboring water molecules, which would even occur in a time-scale shorter than the resolution of the experiment, below 100 fs [50], thus supporting the view of an ultra-fast PT taking place only after the right coordination of the implied water molecules has been achieved, this last being the rate-limiting step of the overall process.

In the following we will analyze the very fundamental proton transfer event between the fragments H_3O^+ and H_2O from a quantum dynamical, time-dependent perspective, and provide a connection to the IR spectroscopy results presented above. An initial wavepacket to study the collision and proton transfer is prepared by applying a perturbing potential depending on the z and R coordinates in order to place the proton closer to one of the two water molecules [11] and to increase their intermolecular distance. This wavepacket corresponds to fragments H_3O^+ and H_2O immediately before their encounter and exchange of a proton. This wavepacket is then propagated on the unperturbed Hamiltonian. At $t = 0$ we have $\langle R \rangle = 5.20$ Bohr (2.75 Å), which roughly corresponds to the equilibrium distance of the hydrogen bond between water molecules. The proton is initially closer to water A (left in the plot). The total vibrational energy of the system in this propagation lies 2,575 cm^{-1} (7.36 kcal/mol) above the ZPE. Figure 5.4a, b present the time evolution of the $\langle R \rangle$ and $\langle z \rangle$ expectation values, respectively. After the dynamics starts the hydrogen bond quickly compresses and reaches its shortest value of $\langle R \rangle = 4.37$ Bohr (2.31 Å) after 40 fs. After 75 fs it reaches its outer turning point at $\langle R \rangle = 4.98$ Bohr, which is, however, shorter than the initial O–O separation. The amplitude of the $\langle R \rangle$ oscillations is damped at each new cycle. The dynamics of the central proton depends to a large extent on the position of the R coordinate. The plot of $\langle z \rangle$ shows how the proton executes a fast motion towards the acceptor oxygen during the first half cycle of the $\langle R \rangle$ oscillation. The proton continues to be transferred during the second half of the $\langle R \rangle$ oscillation, between $t = 40$ and $t = 75$ fs while the R distance is becoming larger again. The rate of proton transfer

is, however, slower during the second half-period. In the next full cycle of $\langle R \rangle$ the proton transfer proceeds slightly in the opposite direction, and after two cycles of $\langle R \rangle$ the expectation value $\langle z \rangle$ stabilizes around 0.

The probability density $\rho(z, R)$ at different times during the dynamics is depicted in Fig. 5.5. After the first two oscillations of $\langle R \rangle$ during the first 150 fs the probability density $\rho(z, R)$ reaches a nearly symmetric distribution in z, which is also evident from the fact that $\langle z \rangle \approx 0$. Although $\langle z \rangle$ attains an equilibrium value in this short period, the $\rho(z, R)$ distribution changes in time by performing almost symmetric motions in z. This is seen by comparing the snapshots of $\rho(z, R)$ at times 180, 210, 240, and 270 fs in Fig. 5.5. After about 120 fs a node develops in the (R) coordinate direction which then remains clearly visible for the rest of the simulation. This indicates that, once internally equilibrated, the (R) coordinate has about one quanta of excitation. Here we would like to emphasize again that the densities in Fig. 5.5 and expectation values in Fig. 5.4 are averaged quantities extracted from the full-dimensional (15-dimensional) propagation of the cluster. The dramatic effect of the strong coupling among vibrational modes becomes now apparent if one compares these dynamics to the kind of periodic and undamped motion that would be expected for a one- or two-dimensional model composed of only the (z) or (z, R) coordinates.

Next, we discuss the dynamics of energy transfer from the (z, R) coordinates to the rest of the system [11]. During the first 50 fs these modes lose about 1,200 cm^{-1} vibrational energy. At the end of the propagation a bit more than 1,500 cm^{-1} of vibrational energy has been redistributed to the rest of the system. Interestingly, the energy transfer is markedly monotonic: the energy transferred from the (z,R) coordinates to the rest of the system is never transferred back during the length of the simulation. Such ultra-fast, irreversible energy transfer is the consequence of strong couplings between the various DOF of the system, which open very effective channels for vibrational energy redistribution. It is interesting to investigate how the vibrational energy redistributes among various vibrational modes. Figure 5.6b shows the vibrational energy in each combined-mode along time. The energy of (α,x,y) highly oscillates with a period that matches the motion of $\langle R \rangle$. These oscillations are not compensated by other modes, which indicates that these energy oscillations are related to an energy transfer from and to the coupling terms, i.e. $\hat{H} - \sum \hat{H}^{(\kappa)}$ (where $\hat{H}^{(\kappa)}$ are separable Hamiltonians of the corresponding subpart of the cluster [11]), of the Hamiltonian. The rocking coordinates (β_A, β_B) also have an oscillatory component, but underlying there is again a monotonic energy increase. The wagging coordinates (γ_A, γ_B) gain energy in a smooth and steady way during the whole dynamics, while the internal coordinates of the water molecules gain energy in a much more abrupt way during the first 50–100 fs. By projection of the total wavefunction onto eigenstates of the $\hat{H}^{(\kappa)}$ Hamiltonians it is possible to learn more about the details of the energy redistribution during the proton transfer process. We find out that the vibrational energy in the (R) coordinate efficiently flows into the orientational DOF of the water monomers via their *gerade* motions [11]. From the internal motions within each water monomer only the bending modes play

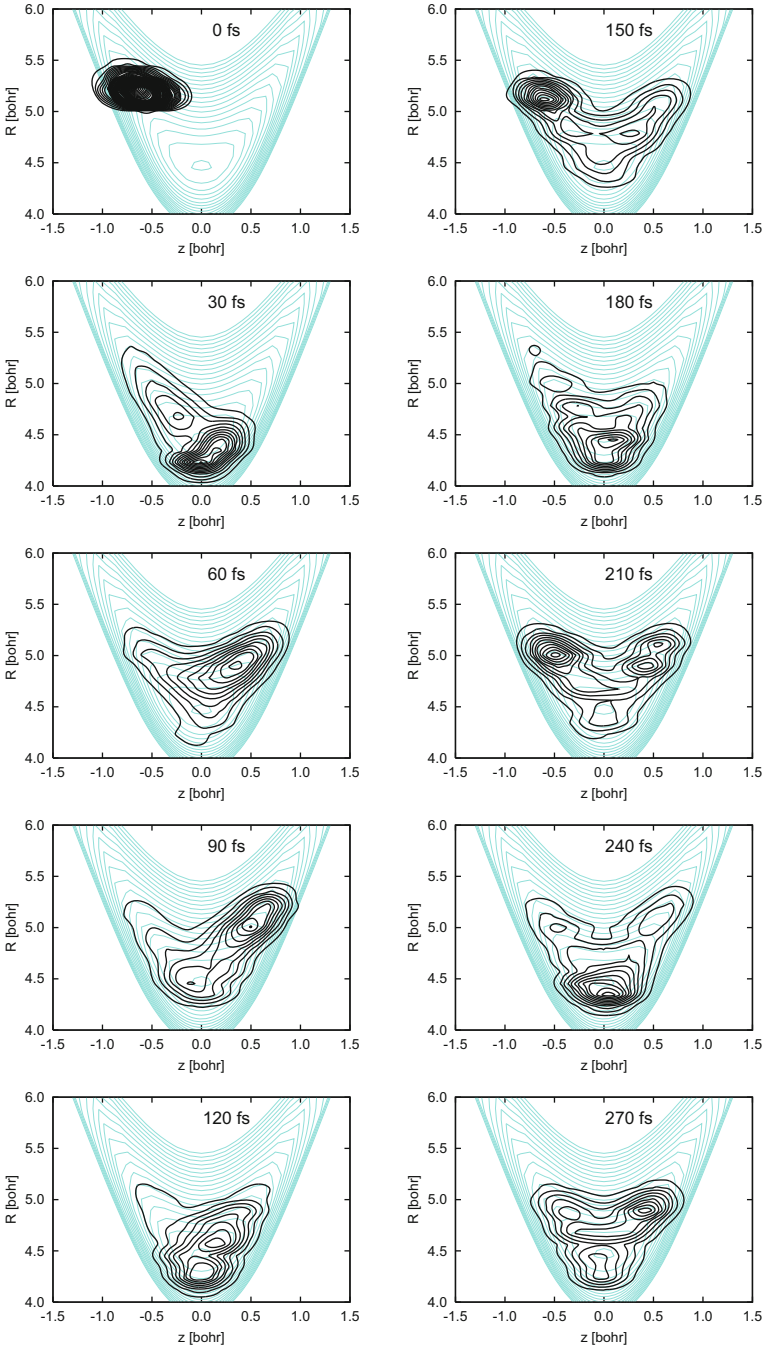

Fig. 5.5 Snapshots of the probability density $\rho(z, R)$ for the simulation with a total vibrational energy of 2,575 cm^{-1} (7.36 kcal/mol) above the zero point energy of the system

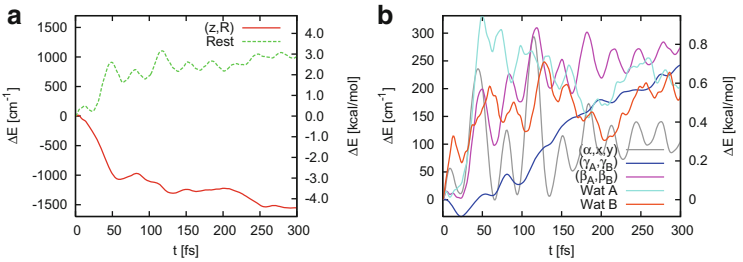

Fig. 5.6 Energy partition among combined modes (for details on the calculation, see [11]). Panel (**a**) presents the change in vibrational energy in the (z, R) coordinates and the sum of the changes of the vibrational energy in all other modes. The initial energy in each mode is used as the energy origin, so that energy changes relative to $t = 0$ are shown. The sum of these two energy changes equals the energy dumped to the coupling terms of the Hamiltonian, and hence differs from zero. Panel (**b**) displays the change in vibrational energy of all combined modes except (z, R) individually

a significant role in the dynamics, while the O–H stretchings remain completely unaffected. All vibrational energy flowing into the internal coordinates of the water molecules is taken by the bending modes, even if the total energy of the system would be enough to appreciably excite the O–H stretchings. The strong coupling between proton transfer and bending modes has been analyzed in the IR spectra discussed previously, where it was shown that it leads to pronounced energy shifts of a few hundred wavenumbers of the corresponding absorption lines. The fact that the energy transfer occurs mostly within the first 100 fs, in which the central proton reaches a distribution close to equilibrium, suggests that there is a very efficient energy flow from the proton-transfer mode to the water bendings, in particular to the *ungerade* bending mode, which has the adequate symmetry for such coupling.

5.4 Tunneling Splitting of Malonaldehyde

Malonaldehyde (propanedial) is studied in many fields of the natural sciences. It is, for instance, an important product of the lipid metabolism and also serves as a biomarker for oxidative stress. In this function it plays an important role in many clinical studies. Also in food processing the presence of malonaldehyde indicates lipid oxidation and hence can be used for quality control purposes. Malonaldehyde is also one of the most prominent molecules that exhibit a keto-enol tautomerization and mainly exists in the enol form, of which in total eight possible but only one stable stereoisomers exist. The stable enol form consists of a horseshoe-shaped backbone of three carbon atoms with conjugated double bonds saturated with hydrogen. To one end of the carbon chain a hydroxyl group is attached while the other end is formed by an aldehyde group. The molecule is planar and the two oxygen atoms are oriented to the same side of the carbon chain (cis-form) such that

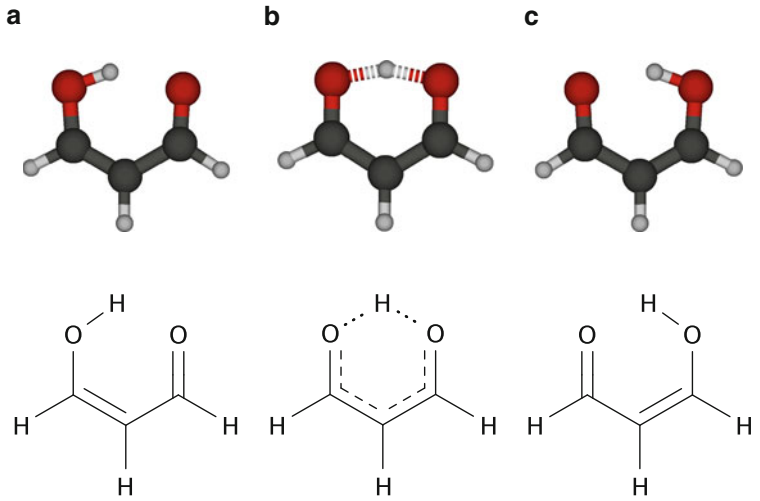

Fig. 5.7 Chemical structure and proton tunneling within the enol form of malonaldehyde. The proton of the hydroxyl group (**a**) is transferred via a transition state (**b**) to the oxygen of the (former) aldehyde group (**c**). During the transfer the single- and double-bonds as well as hydroxyl and aldehyde groups are interchanged resulting in a mirrored variant of the original molecule

they are in close proximity and an intra-molecular hydrogen bond forms between the hydroxyl and the aldehyde group [51].

This particular geometric arrangement gives rise to an interesting effect. The hydrogen of the hydroxyl group can tunnel through a potential barrier towards the other oxygen atom of the aldehyde group, thereby triggering a reorganization of the double bonds—and hence bond lengths—within the carbon backbone. This tunneling process is depicted in Fig. 5.7. The resulting structure corresponds to the perfect mirror image of the original molecule such that the proton transfer process occurs in a symmetric double well potential.

The small size of the molecule and the occurrence of an intra-molecular hydrogen bond alongside with the existence of an intra-molecular tunneling process makes malonaldehyde a model system to study these kinds of processes. In particular the tunneling process has drawn quite some attention within the scientific community and has been described in numerous publications, both experimentally and theoretically. Spectroscopic measurements have already been performed in the late 1970s and early 1980s [52] and first estimates of the ground state tunneling splitting have been given as approximately $21\,\mathrm{cm}^{-1}$ by Wilson and coworkers. Later this value could be refined and the value of the ground state tunneling splitting has been given very accurately as $21.5831383(6)\,\mathrm{cm}^{-1}$ [53, 54].

Higher vibrational eigenstates and tunneling splittings have been measured and reported in a number of papers, most notably already by Wilson et al. [51, 52, 55] and Seliskar and Hoffman [56] in the early 1980s. Most recently Lüttschwager et al. reported [13] spectroscopic measurements and assignments of a larger number of

vibrational states. These measurements allow a detailed comparison of calculated and measured data and hence can be used to construct and test model systems with large amplitude motions such as proton transfer reactions.

From a theoretical point of view an accurate treatment of these kind of processes is a challenging task. For a full quantum treatment, electronic structure calculations to a high level of theory need to be performed which became feasible in the early 2000s [57–60]. The first PES featuring full dimensionality was published by Yagi et al. [61] and a second one by Wang et al. [62]. Following the authors, the latter PES is the most accurate one published to date and in particular features the correct barrier height which the authors state as 4.1 kcal/mol.

However, a numerical reproduction of experimental spectra requires not only a correct PES but also the corresponding wavefunction of the system needs to be accurately represented. The proton motion is strongly coupled to the motion of the backbone atoms and the reorganization processes therein which makes the wavefunction highly correlated. Accurate calculations require a full quantum mechanical treatment of all involved particles. Nevertheless, in the past, a number of approximate methods have been used to overcome this bottleneck. These are, of course, models of reduced dimensionality where some DOF have been neglected [55], reaction surface methods, [63–65], more general methods [60, 62, 66–71], semi-classical approaches [72–77]. However, excitations in other modes than the transfer mode can change the effective barrier height and width for the tunneling process and therefore lead to different splittings. An illustrative example is the vibrational mode describing the distance of the two oxygen atoms. Excitation of this mode facilitates the proton transfer by effectively lowering the barrier and leads to a much larger tunneling splitting than observed for the ground state. The opposite effect can be seen upon excitation of the asymmetric out-of-plane motion of the two oxygen atoms which effectively increases the barrier height as the oxygen atoms move away from the proton.

Recently, a number of full quantum mechanical calculation on malonaldehyde employing MCTDH have been reported [66, 70, 78–80] using the potential energy surface of Yagi et al. [61] as well as for the PES of Wang et al. [62]. Here, the authors report that even the estimation of the ground state energy already reached the limit of today's computational capacities as detailed in the following section, where we present state energies that were obtained using the PES of Wang et al. [62].

5.4.1 Calculated State Energies

The choice of coordinates is of particular importance for the calculations using MCTDH. The length of the A-vector (cf. Eq. (5.2)) is determined by the amount of correlation between the combined modes or particles as discussed in Sect. 5.2. The coordinates should therefore be chosen such that they minimize this correlation in the sense that a simple Hartree ansatz for the wavefunction already yields a good approximation of the wavefunction. Complicated curvilinear coordinates may reduce these "artificial" correlations but, on the other hand, they may complicate the

Table 5.1 Labeling, frequencies in cm^{-1}, type and physical interpretation of the normal mode coordinates obtained at the transition state

Coordinate	Frequency	C_{2v}	Description
$\tilde{q}_1$	346.28	A_2	CH–O—bending
$\tilde{q}_2$	393.37	B_1	CH–C–CH—bending
$\tilde{q}_3$	573.02	B_2	Ring deformation, C–O— bending
$\tilde{q}_4$	608.85	A_1	Ring deformation, O–O— distance
$\tilde{q}_5$	750.20	B_1	C–H—bending
$\tilde{q}_6$	957.92	A_1	Ring deformation, C–O— bending
$\tilde{q}_7$	995.20	B_1	C–C–C—bending
$\tilde{q}_8$	998.18	A_2	C–H—bending
$\tilde{q}_9$	1073.78	A_1	Ring breathing, C–C— stretching
$\tilde{q}_{10}$	1101.40	B_2	C–H—bending
$\tilde{q}_{11}$	1321.98	B_1	Out-of-plane motion of Transfer-proton
$\tilde{q}_{12}$	1340.42	B_2	C–H—bending, C–O stretching
$\tilde{q}_{13}$	1405.12	A_1	C–H—bending, C–O stretching
$\tilde{q}_{14}$	1472.48	B_2	C–H—bending, C–O stretching
$\tilde{q}_{15}$	1617.71	A_1	C–O—stretching
$\tilde{q}_{16}$	1620.12	B_2	C–C–C—stretching
$\tilde{q}_{17}$	1893.66	A_1	In-plane motion of Transfer-proton
$\tilde{q}_{18}$	3126.86	A_1	C–H—stretching
$\tilde{q}_{19}$	3141.39	B_2	C–H—stretching
$\tilde{q}_{20}$	3227.45	A_1	C–H—stretching
$\tilde{q}_{21}$	$i \times 1253.02$	B_2	Proton transfer

calculation of expressions for the kinetic energy operator to such an extent that they become hardly feasible. Often one needs to find a compromise between these two.

For the calculations on malonaldehyde we used a set of mass- and frequency scaled normal mode coordinates $\{\tilde{q}_i\}$ obtained at the transition state depicted in Fig. 5.7b. The coordinate labeling, normal mode frequencies and physical description are outlined in Table 5.1. The coordinates were subsequently modified [78] to minimize the correlation induced by the reorganization of the double bonds. The shifts of the inter atomic distances only depend on the position of the proton along the transfer coordinate $\tilde{q}_{21}$. They can be compensated by the modified coordinates $\{q_i\}$ obtained by the transformation

$$\begin{aligned} q_i &= \tilde{q}_i - F_i(\tilde{q}_{21}), \quad i = 1 \ldots 20, \\ q_{21} &= \tilde{q}_{21}. \end{aligned} \tag{5.13}$$

The F_i describe the displacements and were determined by minimization of the potential and subsequent fitting to polynomials such that the kinetic energy operator can still be obtained in analytic form as given in [78]. Note that in the following global rotation and vibration–rotation interaction terms have been neglected and a non-rotating system is assumed. In this case the vibration–rotation interaction

Table 5.2 Mode combinations for MCTDH calculations

Logical coord.	Physical coords.
Q_1	q_1, q_2, q_{18}
Q_2	q_3, q_{12}, q_{15}
Q_3	q_4, q_{16}, q_{17}
Q_4	q_5, q_{20}, q_6, q_9
Q_5	q_7, q_8, q_{10}, q_{19}
Q_6	$q_{13}, q_{14}, q_{11}, q_{21}$

contributes approximately $2.4\,\mathrm{cm}^{-1}$ to the vibrational ground state energy and increases the tunneling splitting about $0.2\,\mathrm{cm}^{-1}$ [78].

Details about the kinetic and potential operators can be found in [78] and [79]. The latter in particular contains a detailed description of the CE technique Eq. (5.10) used to model the PES. Here, we just note that other than in the previous section, the reference geometry always included the transfer coordinate and that relevant clusters have been identified using a Metropolis algorithm prior to their actual sampling on the primitive grid since a brute force calculation of all clusters was not possible.

For the representation of the wavefunction in MCTDH form, the 21 physical coordinates have been combined into six logical ones, where each mode contains three to four physical coordinates. The mode combination scheme is outlined in Table 5.2. It was chosen such that, where possible, physical coordinates that are strongly correlated are grouped together. This has the advantage that correlations between those modes are already represented on the SPF level and do not enter the A-vector. (Note that when computing the CE, Eq. (5.10), we have used less strongly combined particles. See [79].)

Once having defined the computational setup, the ground state energy was estimated using an extrapolation scheme [78] based on the variational character of the MCTDH algorithm. The extrapolation scheme exploits the fact that adding SPF always leads to lower state energies. Provided an (in terms of number of SPF) almost converged wavefunction this energy drop is mode-local, i.e., it does (almost) not depend on changes in the number of SPF in other modes, so that the sum of energy drops one obtains by independently increasing the number of SPF in all modes, one by one, is an upper estimate for the energy lowering one would obtain if one increases the number of SPF in all modes simultaneously.

The extrapolation scheme is outlined in Table 5.3. Starting from a reference calculation the numbers of SPF are doubled for each mode independently and the energy drops are summed to obtain the true ground state energy and tunneling splitting. Since the energy drop for modes 3 and 6 where larger then for all other modes, we also performed an additional extrapolation by increasing the number of SPF in these two modes simultaneously.

After careful convergence checks the zero point energy was obtained as $14{,}667.3\,\mathrm{cm}^{-1}$ and the ground state tunneling splitting as $23.2\,\mathrm{cm}^{-1}$. Additional calculations confirmed these results with an error of less than $2\,\mathrm{cm}^{-1}$ for the ground state and less than $0.1\,\mathrm{cm}^{-1}$ for the tunneling splitting. Concerning the dynamical calculation, the error introduced by the CE of the potential is difficult to estimate.

Table 5.3 Extrapolation of the state energies

No. of SPF for										
Q_1	Q_2	Q_3	Q_4	Q_5	Q_6	Energy (+)	ΔE	Energy (−)	ΔE	Splitting
10	7	12	10	10	20	14672.784	(ref)	14696.587	(ref)	23.803
20	7	12	10	10	20	14672.273	−0.511	14696.034	−0.553	23.761
10	14	12	10	10	20	14672.209	−0.575	14695.985	−0.602	23.776
10	7	24	10	10	20	14671.321	−1.463	14694.722	−1.865	23.401
10	7	12	20	10	20	14672.115	−0.669	14695.847	−0.740	23.732
10	7	12	10	20	20	14672.144	−0.640	14695.998	−0.589	23.854
10	7	12	10	10	40	14671.518	−1.266	14695.158	−1.429	23.640
Sum							−5.124		−5.778	
Extrapolated energy							14667.660		14690.809	23.149
10	7	24	10	10	40	14669.709	−3.075	14692.999	−3.588	23.290
Sum							−5.470		−6.072	
Extrapolated energy							14667.314		14690.515	23.201

(+) and (−) denote the symmetric and asymmetric ground state, respectively, and ΔE denotes the difference to the reference state.The last three rows outline the extrapolation with the number of SPF increased in modes 3 and 6 simultaneously. We consider the values given in the last line of the table as our best results for ground state energy. All energies are in cm^{-1}

However, we have performed CEs using different mode combinations and different selections of clusters (not discussed here) and obtained very similar results. Upon adding the estimated contributions of the vibration–rotation coupling terms (2.4 and 0.2 cm^{-1}) [78] a zero point energy of 14,670 cm^{-1} and a tunneling splitting of 23.4 cm^{-1} were obtained for the PES of Wang et al. [62]. These results are in very good agreement with the splitting of 23.8 cm^{-1} obtained by Hammer and Manthe [78] who used a multi-layer variant of MCTDH together with the correlation DVR scheme. However, the tunneling splitting differs somewhat from the experimental value of 21.6 cm^{-1}. The zero point energy calculated by us is about 8 cm^{-1} below the one obtained by Hammer and Manthe [78]. Again, this could be due to the CE, but we think the lower ground state energy reflects the fact that the present calculations are better converged.

Excited states and tunneling pairs were obtained using the block improved relaxation algorithm. The calculations were performed in blocks of four using the same computational setup as before but with a larger set of SPFs than for the reference state in Table 5.3 (Q_1:18, Q_2:10, Q_3:16, Q_4:11, Q_5:11, Q_6:22) and the blocks were chosen such that they overlap by one state. Calculated state energies from this work in comparison with values obtained in [80] and experimental energies [13] as well as tunneling splittings are outlined in Table 5.4 together with their assignments. Note that within the calculated energies and splittings the rotation–vibration interaction has been neglected. Since the wavefunctions become more and more structured the higher the state energy, it is not surprising that their accuracy decreases as emerging correlations cannot be completely covered by the A-vector anymore. However, the structure of the corresponding tunneling pairs is

Table 5.4 Vibrational state energies relative to the ground state energy and tunneling splittings, both, calculated (this work and from [80]) and measured (from [13]), as well as their assignment

State energies			Tunneling splittings			
This work	Ref. [80]	Experiment	This work	Ref. [80]	Experiment	Assignment
0	0	0	23.5	23.5	21.6	Ground state
254	259	241	64.8	64.0	57	q_4
271	325	273	17.3	6.7	$6 \cdots 9$	q_1
382	425	390	22.3	16.3	15	q_2
507	–	–	–	–	–	$q_4 \times q_4$
526	566	512	16.8	18.8	15	q_3
527	–	–	53.3	–	–	$q_1 \times q_4$

The state energies refer to the lower one of the tunneling pairs, which is usually the gerade state, except for the q_3 state where the ungerade state has a lower energy. All energies in cm^{-1}

very similar such that this error cancels to quite some extent for the splittings. We therefore consider the splittings reported in Table 5.4 as converged while the state energies are likely to be slightly too large.

The calculated state energies and splittings we obtained as outlined in Table 5.4 are in reasonable agreement with the experiment. This is especially true for the state energies for which we obtain a difference to the experimental values of at most $14\,\mathrm{cm}^{-1}$. However, it is interesting to see that for states q_3 and q_4 the energies are larger than the experimental values, while this is not the case for the q_1 and q_2 fundamentals. Here the experimental value are larger.

For the two lowest eigenstates we obtain very similar splittings as Hammer and Manthe [80], which are, however, somewhat larger than the experimental values. For the two following splittings (q_1 and q_2) Hammer and Manthe observe excellent agreement with the experiment while overestimating the absolute state energies by 35–50 cm^{-1}, presumably because of a lag of full convergence of the wavefunction. In contrast, we observe good agreement of our calculated state energies with the experiment while obtaining larger splittings than Hammer and Manthe. This is especially true for the fundamental of q_1 for which we obtain a splitting of about $17\,\mathrm{cm}^{-1}$, while the experimental value lies between 6 and $9\,\mathrm{cm}^{-1}$. The situation changes for the splitting of q_3. Here, the result of Hammer and Manthe is approximately $4\,\mathrm{cm}^{-1}$ larger than the experimental one, while our result lies $2\,\mathrm{cm}^{-1}$ above the experiment.

In addition to the fundamentals we also show two doubly excited states in Table 5.4. The first double excitation is observed in the mode q_4 (O–O—distance) and the second one as a combination of an excitation within mode q_1 and q_4, which were both obtained among the fundamentals within the block improved relaxation scheme. Note that the sum of the fundamental frequencies yields almost exactly the frequencies of the double excitations, indicating that the anharmonic coupling between these states is small.

The comparison of the calculated values both, of Hammer and Manthe [80] and ourselves as well as the comparison with the experiment is quite interesting. While

our results for the absolute state energies are in very good, the tunneling splitting are in reasonable, but not excellent, agreement with the experiment, the situation is vice versa for the results of Hammer and Manthe. Their splittings are indeed in excellent agreement with the experiment; however, the state energies are consistently too large as discussed above. At this point the origin of these differences remains unclear and further investigations are needed. Hammer and Manthe are using the CDVR scheme [15] and hence do not need to represent the PES in product form. The main source of inaccuracies in their work is most likely due to a not completely converged wavefunction and the errors introduced by the CDVR scheme (which are difficult to estimate). On the other hand, our wavefunction is better converged (although still not completely) and the main source of error may be introduced by the CE. As mentioned above, however, test calculations with different mode combinations and different selections of clusters lead to very similar results as outlined above. This makes us confident that our PES representation is reliable. Moreover, errors in the PES representation should largely cancel when inspecting tunneling splittings. Considering the results outlined above and their discussion, again, shows that the treatment of quantum dynamics in high dimensions is still a formidable task.

5.5 Summary

The protonated water dimer (or Zundel cation) constitutes an anharmonic and vibrationally coupled cluster featuring a complex IR spectrum. This system has been the subject of numerous experimental and theoretical investigations owing to its challenging nature and its importance as a fundamental building block in acidic chemistry. Here we presented a full-dimensional (15D) quantum mechanical calculation and assignment of the IR spectrum of the cluster using the MCTDH method. Vibrational spectroscopy inherently probes quantized vibrational excitations and a quantum mechanical treatment is critical to obtain the right absorption band positions and intensities. For such a strongly coupled and anharmonic system the description has to be full-dimensional and based on curvilinear coordinates, which render the correlation between modes tractable if chosen to represent physically meaningful bond lengths and angles of the system.

The IR spectrum of various isotopomers was discussed. Isotopomers of a system have identical PES but their IR spectra present shifts with respect to each other due to the different masses of some atoms. In the Zundel cation, we showed how different isotopomers have completely different spectra, which is a consequence of the complexity of coupling mechanisms and resonances shaping the IR absorption profile. The proton transfer dynamics of the Zundel cation was discussed as well and related to the IR signatures of the system.

Malonaldehyde with its intra-molecular proton transfer is another important model system to study these kind of processes and is hence a well-studied molecule. Experimental IR and Raman spectra have been recorded over the last decades and allow a detailed evaluation of full-dimensional (21-D) model calculations which only became possible in the recent years. In the present contribution we have

presented full-dimensional calculations on the ground state energy and the lowest excited states. The calculations were performed using the MCTDH algorithm and the most accurate PES published to date [62]. Similarly as done in the Zundel studies, the PES was brought to a numerically useful form by adopting a CE. This re-fitting of the potential is likely the largest source of errors in our calculations.

With this setup and after careful convergence checks a ground state energy of 14,670 cm^{-1} and a tunneling splitting of 23.4 cm^{-1} have been obtained. Also, the first four fundamentals and their tunneling splittings as well as two double excitations were calculated and compared to experimental values as well as numerical results of Hammer and Manthe [80]. Reasonable agreement between calculated and experimental results was found. Slightly different results obtained with different, but related, numerical methods still show that large systems like malonaldehyde are a challenging task for accurate calculations.

References

1. Balint-Kurti GG, Dixon RN, Marston CC (1990) Time-dependent quantum dynamics of molecular photofragmentation processes. J Chem Soc Faraday Trans 86:1741
2. Meyer H-D, Manthe U, Cederbaum LS (1990) The multi-configurational time-dependent Hartree approach. Chem Phys Lett 165:73–78
3. Beck MH, Jäckle A, Worth GA, Meyer H-D (2000) The multi-configuration time-dependent Hartree (MCTDH) method: a highly efficient algorithm for propagating wave packets. Phys Rep 324:1–105
4. Meyer H-D, Worth GA (2003) Quantum molecular dynamics: propagating wavepackets and density operators using the multiconfiguration time-dependent Hartree (MCTDH) method. Theor Chem Acc 109:251–267
5. Meyer H-D (2012) Studying molecular quantum dynamics with the multiconfiguration time-dependent Hartree method. Wiley Interdiscip Rev Comput Mol Sci 2:351
6. Worth GA, Meyer H-D, Cederbaum LS (1996) The effect of a model environment on the S_2 absorption spectrum of pyrazine: a wavepacket study treating all 24 vibrational modes. J Chem Phys 105:4412
7. Raab A, Worth G, Meyer H-D, Cederbaum LS (1999) Molecular dynamics of pyrazine after excitation to the S_2 electronic state using a realistic 24-mode model Hamiltonian. J Chem Phys 110:936–946
8. Vendrell O, Gatti F, Meyer H-D (2007) Dynamics and infrared spectroscopy of the protonated water dimer. Angew Chem Int Ed 46:6918–6921
9. Vendrell O, Gatti F, Lauvergnat D, Meyer H-D (2007) Full dimensional (15D) quantum-dynamical simulation of the protonated water dimer I: Hamiltonian setup and analysis of the ground vibrational state. J Chem Phys 127:184302
10. Vendrell O, Gatti F, Meyer H-D (2007) Full dimensional (15D) quantum-dynamical simulation of the protonated water dimer II: infrared spectrum and vibrational dynamics. J Chem Phys 127:184303
11. Vendrell O, Meyer H-D (2008) A proton between two waters: insight from full-dimensional quantum-dynamics simulations of the $[H_2O–H–OH_2]^+$ cluster. Phys Chem Chem Phys 10:4692–4703
12. Vendrell O, Gatti F, Meyer H-D (2009) Strong isotope effects in the infrared spectrum of the zundel cation. Angew Chem Int Ed 48:352–355
13. Lüttschwager NOB, Wassermann TN, Cousan S, Suhm MA (2013) Vibrational tuning of the hydrogen transfer in malonaldehyde: a combined FTIR and Raman jet study. Mol Phys 111:2211

14. Born M, Oppenheimer R (1927) Zur Quantentheorie der Molekeln. Ann Phys 84:457
15. Manthe U (1996) A time-dependent discrete variable representation for (multi-configuration) Hartree methods. J Chem Phys 105:6989
16. Jäckle A, Meyer H-D (1996) Product representation of potential energy surfaces. J Chem Phys 104:7974
17. Jäckle A, Meyer H-D (1998) Product representation of potential energy surfaces II. J Chem Phys 109:3772
18. Meyer H-D, Gatti F, Worth GA (eds) (2009) Multidimensional quantum dynamics: MCTDH theory and applications. Wiley-VCH, Weinheim
19. Gatti F, Meyer H-D (2004) Intramolecular vibrational energy redistribution in toluene: a nine-dimensional quantum mechanical study using the MCTDH algorithm. Chem Phys 304:3–15
20. Peláez D, Meyer H-D (2013) The multigrid POTFIT (MGPF) method: grid representations of potentials for quantum dynamics of large systems. J Chem Phys 138:014108
21. Carter S, Culik SJ, Bowman JM (1997) Vibrational self-consistent field method for many-mode systems: a new approach and application to the vibrations of CO adsorbed on Cu(100). J Chem Phys 107:10458
22. Bowman JM, Carter S, Huang X (2003) MULTIMODE: a code to calculate rovibrational energies of polyatomic molecules. Int Rev Phys Chem 22:533–549
23. Rabitz H, Alis OF (1999) General foundations of high-dimensional model representations. J Math Chem 25:197
24. Alis OF, Rabitz H (2001) Efficient implementation of high dimensional model representations. J Math Chem 29:127–142
25. Li GY, Hu JS, Wang SW, Georgopoulos PG, Schoendorf J, Rabitz H (2006) Random sampling-high dimensional model representation (RS-HDMR) and orthogonality of its different order component functions. J Phys Chem A 110:2474–2485
26. Manzhos S, Carrington T (2006) A random-sampling high dimensional model representation neural network for building potential energy surfaces. J Chem Phys 125:084109
27. Headrick JM, Diken EG, Walters RS, Hammer NI, Christie RA, Cui J, Myshakin EM, Duncan MA, Johnson MA, Jordan KD (2005) Spectral signatures of hydrated proton vibrations in water clusters. Science 308(5729):1765–1769
28. Asmis KR, Pivonka NL, Santambrogio G, Brummer M, Kaposta C, Neumark DM, Woste L (2003) Gas-phase infrared spectrum of the protonated water dimer. Science 299:1375–1377
29. Fridgen TD, McMahon TB, MacAleese L, Lemaire J, Maitre P (2004) Infrared spectrum of the protonated water dimer in the gas phase. J Phys Chem A 108:9008–9010
30. Headrick JM, Bopp JC, Johnson MA (2004) Predissociation spectroscopy of the argon-solvated $H_5O_2^+$ "Zundel" cation in the 1000–1900 cm^{-1} region. J Chem Phys 121:11523–11526
31. Hammer NI, Diken EG, Roscioli JR, Johnson MA, Myshakin EM, Jordan KD, McCoy AB, Bowman JM, Carter S (2005) The vibrational predissociation spectra of the $H_5O_2^+ \cdot RG_n$ (RG = Ar,Ne) clusters: correlation of solvent perturbations in the free OH and shared proton transitions of the Zundel ion. J Chem Phys 122:244301
32. McCunn LR, Roscioli JR, Johnson MA, McCoy AB (2008) An H/D isotopic substitution study of the $H_5O_2^+ \cdot$Ar vibrational predissociation spectra: exploring the putative role of fermi resonances in the bridging proton fundamentals. J Phys Chem B 112:321–327
33. Dai J, Bacic Z, Huang XC, Carter S, Bowman JM (2003) A theoretical study of vibrational mode coupling in $H_5O_2^+$. J Chem Phys 119:6571–6580
34. Huang X, Braams BJ, Bowman JM (2005) *Ab initio* potential energy and dipole moment surfaces for $H_5O_2^+$. J Chem Phys 122:044308
35. McCoy AB, Huang X, Carter S, Landeweer MY, Bowman JM (2005) Full-dimensional vibrational calculations for $H_5O_2^+$ using an *Ab initio* potential energy surface. J Chem Phys 122:061101
36. Sauer J, Dobler J (2005) Gas-phase infrared spectrum of the protonated water dimer: molecular dynamics simulation and accuracy of the potential energy surface. Chem Phys Chem 6:1706–1710

37. Kaledin M, Kaledin AL, Bowman JM (2006) Vibrational analysis of the H5O2+ infrared spectrum using molecular and driven molecular dynamics. J Phys Chem A 110:2933–2939
38. Kulig W, Agmon N (2013) A “clusters-in-liquid" method for calculating infrared spectra identifies the proton-transfer mode in acidic aqueous solutions. Nat Chem 5:29–35
39. Vendrell O, Brill M, Gatti F, Lauvergnat D, Meyer H-D (2009) Full dimensional (15D) quantum-dynamical simulation of the protonated water dimer III: mixed Jacobi-valence parametrization and benchmark results for the zero-point energy, vibrationally excited states and infrared spectrum. J Chem Phys 130:234305. See supplementary material, EPAPS document E-JCPSA6-130-023924, which can be downloaded from: ftp://ftp.aip.org/epaps/journ_chem_phys/E-JCPSA6-130-023924/
40. Vendrell O, Gatti F, Meyer H-D (2009) Full dimensional (15D) quantum-dynamical simulation of the protonated water dimer IV: isotope effects in the infrared spectra of $D(D_2O)_2^+$, $H(D_2O)_2^+$ and $D(H_2O)_2^+$ isotopologues. J Chem Phys 131:034308
41. Xantheas SS (2009) Computational chemistry dances with hydrogen cations. Nature 457:673–674
42. von Grotthus CJD (1806) Memoire sur la decomposition de l’eau et des corps qu’elle tien en dissolution a l’aide de l’électricité galvanique. Ann Chim 58:54–74
43. Zundel G, Metzger H (1968) Z Physik Chem 58:225
44. Wicke E, Eigen M, Ackermann T (1954) Über den Zustand des Protons (Hydroniumions) in wässriger Lösung. Z Phys Chem 1:340
45. Marx D, Tuckerman ME, Hutter J, Parrinello M (1999) The nature of the hydrated excess proton in water. Nature 397:601–604
46. Agmon N (1999) Proton solvation and proton mobility. Isr J Chem 39:493–502
47. Marx D (2006) Proton transfer 200 years after von grotthuss: insights from ab initio simulations. Chem Phys Chem-Eur J 7:1848–1870
48. Schmitt UW, Voth GA (1999) The computer simulation of proton transfer in water. J Chem Phys 111:9361–9381
49. Chandra A, Tuckerman ME, Marx D (2007) Connecting solvation shell structure to proton transport kinetics in hydrogen-bonded networks via population correlation functions. Phys Rev Lett 99(14):145901
50. Woutersen S, Bakker HJ (2006) Ultrafast vibrational and structural dynamics of the proton in liquid water. Phys Rev Lett 96(13):138305
51. Rowe WF, Duerst RW, Wilson EB (1975) The intramolecular hydrogen bond in malonaldehyde. J Am Chem Soc 98:4021
52. Baughcum SL, Duerst RW, Rowe WF, Smith Z, Wilson EB (1981) Microwave spectroscopic study of malonaldehyde. 2. Structure, dipole moment, and tunneling. J Am Chem Soc 103:6296
53. Firth DW, Beyer K, Dvorak MA, Reeve SW, Grushow A, Leopold KR (1991) Tunable far-infrared spectroscopy of malonaldehyde. J Chem Phys 94:1812
54. Baba T, Tanaka T, Morino I, Yamada KMT, Tanaka K (1999) Detection of the tunneling-rotation transitions of malonaldehyde in the submillimeter-wave region. J Chem Phys 110:4131
55. Baughcum SL, Smith Z, Wilson EB, Duerst RW (1984) Microwave spectroscopic study of malonaldehyde. 3. Vibration-rotation interaction and one-dimensional model for proton tunneling. J Am Chem Soc 106:2260
56. Seliskar CJ, Hoffman RE (1982) On the infrared spectrum of malonaldehyde, a tunneling hydrogen-bonded molecule. J Mol Struct (Theochem) 96:146
57. Tautermann CS, Voegele AF, Loerting T, Liedl KL (2002) The optimal tunneling path for the proton transfer in malonaldehyde. J Chem Phys 117:1962
58. Tautermann CS, Voegele AF, Loerting T, Liedl KL (2002) An accurate semiclassical method to predict ground-state tunneling splittings. J Chem Phys 117:1967
59. Mil’nikov GV, Yagi K, Taketsugu T, Nakamura H, Hirao K (2003) Tunneling splitting in polyatomic molecules: application to malonaldehyde. J Chem Phys 119:10
60. Mil’nikov GV, Yagi K, Taketsugu T, Nakamura H, Hirao K (2004) Simple and accurate method to evaluate tunneling splitting in polyatomic molecules. J Chem Phys 120:5036

61. Yagi K, Taketsugu T, Hirao K (2001) Generation of full-dimensional potential energy surface of intramolecular hydrogen atom transfer in malonaldehyde and tunneling dynamics. J Chem Phys 115:10647
62. Wang Y, Braams BJ, Bowman JM, Carter S, Tew DP (2008) Full-dimensional quantum calculations of ground-state tunneling splitting of malonaldehyde using an accurate ab initio potential energy surface. J Chem Phys 128(22):224314
63. Carrington T Jr, Miller WH (1986) J Chem Phys 84:4364
64. Shida N, Barbara PF, Almöf JE (1989) J Chem Phys 91:4061
65. Tew DP, Handy NC, Carter S (2003) J Chem Phys 125:084313
66. Coutinho-Neto MD, Viel A, Manthe U (2004) The ground state tunneling splitting of malonaldehyde: accurate full dimensional quantum dynamics calculations. J Chem Phys 121:9207–9210
67. Viel A, Coutinho-Neto MD, Manthe U (2007) The ground state tunneling splitting and the zero point energy of malonaldehyde: a quantum Monte Carlo determination. J Chem Phys 126(2):024308
68. Hazra A, Skone JH, Hammes-Schiffer S (2009) Combining the nuclear-electronic orbital approach with vibronic coupling theory: calculation of the tunneling splitting for malonaldehyde. J Chem Phys 130:054108
69. Wang Y, Bowman JM (2008) One-dimensional tunneling calculations in the imaginary-frequency, rectilinear saddle-point normal mode. J Chem Phys 129:121103
70. Hammer T, Coutinho-Neto MD, Viel A, Manthe U (2009) J Chem Phys 131:224109
71. Yang Y, Meuwly M (2010) A generalized reactive force field for nonlinear hydrogen bonds: hydrogen dynamics and transfer in malonaldehyde. J Chem Phys 133:064503
72. Makri N, Miller WH (1989) J Chem Phys 91:4026
73. Smedarchina Z, Siebrand W, Zgierski MZ (1995) J Chem Phys 103:5326
74. Sewell TD, Guo Y, Thompson DL (1995) Semiclassical calculations of tunneling splitting in malonaldehyde. J Chem Phys 103:8557
75. Ben-Nun M, Martínez TJ (1999) J Phys Chem A 103:6055
76. Benderskii VA, Vetoshkin EV, Irgibaeva IS, Trommsdroff HP (2000) Chem Phys 262:393
77. Tuckermann ME, Marx D (2010) Heavy-atom skeleton quantization and proton tunneling in intermediate-barrier hydrogen bonds. Phys Rev Lett 86:4946
78. Hammer T, Manthe U (2011) Intramolecular proton transfer in malonaldehyde: accurate multilayer multi-configurational time-dependent Hartree calculations. J Chem Phys 134:224305
79. Schröder M, Gatti F, Meyer H-D (2011) Theoretical studies of the tunneling splitting of malonaldehyde using the multiconfiguration time-dependent Hartree approach. J Chem Phys 134:234307
80. Hammer T, Manthe U (2012) Iterative diagonalization in the state-averaged multi-configurational time-dependent Hartree approach: excited state tunneling splitting in malonaldehyde. J Chem Phys 136:054105

Vibronic Coupling Effects in Spectroscopy and Non-adiabatic Transitions in Molecular Photodynamics

6

Horst Köppel

Abstract

A brief historic and systematic survey is given of our efforts to elucidate important features of the nuclear motion on interacting potential energy surfaces (PESs). Starting with our early work in 1977, a variety of small to medium-sized polyatomic molecules have been treated by quantum-dynamical methods. As the key topological feature signalling the effects in question, conical intersections of PESs have been established. The associated strong nonadiabatic coupling effects manifest themselves as diffuse (at low resolution) or irregular (at high resolution) spectral structures upon electronic transitions. The concomitant fs electronic population decay governs the photophysical and photochemical properties of these systems. Representative examples with 2–5 strongly coupled electronic states are given, and the quantum nature of the phenomena is emphasized.

6.1 General Introduction

In this contribution our quantum-dynamical treatment of nuclear motion on coupled potential energy surfaces (PESs) is surveyed. The present general introduction deals with the early history of the field (i.e. from 1977 to 1991), followed by a more systematic classification of types of surface intersections and a phenomenology of the ensuing nuclear dynamics.

H. Köppel (✉)
Theoretical Chemistry, Im Neuenheimer Feld 229, University of Heidelberg, 69120 Heidelberg, Germany
e-mail: Horst.Koeppel@pci.uni-heidelberg.de

F. Gatti (ed.), *Molecular Quantum Dynamics*, Physical Chemistry in Action,
DOI 10.1007/978-3-642-45290-1_6, © Springer-Verlag Berlin Heidelberg 2014

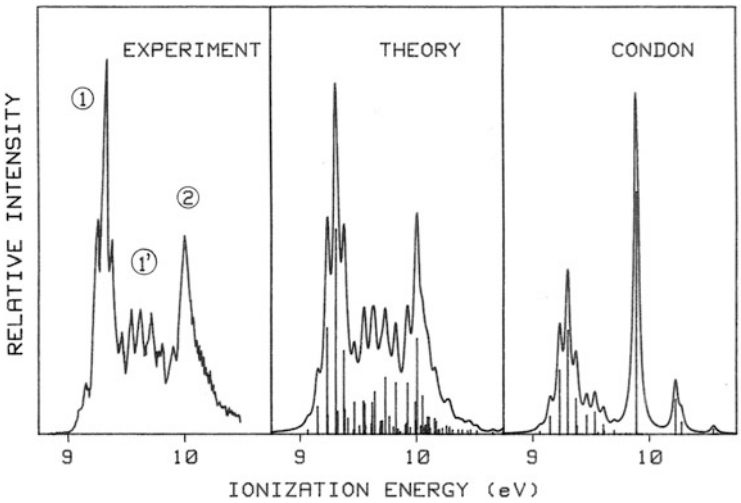

Fig. 6.1 Comparison of the experimental photoelectron spectrum of butatriene with the "full" theoretical result and the one obtained in the Condon approximation with uncoupled PESs (*from left to right*). The band 1′ in the *left* panel was termed "mystery band"

6.1.1 Outline of Early History

In 1974 the group of E. Heilbronner in Basel had measured the photoelectron spectrum of the butatriene molecule, which displays a peculiar shape [1]. In the ionization energy range from 9 to 10 eV they observed three electronic bands where only two states of the radical cation and, hence, only two bands are expected. Moreover, the bands show an asymmetrically broadened profile and a rather complex structure (see Fig. 6.1, left panel). The upper and lower energy bands 1 and 2 could be correlated with electronic states of the radical cation, whereas the intensity of the central band 1′ far exceeds any conceivable mechanism for a corresponding electronic feature of the system. Thus it was also termed "mystery band". In subsequent theoretical work it could be established that the "mystery" band represents a vibronic effect [2]. By setting up a suitable model Hamiltonian for coupling to and through vibrational modes, and based on ab initio values for the system parameters, the band system could be very satisfactorily reproduced, see the central panel in Fig. 6.1. It proved crucial that the model not only describes vibrational excitation (coupling *to* modes) but also allowed for interaction between the electronic states (coupling *through* modes). This is made apparent by the right panel where this latter interaction has been suppressed in the calculation and the mystery band is absent [3]. Apparently the interaction leads to a redistribution and build-up of spectral intensity in the centre and high-energy part of the spectrum, which is vital for the irregularities and the appearance of the mystery band of butatriene.

In later work it was realized that the key feature of the underlying PESs is a conical intersection (CoIn) [3, 4]. This can be understood from Fig. 6.2 which

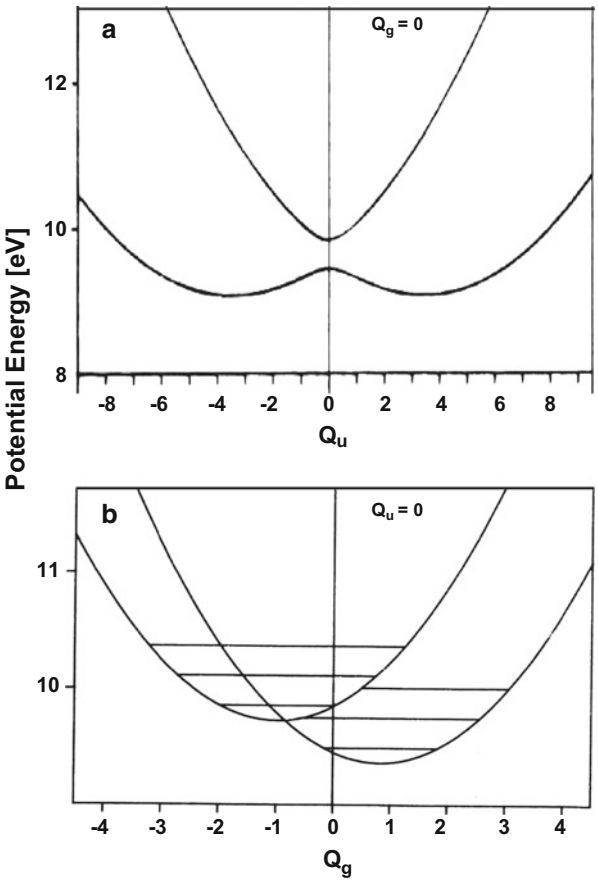

Fig. 6.2 Cuts through the two-dimensional model PES of the butatriene radical cation underlying the theoretical treatment of Fig. 6.1. One coordinate (Q_g or Q_u) is varied as indicated in the panels, and the other fixed at zero.

represents cuts (cross sections) through the ionic PESs along the two nuclear coordinates considered in the model. These feature shifts in opposite directions along the totally symmetric mode Q_g (C = C stretching mode) which leads to a crossing of the PES near the minimum of the upper state (the zeros of coordinate and energy scale denote the neutral ground state equilibrium geometry and energy). For displacements along the non-symmetric coordinate Q_u a repulsion of the PES occurs due to the associated symmetry lowering, which enables an interaction between the states to take place (for $Q_u = 0$ the electronic states have different symmetry). The repulsion leads to a double minimum PES of the ionic ground state, which in turn is responsible for the low-energy progression in the spectra (between 9 and 9.5 eV). The situation is summarized in the perspective drawing of Fig. 6.3 which illustrates the double minimum of the lower adiabatic PES as well as the point of degeneracy

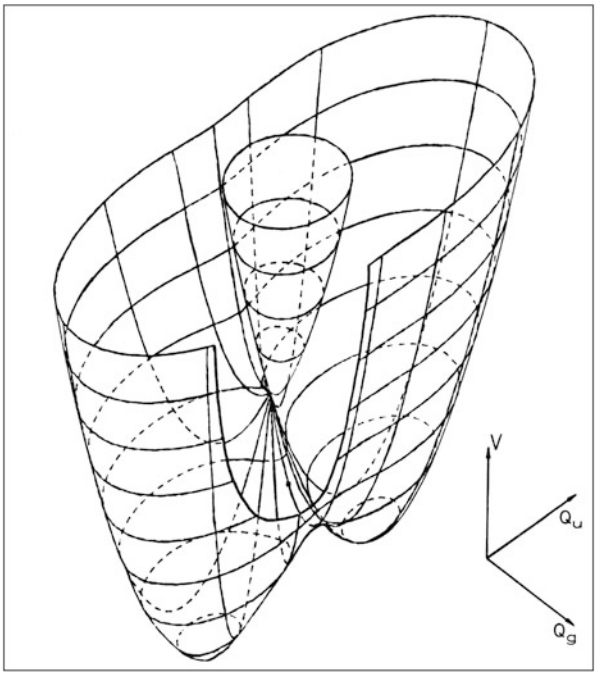

Fig. 6.3 Perspective drawing of the two-dimensional model PES of the butatriene radical cation

between upper and lower adiabatic PES in the centre of the figure. This degeneracy is lifted in first order of the nuclear displacements and is thus of conical shape. From simple arguments the nonadiabatic coupling elements are seen to diverge at these points, causing a severe failure of the Born–Oppenheimer approximation for energies at and above that of the intersection [3]. This is just borne out by the comparison of the spectra in the central and right panels in Fig. 6.1.

What first seemed little more than a theoretical curiosity, of interest only to a few experts, proved later to be of broad relevance, and with ramifications in many different areas of physical chemistry and chemical physics. Nonadiabatic processes following molecular photoexcitation have received broad attention from experiment and theory alike, and CoIns are nowadays recognized as key topological features of molecular PES signalling these effects [5–10]. The above example opened the door to a quantum-dynamical treatment of these phenomena by the Heidelberg group, which has been pursued and widened ever since. In the present contribution I attempt to give a lucid, historic, and also pedagogic overview over the field as it evolved since around 1980, with an emphasis on our line of work. This also fits into the scope of this book, because the quantum nature of the dynamics at CoIns has been a focus of our work over all the years. While nuclear motion is sometimes treated classically or semiclassically in the literature, the consideration of quantum effects is important in at least three different situations, regarding zero point energy effects, tunneling

processes, and coupled electronic PESs. General reasoning in this direction has been presented in the introduction to this book and need not be repeated here. Suffice it to say that a semiclassical treatment of nuclear motion on coupled PES (surface hopping, mean path approach, etc.) has been proposed and is further discussed in another chapter of this book. An a priori justified such treatment in the general case, however, remains problematic and I confine myself to citing a recent in-depth discussion of the topic by one of the pioneers in the field [11].

In the following I continue this outline of historic developments, followed by more systematic considerations on different coupling scenarios. As an important early step, the analysis of the photoelectron (PE) spectrum of ethene revealed that strong nonadiabatic coupling effects can be operative also for seemingly distant electronic states, with well-separated spectral bands [12]. Namely, the combination of several active vibrational modes can lead to a CoIn also when the energetic separation of the states in the centre of the Franck–Condon (FC) zone is as large as 2 eV. While nowadays also relevant CoIns with vertical energy gaps of the PES of 4–5 eV are known (and will be mentioned below) this result proved striking at that time, and strongly indicated that only the energetic accessibility of the CoIn matters for the dynamics, thus rendering it much more important than originally thought. Similarly, it was realized that the well-known paradigm of the dynamic Jahn–Teller (JT) effect [13] is to be considered a special case of a CoIn. In JT systems the electronic degeneracy is enforced by symmetry and, by the very nature of the JT theorem, is lifted in first order of the displacements when distorting the system along the coordinate of a JT active mode. From the point of view of structural chemistry, this makes the symmetry lowering "spontaneous" and occurring independently of actual values of the coupling parameters. Regarding the dynamics, the JT-split PES necessarily take a conical shape near the high-symmetry nuclear configuration, rendering the nuclear motion highly nonadiabatic after an electronic transition from a nondegenerate state (which usually takes the system to the point of degeneracy). In early work, the PE spectra of allene and pentatetraene were investigated [14] and the doubly degenerate ground states identified as structurally related to the cases of ethene and butatriene mentioned above [15]. This established a homologous series of molecules ("cumulene radical cations") with a systematic trend in the PES and dynamics. As a further instructive example we show in Fig. 6.4 the first band of the PE spectrum of benzene [16]. The electronic ground state of the radical cation is doubly degenerate in the D_{6h} point group, and there are four JT active vibrational modes (also doubly degenerate). The photoionization from the nondegenerate neutral ground state creates the radical cation directly at the point of degeneracy (CoIn) and the vibrational modes excited in the spectral band are supported by both JT-split PESs simultaneously. An adiabatic separation would fail equally badly as already demonstrated in Fig. 6.1. This is emphasized because the vibrational structure is quite regular which can thus not be taken as evidence for the validity of the adiabatic (or synonymously: Born–Oppenheimer) approximation, even in such seemingly simple cases. We further see from Fig. 6.4 that in well-resolved spectra as the present one the quantum nature of the vibrational modes is evident, i.e. the discrete level structure becomes directly visible by inspection.

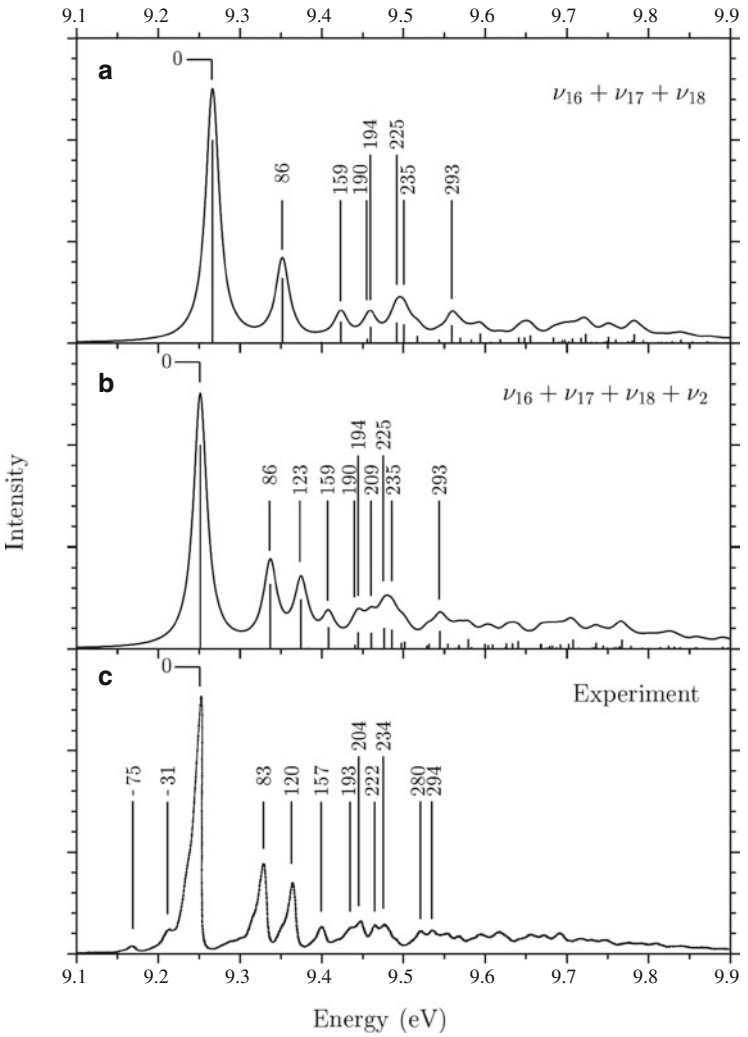

Fig. 6.4 Comparison of experimental (*lowest panel*) and theoretical (*upper two panels*) first photoelectron band of benzene. The *upper panel* represents the results for the JT active modes as indicated in the *panel*, the *central one* displays the full result, obtained by including the totally symmetric C = C stretching mode ν_2

While these developments were important early indications for the relevance of CoIns and nonadiabatic coupling effects, the seminal contributions by Ruedenberg [17], Robb [5, 6], Yarkony [7, 8] and their groups, and subsequently also Martinez and coworkers [18], provided breakthroughs for the field (mostly in the 1990s) and made it known to a broad range of physical and organic chemists and beyond (see also the important work of Klessinger, Michl and

Bonacic–Koutecky [19, 20]). In our group, at about the same time the investigations were becoming broader regarding the phenomena addressed, the introduction of different coupling scenarios and also by considering more than two strongly interacting electronic states. These more systematic aspects shall be addressed in the following sub-section.

6.1.2 Methodology and Phenomena

6.1.2.1 Diabatic Electronic States

The complexity of the theoretical treatment strongly suggests, and often necessitates, to introduce suitable model Hamiltonians. This holds not only in view of the quantum treatment of the nuclear motion but also regarding the underlying electronic structure (ab initio) computations, which are always an essential part of the theoretical methodology. Global PES in more than 6–8 dimensions can hardly be obtained accurately even on present-day computer hardware. The set-up of suitable models is usually combined with the use of a so-called diabatic electronic basis [21–23]. The latter is of special importance since it avoids the singular derivative couplings appearing in the usual adiabatic basis at degeneracies of different molecular PESs (say $V_1(Q)$ and $V_2(Q)$). Denoting the corresponding adiabatic electronic wavefunctions by $\Psi_1(Q)$ and $\Psi_2(Q)$, we have the well-known identity (see, for example, [24])

$$\langle \Psi_1(Q)|\frac{\partial}{\partial Q}|\Psi_2(Q)\rangle = \frac{\langle \Psi_1(Q)|\frac{\partial H}{\partial Q}|\Psi_2(Q)\rangle}{V_2(Q) - V_1(Q)} \tag{6.1}$$

The diabatic wavefunctions are smooth functions of the nuclear coordinates Q also at these degeneracies $V_1(Q) = V_2(Q)$, and so are the potential energy matrix elements in this basis. This allows to introduce a Taylor series expansion which may sometimes be truncated at low order, thus defining the linear (LVC) or linear-plus-quadratic (QVC) coupling scheme [3]. The LVC or QVC schemes have been successfully employed by the Heidelberg, Munich and other groups, and can naturally be extended to carry the expansion to third or fourth (or similar) order. More recently, also a systematic approach to go to considerably higher order has been suggested [25].

The LVC and QVC approaches avoid the explicit construction of diabatic states because they result in a parametrized form of the adiabatic PES; this can be used to determine the coupling parameters by comparing the parametrized form of the adiabatic PES with results from electronic structure calculations for these surfaces (diabatization by ansatz [26]). On the other hand, the fixed functional form leads to a model shape of the PES which may not always be flexible enough to reproduce these data well. To overcome this limitation, a modified construction scheme for the diabatic potential matrix has been introduced [27, 28] where the LVC approach is applied to the adiabatic-to-diabatic (ADT) mixing angle "only". In this form it can

be applied to general adiabatic PESs as given from electronic structure calculations and reproduce them without loss of generality. It can be shown to eliminate the singular derivative couplings rigorously (in principle) and has therefore been coined construction scheme of "regularized diabatic states" [28, 29]. Interestingly, the relevant system parameters can again be determined from potential energy data alone, at least in many relevant cases, for example, if a symmetry is present. The scheme has been successfully applied and its properties have been examined for a Jahn–Teller system [27], a seam of symmetry-allowed CoIns [28] and a general CoIn with two relevant degrees of freedom [29]. Nowadays the concept of regularized states is typically applied to systems with 3 or 4 atoms (H_3 [30], NO_2 [31], SO_2 [32], C_2H_2 [33]) while our treatment of larger systems (such as aromatic and heteroaromatic molecules with 10–12 nuclear degrees of freedom and 2–5 strongly coupled electronic states) relies on the QVC approach.

6.1.2.2 Classification of Two-State Intersections

For apparent reasons the most common type of surface intersections will comprise two states. Here we give a brief survey on their different topologies and symmetries. Three-state intersections (and higher ones) will be discussed below.

Quite generally, the nonadiabatic (or derivative) couplings diverge whenever two different molecular PES become degenerate (intersect). The very notion "conical intersection" implies not only a point or seam of degeneracy but also a topology in the immediate vicinity, namely, a lifting in first order of the nuclear displacements from the degenerate subspace [3, 6, 17]. The phrase "glancing intersection" is used for cases where this degeneracy is lifted in second order only [34, 35], the most prominent example being the Renner–Teller effect in linear molecules (with the bending angle as active coordinate) [36]. Apart from this special situation, a surface degeneracy will mostly be associated with a first-order lifting, i.e. be of the conical type [37]. This is also the generic situation for symmetry-induced degeneracies in nonlinear molecules, where the JT theorem "guarantees" the conical shape as already indicated above.

The appearance of surface intersections can also be understood as a generalization of the famous von Neumann–Wigner noncrossing rule, which states that in diatomic molecules the potential curves of states of the same symmetry do not cross [38]. The simplified proof given by Teller [39] casts the conditions for degeneracy into two algebraic equations, which cannot be normally satisfied at the same time when only a single parameter (the internuclear distance) is to be varied. For a polyatomic system with N atoms and 3N-6 (or 3N-5) internal coordinates this rule is immediately relaxed, and 3N-8 (or 3N-7) coordinates can still be varied after two coordinates have been fixed to fulfill the two aforementioned conditions for degeneracy. The subspace of degeneracy ("intersection space" or "seam") is thus of rather high dimension, while that in which the degeneracy is lifted ("branching space" or "branching plane") has dimension two [3, 5–8, 17]. It emerges naturally that surface intersections are an ubiquitous phenomenon and play an important role for excited-state dynamics as induced by photoexcitation in the visible or UV spectral range.

It is instructive to address the different types of intersections from the point of view of symmetry (see, for example, [35]). The key vibronic coupling constant λ, which governs the first-order interaction between different electronic states $\Psi_1(Q_0)$ and $\Psi_2(Q_0)$ at the nuclear geometry Q_0, can be written as

$$\lambda = \langle \Psi_1(Q_0) | \frac{\partial H}{\partial Q} | \Psi_2(Q_0) \rangle \tag{6.2}$$

Since the molecular Hamiltonian H transforms totally symmetric, λ does not vanish by symmetry only if the following selection rule is fulfilled [3]:

$$\Gamma_1 \otimes \Gamma_2 \otimes \Gamma_Q \supset \Gamma_A. \tag{6.3}$$

Here the irreducible representations Γ on the l.h.s. denote those of the electronic states and nuclear mode, in an obvious notation, and Γ_A stands for the totally symmetric irreducible representation of the respective point group. Several cases can be distinguished.

Without any symmetry, or if $\Gamma_1 = \Gamma_2$ is nondegenerate, the coupling mode Q is totally symmetric (possibly trivially so). No restriction on the point of degeneracy is given by symmetry alone. This is also called accidental intersection and plays a central role, for example, in organic photochemistry (see the contribution by Robb and coworker [40]).

If Γ_1 and Γ_2 differ, the coupling mode Q is non-totally symmetric (coined Q_u). It can thus not coincide with (first-order) Franck–Condon active modes which are characterized by the decomposition of $\Gamma_1 \otimes \Gamma_1$ or $\Gamma_2 \otimes \Gamma_2$ and are totally symmetric (in Abelian point groups). The latter are also called tuning modes in the LVC scheme which forms the body of our early work in the field. The conical intersection is usually termed symmetry-allowed in such a case since it normally occurs (for a single coupling mode) in the subspace $Q_u = 0$ where $\Gamma_1 \neq \Gamma_2$ and a free crossing is possible.

The situation becomes somewhat more complicated (but also richer) in non-Abelian point groups. Limiting ourselves to two-state coupling scenarios, we have $\Gamma_1 = \Gamma_2$ in case of (double) degeneracy. This amounts to a symmetry-induced (also called symmetry-enforced) degeneracy or intersection. By virtue of the JT theorem [13, 41], there exist always non-totally symmetric modes to fulfill the selection rule (6.3). This directly leads to the JT or symmetry-induced conical intersections mentioned earlier. An exception is provided by linear molecules, where such modes do not exist and a coupling between the components of a doubly degenerate (for example, Π) state is provided only by terms of second order in the (bending mode) displacements [41]. These second-order terms necessarily cause the intersection to be of glancing rather than conical type.

As a final distinction, we mention a difference between "trigonal" (such as C_{3v} or D_{3h}) and "tetragonal" (such as C_{4v}, D_4, D_{2d}) point groups. In the first case doubly degenerate modes are JT active, in the second case nondegenerate, non-totally symmetric modes are JT active [3]. In the former case the JT-split PESs have

cylindrical or (more generally) threefold symmetry, in the latter case the symmetry is twofold, thus reflecting the different symmetry of the underlying nuclear framework.

6.1.2.3 Dynamics at Conical Intersections

It has already been reiterated above that nonadiabatic couplings generally diverge at degeneracies of different molecular PESs. A vast amount of numerical results has shown that these degeneracies are almost invariably of the conical type. This is also supported by general theoretical reasoning [37]. In what follows I will therefore identify degeneracies with conical intersections, also bearing in mind that in all specific cases reported below the intersections are of the conical type.

From semiclassical reasoning it is expected that nonadiabatic coupling effects are strong for energies at and above that of a CoIn. At a CoIn, nearly isoenergetic vibrational eigenfunctions of the intersecting PES have similar classical turning points, rendering their overlap integral substantial. For lower energies either the vibrational states are not isoenergetic or their overlap becomes exponentially small. This general situation was already exemplified by the study of the ethene radical cation mentioned above [12]. Strong nonadiabatic couplings manifest themselves in distinct ways, in either the energy or time domain. Concerning the vibronic structure of electronic spectra they lead to a thorough mixing of upper and lower-surface vibrational wavefunctions [3]. This implies a highly irregular line structure, and any regular FC patterns will be completely lost. If the CoIn occurs well outside the FC zone, the interacting electronic states give rise to well-separated spectral bands; for the higher-energy band, the spectral intensities of the vibronic eigenstates will derive from the admixture of the upper-surface vibrational levels and their density from the lower-surface levels (being of much larger density than the upper-surface levels). Under low resolution the spectral envelope will look diffuse, and in extreme cases this will hold even under high resolution (provided the intrinsic lifetime broadening exceeds the average line spacings). Concerning the time domain, the system undergoes an ultrafast internal conversion (IC) process from the upper to the lower PES, proceeding on the same time scale as the nuclear vibrations. If the CoIn, on the other hand, is not classically accessible to the nuclear motion, and a "surface hop" becomes possible only through tunneling, the nonradiative transition is slowed down and may become much slower than vibrational periods, ultimately reaching the golden rule limit of traditional radiationless decay theory.

The heteroaromatic radical cations furan, pyrrole, thiophene represent a beautiful series of molecules to illustrate this dependence [42,43]. Their two lowest electronic states exhibit a characteristic change in their vertical ionization potentials such that their difference substantially decreases in the series. As a consequence also the minimum energy of the resulting CoIn decreases, not only absolutely but also in relation to the upper adiabatic PES, see Fig. 6.5 for a schematic drawing. For furan the CoIn occurs well above ($\sim$0.5 eV) the upper state minimum, for pyrrole and thiophene it is very close (within 0.01 and 0.04 eV). Thus the IC process in the latter cases is expected to compete with the vibrational motion, while in the former it should be slower. This is nicely confirmed by the electronic populations obtained from ab initio-based WP propagations and displayed in Fig. 6.6. A typical stretching

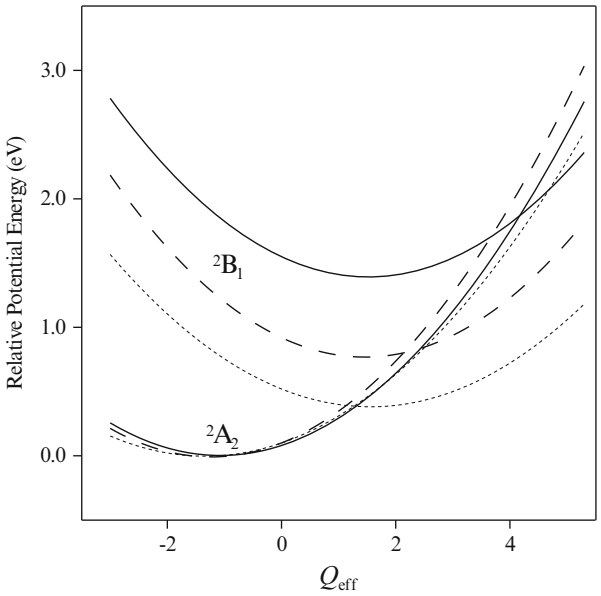

Fig. 6.5 Cut through the lowest PES of the furan, pyrrole, and thiophene radical cations along the coordinate of an effective mode. The latter is given by a *straight line* connecting the minimum of the $^2A_2$ ionic ground state (taken to be the zero of energy in all cases) to the minimum of the CoIn between the ground and first excited ($^2B_1$) ionic states. The *dotted lines* refer to thiophene, the *dashed ones* to pyrrole and the *full lines* to the furan radical cation

vibrational period amounts to ∼20 fs, which is the time scale of the $^2B_1 -^2 A_2$ population transfer (IC) for pyrrole and thiophene. In the case of furan, on the other hand, the IC time scale is considerably slower (∼150 fs) which is completely in line with the higher energy of the surface crossing in Fig. 6.5. Consequently, also the PE spectral bands of the three systems differ in a characteristic way [42, 43]. In furan the nonadiabatic couplings lead to small line splittings and moderate broadening effects only (forming non-overlapping quasi-resonances), while in pyrrole and thiophene they cause a complete redistribution of spectral lines with no correlation between unperturbed vibrational levels and vibronic eigenstates. The high density and irregularity of vibronic eigenstates in these two examples is similar to the cases of $C_2H_4^+$ (see Sect. 6.1.1) and excited states of Bz^+ to be discussed below.

6.1.2.4 Two-State vs. Three-State Coupling Scenarios

Degeneracies or near-degeneracies of more than two electronic states may play a role in two distinctly different ways. They can (1) affect the dynamics sequentially, i.e. as series of two-state (quasi-)degeneracies, which the system encounters separately during its time evolution and which both play a comparable role. An example of this type has been reported to occur in highly excited states of formaldehyde, severely affecting its VUV absorption spectrum [44]. (2) More than two electronic

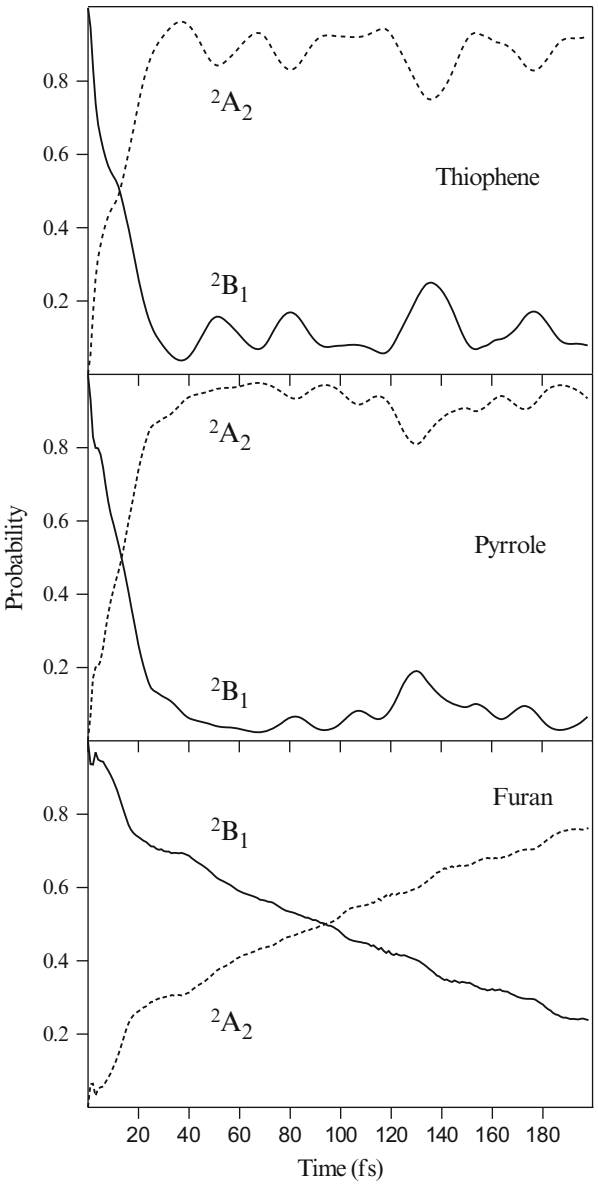

Fig. 6.6 Electronic populations of the ground and first excited electronic states of the three radical cations given in the panels, following a vertical excitation to the upper ($^2B_1$) electronic state. Consistent with the energetic positions of the surface crossings in the preceding figure, the transition occurs within a single vibrational period for pyrrole and thiophene, but is considerably slower in the case of the furan radical cation

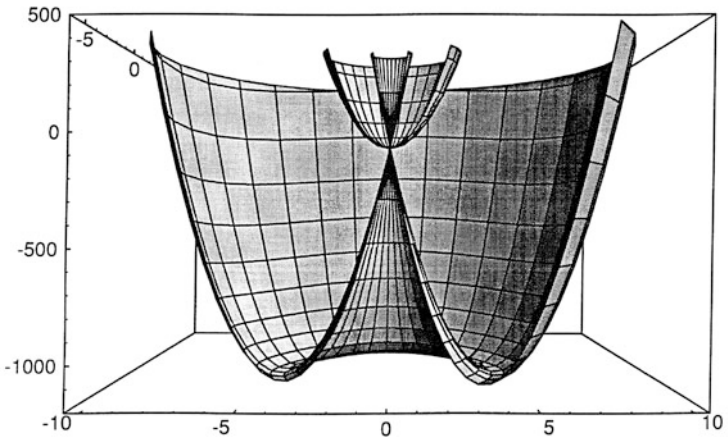

Fig. 6.7 Perspective drawing of a rotationally symmetric three-state ("triple") conical intersection such as occurs, for example, at an accidental crossing of a doubly degenerate state with a nondegenerate state. The coordinates are the components of a doubly degenerate mode, causing a linear coupling between the electronic states

states may come close or intersect also at a single point in nuclear coordinate space. These three-state intersections are of particular interest and should appear frequently as accidental intersections (see above) in non-Abelian point groups, when a doubly degenerate (by symmetry) electronic state may cross freely with a nondegenerate state. (In principle, though less likely in practice, also two doubly degenerate states of different symmetry may cross freely thus producing a fourfold degeneracy.) A typical scenario is given by the first and second excited states of the benzene radical cation (Bz^+), which are doubly degenerate and nondegenerate, respectively (of $^2E_{2g}$ and $^2A_{2u}$ symmetry in the D_{6h} molecular point group) [45, 46]. This system features the coexistence of two different pairs of electronic (component) states with two different nonadiabatic coupling mechanisms and an $^2A_{2u} -^2 E_{2g}$ energy gap which changes sign as a function of the C = C stretching coordinate Q_2. For low energies there is nonadiabatic coupling within the $^2E_{2g}$ manifold, which is characterized by a sparse and rather regular level structure such as occurs for the ground electronic state of Bz^+ (Fig. 6.4). For high energies the crossing point of the $^2A_{2u} -^2 E_{2g}$ PESs plays a decisive role for the dynamics. This amounts to a triple degeneracy as is displayed by the perspective drawing of Fig. 6.7. The vibronic structure of the PE spectrum [45, 47] becomes similarly complex and erratic as discussed above for the ethene, pyrrole and thiophene radical cations.

The triple intersection of Fig. 6.7 deserves special mentioning with respect to low-energy vibronic motion. It has been pointed out above that the surface topology near a degeneracy (conical or not) is not of central importance for the strength of the nonadiabatic coupling effects. For low-energy motion this shape does matter,

and conical intersections are highlighted by the appearance of the geometric phase phenomenon [48, 49]. Very briefly, the conical nature of the PES topography necessarily leads to a sign change of the real electronic wavefunction whenever the point of degeneracy is encircled in a closed loop. Since the whole wavefunction must be single valued, the nuclear wavefunction also has to undergo a sign change, which amounts to a different boundary condition for this ("pseudorotational") motion [50]. In other words, the vibronic eigenvalues are affected by the presence of the CoIn, although it may be high in energy and not be in reach for the nuclear motion. This is counterintuitive, but not contradicting the above statements about the adiabatic approximation, because the product nature of the molecular wavefunction is not affected. Rather, it may be termed adiabatic separation with modified boundary conditions.

As is well known, glancing intersections as occur in the Renner–Teller effect do not exhibit the geometric phase phenomenon [51], and neither do triple intersections like the one in Fig. 6.7 [52]. This can be traced to the different surface topography near the degeneracy (glancing intersections) and to the cancellation of phase contributions from the different degenerate pairs (triple intersections). The situation is illustrated by the drawings of Fig. 6.8 which shows a time-dependent WP evolving on a double (right panels) or triple (left panels) intersection [53]. Otherwise the PESs in question are identical in the two sets of panels. By virtue of the geometric phase there is destructive interference in the case of a two-state conical intersection but constructive interference for a three-state intersection. This shows up nicely in the lowerhalf-plane, opposite to that where the initial WP is located, and leads to a completely different shape of the WP for longer propagation times (see lowest panels).

I mention that this type of surface topography and WP evolution plays a role for the two-photon ionization spectrum of the sodium trimer, and considerations of the type presented here have led to a thorough re-interpretation of the experimental spectrum [52, 54]. For a more complete overview over different coupling scenarios regarding interactions within the degenerate state and between the degenerate and a nondegenerate state, I refer to [55].

6.1.2.5 Vibronic Coupling and Localization Phenomena

We briefly mention that near-degenerate electronic states may also emerge for systems with weakly coupled subsystems, such that the symmetry-adapted linear combinations of the locally excited states show only a rather small energetic separation. Despite this weak interaction between locally excited subsystems the vibronic interactions in the whole aggregate or molecule may be substantial. Two prominent cases are (1) molecules with several equivalent core hole sites; here, the vibrational motion may destroy the nominal equivalence of the sites and lead to excitation of asymmetric modes in odd quanta in the spectrum (proceeding on diabatic PES with localized core holes) [56–58]. Another case are (2) dimeric systems with weakly coupled subsystems (e.g. through hydrogen bonding or long covalent linkers). Again, asymmetric modes can be excited, which may lead here to a substantial reduction of the excitonic energy splittings and amount to nonadiabatic tunneling on the lowest (double-well) adiabatic PES of the dimer [59–61].

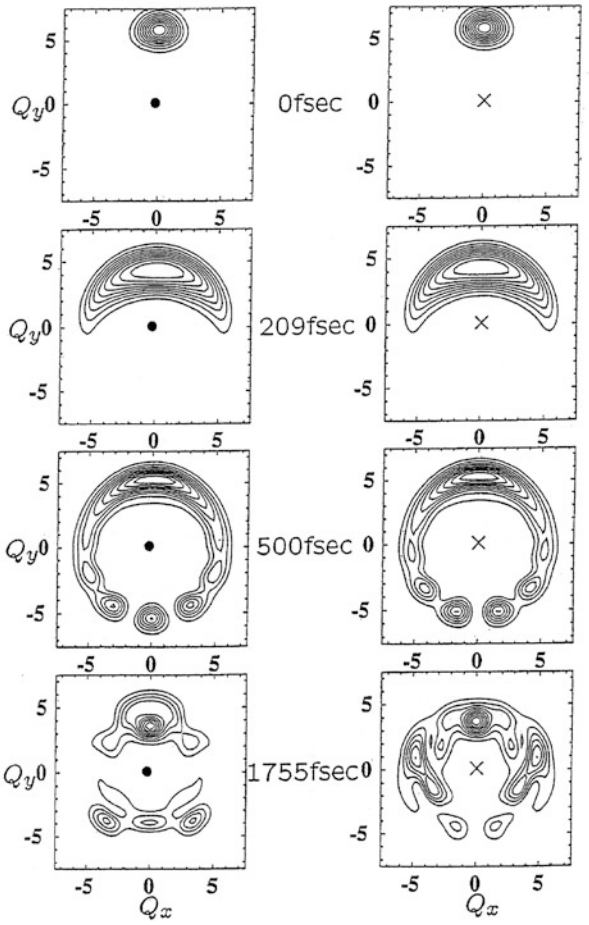

Fig. 6.8 Comparison of time-evolution on doubly (*right panels*) and triply (*left panels*) intersecting molecular PES. The lowest adiabatic PES on which the evolution starts is the same in all panels. The effect of constructive (no geometric phase) and destructive (geometric phase) interference shows up in the *third panels* from above and leads to a completely different shape of the WP for longer times (*lowest panels*)

6.2 Applications in Spectroscopy

In the previous section we have already discussed a few examples of two-state vibronic coupling effects in spectroscopy. They all relied on the LVC or QVC approach and were based on extended ab initio calculations for the underlying system parameters (frequencies and coupling constants). The latter is a generic element of our approach and applies to all examples presented here; for details we refer to the original publications.

In the present section I discuss examples where the treatment has been extended in two different ways, either going beyond the QVC approach or including more than two strongly coupled states in the analysis.

Over the years, a series of related triatomic molecules and cations has been investigated by the Heidelberg group, notably NO_2 [31], O_3^+ [62], and SO_2 [32, 63], and also H_3 [30, 64]. NO_2 and SO_2 are famous (and notorious) showcases in molecular spectroscopy with exceedingly complex spectra which could only incompletely be assigned despite intense efforts by several groups. An even partly systematic list of references is well beyond the scope of this short article. The heavy mixing of vibrational wavefunctions of different molecular PES is an immediate cause for such complications. Consider the photoelectron spectrum of ozone in Fig. 6.9, which shows a comparison of experimental (upper panel) with theoretical (lower panel) results [62]. In the theoretical treatment the line spectrum actually computed has been phenomenologically broadened with Lorentzians (FWHM = 0.04 eV) to account for finite experimental resolution. Overall, the experiment is well reproduced, in particular, the regular peak progression at lower energies and the irregular structures at higher energies. Two electronic states contribute to the spectral intensity, the $^2A_1$ ground and $^2B_2$ first excited states of O_3^+. The regular progression can be understood as excitation of the bending mode because of different equilibrium geometries in the neutral and ionic ground states. The situation can be visualized in Fig. 6.10 which shows contour line drawings of the relevant PES for C_{2v} geometries. The ground and first excited states of O_3^+ have their minima near bond angles of 130° and 105°, respectively, while the centre of the FC zone occurs near 117°. Following the FC principle, extended bending progressions are expected not only for the $^2A_1$ state as observed, but also for the higher-energy $^2B_2$ state. For the latter state the experimental spectral profile shows distinct irregularities, and the theoretical results reveal their origin, namely, a highly irregular underlying line structure beyond an energy of ∼12.8 eV. This is just the minimum energy of a seam of conical intersections also displayed in Fig. 6.10. It is symmetry-allowed according to the classification of Sect. 6.1.2.2, and further exemplifies corresponding statements of Sect. 6.1.2.3 about the energy range of strongly nonadiabatic motion. The seam is substantially bent and affected by the anharmonicity of the C_{2v} PES of the system. This has been fully included in the numerical computations, while the coupling has been taken to be a linear function of the asymmetric stretch coordinate (LVC scheme).

In later work, the concept of regularized diabatic states (Sect. 6.1.2.1) has been more fully adopted to treat the cases of NO_2 and SO_2. In Fig. 6.11 we show the dependence of the vibronic coupling constant λ on the symmetric stretch coordinate or bond length r (which is basically the seam coordinate) near the seam minimum for NO_2 [31]. It is seen to increase markedly for increasing bond length r which corresponds to an increase of the energy along the seam and to a larger energy after photoexcitation. It rationalizes the (originally surprising) fact that for lower energies (namely, in the photodetachment spectrum) the spectral irregularities are considerably smaller than in the visible absorption spectrum of NO_2 which probes the dynamics for higher energies and which is well known for its notorious

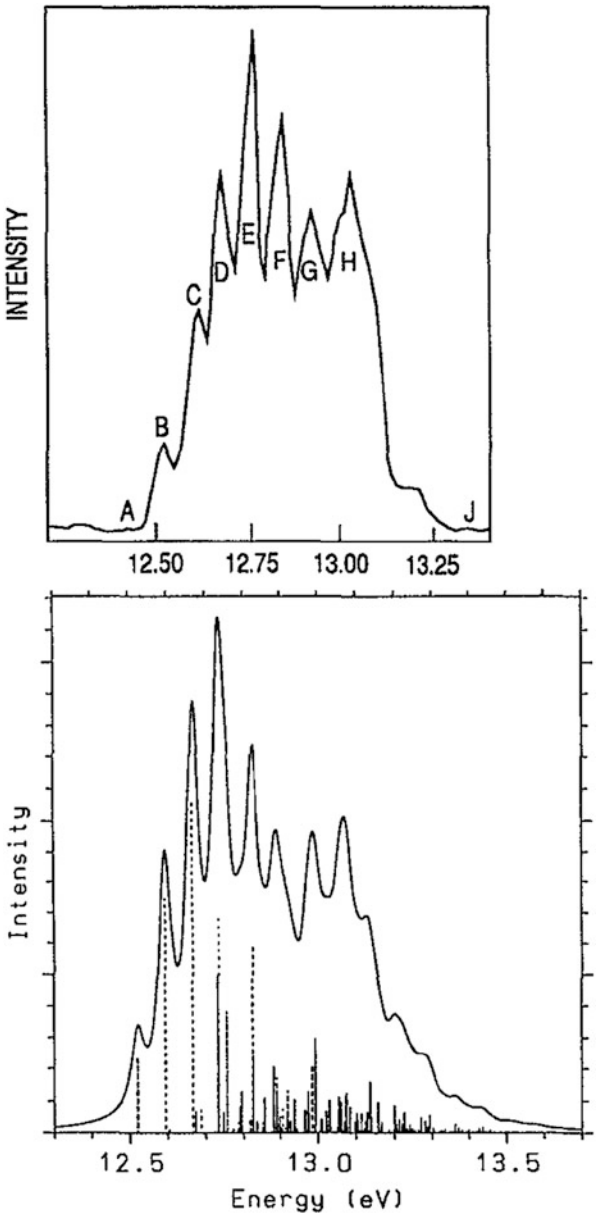

Fig. 6.9 Comparison of experimental (*upper panel*) and theoretical (*lower panel*) first photoelectron band system of ozone, corresponding to the lowest electronic states of the radical cation. Peak A in the experimental recording is assumed to be a hot band

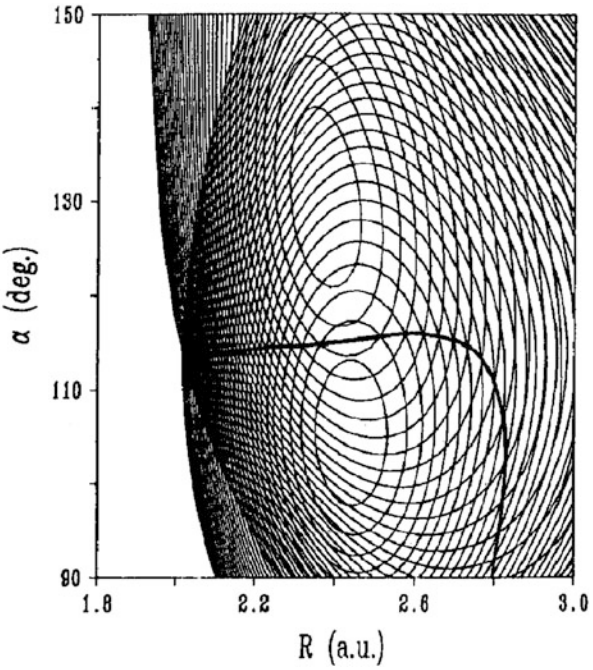

Fig. 6.10 Contour line drawing of the C_{2v} PES of the ozone radical cation. The *single full (bent) line* represents the seam of ${}^2A_1 - {}^2B_2$ conical intersections

complexity [65]. The UV absorption spectrum of SO_2 is similarly intricate and could recently be well reproduced by us theoretically, see Fig. 6.12 [32]. Under low resolution, it features a seemingly regular progression of the bending mode, extending until $\sim$34,000 cm^{-1} [66]. However, there is a very complex line structure under the spectral envelope which becomes itself most irregular in the higher energy part of the spectrum. The work of [32] is the first in the literature achieving the remarkable agreement with experiment shown, and I refer to this reference for all further details of the analysis, including a comparison with uncoupled-surface spectra.

Let us now address a multi-state coupling problem where up to five interacting states have been included in the treatment, namely, the benzene radical cation Bz^+. Figure 6.13 shows results of ab initio calculations for the lowest five electronic states of Bz^+ along the two components of the JT active coordinate Q_{18} [46]. The latter is doubly degenerate and so are three of the electronic states, amounting to eight component states or PESs in total. The individual symbols denote the ab initio data points, while the contiguous (full and dashed) lines stand for the fitted model curves resulting from the LVC approach. Overall, an impressive set of mutually crossing PES is revealed with a whole network of CoIns which lets one expect a rich variety of vibronic phenomena. The crossings at the origin $Q_{18} = 0$ represent cuts through

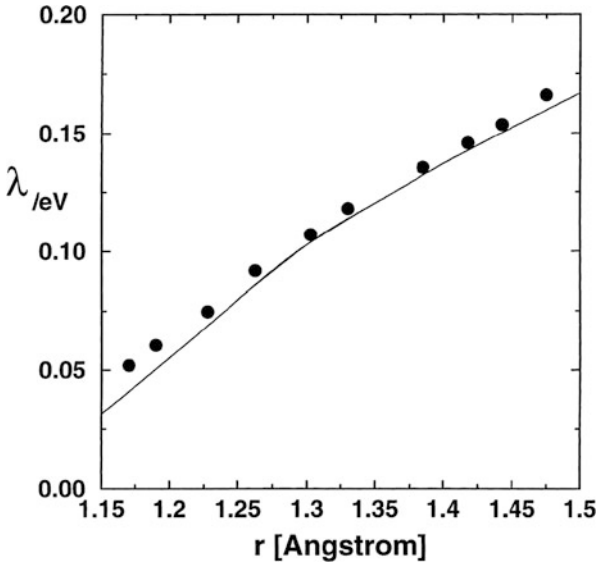

Fig. 6.11 Variation of the vibronic coupling constant λ along the $^2A_1 - {}^2B_2$ conical intersection seam of NO_2

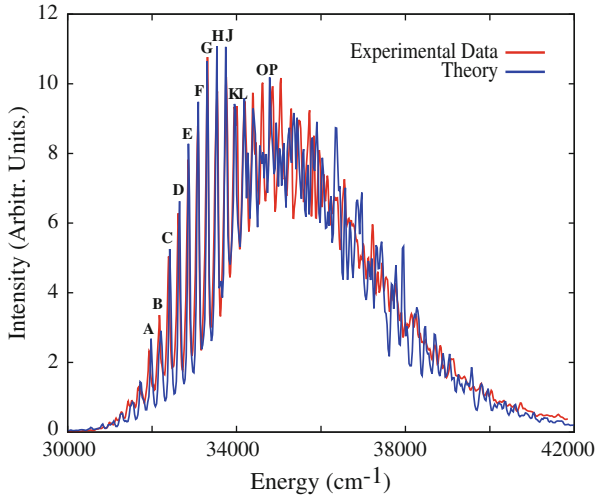

Fig. 6.12 Comparison of experimental and theoretical UV absorption spectrum of SO_2

JT intersections while those for $Q_{18} \neq 0$ involve a degenerate (at the D_{6h} point) and a nondegenerate state, which we term pseudo-JT effect or intersection [45].

The $(^2E_{1g})$ ground state intersection represents the JT effect in this state which has already been documented in the spectrum of Fig. 6.4. The next electronic

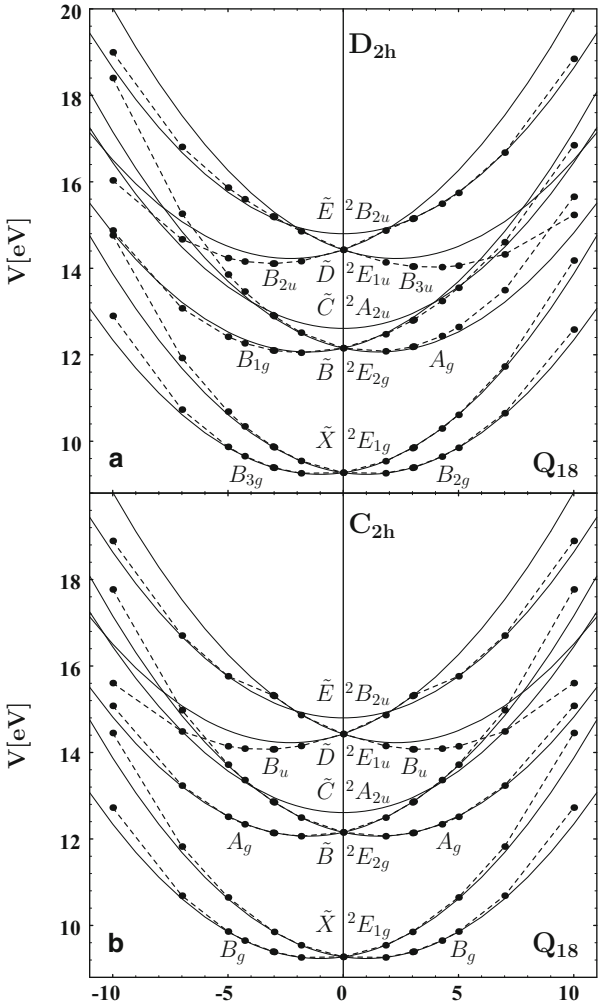

Fig. 6.13 Cut through the lowest 8 PESs of the benzene radical cation along the coordinate Q_{18} of a doubly degenerate mode. The *filled symbols* denote the individual ab initio data points, the *interconnecting lines* the fitted model PES. The *crossings* at the origin $Q_{18} = 0$ represent cuts through JT intersections, those at $Q_{18} \neq 0$ are cuts through pseudo-JT intersections

state ($^2E_{2g}$ first excited state) is likewise subject to the JT effect with similar implications for the spectrum, see Fig. 6.14 (upper panel) [47]. There is moderate excitation of the JT active modes with a rather sparse level structure which has been assigned in the original work. Moreover, Fig. 6.13 gives evidence of a slightly higher, nondegenerate ($^2A_{2u}$) state which approaches and also crosses the $^2E_{2g}$ state along the C = C stretching coordinate Q_2. This, among others, leads to the triple intersection mentioned in Sect. 6.1.2.4. We thus have a pseudo-JT intersection

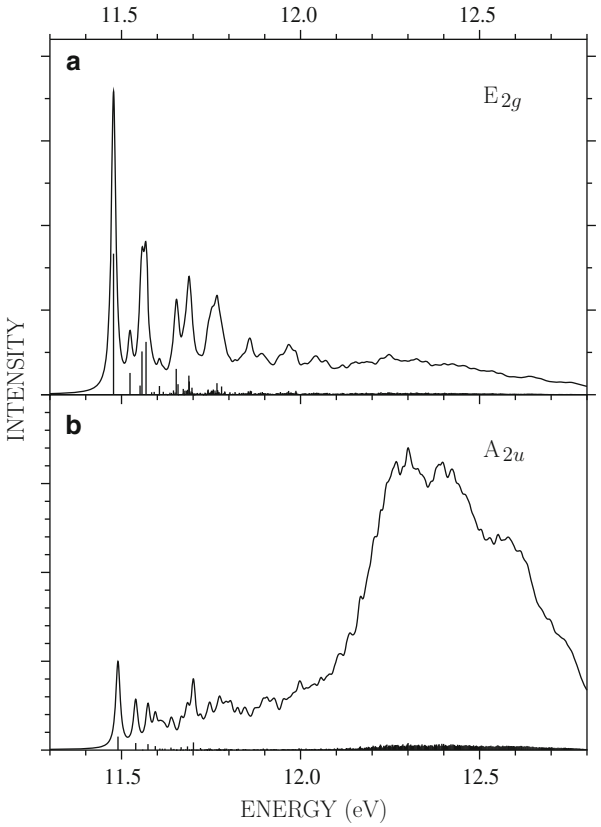

Fig. 6.14 Second and third PE spectral bands of benzene as computed with the present vibronic coupling approach. The *upper panel* corresponds to the ($^2E_{2g}$) first excited state, the *lower panel* to the ($^2A_{2u}$) second excited state. The composite theoretical band compares favourably with experiment

and coupling between the $^2A_{2u}$ and $^2E_{2g}$ states which, in conjunction with the JT coupling in the $^2E_{2g}$ state, leads to the coexistence and interplay of two different interaction mechanisms for the different pairs of component states [45]. Ultimately, this also renders the motion in the nondegenerate state highly nonadiabatic and leads to a complex vibronic structure in the corresponding PE band, see lower panel of Fig. 6.14 [47]. There, numerous individual lines are seen (despite being somewhat small in the drawing) to contribute to the broad and structureless spectral envelope. Their density exceeds that of the unperturbed upper-surface vibrational levels by about two orders of magnitude. The computed spectral profile for the composite band is in fair agreement with the observations. The very high density and complexity of the vibronic lines resembles the situation, for example, in the ethene, pyrrole, and thiophene cations mentioned above; however, the coexistence

of different coupling mechanisms renders the situation even more complex in the present example.

The situation becomes further intriguing after realizing that, in addition, some branches of the JT-split $^2E_{1g}$ and $^2E_{2g}$ PES intersect each other. This leads to an ultrafast IC process in Bz^+ comprising all five component states of the $^2E_{1g}$, $^2E_{2g}$, and $^2A_{2u}$ electronic manifold. More details and, in particular, the effect which fluorination has on these multi-state nonradiative transitions will be discussed in the next section.

6.3 Applications in Photophysics and Photochemistry

In the present section we address time-dependent phenomena governed by CoIns and strong nonadiabatic couplings, notably the electronic population dynamics of strongly coupled PES and the consequences it has on observable quantities. It has already been demonstrated above in Sect. 6.1.2.3 that, if the CoIn is in reach energetically, the IC process may proceed on the time scale of nuclear vibrations (otherwise it is slower). However, it should be emphasized that the actual nonradiative transition can be even faster. A striking example is provided by the Rydberg de-excitation of triatomic hydrogen: here the population transfer from the upper to the lower adiabatic sheet of the JT-split ground state PES of H_3 proceeds within only 4 fs [30, 67]! The reason is that for the Rydberg de-excitation, starting from a near-D_{3h} geometry, the initial state in the decay process is generated directly at the JT ground-state intersection seam. It does not need to time-evolve towards the CoIn, and the population transfer gives a direct measure of the nonradiative transition itself. In most other cases the time evolution of the electronic population includes the time needed for the system to arrive at the CoIn, and it is thus more an upper limit to the time needed for the actual "surface hop".

6.3.1 Ultrafast Internal Conversion and Its Competition with Fluorescence

Let us now return to Bz^+, discussed in Sect. 6.2. For this prototypical system the $^2E_{2g}$ and $^2A_{2u}$ set of states has also been treated by time-dependent methods and the aforementioned population transfer from the upper to the lower state been found to proceed within 20–30 fs (one period of the C = C stretching mode is 33 fs) [45]. This parallels the pyrrole and thiophene cases and other systems treated by us over the years. Moreover, also the complete set of all above CoIns comprising the lowest five component states of Bz^+ (within the LVC approach) could be treated quantum dynamically [47] using the powerful MCTDH wavepacket propagation method [68, 69]. The resulting time-dependent electronic populations are presented in Fig. 6.15. They reveal a step-wise nonradiative transition—within 100–200 fs—from the (dipole-allowed) $^2A_{2u}$ over the (dipole-forbidden) $^2E_{2g}$ state to the $^2E_{1g}$ ground state of the radical cation. This is remarkable in view of the large energy

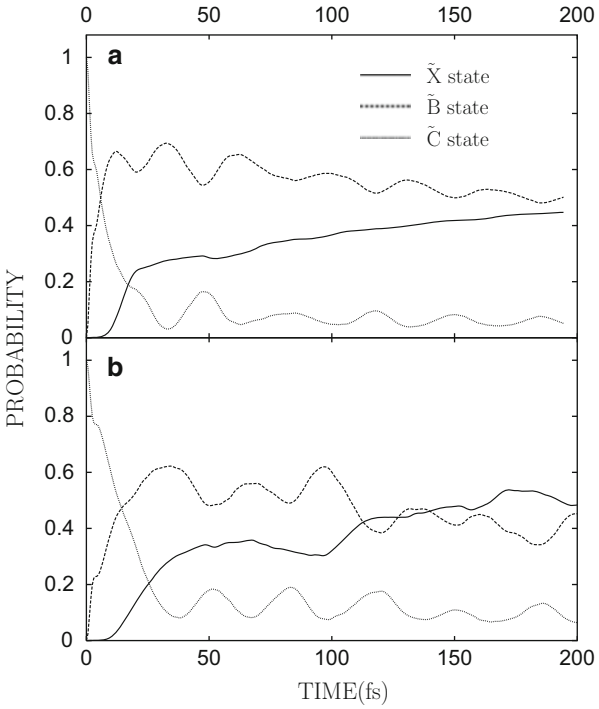

Fig. 6.15 Time-dependent electronic populations of the $\tilde{C}(^2A_{2u}) - \tilde{B}(^2E_{2g}) - \tilde{X}(^2E_{1g})$ manifold of Bz^+ following a vertical transition to the $\tilde{C}(^2A_{2u})$ state of the system. The full calculation, with all degeneracies retained (*upper panel*) is compared with an approximate one where the electronic and vibrational degeneracies are suppressed (*lower panel*)

gaps of ∼3 eV involved, the indirect couplings operative and the sub-ps dynamics resulting from the multi-state interactions [47]. It provides a natural explanation for the absence of detectable fluorescence in Bz^+ [70, 71] which cannot compete with the efficient IC process identified. We mention in passing that the whole set of CoIns identified for Bz^+ comprises also higher energy electronic states included in Fig. 6.13, and a (more approximate) modeling has been undertaken to account for them also [72].

A further intriguing perspective is offered by the fluoro derivatives of Bz^+. It has been known for a long time experimentally that the monofluoro derivative is non-fluorescent like the Bz^+ parent cation [73]. The difluoro derivatives constitute a limiting case, while the trifluoro and all further, more completely fluorinated cations do exhibit (strong) fluorescence [71, 73, 74], which has actually been used to gather substantial information on the structural and spectroscopic properties of the systems (see, for example, [75–79]).

It is gratifying that the present coupling mechanism can naturally account for these interrelations. Consider the correlation diagram of Fig. 6.16 between

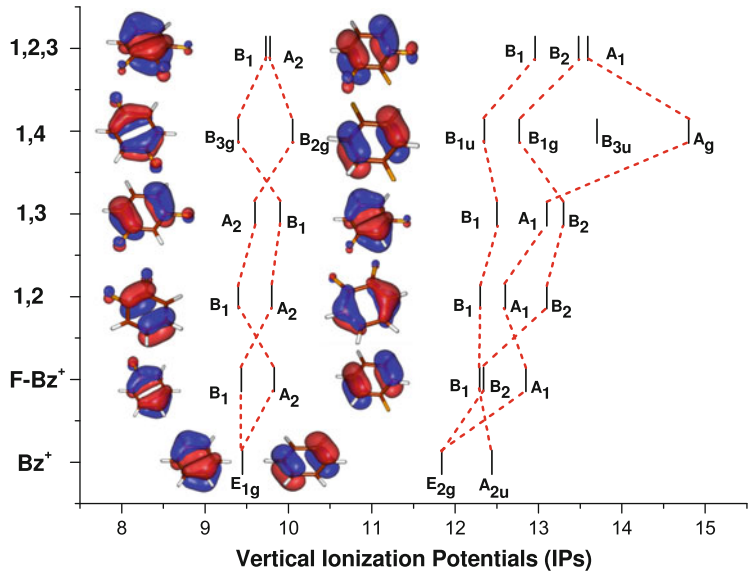

Fig. 6.16 Correlation diagram between ionization potentials of benzene and its mono-, di- and a trifluoro-derivative. Some of the molecular orbitals are also shown for comparison

the orbitals and state energies of Bz^+ and some of its fluoro derivatives [80]. There are two noteworthy trends visible in the figure, first the expected lifting of the degeneracies due to the loss of symmetry upon asymmetric fluorination and, second, a gradual but substantial shift to higher energy of the $\tilde{B}^2E_{2g}$—derived states. The latter relate to ionization out of a σ orbital which is C–F bonding and stabilized energetically by fluorination. On the other hand, the π-type ionization potentials, correlating with the $\tilde{C}^2A_{2u}$ and $\tilde{X}^2E_{1g}$ states of Bz^+, stay nearly the same as for the parent system. One should be aware that in Bz^+ the $\tilde{C}^2A_{2u}$ and $\tilde{X}^2E_{1g}$ states are not coupled directly, but rather indirectly, through the $\tilde{B}^2E_{2g}$ state as intermediate [46]. (The same holds for the fluoro derivatives because of high energies of the corresponding CoIn seams in all species [80–82].) The increase in relative energy of the $\tilde{B}^2E_{2g}$—derived states in the fluoro derivatives causes a similar energetic increase of the respective seams of CoIns and thus an effective weakening of the coupling between their two lowest ($\tilde{X}^2E_{1g}$-derived) states and their next higher excited states. Consequently also the population transfer to the ground state is slowed down and becoming increasingly less efficient for an increasing number of F atoms in the compound [80, 81, 83]. I refer to the original literature for the actual numbers and all further details, and confine myself to presenting the time-dependent populations of Fig. 6.17 as representative examples. The figure shows the populations of the lowest five electronic states of the mono- and 1,2,3-trifluoro derivative [80, 81], which correspond to those shown in Fig. 6.15 for the parent cation (due to the degeneracies for Bz^+ only three curves are shown there). The initial state is the B_1 state for F-Bz^+ (same as for the parent system in

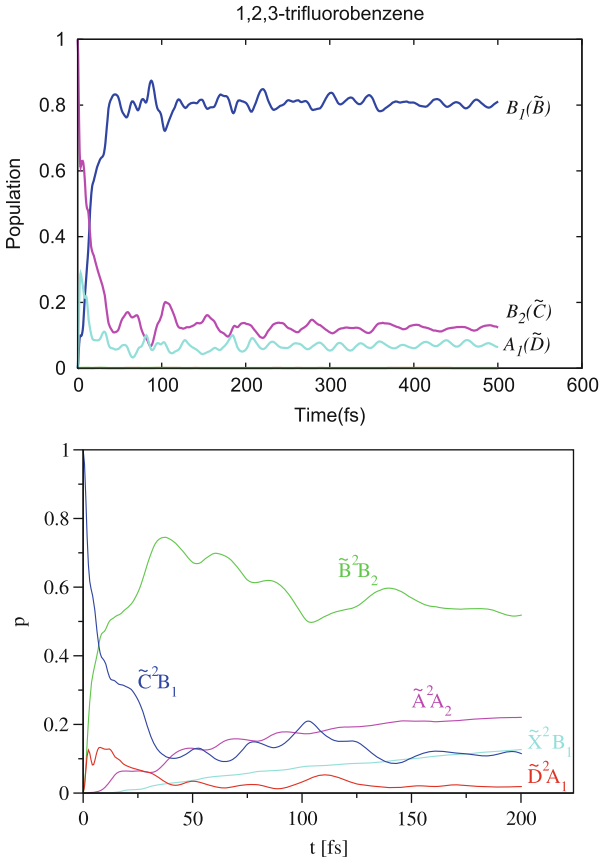

Fig. 6.17 Time-dependent electronic populations of the lowest five electronic states of the mono- and 1,2,3-trifluorobenzene radical cations (*lower* and *upper panel*, respectively). The initial electronic state is visible from the curves

Fig. 6.15) and the next higher state (B_2 state) for the trifluoro derivative in question. The reason for the latter choice is to be able to show any nontrivial dynamics at all, because for the B_1 state as initial state the electronic populations stay virtually constant over time.

Comparing Fig. 6.17 with Fig. 6.15 we easily notice the characteristic change of the IC process with increasing fluorination. For the monofluoro derivative the populations evolve in a similar way as in the parent system Bz^+, and the upper state for a potential dipole-allowed transition, the B_1 state, again decays on a femtosecond time scale. For the trifluoro derivative 3F-Bz^+ the situation is entirely different, and the B_1 population stays constantly large. The competition between the IC process and fluorescence thus disappears according to the theoretical treatment and, in line with this finding, 3F-Bz^+ shows clear emission, as do the higher fluoro-derivatives of Bz^+ [71, 73, 74]. The reason, as already stated above, is the energetic

increase of the B_2 state and hence, of the CoIn between its PES and that of the A_2 and B_1 states deriving from the ground state of Bz^+ (see Fig. 6.16). The difluoro cations represent an intermediate case where only the 1,3 (meta) isomer shows weak emission [73]. Even this more subtle difference seems to be captured qualitatively by our treatment [83]. I conclude this discussion by mentioning that there are further characteristic changes upon (partial) fluorination which have to do more with the symmetry breaking in general than with fluorination in particular [80, 81, 83]. The interested reader is referred to the original literature for more details.

6.3.2 Elementary Photochemical Transformations

So far the discussion has focussed on rather small-amplitude displacements affecting photophysical properties like fluorescence behaviour. Now I address radiationless processes associated with larger-amplitude displacements or photochemical transformations. This is indeed the subject of ongoing interest in the literature and of intense work by several groups. In our work, we have, for example, considered the quantum dynamics of nonadiabatic cis–trans isomerization of acetylene following excitation to the S_2 state [33]. This state features a CoIn seam with the bending mode potentials of the lower-lying S_1 state. Even through this symmetry-lowering the two states do not interact unless the torsional mode is activated and any symmetry is lost in the system. The equilibrium geometry of the S_1 state is trans-bent while the S_2 state takes a cisoid shape (C_s symmetry). From there the IC process takes the system over the out-of-plane distortion to the trans-bent structure of the S_1 state where it preferentially remains, although not entirely. The complexity of the UV absorption spectrum of acetylene is severely affected by the nonadiabatic interactions, although the pronounced anharmonicity associated with the deep wells of the bending mode potentials also plays an important role [84].

The radical cations of the five-membered heterocycles furan, pyrrole, and thiophene have already been discussed above. The photophysics and photochemistry of the neutral species have received considerably more attention in the literature. Concerning furan, I only mention the theoretical (dynamical) studies on the ring-opening process following UV photoexcitation [85–87]. In pyrrole, in addition N-H photodissociation comes into play as a further radiationless deactivation channel (see, for example, [88–90]). Following earlier work by Domcke and co-workers [91,92] we have extended the quantum-dynamical treatment by considering also the higher-excited states populated by a dipole-allowed transition from the ground state. Figure 6.18 shows the potential curves of the lowest five singlet states of pyrrole along the N–H stretching normal coordinate Q_{24}. Near the ground state equilibrium geometry there are two $\pi - \sigma^*$ excited states, followed by two $\pi - \pi^*$ excited states [92, 93]. The latter carry most of the oscillator strength, the former decrease in energy for increasing N–H bond length and cross with the nominal $A_1(S_0)$ state in the asymptotic region. All four excited states are interconnected through a set of CoIns similar to the case of Bz^+ discussed above. Within the QVC approach the excited states would be decoupled from the $A_1(S_0)$ state, but by virtue

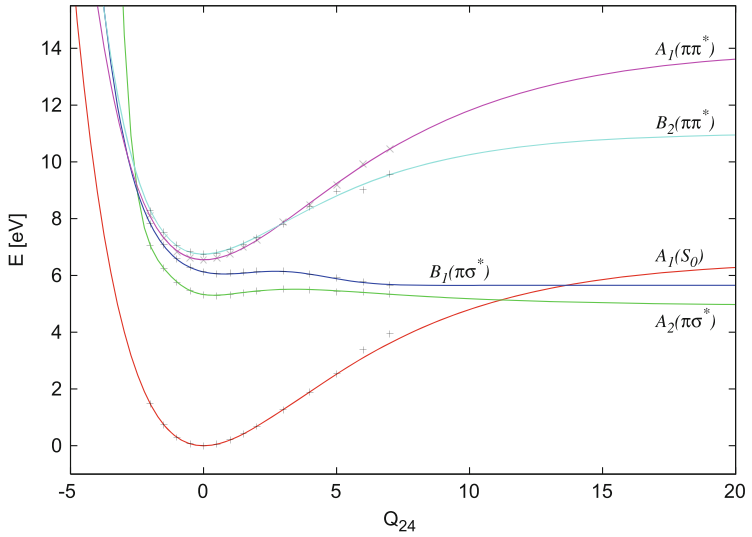

Fig. 6.18 Potential energy curves of the five lowest singlet states of pyrrole along the N–H stretching normal coordinate Q_{24}

of the anharmonic potentials along Q_{24} there can be a sequence of IC processes comprising all five states in question, extending over an energy range of ∼6 eV and leading to N–H photodissociation on three different channels, see Fig. 6.18. This is indeed confirmed by extensive WP calculations using the MCTDH method [68,69], for which a selected result is shown in Fig. 6.19 [94]. The electronic populations in the upper panel show indeed that the population is transferred within less than 50 fs from the optically bright $\pi - \pi^*$ state to one of the $\pi - \sigma^*$ states where it can dissociate. Moreover, a small fraction undergoes a further transition to the $A_1(S_0)$ state where it can also dissociate, but with a considerably smaller excess energy. This is of interest because photofragmentation is known to lead to slow and fast H atoms in the system [89]. Using well-known techniques [95, 96], the reactive flux can be extracted from the present WP calculations, and the results are shown in the lower panel of Fig. 6.19 [94]. The figure indeed gives evidence of N–H photodissociation on the three channels visible in Fig. 6.18. Consistent with the smaller population of the $A_1(S_0)$ state, also the reactive flux on this state is smaller than for the other states. The flux on the $A_1(S_0)$ state can be considered to represent slow H atoms while that on the $\pi - \sigma^*$ states represents fast H atoms. From the results of [94] their ratio, and in particular its energy dependency can be determined. In line with observations, the ratio of slow to fast H atoms is found to increase with increasing energy of the system. This agreement is intriguing, although the absolute values (of the ratio) are considerably too small in comparison with experiment [89]. Presumably other vibrational redistribution mechanisms, such as occurring through the ring-puckering CoIns emphasized by Lischka et al. [93], should be included to arrive at a more quantitative agreement regarding the absolute numbers. To conclude

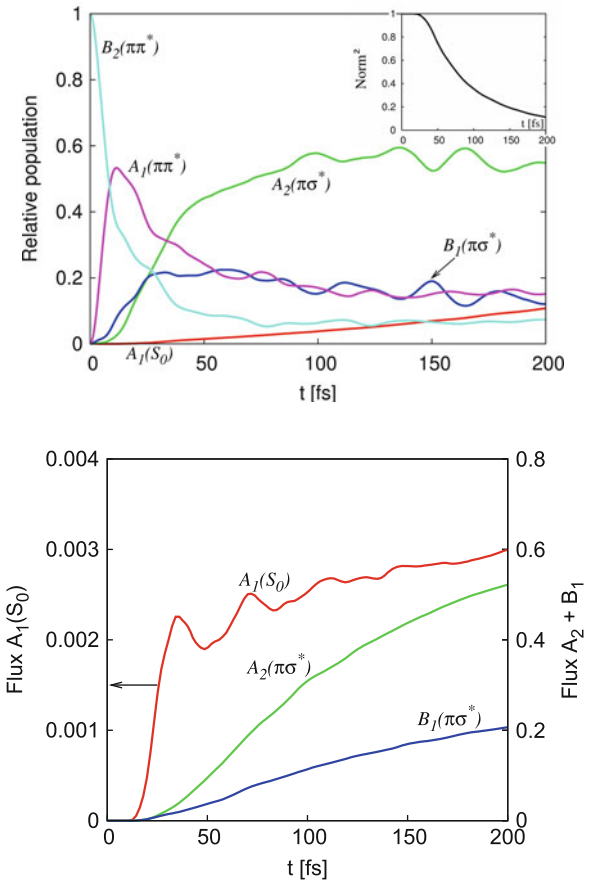

Fig. 6.19 Time-dependent electronic populations (*upper panel*) and reactive flux (*lower panel*) for the relevant states of pyrrole after excitation to the B_2 state of Fig. 6.18

this section I mention the extensive work by Domcke and Sobolewski to demonstrate the vital importance of nonadiabatic photochemistry governed by CoIns for the photostability of biologically relevant molecules and related processes [97, 98].

6.4 Outlook and Future Perspectives

In the present contribution I have attempted to give a condensed overview over our work on the quantum dynamics on vibronically coupled PES, considering pedagogic, historic, and systematic aspects in a balanced way. Time-independent and time-dependent phenomena have been addressed. While the examples discussed were necessarily not exhaustive, a set of representative cases has been selected which should cover the most important aspects and their interrelations. In particular, the quantum nature of the phenomena is apparent whenever the discrete level structure of the vibronically coupled states plays a role. Also regarding electronic

populations, and other time-dependent quantities not explicitly addressed here, a general-purpose, reliable, and accurate treatment requires to consider the quantum nature of the nuclear motion.

Special realizations of vibronic coupling systems, such as occur for well-localized, weakly coupled molecular subsystems have been touched upon only briefly, in Sect. 6.1.2.5. Another special case, that of light-induced CoIns [99, 100] has not been discussed above, but is expected to emerge as highly relevant in strong laser fields in the future. This may, of course, also apply to other realizations of specific systems, and likewise regarding their experimental detection.

General lines of future developments may concern, for example, applications in photobiology and the related design of methods dealing with increasingly larger systems. The use of the MCTDH method has already defined new limits in applications of the QVC scheme, where systems with more than 20 nuclear degrees of freedom can be treated accurately (including the introductory example of the butatriene cation discussed in Sect. 6.1) [101–103]. To carry the developments systematically further, more extended strategies may prove helpful or even crucial. As done in electronic structure theory, the whole system of interest may be divided into a central part and external parts treated with successively decreasing accuracy. For example, the inner part should be treated with the highest-level methods, allowing for finer details to be covered accurately. The next outer part could be described by the LVC or QVC approach, the subsequent one be considered as an "environment". For the latter, efficient effective-mode schemes have been introduced recently which capture the influence of many modes by a hierarchy of 3, 6 or 9 (etc.) modes which describes the evolution of the system for increasingly longer times (see, for example, [104–106]). For the most remote parts of the whole "aggregate" even more approximate schemes may prove useful. In line with the treatment of the nuclear dynamics, also the electronic-structure methodology is to be adapted. In this way it is hoped that the range of applicability of the quantum treatment, and the phenomena to be covered, can be continuously extended and the field may prove useful for many years to come.

Acknowledgements The author is indebted to L.S. Cederbaum, W. Domcke and S. Mahapatra for a long-term collaboration on the vibronic coupling problem. It is also a pleasure to acknowledge a fruitful cooperation with E. Gromov, S. Kopec, C. Lévêque and A. Komainda on current problems in the field.

References

1. Brogli F, Heilbronner E, Kloster-Jensen E, Schmelzer A, Manocha AS, Pople JA, Radom L (1974) The photoelectron spectrum of butatriene. Chem Phys 4:107
2. Cederbaum LS, Domcke W, Köppel H, von Niessen W (1977) Strong vibronic coupling effects in ionization spectra: the "mystery band" of butatriene. Chem Phys 26:169
3. Köppel H, Domcke W, Cederbaum LS (1984) Multi-mode molecular dynamics beyond the born-oppenheimer approximation. Adv Chem Phys 57:59
4. Domcke W, Köppel H, Cederbaum LS (1981) Spectroscopic effects of conical intersections of molecular potential surfaces. Mol Phys 43:851

5. Robb M, Bernardi F, Olivucci M (1995) Conical intersections as a mechanistic feature of organic photochemistry. Pure Appl Chem 67:783
6. Bernardi F, Olivucci M, Robb MA (1966) Potential energy surface crossings in organic photochemistry. Chem Soc Rev 25:321
7. Yarkony DR (1996) Diabolical conical intersections. Rev Mod Phys 68:985
8. Yarkony DR (1998) Conical intersections: diabolical and often misunderstood. Acc Chem Res 31:511
9. Domcke W, Yarkony DR, Köppel H (eds) (2004) Conical intersections: electronic structure, dynamics and spectroscopy. World Scientific, Singapore
10. Domcke W, Yarkony DR, Köppel H (eds) (2011) Conical intersections: theory, computation and experiment. World Scientific, Singapore
11. Tully JC (2012) Perspective: nonadiabatic dynamics theory. J Chem Phys 137:22A301
12. Köppel H, Cederbaum LS, Domcke W (1982) Strong nonadiabatic effects and conical intersections in molecular spectroscopy and unimolecular decay: $C_2h_4^+$. J Chem Phys 77:2014
13. Bersuker IB (2006) The Jahn-Teller effect. University Press, Cambridge
14. Cederbaum LS, Domcke W, Köppel H (1978) Jahn-Teller effect induced by non-degenerate vibrational modes in cumulenes. Chem Phys 33:319
15. Köppel H, Cederbaum LS, Domcke W, Shaik SS (1983) Symmetry breaking and non-born-oppenheimer effects in radical cations. Angew Chem Int Ed Engl 22:210
16. Eiding J, Schneider R, Domcke W, Köppel H, von Niessen W (1991) Ab initio investigation of the multi-mode dynamical Jahn-Teller effect in the ground state of the benzene cation. Chem Phys Lett 177:345
17. Atchity GJ, Xantheas SS, Ruedenberg K (1991) Potential energy surfaces near intersections. J Chem Phys 95:1862
18. Levine BG, Martinez T (2007) Isomerization through conical intersections. Annu Rev Phys Chem 58:613
19. Bonacic-Koutecky V, Koutecky J, Michl J (1987) Neutral and charged biradicals, zwitterions, funnels in s_1, and proton translocation: their role in photochemistry, photophysics, and vision. Angew Chem Int Ed Engl 26:170
20. Klessinger M, Michl J (1995) Excited states and photochemistry of organic molecules. VCH Publishers, New York
21. Sidis V (1992) Diabatic potential energy surfaces for charge-transfer processes. Adv Chem Phys 82:73
22. Pacher T, Cederbaum LS, Köppel H (1993) Adiabatic and quasidiabatic states in a gauge theoretical framework. Adv Chem Phys 84:293
23. Köppel H (2004) In: Domcke W, Yarkony DR, Köppel H (eds) Conical intersections: electronic structure, dynamics and spectroscopy. Word Scientific, Singapore, p 175
24. Cederbaum LS (2004) In: Domcke W, Yarkony DR, Köppel H (eds) Conical intersections: electronic structure, dynamics and spectroscopy. World Scientific, Singapore, p 3
25. Opalka D, Domcke W (2010) High-order expansion of $t_2 \times t_2$ Jahn-Teller potential-energy surfaces in tetrahedral molecules. J Chem Phys 132:154108
26. Zhu X, Yarkony DR (2012) Quasi-diabatic representations of adiabatic potential energy surfaces coupled by conical intersections including bond breaking: a more general construction procedure and an analysis of the diabatic representation. J Chem Phys 137:22A511
27. Thiel A, Köppel H (1999) Proposal and numerical test of a simple diabatization scheme. J Chem Phys 110:9371
28. Köppel H, Gronki J, Mahapatra S (2001) Construction scheme for regularized diabatic states. J Chem Phys 115:2377
29. Köppel H, Schubert B (2006) The concept of regularized diabatic states for a general conical intersection. Mol Phys 104:1069
30. Mahapatra S, Köppel H (1998) Spectra and time-dependent dynamics of h_3 near the conical intersection in the $(2p)1e'$ ground electronic manifold. J Chem Phys 109:1721

31. Mahapatra S, Köppel H, Cederbaum LS, StampfußP, Wenzel W (2000) Nonadiabatic wave packet dynamics on the coupled $\tilde{X}\ ^2a_1/\tilde{A}\ ^2b_2$ electronic states of no_2 based on new ab initio potential energy surfaces. Chem Phys 259:211
32. Lévêque C, Komainda A, Taieb R, Köppel H (2013) Ab initio quantum study of the photodynamics and absorption spectrum for the coupled 1^1a_2 and 1^1b_1 states of so_2. J Chem Phys 138:044320
33. Köppel H, Schubert B, Lischka H (2008) Conical intersections and strong nonadiabatic coupling effects in singlet-excited acetylene: an ab initio quantum dynamical study. Chem Phys 343:319
34. Carrington T (1972) Triatomic potential surfaces. A catalogue of intersections. Discuss Faraday Soc 53:27
35. Carrington T (1974) Geometry of intersecting potential surfaces. Acc Chem Res 7:20
36. Renner R (1934) Zur theorie der wechselwirkung zwischen elektronen- und kernbewegung bei dreiatomigen, stabförmigen molekülen. Z Phys 92:172
37. Truhlar DG, Mead CA (2003) Relative likelihood of encountering conical intersections and avoided intersections on the potential energy surfaces of polyatomic molecules. Phys Rev A 68:032501
38. von Neumann J, Wigner E (1929) Über das verhalten von eigenwerten bei adiabatischen prozessen. Phys Z 30:467
39. Teller E (1937) The crossing of potential surfaces. J Phys Chem 41:109
40. Lasorne B, Robb MA (2013) Non-adiabatic photochemistry: ultrafast electronic state transitions and nuclear wavepacket coherence. In Gatti F (ed) Molecular quantum dynamics: from theory to applications. Springer, Heidelberg
41. Jahn HA, Teller E (1937) Stability of polyatomic molecules in degenerate electronic states. I. Orbital degeneracy. Proc R Soc Lond A 161:220
42. Trofimov AB, Köppel H, Schirmer J (1998) Vibronic structure of the valence π-photoelectron bands in furan, pyrrole, and thiophene. J Chem Phys 109:1025
43. Köppel H, Gromov E, Trofimov A (2004) Multi-mode: multi-state quantum dynamics of key five-membered heterocycles: spectroscopy and ultrafast internal conversion. Chem Phys 304:35
44. Gomez-Carrasco S, Müller Th, Köppel H (2010) Ab initio study of the vuv-induced multistate photodynamics of formaldehyde. J Phys Chem A 114:11436
45. Köppel H, Cederbaum LS, Domcke W (1988) Interplay of Jahn-Teller and pseudo-Jahn-Teller vibronic dynamics in the benzene cation. J Chem Phys 89:2023
46. Döscher M, Köppel H, Szalay PG (2002) Multistate vibronic interactions in the benzene radical cation. I. Electronic structure calculations. J Chem Phys 117:2645–2656
47. Köppel H, Döscher M, Bâldea I, Meyer H-D, Szalay PG (2002) Multistate vibronic interactions in the benzene radical cation. II. Quantum dynamical simulations. J Chem Phys 117:2657
48. Longuet-Higgins HC (1975) The intersection of potential energy surfaces in polyatomic molecules. Proc R Soc Lond A 344:147
49. Mead A, Truhlar DG (1979) On the determination of born-oppenheimer nuclear motion wave functions including complications due to conical intersections and identical nuclei. J Chem Phys 70:2284
50. Longuet-Higgins HC, Öpik U, Pryce MH, Sack RA (1958) Studies of the Jahn-Teller effect. II. The dynamical problem. Proc R Soc A 244:1
51. Zwanziger JW, Grant ER (1987) Topological phase in molecular bound states: application to the $e \otimes e$ system. J Chem Phys 87:2954
52. Meiswinkel R, Köppel H (1990) A pseudo-Jahn-Teller treatment of the pseudorotational spectrum of na_3. Chem Phys 144:117
53. Schön J, Köppel H (1994) Femtosecond time-resolved ionization spectroscopy of na_3(b) and the question of the geometric phase. Chem Phys Lett 231:55
54. Ernst W, Rakowsky S (1995) Integer quantization of the pseudorotational motion in na_3(b). Phys Rev Lett 74:58

55. Köppel H, Cederbaum LS, Mahapatra S (2011) Theory of the Jahn-Teller effect. In: Quack M, Merkt F (eds) Handbook of high-resolution spectroscopy. Wiley, New York, p 1517
56. Köppel H, Gadea FX, Klatt G, Schirmer J, Cederbaum LS (1997) Multistate vibronic coupling effects in the k-shell excitation spectrum of ethylene: symmetry breaking and core-hole localization. J Chem Phys 106:4415
57. Kempgens B, Köppel H, Kivimäki A, Neeb M, Cederbaum LS, Bradshaw AM (1997) Core level energy splitting in the c 1s photoelectron spectrum of c_2h_2. Phys Rev Lett 79:3617
58. Dobrodey N, Köppel H, Cederbaum LS (1999) Vibrational structure of the o 1s ionization spectrum of co_2. Phys Rev A 60:1988
59. Ottiger P, Leutwyler S (2011) Excitonic splittings in jet-cooled molecular dimers. Chimia 65:228
60. Ottiger P, Leutwyler S, Köppel H (2012) Vibrational quenching of excitonic splittings in h-bonded molecular dimers: the electronic davydov splittings cannot match experiment. J Chem Phys 136:174308
61. Kopec S, Ottiger P, Leutwyler S, Köppel H (2012) Vibrational quenching of excitonic splittings in h-bonded molecular dimers: adiabatic description and effective mode approximation. J Chem Phys 137:184312
62. Müller H, Köppel H, Cederbaum LS (1994) Three-dimensional nuclear dynamics on conically intersecting potential energy surfaces of o_3^+ ($^2a_1 -^2 b_2$). J Chem Phys 101:10263
63. Müller H, Köppel H (1994) Adiabatic wave-packet motion on conically intersecting potential energy surfaces: the case of $so_2(^1b_1 -^1 a_2)$. Chem Phys 183:107
64. Mahapatra S, Köppel H (1998) Quantum mechanical study of optical emission spectra rydberg-excited h_3 and its isotopomers. Phys Rev Lett 81:3116
65. Haller E, Köppel H, Cederbaum LS (1985) The visible absorption spectrum of no_2: a three-mode nuclear dynamics investigation. J Mol Spectrosc 111:377
66. Vandaele AC, Hermans C, Fally S (2009) Fourier transform measurements of SO2 absorption cross sections ii. J Quant Spectrosc Radiat Transf 110:2115
67. Bruckmeier R, Wunderlich Ch, Figger H (1994) New experimental insight into the ground state potential surface of triatomic hydrogen. Phys Rev Lett 72:2250
68. Beck MH, Jäckle A, Worth GA, Meyer H-D (2000) The multiconfiguration time-dependent hartree (mcdth) method: a highly efficient algorithm for propagating wavepackets. Phys Rep 324:1
69. Meyer H-D, Gatti F, Worth GA (eds) (2009) Multidimensional Quantum Dynamics: MCTDH theory and applications. Wiley-VCH, Weinheim
70. Braitbart O, Castellucci E, Dujardin G, Leach S (1983) Radiationless transitions in excited electronic states of the benzene cation in the gas phase. J Phys Chem 87:4799
71. Maier JP (1979) Decay processes of the lowest excited electronic states of polyatomic radical cations. In: Ausloos P (ed) Kinetics of ion-molecule reactions. Plenum Press, New York, p 437
72. Bâldea I, Köppel H (2006) Multistate multimode vibronic dynamics: entanglement of electronic and vibrational degrees of freedom in the benzene radical cation. J Chem Phys 124:064101
73. Allan M, Maier JP, Marthaler O (1977) Radiative relaxation of the $\tilde{B}(\pi^{-1})$ excited electronic states of the radical cations of hexafluorobenzene, pentafluorobenzene, 1,2,3,4-, 1,2,3,5-, 1,2,4,5-tetrafluorobenzene, 1,3,5-, 1,2,4-trifluorobenzene and 1,3-difluorobenzene. Chem Phys 26:131
74. Cossart-Magos C, Cossart D, Leach S (1979) Emission spectra of seven fluorobenzene cations—dynamical Jahn-Teller effect in sym-$c_6f_3h_3^+$ and $c_6f_6^+$. Mol Phys 37:793
75. Sears TJ, Miller TA, Bondybey VE (1981) Laser excitation and emission spectra of the hexafluorobenzene cation in the gas phase. J Am Chem Soc 103:326
76. Cossart-Magos C, Cossart D, Leach S, Maier JP, Misev L (1983) High-resolution gas phase emission and laser induced fluorescence excitation spectra of 1,3,5-$c_6f_3h_3^+$ and 1,3,5-$c_6f_3d_3^+$: critical bands in the Jahn-Teller effect analysis. J Chem Phys 78:3673

77. Miller T, Bondybey VE (1983) The Jahn-Teller effect in benzenoid cations: theory and experiment. In: Molecular ions: spectroscopy, structure and chemistry. North-Holland, Amsterdam, p 201
78. Winkoun D, Champoulard D, Dujardin G, Leach S (1984) Vibrational dependence of electronic nonradiative processes in the $\tilde{B}$ state of $c_6f_6^+$ and 1,2,4,5-$c_6f_4h_2^2$. Can J Phys 62:1361
79. Klapstein D, Leutwyler S, Maier JP (1984) The $a_2'' \rightarrow e''$ transition of 1,3,5-$c_6f_3h_3^+$ and 1,3,5-$c_6f_3d_3^+$ in discharge and supersonic free jet emission. Mol Phys 51:413
80. Faraji S, Köppel H (2012) Multi-state vibronic interactions in the 1,2,3-trifluorobenzene radical cation. J Chem Phys 137:22A531
81. Gindensperger E, Bâldea I, Franz J, Köppel H (2007) Multi-state vibronic interactions in the fluorobenzene radical cation: the importance of quadratic coupling terms. Chem Phys 338:207
82. Faraji S, Köppel H (2008) Multistate vibronic interactions in difluorobenzene radical cations. I. Electronic structure calculations. J Chem Phys 129:074310
83. Faraji S, Meyer H-D, Köppel H (2008) Multistate vibronic interactions in difluorobenzene radical cations. II. Quantum dynamical simulations. J Chem Phys 129:074311
84. Schubert B, Köppel H, Lischka H (2005) A wave-packet simulation of the low-lying singlet electronic transitions of acetylene. J Chem Phys 122:184312
85. Fuji T, Suzuki Y, Horio T, Suzuki T, Mitric R, Werner U, Bonacic-Koutecky V (2010) Ultrafast photodynamics of furan. J Chem Phys 133:234303
86. Stenrup M, Larson Å (2011) A computational study of radiationless deactivation mechanisms of furan. Chem Phys 379:6
87. Gromov EV, Lévêque C, Gatti F, Burghardt I, Köppel H (2011) *Ab initio* quantum dynamical study of photoinduced ring opening in furan. J Chem Phys 135:164305
88. Sobolewski AL, Domcke W (2000) Conical intersections induced by repulsive $^1\pi\sigma^*$ states in planar organic molecules: malonaldehyde, pyrrole and chlorobenzene as photochemical model systems. Chem Phys 259:181
89. Cronin B, Nix MGD, Qadiri RH, Ashfold MNR (2004) High resolution photofragment translational spectroscopy of the near ultraviolet photolysis of pyrrole. Phys Chem Chem Phys 6:5031
90. Wei J, Riedel J, Kuczmann A, Renth F, Temps F (2004) Photodissociation dynamics of pyrrole: evidence for mode specific dynamics from conical intersections. J Chem Soc Faraday Discuss 127:267
91. Vallet V, Lan Z, Mahapatra S, Sobolewski AL, Domcke W (2004) Time-dependent quantum wave-packet description of the $^1\pi\sigma^*$ photochemistry of pyrrole. J Chem Soc Faraday Discuss 127:283
92. Vallet V, Lan Z, Mahapatra S, Sobolewski AL, Domcke W (2005) Photochemistry of pyrrole: time-dependent quantum wave-packet description of the dynamics at the $^1\pi\sigma^* - s_0$ conical intersections. J Chem Phys 123:144307
93. Barbatti M, Vazdar M, Aquino AJA, Eckert-Maksić M, Lischka H (2006) The nonadiabatic deactivation paths of pyrrole. J Chem Phys 125:164323
94. Faraji S, Vazdar M, Reddy S, Eckert-Maksic M, Lischka H, Köppel H (2011) Ab initio quantum dynamical study of the multi-state nonadiabatic photodissociation of pyrrole. J Chem Phys 135:154310
95. Balint-Kurti GG, Dixon RN, Marston CC (1990) Time-dependent quantum dynamics of molecular photofragmentation processes. J Chem Soc Faraday Trans 86:1741
96. Jäckle A, Meyer H-D (1996) Time-dependent calculation of reactive flux employing complex absorbing potentials: general aspects and application within the mctdh approach. J Chem Phys 105:6778
97. Sobolewski AL, Domcke W (2006) The chemical physics of the photostability of life. Europhys News 37:20

98. Sobolewski AL, Domcke W (2011) Efficient excited-state deactivation in organic chromophores and biologically relevant molecules. In: Domcke W, Yarkony DR, Köppel H (eds) Conical intersections: theory, computation and experiment. World Scientific, Singapore, p 51
99. Moiseyev N, Sindelka M, Cederbaum LS (2008) Laser-induced conical intersections in molecular optical lattices. J Phys B 41:221001
100. Halasz G, Sindelka M, Moiseyev N, Cederbaum LS, Vibok A (2012) Light-induced conical intersections: topological phase, wave packet dynamics and molecular alignment. J Phys Chem A 116:2636
101. Raab A, Worth GA, Meyer H-D, Cederbaum LS (1999) Molecular dynamics of pyrazine after excitation to the s2 electronic state using a realistic 24-mode model hamiltonian. J Chem Phys 110:936
102. Cattarius C, Worth GA, Meyer H-D, Cederbaum LS (2001) All-mode dynamics at the conical intersection of an octa-atomic molecule: Mctdh investigation on the butatriene cation. J Chem Phys 115:2088
103. Markmann A, Worth GA, Mahapatra S, Meyer H-D, Köppel H, Cederbaum LS (2005) Simulation of a complex spectrum: interplay of five electronic states and 21 vibrational degrees of freedom in $c_5h_4^+$. J Chem Phys 123:204310
104. Gindensperger E, Burghardt I, Cederbaum LS (2006) Short-time dynamics through conical intersections in macrosystems. I. Theory: effective-mode formulation. J Chem Phys 124:144103
105. Gindensperger E, Köppel H, Cederbaum LS (2007) Hierarchy of effective modes for the dynamics through conical intersections in macrosystems. J Chem Phys 126:034106
106. Nikoobakht B, Köppel H, Gindensperger E, Cederbaum LS (2012) Efficient computation of adiabatic electronic populations in multi-mode vibronic systems: theory, implementation, and application. J Chem Phys 137:114110

Non-adiabatic Photochemistry: Ultrafast Electronic State Transitions and Nuclear Wavepacket Coherence

7

Benjamin Lasorne, Graham A. Worth, and Michael A. Robb

Abstract

Chemistry that takes place exclusively in the ground electronic state can be well described by a reaction path in which the reactants pass over a transition state to the products. After photoexcitation, a molecule is in an excited electronic state and new topographical features joining different states, known as conical intersections, also need to be considered to describe the time-evolution from reactants to products. These intersections are due to the coupling between electrons and nuclei. In addition to providing new pathways, they provide a quantum-mechanical phase to the system which means that to describe the nuclear motion properly methods are required that include the resulting quantum-mechanical coherences in the nuclear motion. In this chapter, we review the nature and topography of conical intersections and simulation methods that have been developed to describe a molecule passing through one. These range from the full solution of the time-dependent Schrödinger equation to approximate methods based on Newtonian mechanics. Using examples the advantages and disadvantages of each are discussed.

B. Lasorne
Institut Charles Gerhardt Montpellier - CNRS - Université Montpellier 2, CC 15001 Place Eugène Bataillon, 34095 Montpellier, France
e-mail: blasorne@univ-montp2.fr

G.A. Worth (✉)
School of Chemistry, University of Birmingham, Edgbaston B15 2TT, UK
e-mail: g.a.worth@bham.ac.uk

M.A. Robb
Department of Chemistry, Imperial College London, South Kensington, London SW7 2AZ, UK
e-mail: mike.robb@imperial.ac.uk

F. Gatti (ed.), *Molecular Quantum Dynamics*, Physical Chemistry in Action,
DOI 10.1007/978-3-642-45290-1_7, © Springer-Verlag Berlin Heidelberg 2014

7.1 Introduction

The development of software able to efficiently treat a range of problems can have a huge effect on the development of science. This is exemplified in the field of chemistry where the existence of quantum chemistry programs such as Gaussian and Molpro has resulted in molecular structure calculations and energetic analysis becoming a ubiquitous tool providing mechanistic information in chemical research. Similarly, classical molecular dynamics programs such as CHARMm and AMBER have helped to focus thinking onto the dynamical nature of, in particular, condensed phase and biological processes.

Photochemistry, however, has mechanistic features that cannot be adequately described by standard quantum chemistry and classical molecular dynamics calculations. First, the reaction is initiated by absorption of a photon, which means we need to be able to treat excited electronic states. Second, it is found that there are molecular geometries where the excited- and ground state potential energy surfaces are close in energy or even meet. At these geometries the nuclear and electronic motions couple and the molecule undergoes *non-adiabatic* dynamics.

Given the importance of photochemistry in actual and emerging technologies, such as solar energy, photodynamic therapy, and optical storage, methods to understand and describe the energy flow in these molecular systems have an important role to play in the development of these fields of research. Also, time-resolved spectroscopy and coherent control experiments, in which a laser field is used to observe, or even direct, a molecule as it goes from photo-excited reactant to product are now well established. Being able to perform appropriate simulations is essential for understanding these experiments probing the fundamental behaviour of molecules.

In non-adiabatic dynamics it is necessary to treat the nuclei as moving over a set of coupled potential energy surfaces rather than the single surface of classical molecular dynamics. The surfaces can then approach to form *avoided crossings* or meet as *conical intersections* that provide pathways where the initially excited molecule can cross back to the ground electronic state in a non-radiative manner. This crossing is particularly efficient at a conical intersection, which is why these features play a central role in the mechanistic description of photochemistry, in a similar way to the role played by the transition state in thermal chemistry.

The recent availability of theoretical developments implemented in widely available quantum chemistry software means that the theoretical study of non-adiabatic chemistry is also "coming of age", with many applications oriented practitioners now using calculations to support their ideas and experiments. For example, an algorithm for finding the minimum energy point on a conical intersection [1] was made available in Gaussian in the 1990s, and most quantum chemistry codes now have this feature.

Just knowing the positions and energies of conical intersections is, however, not enough to understand the mechanism of a reaction and dynamical information is also required. For example, how efficient the crossing process is requires knowledge

of the time scale and population transfer at an intersection. Here, dynamics methods embedded in quantum chemistry programs can be used to great effect once adapted to treat non-adiabatic processes. For example, the direct dynamics methods developed by Schlegel in the Gaussian program have been adapted to non-adiabatic dynamics since the late 1990s [2].

Just as for thermal chemistry, for photochemistry the easiest and most pictorial dynamics uses classical trajectories. The non-adiabatic process is then modelled by computing the probability of hopping between the surfaces using some approximate solution of the Schrödinger equation [3, 4]. From the starting point given by absorbing a photon, the trajectories thus show where the system can go, and where and when it can cross to the ground state. The hopping probabilities then give how efficient this process is. For an excellent overview of non-adiabatic dynamics from the semi-classical perspective the reader may consult the recent review of Tully [5] and the many papers in the same edition of J. Chem. Phys.

Trajectory surface hopping is, however, only an approximate treatment of the dynamics and the full quantum dynamics description requires a full solution of the time-dependent Schrödinger equation (TDSE) [6]. The main failure of the semi-classical surface hopping approach is that the different trajectories are independent and so the coherence of the nuclear motion as it passes through a conical intersection is lost. How important is this coherence? The answer to this is not known in general, but coherence will play a role in the short-term dynamics of phenomena. For example, recrossing at an intersection is known from full quantum dynamics simulations, but is not seen in surface hopping. Such methods are therefore potentially essential for understanding short time-scale fundamental processes such as electron transfer and proton transfer–essential for many chemical and biological systems. Furthermore, recent experiments have implicated nuclear coherence as being involved in certain biological processes over a long time-scale [7, 8].

The computational resources required to solve the TDSE meant that until recently only a few atoms could be treated in this way. However, programs to treat molecular systems with quantum dynamics are now becoming more widely used. The Heidelberg MCTDH package is probably the only quantum dynamics code that has been developed with the aim of generality [9]. Recent advances in algorithms such as the development of the variational multi-configuration Gaussian (vMCG) method [10, 11] and multiple spawning [12, 13] also are moving quantum dynamics to become a mainstream simulation tool and comparisons with the simpler surface hopping can now be made [14].

This chapter sets out to focus on the information available from computational tools to describe non-adiabatic dynamics and photochemical reactivity. From a general mechanistic point of view the non-adiabatic event takes place near a conical intersection. It is the "shape" of the extended seam of the intersection and its position on the reaction path that controls the outcome of a photochemical reaction. The concepts of this topic are reviewed, with examples, in Sect. 7.2. In Sect. 7.3 we introduce the main methods for performing dynamics using a potential derived from quantum chemistry electronic structure methods, starting from an exact solution of

the TDSE and moving to more approximate techniques. In Sect. 7.4 we "showcase" these methods with some representative examples.

7.2 Classifying Conical Intersections: Shapes and Positions

We shall begin our exploration of conical intersections with an example constructed from a classic textbook photochemistry case, the 2+2 cyclo-addition of two ethylene molecules [15–17]. The potential energy surface is illustrated schematically in Fig. 7.1. We shall consider the face to face approach (centred on points with geometry A or A′ in Fig. 7.1a) where the new σ-bonds are formed synchronously, as well as a bi-radical approach (passing through the geometry C in Fig. 7.1a), where one σ-bond is formed first to yield a diradical intermediate. The coordinate that connects the two approaches is a trapezoidal distortion coordinate A–C. The potential energy surface in the space of these two coordinates for the ground and excited states is shown in Fig. 7.1. In thermal chemistry, reactivity is confined to the ground state or the lower potential energy surface. In photochemistry, the reaction begins by excitation from the ground state potential energy surface to the excited state potential energy surface. For our purposes, we imagine that the starting point of the photochemical cyclo-addition, the so-called Franck–Condon geometry, corresponds to two isolated ethylene molecules, and the product is cyclobutane in a square planar geometry.

We can use the potential surfaces shown in Fig. 7.1 to compare and contrast what might happen in thermal and photochemical reaction, and thus to illustrate the role of a conical intersection. We have distinguished two molecular motions X_1 and X_2 in which to plot the surfaces. The variable X_1 is a reaction coordinate corresponding to the approach of the two ethylenes passing via point A A′. The variable X_2 is a rhomboidal distortion passing through E and connecting A and C. As we will presently discuss, a photochemical mechanism via a conical intersection must involve two distinguished coordinates, while a transition state associated with a thermal reaction is associated with one distinguished coordinate, X_1 in this case, corresponding to the reaction path.

In a 2+2 thermal reaction, there are two possible transition states, shown as A′ for the synchronous reaction, where both bonds are formed simultaneously, and C for the asynchronous reaction where one bond was formed first. The Woodward–Hoffman (WH) [17] rules predict that the asynchronous reaction (via C) has the lower energy. Now let us examine a region of the potential energy surface along a line connecting the two transition states A′ and C. We can see that the ground state energy passes through a very high-energy point E where the ground state and excited state become degenerate. This is known as a conical intersection [18]. Of course, a thermal reaction would not pass close to point E that is so high in energy. At this point, we also observe that the double cone at point E requires two coordinates X_1X_2 to describe it.

Now, let us consider the photochemical reaction. The reaction begins with photoexcitation at the FC geometry, corresponding to two separated ethylenes. The

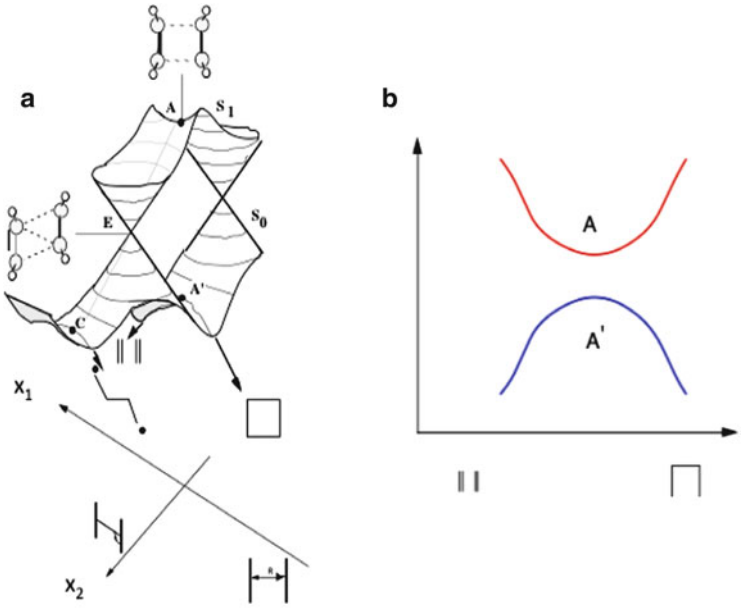

Fig. 7.1 Cartoons of the potential energy surfaces describing the 2+2 cyclo-addition of two ethylene molecules (adapted from [16])

reaction would progress along a coordinate leading to a minimum A, if the system were constrained to have a rectangular geometry. However, the potential energy is unstable along this coordinate with respect to rhomboidal distortion. Notice that along a reaction path directed towards the point E, there is a negative direction of curvature so that A, rather than being a local minimum, is in fact, a transition state along the reaction path leading to the point E. Thus the geometrical changes corresponding to reaction paths on the excited state are quite different than on the ground state. On the one hand, the motion which brings the two ethylenes together along the coordinate which preserves rectangular symmetry is a maximum on the ground state involving a transition state at A′ while it is a local minimum on the excited state at A. This one-dimensional picture is shown in Fig. 7.1b. However, this excited state reaction path is not stable, and a lower energy pathway is available which involves motion along the rhomboidal distortion coordinate, leading via point E to the ground state asynchronous pathway at point C. Thus, reaction pathways (the geometries traced out) along excited state or ground state evolution are in general very different in the ground and excited states. Also, we can see from Fig. 7.1 that the reaction path from the excited state to the ground state passes via a point E where the two states have the same energy. This is the point where radiationless decay takes place and the system moves from the excited state to the ground state without emitting light. This type of degenerate point is known as a conical intersection [17] and we will have more to say about that as we continue our development.

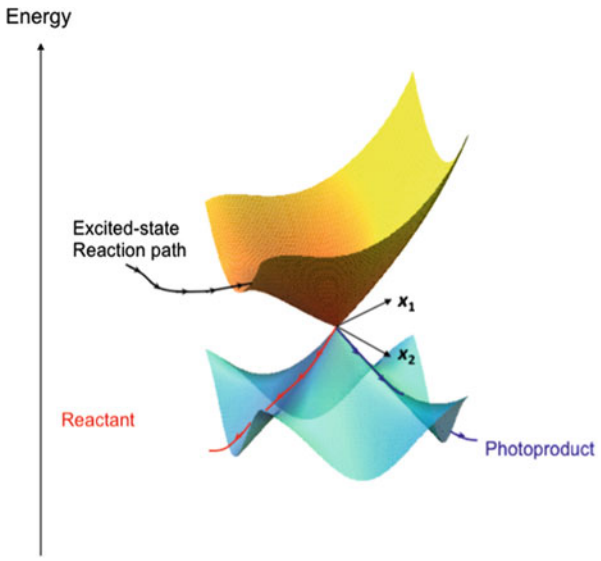

Fig. 7.2 Cartoon of a "classic" double cone conical intersection, showing the excited state reaction path and two ground state reaction paths (adapted from Paterson et al. [21])

Before leaving discussion of Fig. 7.1 it is important to mention that this figure is a "cartoon". With present-day computational methods, one computes the geometries of points where the gradient is zero, such as minima and transition states. One can also compute the energies and geometries of low-energy conical intersection points such as E [19]. The cartoon that one draws in Fig. 7.1 is intended to convey the shape of the potential energy surface and the way in which various critical points (minima, etc.) are connected rather than presenting the results of actual computations on a grid.

If the mechanistic information just discussed in Fig. 7.1 is to be really useful then it must be an intrinsic property of the chromophores themselves, i.e. the two ethylene molecules. For example, it is the key feature in intra-strand thymine dimerisation and these dimers can disrupt the function of DNA and trigger complex biological responses, including apoptosis, immune suppression, and carcinogenesis. One can identify the geometry corresponding to the point E in Fig. 7.1 as well as the computed directions [20] X_1 and X_2 for the 2+2 cyclo-addition reaction of two thymine molecules.

Using Fig. 7.1 we briefly introduced the idea that a conical intersection requires two geometrical coordinates in order to define the double cone. We now extend these ideas more rigorously.

In Fig. 7.2, we show a general cartoon of a conical intersection. In addition to the energy, the double cone like structure is defined by two geometrical coordinates X_1 and X_2 (first introduced in Fig. 7.1). Thus, as one moves away from the apex of the cone, the degeneracy is lifted. In Fig. 7.3 we show another important effect,

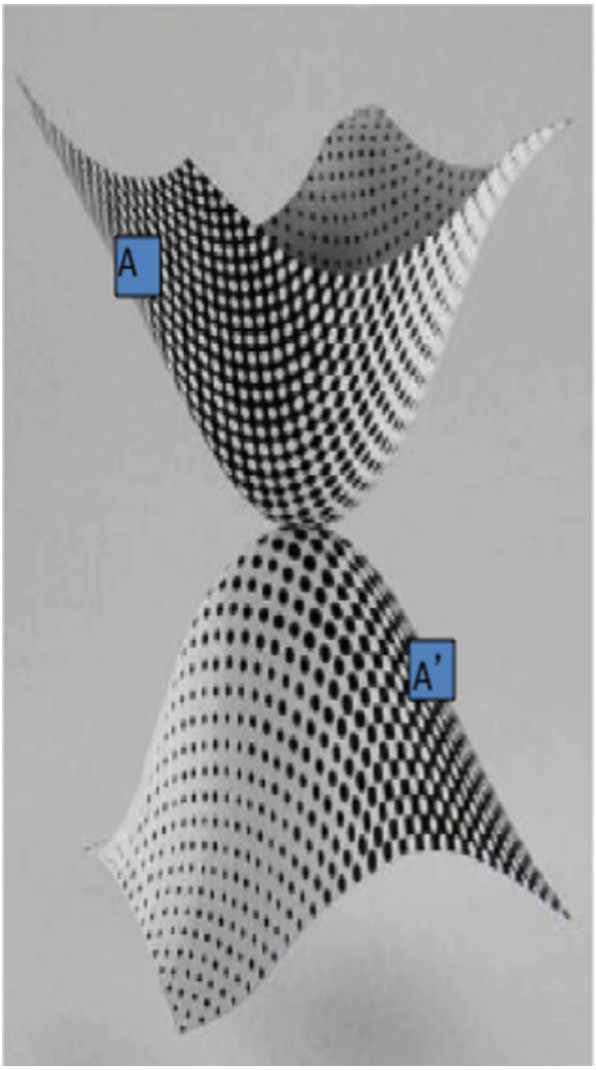

Fig. 7.3 A representation of the electronic wavefunction around a conical intersection. The *black* and *white tessellations* correspond to different "diabatic states"

the nature of the wavefunction represented by a superimposed tessellation pattern. The tessellation indicates the nature of the diabatic states at any point on the conical intersection; pure white is one diabat and pure black a different diabat. The essential idea is that if one takes a point on the upper surface and suppose that it has electronic structure A, then the corresponding point A′ on the lower surface, related by inversion (180° rotation plus reflection in the X_1X_2 plane) has the same electronic structure. Similarly, at an avoided crossing (e.g. Fig. 7.1) one

has an overall wavefunction composed of both states $\Psi_+ = c_1\psi_{\text{Black}} + c_2\psi_{\text{White}}$ on the upper surface and $\Psi_- = c_1\psi_{\text{White}} - c_2\psi_{\text{Black}}$ on the lower surface.

The two coordinates X_1X_2 thus play a central role in mechanistic photochemistry. In a thermal reactivity problem, we are normally interested in the energy and the reaction path. In a photochemical problem, where the reaction path passes through a conical intersection, we are interested in the energy and *two* coordinates X_1 and X_2. Thus the thermal reaction path, a single coordinate, gets replaced in photochemistry, by the two coordinates X_1 and X_2. In a thermal reactivity problem, the reaction path is precisely defined at the transition state itself. It is just the direction associated with the normal coordinate corresponding to the imaginary frequency. The imaginary frequency is associated with the curvature of the potential energy surface at the transition state (i.e. the second derivative of the energy). In contrast at a conical intersection, the two directions X_1 and X_2 are defined by the equations

$$x_1^{(i\gamma)} = \frac{\partial\left(E_{\text{B}} - E_{\text{A}}\right)}{\partial\xi_{i\gamma}} \tag{7.1a}$$

$$x_2^{(i\gamma)} = \frac{\partial\left\langle\Psi_{\text{A}}\left|\widehat{H}\right|\Psi_{\text{B}}\right\rangle}{\partial\xi_{i\gamma}}, \tag{7.1b}$$

i.e. associated with gradients and transition gradients. They are usually referred to as the gradient difference and derivative coupling vectors.

In Eq. (7.1), states A and B are the two electronic states: ground and excited states associated with the conical intersection, $\xi_{i\gamma}$ is the γth mass-weighted Cartesian coordinate of the ith atom, the index i labels the N atoms and γ the Cartesians components, x, y, and z. These quantities are in principle obtainable only from a theoretical calculation. Nevertheless, as we shall discuss subsequently, they have a simple interpretation and one can often make a reasonable guess as to the nature of these two vectors using qualitative valence bond theory.

The coordinates X_1 and X_2 are precisely defined quantities that can be computed explicitly [22] from electronic structure theory. Similarly, the apex of the cone corresponds in general to an optimised molecular geometry [23]. (See also the more recent works of Sicilia et al. [24], Martinez et al. [25] and Thiel et al. [26].) The shape or topology in the region of the apex of the double cone will change from one photochemical system to another [27], and it is the generalities associated with the shape that form part of the mechanistic scenario that we will discuss. All ideas follow from a development of a two-level quadratic expansion (for S_1 and S_0) simultaneously. Such an expansion involves gradients (X_1) and off-diagonal gradients (X_2). However, such developments require more specialised knowledge and for details the reader is referred to the literature [21, 24, 27–33].

Now let us turn to the situation where the reaction path does not lie in the plane X_1X_2. In this case we need three coordinates to define the course of a photochemical reaction through a conical intersection: the reaction path X_3 and the coordinates X_1X_2. In order to draw a picture similar to Fig. 7.2, we would need four dimensions.

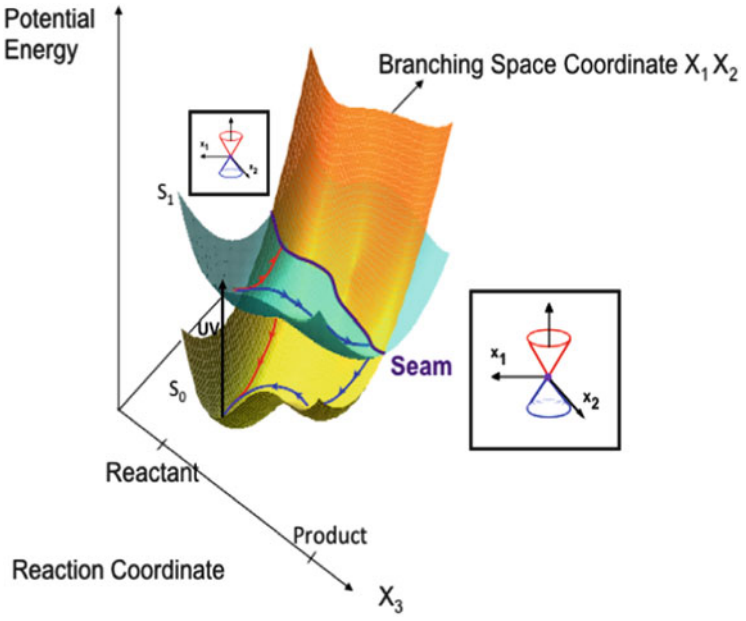

Fig. 7.4 The conical intersection hyperline traced out by a coordinate X_3 plotted in a space containing the coordinate X_3 and one coordinate from the degeneracy-lifting space X_1 X_2 (adapted from Paterson et al. [21])

Thus for simplicity, we will plot the energy as a function of one ($X_{1/2}$) of the two coordinates X_1 or X_2 and the reaction path X_3. The corresponding cartoon is shown in Fig. 7.4. In this case, the conical intersection appears as a line or a seam which we shall refer to as a *conical intersection seam*. In Fig. 7.4, we use the coordinate X_3 to denote the reaction coordinate, and the axis ($X_{1/2}$) labelled "branching space coordinate X_1 X_2" is designed to indicate a vector which is a linear combination of X_1 X_2. Motion along this composite coordinate, $X_{1/2}$, is at right angles to the seam, and the degeneracy is lifted. In the figure, we have shown the double cone along this seam in order to remind ourselves that there are three geometrical coordinates involved in this picture.

Thus, Fig. 7.4 illustrates the general situation where the reaction path is not contained in the branching plane, X_1 X_2. There are many examples where this type of topology presents itself [34–38].

In Figs. 7.2 and 7.4 we have illustrated cartoons for different ways of visualising the topology of a conical intersection. In general, there are two coordinates X_1 and X_2, which form what is known as the branching space where the degeneracy of the common intersection is lifted. Then we introduced a third coordinate as X_3, which we referred to as the reaction coordinate. Of course, there are more than three geometrical variables in the typical photochemical reactivity problem. In modern computational methods one uses all the molecular degrees of freedom in

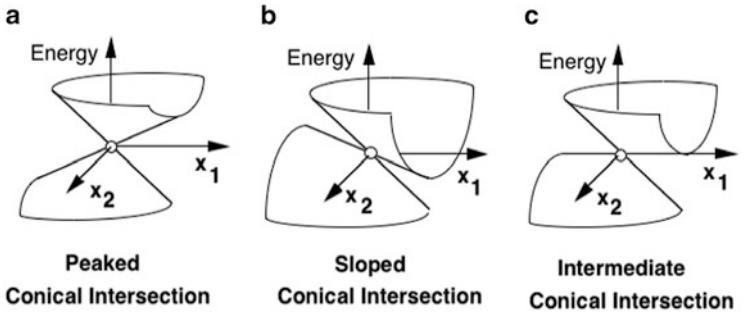

Fig. 7.5 Classification of conical intersections according to their local topography (from [27, 39])

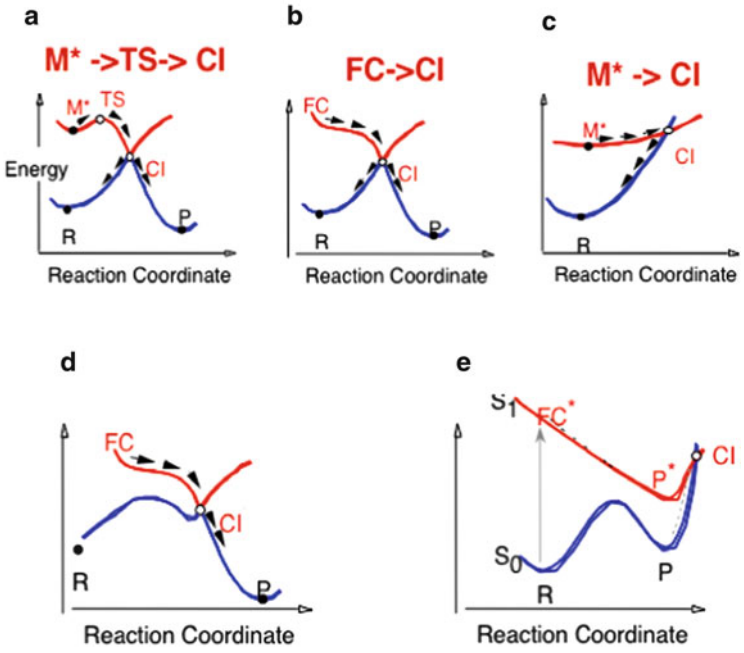

Fig. 7.6 Different topographies of conical intersections along a reaction coordinate (extended version adapted from [39])

numerical computations. Then, a posteriori, we identify three variables to visualise and understand any particular problem. However, the two directions X_1 and X_2 computed according to Eq. (7.1) are precisely defined.

To conclude this section on local topology we briefly discuss two other concepts: the *slope* [27] of the conical intersection and the *position of the conical intersection on the reaction coordinate* [39]. These concepts are illustrated in Figs. 7.5 and 7.6.

In Fig. 7.5 we indicate the slope of the conical intersection [27]. Of course X_3 does not appear on these figures. The peaked intersection corresponds to the

simple case where the system simply "falls down" from one state to the other. The sloped/intermediate intersection is particularly interesting mechanistically. This type of topology is associated with photostability (i.e. no new chemical species is produced after decay from the conical intersection) and we will return to discuss this in our section on case studies. However, it should be apparent that in a sloped intersection a trajectory may recross the apex of the cone many times before decaying to the ground state energy sheet.

The position of the surface crossing and whether or not it is preceded by a local minimum on the excited state reaction path is illustrated in Fig. 7.6. Comparing Fig. 7.6a versus b we can examine the competition between passing over a barrier when a conical intersection is separated from a local minimum (Fig. 7.6a) versus passing directly from the Franck–Condon region of the potential energy surface to the conical intersection (Fig. 7.6b). In the first case, there must be a competition between fluorescence decay at the minimum versus passage over the barrier to the conical intersection. In the second case there is no barrier and the system decays on the time scale of vibrational motion after excitation to the Franck–Condon region: an ultrafast reaction. In Fig. 7.6c we show the sloped conical intersection discussed in the previous figure. It is now obvious that such a topology must be associated with photostability because the excited state intermediate when it decays at the conical intersection returns to the ground state intermediate. Figures 7.6d and 7.6e are intended to illustrate, in a schematic way, the effect of the position of the surface crossing on the reaction coordinate. In Fig. 7.6d we illustrate the case where the surface crossing occurs on the product side of a ground state transition state. In such a case one has an adiabatic reaction, and the decay to the ground state takes place in the product region. In Fig. 7.6e we show the situation with an adiabatic reaction terminating at a sloped conical intersection.

Thus in the same way that one can characterise topographical features on a potential energy surface where the gradient goes to zero at maxima and minima, it is possible to systematically map out and characterise the seam. These ideas lie beyond the scope of this review. However, they can be useful in further characterising mechanistic effects [21, 24, 27–33, 40–44].

7.3 Simulating Non-adiabatic Transitions

When a molecule has a configuration near to that of a conical intersection it is able to undergo non-adiabatic transitions, whereby it can move from one electronic state to another instantaneously in a radiationless manner. These transitions are due to coupling between the nuclear and electronic motion and as a result are quantum-mechanical processes. Thus to simulate them requires solving the TDSE

$$i\hbar\frac{\partial\Psi}{\partial t} = \widehat{H}\Psi \tag{7.2}$$

for the nuclear wavefunction Ψ to capture the evolution of the molecular system as it flows over the coupled potential energy surfaces.

The potential energy information is contained in the Hamiltonian, $\widehat{H}$, which can be written in two different ways: the adiabatic or diabatic form [6, 45]. In the adiabatic form the coupling is part of the kinetic energy operator and the potential energy surfaces are simply ordered in energy. In the diabatic form the coupling is part of the potential operator and potential energy surfaces can be associated with an electronic configuration or molecular property. The relationship between the two forms is not straightforward, but the adiabatic picture is that used in quantum chemistry, while in general the TDSE is solved in the diabatic picture as in the adiabatic picture conical intersections result in singularities that provide problems.

Over the last 20 years powerful methods to solve the TDSE have been developed [46, 47]. These are based on using a grid-based representation of the wavefunction and Hamiltonian and have provided detailed descriptions of non-adiabatic events. Unfortunately, such numerically exact solutions of the TDSE require huge computer resources as they scale exponentially with the number of degrees of freedom and approximations must be introduced to treat systems with more than 20 atoms, which include the majority of photochemistry.

There are two classes of approximations that are commonly used. The first is to use what are called Gaussian wavepackets (GWPs) to describe the wavefunction. This wavepacket description means a grid is not required, and the scaling is improved. Often the GWPs follow classical trajectories and other approximations are made to improve efficiency.

The second approach is to discretise the wavepacket into a "swarm of trajectories" that evolve according to Newton's equations of motion. Non-adiabatic events are then simulated either by "hopping" between potential energy surfaces, in what is termed trajectory surface hopping, or by each trajectory carrying an evolving weight associated with each potential energy surface in Ehrenfest dynamics.

In addition to the bottleneck due to memory requirements, grid-based quantum dynamics suffers from the basic problem that they are global methods, i.e. the potential energy surfaces and wavefunctions must be defined globally before the propagation can be made. Calculating accurate global potential energy surfaces, particularly for multi-state calculations where couplings are also required, is a huge challenge. The more approximate GWP- and trajectory-based methods have the advantage that they can be used in a direct dynamics approach in which the potential energy surfaces are calculated on-the-fly as and when required.

7.3.1 Grid-Based Quantum Dynamics

The wavefunction can be expanded in a basis set of functions for each degree of freedom, $\{\chi\}^{(\kappa)}$. The wavefunction is then written

$$\Psi = \sum_{j_1 j_2 \cdots j_f} A_{j_1 j_2 \cdots j_f}(t) \chi^{(1)}_{j_1}(q_1)\, \chi^{(2)}_{j_2}(q_2) \ldots \chi^{(f)}_{j_f}(q_f) \tag{7.3}$$

And the TDSE is reduced to solving a set of equations for the time-evolution of the expansion coefficients

$$i\dot{A}_I = \sum_J H_{IJ} A_J \tag{7.4}$$

where $J = j_1 j_2 \ldots j_f$ is a composite index and H_{IJ} are the matrix elements of the Hamiltonian represented in the basis set. These basis functions may be harmonic oscillator eigenfunctions or some other suitable set. Discrete variable representations are particularly useful as they allow the wavefunction to be mapped onto a spatial grid as well as providing accurate integrals of the matrix elements (see Appendix B in [49]).

Equation (7.4) is very easy to implement on a computer. The matrix is built once at the beginning and then straightforward matrix–vector operations are used to propagate the wavefunction forwards in time. A number of integration schemes have been developed to do this [47]. The scaling problem is, however, obvious. For a system with f degrees of freedom and N basis functions for each there are N^f expansion coefficients that must be propagated. As of the order of 50–100 basis functions per degree of freedom are required, these numerically exact calculations are in general restricted to 3–4 atom systems.

The multi-configuration time-dependent Hartree (MCTDH) method [48–50] is a grid-based method that is able to treat larger systems. It uses a similar wavefunction ansatz

$$\Psi = \sum_{j_1 j_2 \cdots j_f} A_{j_1 j_2 \cdots j_f}(t) \varphi_{j_1}^{(1)}(q_1, t)\, \varphi_{j_2}^{(2)}(q_2, t) \ldots \varphi_{j_f}^{(f)}\left(q_f, t\right) \tag{7.5}$$

But now the basis functions are also time-dependent. The resulting description is more compact as the basis functions follow the evolving wavepacket using variationally derived equations of motion and so effort is not wasted describing regions of space where the wavefunction is negligible. Using this method up to 15 atoms may be treated [51].

The method is still a grid-based one as the basis functions (known as single-particle functions) are still described using time-independent DVR functions

$$\varphi_i^{(\kappa)} = \sum_\alpha c_{i\alpha} \chi_\alpha^{(\kappa)} \tag{7.6}$$

It also has a higher overhead than the standard numerically exact method as the Hamiltonian matrix elements are also now time-dependent and the potential energy function requires a special form for maximum efficiency.

7.3.2 Gaussian-Based Quantum Dynamics

Methods based on GWPs, also known as coherent states (CSs), all derive from the seminal work of Heller [52]. They can capture the full quantum-mechanical character of molecular processes and promise better scaling than grid-based methods. A big advantage is that they allow direct dynamics approaches [6], whereby the potential energy and its derivatives with respect to the nuclear coordinates are calculated "on-the-fly", such as in trajectory-based classical and semi-classical dynamics (e.g. ab initio molecular dynamics and trajectory surface hopping). This strategy thus promises reasonable multidimensional quantum dynamics simulations at low effort. They may, however, suffer from numerical problems in terms of convergence, which often restricts them to semi-quantitative applications, as opposed to the more involved—but more accurate—grid-based methods.

The ideal field of application of Gaussian-based quantum dynamics methods is certainly non-adiabatic photochemistry [53]. In this context, they hold a midway position between grid-based quantum dynamics methods and trajectory-based semi-classical methods. The former are plagued by the time and memory requirements of first generating analytical multidimensional expressions for the potential energy surfaces and non-adiabatic couplings. This is an involved task that often implies the preliminary identification of a subset of active nuclear coordinates and a simplified model for the treatment of the remaining degrees of freedom. In contrast, semi-classical methods, such as trajectory surface hopping or Ehrenfest dynamics, are easier to utilise and yield correct estimates for the characteristic rates and efficiencies of non-adiabatic transitions. However, they remain limited to describing the very first radiationless events because of their inadequate treatment of quantum coherence or entanglement (excess or lack of) among the coupled electronic states.

GWP or CS methods have in common the expansion of the total wavepacket in a basis set of multidimensional time-dependent Gaussian functions, $g_j^{(s)}(\mathbf{R}, t)$, on one or several coupled electronic states, $|s; \mathbf{R}\rangle$,

$$|\Psi(\mathbf{R}, t)\rangle = \sum_s \sum_j A_j^{(s)}(t) g_j^{(s)}(\mathbf{R}, t) |s; \mathbf{R}\rangle \tag{7.7}$$

where s denotes the state index and $\mathbf{R}$ the nuclear coordinate vector. In the majority of these methods the centres of the frozen-width Gaussian basis functions follow classical trajectories and so are unable to model individually certain situations such as tunnelling. The latter is retrieved through the quantum superposition of trajectories of various total energies through the coupled propagation of the expansion coefficients, $A_j^{(s)}(t)$. These evolve according to a secular formulation of the TDSE in a non-orthogonal basis set.

The full multiple spawning (FMS) method [12, 13, 54–58] is an adaptive-basis-set approach that uses classically driven Gaussian functions. Simulations start with a relatively small basis set on the initial electronic state. The spawning procedure

generates extra basis functions if branching events require them, such as when a conical intersection is reached, and population must be transferred to the other electronic state. This method will in principle be numerically exact at convergence. The multiple independent spawning (MIS) approach is an approximate classical-like variant based on uncoupled trajectories.

In the variational multi-configuration Gaussian wavepacket (vMCG) method [10, 11, 59–63] the basis functions follow coupled "quantum trajectories" whereby the mean positions and momenta are treated as variational basis-function parameters that evolve according to the Dirac–Frenkel principle applied to the TDSE. Each basis function directly simulates quantum phenomena in a rigorous way, and the method thus promises much faster convergence than classical-trajectory-based methods due to a better sampling of the phase space.

Somewhat midway between FMS and vMCG techniques, the multi-configurational Ehrenfest (MCE) method [64–68] assumes Gaussian basis functions following coupled Ehrenfest trajectories that are thus governed by a weighted average of several potential energies. Ehrenfest trajectories are more quantum in essence than FMS trajectories but are generated from an approximate solution to the vMCG equations of motion where only the leading term is accounted for and thus the Gaussian functions again follow classical trajectories. The multi-configurational character of the description relieves them of the typical issue of contradictory average gradients in single-configuration Ehrenfest dynamics.

The limited spatial expansion of frozen-width Gaussian functions means that a local harmonic approximation of the potential energy surface around the centre of each GWP is a decent approximation ("thawed" Gaussian functions have proved to be inadequate numerically due to excessive spreading compared to the range of validity of the local harmonic approximation). The potential energy and its derivatives can thus be calculated along the trajectories followed by their centres. Such treatments free quantum dynamics of the numerically expensive and time-consuming requirement of calculating and fitting potential energy surfaces beforehand. The corresponding extensions of the three aforementioned methods are termed ab initio multiple spawning (AIMS), direct dynamics vMCG (DD-vMCG), and ab initio MCE (AI-MCE).

Direct dynamics implementations of Gaussian-based quantum dynamics methods are a turning point from a computational perspective. Fully accounting for the quantum nature of Gaussian basis functions over their widths requires repeated evaluations of gradients and Hessians at their centres. Obviously, despite the exponential scaling of grid-based methods, long-lived trajectories also require a large number of electronic-structure calculations, which can also happen to be a practical bottleneck. However, using Hessian-update procedures and/or a physically sound hierarchical description based on a QM/MM treatment in lieu of fully ab initio calculations is a promising strategy for the adequate description of quantum effects in large systems or medium-sized systems embedded in an environment [69].

7.3.3 Trajectory-Based Semi-classical Dynamics

The lowest level of approximation that can be used to solve the TDSE is also the one that gives the best scaling with system size. Using a polar representation of the wavefunction, in the classical limit $\hbar \to 0$, it is possible to model the evolving density

$$\rho\left(\mathbf{R}, t\right) = \Psi^{*}\left(\mathbf{R}, t\right) \Psi\left(\mathbf{R}, t\right) \tag{7.8}$$

as a set of trajectories that follow classical equations of motion [70], often referred to as a swarm, i.e. for each coordinate

$$M\,\ddot{R} = -\frac{\partial V}{\partial R} \tag{7.9}$$

This approach, originated by Bohm, has the further advantage that it can be used in direct dynamics in a straightforward way: calculating the potential and gradient at each point along the trajectories is straightforward using quantum chemistry methods.

Initial conditions for the trajectories must be chosen by sampling an appropriate distribution. To sample a particular initial wavefunction, the ground vibrational state, for example, the Wigner distribution can be used [6]. This is a transformation of the density in configuration space to a set of phase space variables and so randomly sampling this distribution provides trajectories that effectively discretise the quantum density. For states where the Wigner function has negative regions that cannot be interpreted as a probability, the Husimi function may be used. Alternatively, simpler sampling can be used based on a single representative trajectory or on a microcanonical distribution that can include the zero-point energy in an approximate way.

What happens if more than one potential energy surface is present? The standard way to tackle this problem is to use "surface hopping", which recognises that the main result of non-adiabatic coupling is to effect a transfer of population between states in the region of the coupling [71–74]. Each trajectory is propagated on a surface until it reaches a non-adiabatic region where the coupling is non-negligible. The trajectory may then hop to the other surface with a probability calculated to model the quantum-mechanical population transfer. This inclusion of some degree of quantum-mechanical behaviour to the nuclear motion is why these methods are referred to as semi-classical.

There are a variety of ways in which the hop can be calculated. The most commonly used variant is Tully's least switches algorithm [73]. This is designed to reproduce the correct electronic state populations with the least number of hops. The probability of changing from electronic state 2 to 1 is here given by

$$P_{2\to 1} = -\frac{\mathrm{d}}{\mathrm{d}t} \log |c_2|^2 \Delta t \tag{7.10}$$

where c_2 is the coefficient of the upper state component in the electronic wavefunction

$$\Psi_{\mathrm{el}}(\mathrm{r}, t) = c_1(t)\psi_1(\mathrm{r}) + c_2(t)\psi_2(\mathrm{r}) \tag{7.11}$$

and Δt the step size in the propagation. A simpler method is inspired by the Landau–Zener crossing probability [74]

$$P_{2\to 1} = \exp\left(-\frac{2\pi V_{12}^2}{\hbar v\,|F_2 - F_1|}\right)\Delta t \tag{7.12}$$

where V_{12} is the coupling between the states, F_i the forces on the atoms on the different surfaces, and v the velocity of the atoms passing through the intersection.

Trajectory surface hopping is inherently an approximate method. There is no rigorous derivation for the hop probability, hence the different possibilities, and various ad hoc corrections need to be made to conserve energy after a hop and to cope with "frustrated hops" when a hop is required but energetically not possible. A potentially more serious problem is that as the trajectories are independent nuclear coherences are not included. Quantum effects such as tunnelling and zero-point energy are thus not correctly treated and much work, particularly by Truhlar and co-workers, has been made to assess the validity of surface hopping [75, 76]. New approaches are also still being developed to correct for these problems [77, 78].

An alternative formulation that uses classical trajectories to model non-adiabatic behaviour is the Ehrenfest approach [79, 80]. In this, each trajectory point (p, q) is driven by a "mean-field" force

$$\dot{p} = -\frac{\mathrm{d}}{\mathrm{d}q}\,\langle \Psi_{\mathrm{el}}(t)\,|H_{\mathrm{el}}|\,\Psi_{\mathrm{el}}(t)\rangle \tag{7.13}$$

with the electronic wavefunction being given by Eq. (7.11). It thus has components on all electronic states and so the trajectory has associated with it a probability for being on the various states. The force is also an average of forces from the various states. This can lead to unphysical behaviour [81].

Despite the problems due to the inexact nature of the approximations being made, the simplicity of surface hopping and Ehrenfest dynamics means it can be used to extract information on the dynamics of large systems. This is exemplified by the work of Tavernelli and co-workers who combine surface hopping with TDDFT to study protein and condensed phase systems [80].

7.4 Case Studies of Non-adiabatic Photochemistry

We report here on some of our recent case studies that highlight the methods presented in Sect. 7.3 and how they help interpret experimental findings. This

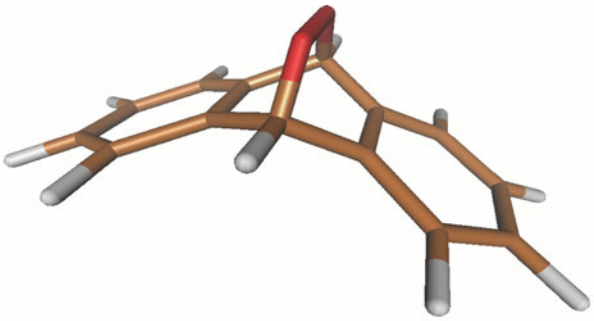

Fig. 7.7 Structure of anthracene-9,10-endoperoxide (APO)

selection is, of course, partial and non-exhaustive. We show an example per method with challenges of different natures that require different treatments: the most adequate depending on the context. At one end of the spectrum, we exemplify how full quantum information can be retrieved with a grid-based approach on a non-trivial case involving a four-state crossing. Multiple recrossings and complicated interferences are observed, but a simplified model must be used for the potential energies. Other examples along this line can be found in Chap. 6. At the other end of the spectrum, our third example considers a semi-classical-trajectory-based treatment, which includes quantum effects only approximately, but is able to treat the photodynamics of a large molecule embedded in a protein environment. The second example illustrates how a Gaussian-based method can be a good compromise between efficiency and accuracy, with quantum effects described from first principles while keeping a simple trajectory-based picture that makes the interpretation of results easier.

7.4.1 MCTDH Study of the Homolysis of the O–O Bond in Anthracene-9,10-endoperoxide

Anthracene-9,10-endoperoxide (APO, see Fig. 7.7) is an aromatic endoperoxide which, upon excitation to S_1, shows a cleavage of the oxygen–oxygen bond, leading to rearrangement products such as diepoxides or to the decomposition into quinones, whereas excitation to higher excited states leads to cycloreversion and the release of singlet molecular oxygen [82].

The photodynamics of the O–O cleavage is modulated by a four-state conical intersection (4CI) [83]. The most important modes are the opening angle of the O–O bond (β) and the twisting angle of the oxygen atoms around the molecular axis (τ). These two degrees of freedom were employed to calculate two-dimensional potential energy surfaces for the four interacting singlet states (see Fig. 7.8).

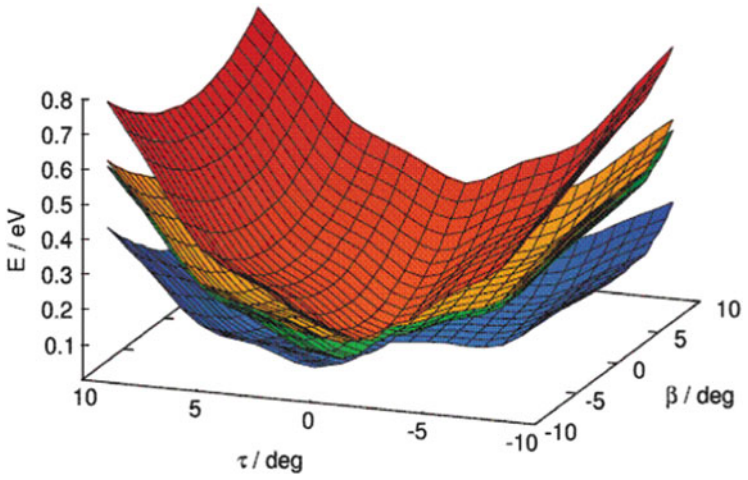

Fig. 7.8 The four adiabatic potential energy surfaces along β and τ close to the 4CI point (adapted from [84])

Using the grid-based MCTDH method, simulations were performed, first in two dimensions [84]. The resulting dynamics show that the 4CI point is reached very fast (in less than 30 fs after photoexcitation), and the wavepacket distributes over all states (see Fig. 7.9).

The efficiency of the population transfer is due to the strong couplings in the twisting mode, even though the wavepacket does not spread in this degree of freedom; instead, the wavepacket only spreads along the O–O opening mode. In order to allow for a more adequate dissipation of the energy, two sets of different bath modes were added as harmonic oscillators, and quantum dynamics simulations were run in up to nine dimensions. The degree of distribution into the four states proved to be very much dependent on which modes are included in the simulation.

All the quantum dynamics simulations performed show that upon excitation to S_1, the β-coordinate dominates the photodynamics, whereas splitting off singlet molecular oxygen (for which the τ-coordinate is an important mode) does not play any role. This result is in agreement with the available experiments that found that $^1O_2$ is obtained after excitation to states higher than S_1 [82].

The present grid-based quantum dynamics simulations retrieve quantum effects such as recrossings and interferences but are too limited in terms of number of degrees of freedom to provide the reaction pathways to form rearrangement products. This study could thus be complemented by less accurate trajectory-based semi-classical dynamics simulations or Gaussian-based quantum dynamics simulations in full dimensions like those presented in the next application cases.

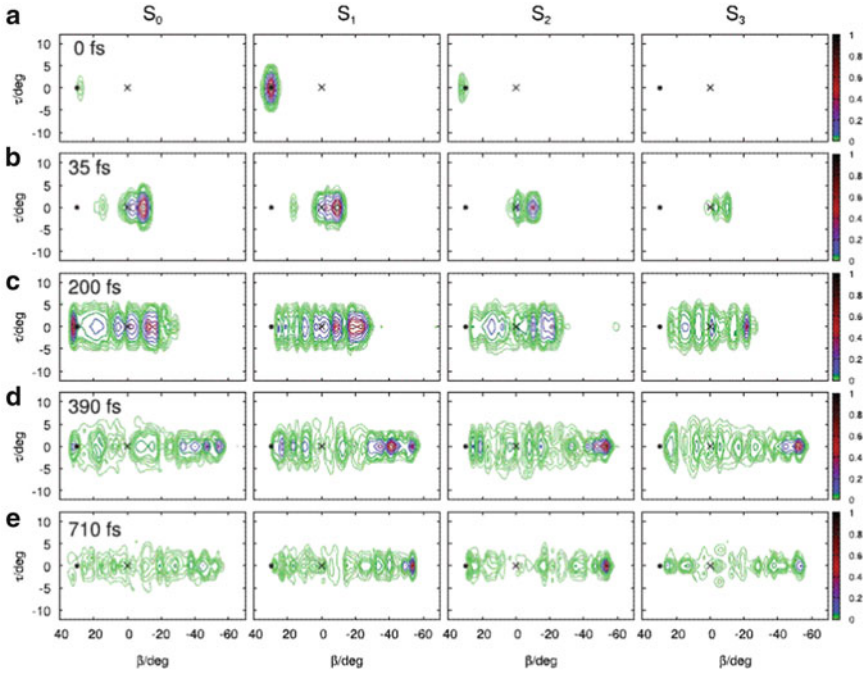

Fig. 7.9 Selected snapshots of the four adiabatic wavepacket densities. The black cross indicates the position of the 4CI point and the dot the FC point (adapted from [84])

7.4.2 DD-vMCG Study of the Photoisomerisation of a Cyanine Model

Cyanines are a class of conjugate organic dyes. Fluorescence of the *trans* species is in competition with a photoisomerisation towards the *cis* species, which represents a technological obstacle to their use as fluorescent molecular probes in imagery [85].

Calculations on model cyanines (H_2N–$(CH)_n$–NH_2^+ with $n = 3$, 5 or 7) showed [86, 87]: (1) a systematic relationship between the size of the polymethine chain and the time scale of the *cis–trans* torsion; (2) an extended seam of conical intersection along the torsional coordinates; and (3) that high-frequency skeletal deformations were required to access the seam. The last two points were demonstrated with qualitative results based on semi-classical trajectories for the simplest trimethine cyanine (see Fig. 7.10).

This work prompted optimal control experiments on a large cyanine [88, 89], which confirmed that the branching ratio could be controlled by a pulse leading to excitation of the same skeletal deformations in the initial wavepacket (see Fig. 7.11). This control strategy was further validated in a quantum dynamics context with Gaussian-based direct dynamics simulations [90].

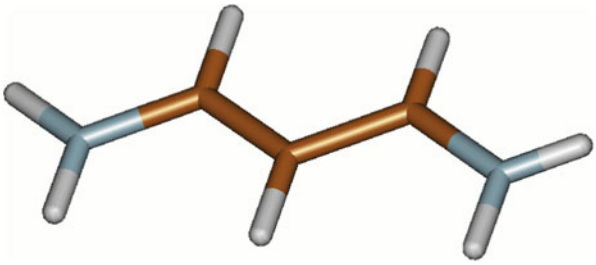

Fig. 7.10 Structure of the trimethine cyanine model $H_2N–(CH)_3–NH_2^+$

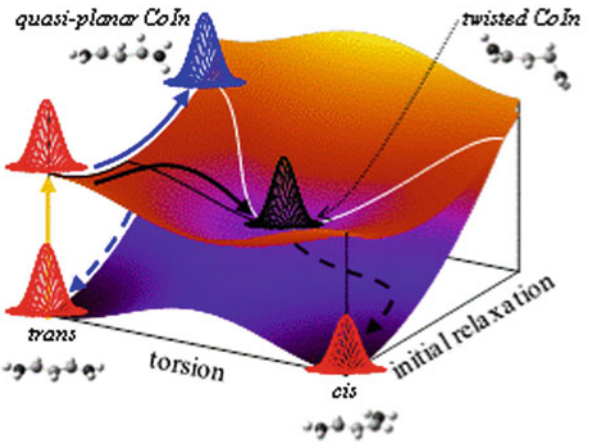

Fig. 7.11 Cartoon of the two radiationless decay mechanisms for the cyanine model. The *white line* represents the seam of intersection between the S_1 and S_0 potential energy surfaces (from [90])

These simulations showed that directly addressing the torsional modes was not efficient. After the initial in-plane relaxation has taken place, twisting dominates the reaction coordinate, so that in the absence of control the system naturally decays down the minimum-energy path to a twisted conical intersection. The only way to avoid twisting is to excite orthogonal motions such that the dynamical pathway can deviate from the minimum-energy path. Increasing/decreasing the momentum in the skeletal deformation coordinates is thus expected to induce radiationless decay at small/large twist angles (see Fig. 7.11). This was proved by running simulations whereby the initial wavepacket was given an extra mean momentum pointing from the Franck–Condon point to a point on the seam corresponding to a quasi-planar geometry. Systematically reducing the magnitude of the momentum vector resulted in a larger average twist angle of the crossing geometries.

This work also was an opportunity to analyse the concept of quantum coherence and non-locality in the context of Gaussian-based methods. Semi-classical non-locality is related to the statistical spreading of the points where surface hopping

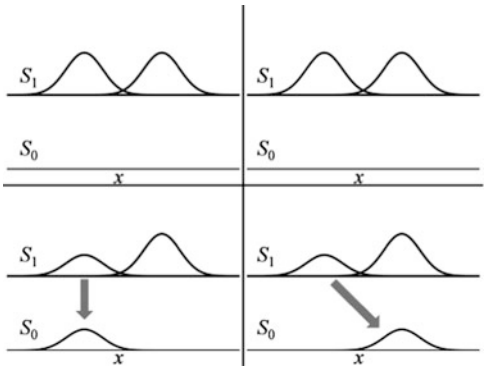

Fig. 7.12 Local transfer (*left panel*) versus non-local transfer (*right panel*) for a generic nuclear coordinate x (from [90])

occurs. The population transfer occurs at different times for different trajectories. Of course, this also means different geometries, but we will refer to such results as non-local in time. In contrast, quantum non-locality has to do with the fact that quantum trajectories communicate with each other at all times. Results will be called non-local in space if the population transfer involves a decrease of the weight of a given function on a given electronic state correlated with an increase of the weight of a different function on a different state (see Fig. 7.12). For example, some limited non-local transfer occurs between 18 and 20 fs for the first and the fourth basis functions in Fig. 7.13.

In contrast with grid-based methods, there is no need to first build analytical models for the potential energy surface, which makes Gaussian-based methods easier to use. In addition, an approximate description based on a limited number of "quantum trajectories" can provide a more intuitive interpretation of the reaction mechanism than the evolution of a wavepacket on a grid. However, increasing the size and complexity of the system may require an even more approximate description such as semi-classical trajectories presented below.

7.4.3 TSH Study of the Photoactivation of the Photoactive Yellow Protein

Treating the non-adiabatic photochemistry of large systems in an environment is computationally demanding. A possible strategy can be QM/MM trajectory-based semi-classical dynamics, as exemplified by simulations of the photoactivation of the photoactive yellow protein (PYP) [91–93], a bacterial photoreceptor believed to be responsible for negative phototactic response to blue light of Halorhodospira halophila bacteria.

Trans-to-*cis* isomerisation of photoactive chromophores usually occurs through a standard one-bond-flip mechanism in the gas phase. In contrast, spatial constraints

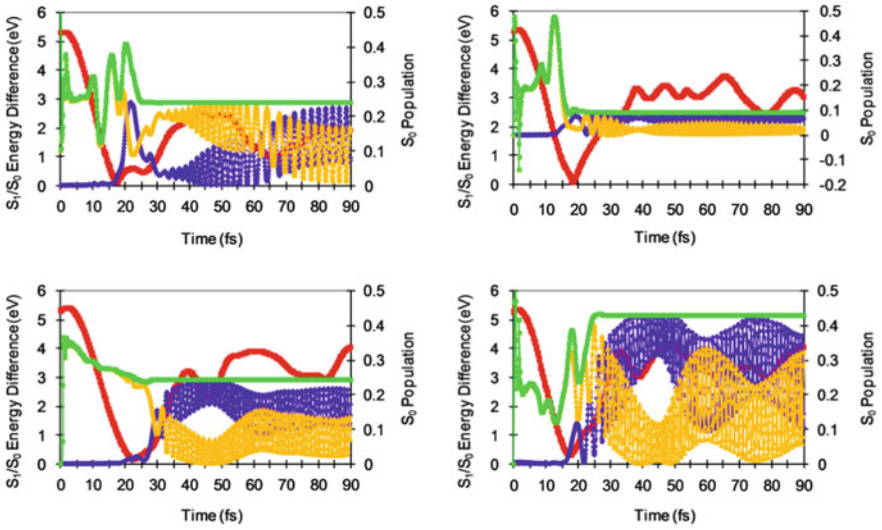

Fig. 7.13 S_1/S_0 adiabatic energy differences for the trajectories followed by the centres of four coupled Gaussian basis functions over time (*red*); weight of each individual basis function to the global wavepacket (*green*), and corresponding S_0 and S_1 populations (*purple* and *orange*, respectively) over time (from [90])

in a protein environment probably favour volume-conserving mechanisms where concerted atomic motions are expected. The isomerisation of the *p*-coumaric acid chromophore in PYP (see Fig. 7.14) has recently been observed with time-resolved X-ray crystallography experiments [94, 95]. These have suggested the involvement of an early twisted intermediate that can bifurcate into two structurally distinct *cis* intermediates via hula-twist and bicycle-pedal pathways. This highly strained structure had been predicted from the aforementioned theoretical study [92].

Simulations showed that the isomerisation is enhanced in the protein by altering the stability of the global S_1 minimum (i.e. by moving the position of the S_1/S_0 seam and lowering the trans-to-twisted barrier on S_1, see Fig. 7.15), and by sterically constraining the motion of the chromophore, which allows the isomerisation of the double bond (torsion *b*) to be favoured over isomerisation of the single bond (torsion *a*). These interactions significantly restrain the torsional motion of the ring about the single bond and enhance the torsional motion about the double bond. The increased population of the twisted global minimum ultimately ensures a higher quantum yield.

Semi-classical simulations are not aimed at providing an exhaustive and definitive understanding of photoreactivity. They should be improved on different fronts to become more predictive. Gaussian-based quantum dynamics could also provide a more accurate description of the quantum effects involved in such processes. However, semi-classical simulations are useful to generate ideas for designing new experiments, which in turn can be designed to validate specific aspects of the

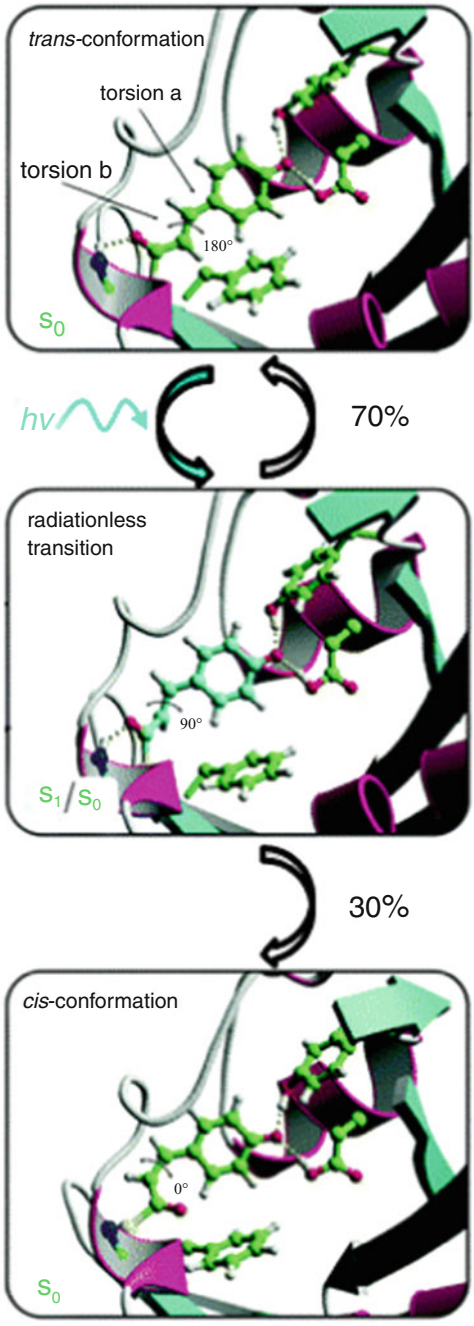

Fig. 7.14 Snapshots from semi-classical trajectories of PYP, showing the *p*-coumaric acid chromophore in the active site pocket. The first snapshot is at the photoexcitation. The second shows the configuration at the radiationless transition from S_1 to S_0. The third snapshot shows the photoproduct (from [93])

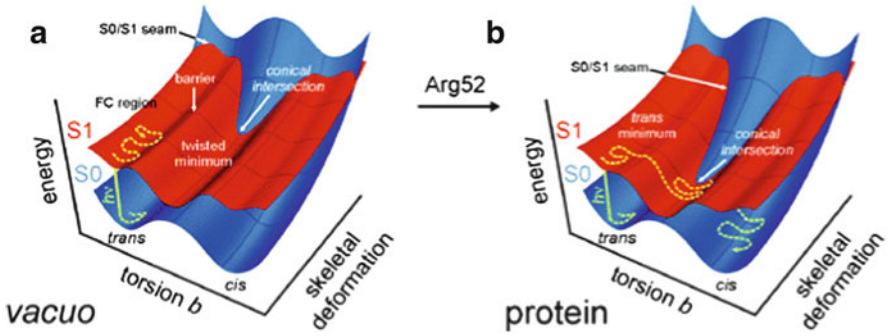

Fig. 7.15 Potential energy surfaces of the excited and ground states of the deprotonated chromophore in the *trans*-to-*cis* isomerisation coordinate (torsion *b*) and a skeletal deformation of the bonds in vacuo (**a**) and in the protein (**b**) (from [91])

Table 7.1 Dynamics studies of photochemistry

Method	System	Photochemistry	References
DD-vMCG [11, 60]	Butatriene	PE	[10]
	Benzene	PS versus PI	[96]
	Formaldehyde	PD	[97]
	Thymine	PS	[98]
	Cyanine	PS versus PI	[98]
AIMS [12, 13]	Ethylene	PI	[13, 99]
	Uracil, thymine	PS	[100]
	Protein chromophores	PS versus PI	[69]
	Butadiene	PI	[101]
	Cyclobutene	PI	[102]
Semi-classical	Benzene	PI	[103]
Surface hopping [71, 73]	Fulvene	PS versus PI	[104]
	Diarylethene	PS versus PI	[105]
	Cyanine	PS versus PI	[36]
	Ethylene	PI	[106]
	Protein chromophore	PI	[107, 108]
	Thymine	PS	[109]
	Uracil, thymine, cytosine	PS	[110]
	Thymine	PS	[111]

PA photoabsorption spectrum, *PE* photoelectron spectrum, *PD* photodissociation, *PS* photostability, *PI* photoisomerisation, *PHT* photo-induced H transfer

theoretical explanation (involvement of single-bond isomerisation, role of Arg52 in the protein, etc.) and to calibrate the level of theory required for an adequate computation.

7.5 Conclusions

In this chapter we have reviewed the central features of the theoretical aspects of non-adiabatic processes in photochemistry that can be computed using standard electronic structure methods: conical intersections and dynamics through an intersection using either trajectories with surface hoping or quantum dynamics. We have illustrated these ideas with some case studies. Of course these case studies are a small sample drawn from our own work. Thus to extend this we have prepared a non-exhaustive bibliography (Table 7.1) where the reader can find other interesting examples.

As we have mentioned in the Introduction, we believe that the age of dynamics and quantum dynamics in particular is upon us. The applications to photochemistry that have been performed so far have progressed beyond benchmarks and are uncovering new mechanistic features. Within our own research groups we have non-specialists carrying out computations to support experimental work. The general codes will be available in general packages soon.

References

1. Bearpark MJ, Robb MA, Schlegel HB (1994) A direct method for the location of the lowest energy point on a potential surface crossing. Chem Phys Lett 223:269
2. Vreven T, Bernardi F, Garavelli M, Olivucci M, Robb MA, Schlegel HB (1997) Ab initio photoisomerization dynamics of a simple retinal chromophore model. J Am Chem Soc 119:12687
3. Jasper A, Nangia S, Zhu C, Truhlar D (2006) Non-Born–Oppenheimer molecular dynamics. Acc Chem Res 39:101
4. Barbatti M, Granucci G, Persico M, Ruckenbauer M, Vazdar M, Eckert-Maksic M, Lischka H (2007) The on-the-fly surface-hopping program system NEWTON-X: application to ab initio simulation of the nonadiabatic photodynamics of benchmark systems. J Photochem Photobiol A 190:228
5. Tully JC (2012) Perspective: nonadiabatic dynamics theory. J Chem Phys 137:22A301
6. Worth GA, Robb MA (2002) Applying direct molecular dynamics to non-adiabatic systems. Adv Chem Phys 124:355
7. Wolynes PG (2009) Some quantum weirdness in physiology. Proc Natl Acad Sci U S A 106:17247
8. de la Lande A, Rezac J, Levy B, Sanders BC, Salahub DR (2011) Transmission coefficients for chemical reactions with multiple states: role of quantum decoherence. J Am Chem Soc 133:3883
9. Worth GA, Beck MH, Jäckle A, Meyer H-D (2003) The MCTDH package, version 8.3. University of Heidelberg, Germany. See http://mctdh.uni-hd.de
10. Worth GA, Robb MA, Burghardt I (2004) A novel algorithm for non-adiabatic direct dynamics using variational Gaussian wavepackets. Faraday Discuss 127:307
11. Worth GA, Robb MA, Lasorne B (2008) Solving the time-dependent Schrodinger equation for nuclear motion in one step: direct dynamics of non-adiabatic systems. Mol Phys 106:2077
12. Ben-Nun M, Martinez TJ (2002) Ab initio quantum molecular dynamics. Adv Chem Phys 121:439
13. Quenneville J, Ben-Nun M, Martinez TJ (2001) Photochemistry from first principles—advances and future prospects. J Photochem Photobiol A 144:229

14. Hack MD, Wensmann AM, Truhlar DG, Ben-Nun M, Martinez TJ (2001) Comparison of full multiple spawning, trajectory surface hopping, and converged quantum mechanics for electronically nonadiabatic dynamics. J Chem Phys 115:1172
15. Bernardi F, De S, Olivucci M, Robb MA (1990) Mechanism of ground-state-forbidden photochemical pericyclic-reactions—evidence for real conical intersections. J Am Chem Soc 112:1737
16. Celani P, Robb MA, Garavelli M, Bernardi F, Olivucci M (1995) Geometry optimization on a hypersphere—application to finding reaction paths from a conical intersection. Chem Phys Lett 243:1
17. Woodward RB, Hoffmann R (1965) Stereochemistry of electrocyclic reactions. J Am Chem Soc 87:395
18. Bernardi F, Olivucci M, Robb MA (1996) Potential energy surface crossings in organic photochemistry. Chem Soc Rev 25:321
19. Bearpark M, Robb M, Bernardi F, Olivucci M (1994) Molecular mechanics valence-bond methods for large active spaces—application to conjugated polycyclic-hydrocarbons. Chem Phys Lett 217:513
20. Boggio-Pasqua M, Groenhof G, Schafer LV, Grubmuller H, Robb MA (2007) Ultrafast deactivation channel for thymine dimerization. J Am Chem Soc 129:10996
21. Paterson M, Bearpark M, Robb M, Blancafort L, Worth G (2005) Conical intersections: a perspective on the computation of spectroscopic Jahn–Teller parameters and the degenerate 'intersection space'. Phys Chem Chem Phys 7:2100
22. Lengsfield BH, Yarkony DR (1992) Nonadiabatic interactions between potential-energy surfaces—theory and applications. Adv Chem Phys 82:1
23. Bearpark M, Robb M, Schlegel H (1994) A direct method for the location of the lowest energy point on a potential surface crossing. Chem Phys Lett 223:269
24. Sicilia F, Blancafort L, Bearpark MJ, Robb MA (2008) New algorithms for optimizing and linking conical intersection points. J Chem Theory Comput 4:257
25. Levine BG, Coe JD, Martinez TJ (2008) Optimizing conical intersections without derivative coupling vectors: application to multistate multireference second-order perturbation theory (MS-CASPT2). J Phys Chem B 112:405
26. Keal TW, Koslowski A, Thiel W (2007) Comparison of algorithms for conical intersection optimisation using semiempirical methods. Theor Chem Account 118:837
27. Atchity G, Xantheas S, Ruedenberg K (1991) Potential-energy surfaces near intersections. J Chem Phys 95:1862
28. Yarkony DR (1996) Diabolical conical intersections. Rev Mod Phys 68:985
29. Paterson MJ, Bearpark MJ, Robb MA, Blancafort L (2004) The curvature of the conical intersection seam: an approximate second-order analysis. J Chem Phys 121:11562
30. Lasorne B, Sicilia F, Bearpark MJ, Robb MA, Worth GA, Blancafort L (2008) Automatic generation of active coordinates for quantum dynamics calculations: application to the dynamics of benzene photochemistry. J Chem Phys 128:124307
31. Sicilia F, Blancafort L, Bearpark MJ, Robb MA (2007) Quadratic description of conical intersections: characterization of critical points on the extended seam. J Phys Chem A 111:2182
32. Sicilia F, Bearpark MJ, Blancafort L, Robb MA (2007) An analytical second-order description of the S-0/S-1 intersection seam: fulvene revisited. Theor Chem Account 118:241
33. Desouterlecomte M, Galloy C, Lorquet JC, Pires MV (1979) Non-adiabatic interactions in unimolecular decay 5. Conical and Jahn–Teller intersections. J Chem Phys 71:3661
34. Boggio-Pasqua M, Ravaglia M, Bearpark M, Garavelli M, Robb M (2003) Can diarylethene photochromism be explained by a reaction path alone? A CASSCF study with model MMVB dynamics. J Phys Chem A 107:11139
35. Boggio-Pasqua M, Bearpark M, Hunt P, Robb M (2002) Dihydroazulene/vinylheptafulvene photochromism: a model for one-way photochemistry via a conical intersection. J Am Chem Soc 124:1456

36. Hunt PA, Robb MA (2005) Systematic control of photochemistry: the dynamics of photoisomerization of a model cyanine dye. J Am Chem Soc 127:5720
37. Allan CSM, Lasorne B, Worth GA, Robb MA (2010) A straightforward method of analysis for direct quantum dynamics: application to the photochemistry of a model cyanine. J Phys Chem A 114:8713
38. Nenov A, Kolle P, Robb MA, de Vivie-Riedle R (2009) Beyond the van der Lugt/Oosterhoff model: when the conical intersection seam and the S_1 minimum energy path do not cross. J Org Chem 75:123
39. Robb M, Garavelli M, Olivucci M, Bernardi F (2000) A computational strategy for organic photochemistry. Rev Comput Chem 15:87
40. Blancafort L, Lasorne B, Worth GA, Robb MA (2009) In: Köppel H, Yarkony DR, Barentzen H (eds) The Jahn–Teller-effect fundamentals and implications for physics and chemistry. Springer, Heidelberg, pp 169–200
41. Yarkony DR (2005) Escape from the double cone: optimized descriptions of the seam space using gateway modes. J Chem Phys 123:134106
42. Yarkony DR (2005) On the connectivity of seams of conical intersection: seam curvature. J Chem Phys 123:204101
43. Bearpark MJ, Robb MA (2007) In: Platz MS, Maitland RA (eds) Reviews of reactive intermediate chemistry, Wiley, Hoboken, pp 379–414
44. Worth GA, Bearpark MJ, Robb MA (2005) In: Olivucci M (ed) Computational photochemistry. Elsevier, Amsterdam, pp 171–190
45. Worth GA, Cederbaum LS (2004) Beyond Born–Oppenheimer: molecular dynamics through a conical intersection. Annu Rev Phys Chem 55:127
46. Kosloff R (1988) Time-dependent quantum-mechanical methods for molecular-dynamics. J Phys Chem 92:2087
47. Cerjan C (ed) (1993) Numerical grid methods and their application to Schrödinger's equation. Kluwer, Dordrecht
48. Manthe U, Meyer H-D, Cederbaum LS (1992) Wave-packet dynamics within the multiconfiguration Hartree framework—general-aspects and application to NOCl. J Chem Phys 97:3199
49. Beck M, Jäckle A, Worth GA, Meyer H-D (2000) The multiconfiguration time-dependent Hartree (MCTDH) method: a highly efficient algorithm for propagating wavepackets. Phys Rep 324:1
50. Meyer H-D, Gatti F, Worth Eds GA (2009) MCTDH: basic theory, extensions and applications to multidimensional quantum dynamics. VCH, Weinheim
51. Worth GA, Meyer H-D, Köppel H, Cederbaum LS, Burghardt I (2008) Using the MCTDH wavepacket propagation method to describe multimode non-adiabatic dynamics. Int Rev Phys Chem 27:569
52. Heller EJ (1975) Time-dependent approach to semiclassical dynamics. J Chem Phys 62:1544
53. Lasorne B, Worth GA, Robb MA (2011) "Excited-state dynamics" WIREs. Comput Mol Sci 1:460
54. Martínez TJ, Ben-Nun M, Levine RD (1996) Multi-electronic-state molecular dynamics: a wave function approach with applications. J Phys Chem 100:7884
55. Ben-Nun M, Martínez TJ (1998) Nonadiabatic molecular dynamics: validation of the multiple spawning method for a multidimensional problem. J Chem Phys 108:7244
56. Ben-Nun M, Martínez TJ (2000) Photodynamics of ethylene: ab initio studies of conical intersections. Chem Phys 259:237
57. Levine BG, Coe JD, Virshup AM, Martínez TJ (2008) Implementation of ab initio multiple spawning in the MOLPRO quantum chemistry package. Chem Phys 347:3
58. Yang S, Coe JD, Kaduk B, Martínez TJ (2009) An "optimal" spawning algorithm for adaptive basis set expansion in nonadiabatic dynamics. J Chem Phys 130:134113
59. Burghardt I, Meyer H-D, Cederbaum LS (1999) Approaches to the approximate treatment of complex molecular systems by the multiconfiguration time-dependent Hartree method. J Chem Phys 111:2927

60. Lasorne B, Robb MA, Worth GA (2007) Direct quantum dynamics using variational multi-configuration Gaussian wavepackets. Implementation details and test case. Phys Chem Chem Phys 9:3210
61. Lasorne B, Worth GA (2009) In: Meyer H-D, Gatti F, Worth GA (eds) Multidimensional quantum dynamics: MCTDH theory and applications. Wiley-VCH, Weinheim, pp 113–129
62. Frankcombe TJ, Collins MA, Worth GA (2010) Converged quantum dynamics with modified Shepard interpolation and Gaussian wave packets. Chem Phys Lett 489:242
63. Mendive-Tapia D, Lasorne B, Worth GA, Robb MA, Bearpark MJ (2012) Towards converging non-adiabatic direct dynamics calculations using frozen-width variational Gaussian product basis functions. J Chem Phys 137:22A548
64. Shalashilin DV, Irene Burghardt (2008) Gaussian-based techniques for quantum propagation from the time-dependent variational principle: formulation in terms of trajectories of coupled classical and quantum variables. J Chem Phys 129:084104
65. Shalashilin DV (2009) Quantum mechanics with the basis set guided by Ehrenfest trajectories: theory and application to spin-boson model. J Chem Phys 130:244101
66. Shalashilin DV (2010) Nonadiabatic dynamics with the help of multiconfigurational Ehrenfest method: improved theory and fully quantum 24D simulation of pyrazine. J Chem Phys 132:244111
67. Shalashilin DV (2011) Multiconfigurational Ehrenfest approach to quantum coherent dynamics in large molecular systems. Faraday Discuss 153:105
68. Saita K, Shalashilin DV (2012) On-the-fly ab initio molecular dynamics with multiconfigurational Ehrenfest method. J Chem Phys 137:22A506
69. Virshup AM, Punwong C, Pogorelov TV, Lindquist BA, Ko C, Martínez TJ (2009) Photodynamics in complex environments: ab initio multiple spawning quantum mechanical/molecular mechanical dynamics. J Phys Chem B 113:3280
70. Messiah A (1962) Quantum mechanics, vol 1. Wiley, New York
71. Tully JC, Preston RK (1971) Trajectory surface hopping approach to nonadiabatic molecular collisions—reaction of H + with D_2. J Chem Phys 55:562
72. Chapman S (1992) The classical trajectory-surface-hopping approach to charge-transfer processes. Adv Chem Phys 82(Pt II):423
73. Tully JC (1990) Molecular-dynamics with electronic-transitions. J Chem Phys 93:1061
74. Landau LD (1932) On the theory of transfer of energy at collisions II. Phys Z Sow 2:46
75. Herman MF (1984) Nonadiabatic semiclassical scattering. 1. Analysis of generalized surface hopping procedures. J Chem Phys 81:754
76. Topaler MS, Hack MD, Allison TC, Liu Y-P, Mielke SL, Schwenke DW, Truhlar DJ (1997) Validation of trajectory surface hopping methods against accurate quantum mechanical dynamics and semiclassical analysis of electronic-to-vibrational energy transfer. J Chem Phys 106:8699
77. Volobuev YL, Hack MD, Topaler MS, Truhlar DG (2000) Continuous surface switching: an improved time-dependent self-consistent-field method for nonadiabatic dynamics. J Chem Phys 112:97162
78. Curchod BFE, Tavernelli I, Rothlisberger U (2011) Trajectory-based solution of the nonadiabatic quantum dynamics equations: an on-the-y approach for molecular dynamics simulations. PCCP 13:3231
79. Ehrenfest P (1927) Bemerkung über die angenäherte Gültigkeit der klassischen Mechanik innerhalb der Quantenmechanik. Z Phys 45:455
80. Curchod BFE, Rothlisberger U, Tavernelli I (2013) Trajectory-based nonadiabatic dynamics with time-dependent density functional theory. ChemPhysChem 14:1314
81. Kuntz PJ (1991) Classical path surface-hopping dynamics. 1. General-theory and illustrative trajectories. J Chem Phys 95:141
82. Fidder H, Lauer A, Freyer W, Koeppe B, Heyne K (2009) Photochemistry of anthracene-9,10-endoperoxide. J Phys Chem A 113:6289
83. Mollenhauer D, Corral I, González L (2010) Four plus four state degeneracies in the O–O photolysis of aromatic endoperoxides. J Phys Chem Lett 1:1036

84. Assmann M, Worth GA, González L (2012) 9D nonadiabatic quantum dynamics through a four-state conical intersection: investigating the homolysis of the O–O bond in anthracene-9,10-endoperoxide. J Chem Phys 137:22A524
85. Yartsev A, Alvarez JL, Aberg U, Sundstrom V (1995) Overdamped wavepacket motionalong a barrierless potential-energy surface in excited-state isomerization. Chem Phys Lett 243:281
86. Hunt PA, Robb MA (2005) Systematic control of photochemistry: the dynamics of photoisomerization of a model cyanine dye. J Am Chem Soc 127:5270
87. Sanchez-Galvez A, Hunt P, Robb MA, Olivucci M, Vreven T, Schlegel HB (2000) Ultrafast radiationless deactivation of organic dyes: evidence for a two-state two-mode pathway in polymethine cyanines. J Am Chem Soc 122:2911
88. Dietzek B, Bruggemann B, Pascher T, Yartsev A (2006) Mechanisms of molecular response in the optimal control of photoisomerization. Phys Rev Lett 97:258301
89. Dietzek B, Bruggemann B, Pascher T, Yartsev A (2007) Pump-shaped dump optimal control reveals the nuclear reaction pathway of isomerization of a photoexcited cyanine dye. J Am Chem Soc 129:13014
90. Allan CSM, Lasorne B, Worth GA, Robb MA (2010) A straightforward method of analysis for direct quantum dynamics: application to the photochemistry of a model cyanine. J Phys Chem A 114:8713
91. Groenhof G, Bouxin-Cademartory M, Hess B, de Visser SP, Berendsen HJC, Olivucci M, Mark AE, Robb MA (2004) Photoactivation of the photoactive yellow protein: why photon absorption triggers a trans-to-cis isomerization of the chromophore in the protein. J Am Chem Soc 126:4228
92. Boggio-Pasqua M, Robb MA, Groenhof G (2009) Hydrogen bonding controls excited-state decay of the photoactive yellow protein chromophore. J Am Chem Soc 131:13580
93. Boggio-Pasqua M, Burmeister CF, Robb MA, Groenhof G (2012) Photochemical reactions in biological systems: probing the effect of the environment by means of hybrid quantum chemistry/molecular mechanics simulations. PCCP 14:7912
94. Schotte F, Cho HS, Kaila VRI, Kamikubo H, Dashdorj N, Henry ER, Graber TJ, Henning R, Wulff M, Hummer G, Kataoka M, Anfinrud PA (2012) Watching a signaling protein function 3 in real time via 100-ps time-resolved Laue crystallography. Proc Natl Acad Sci U S A 109:19256
95. Jung YO, Lee JH, Kim J, Schmidt M, Moffat K, Srajer V, Ihee H (2013) Volume-conserving trans-cis isomerization pathways in photoactive yellow protein visualized by picosecond X-ray crystallography. Nat Chem 5:212
96. Lasorne B, Bearpark MJ, Robb MA, Worth GA (2008) Controlling S1/S0 decay and the balance between photochemistry and photostability in benzene: a direct quantum dynamics study. J Phys Chem A 112:13017
97. Araujo M, Lasorne B, Magalhaes AL, Worth GA, Bearpark MJ, Robb MA (2009) The molecular dissociation of formaldehyde at medium photoexcitation energies: a quantum chemistry and direct quantum dynamics study. J Chem Phys 131:144301
98. Asturiol D, Lasorne B, Worth GA, Robb MA, Blancafort L (2010) Exploring the slopedto-peaked S2/S1 seam of intersection of thymine with electronic structure and direct quantum dynamics calculations. PCCP 12:4949
99. Tao HL, Levine BG, Martinez TJ (2009) Ab initio multiple spawning dynamics using multi-state second-order perturbation theory. J Phys Chem A 113:13656
100. Hudock HR, Levine BG, Thompson AL, Satzger H, Townsend D, Gador N, Ullrich S, Stolow A, Martinez TJ (2007) Ab initio molecular dynamics and time-resolved photoelectron spectroscopy of electronically excited uracil and thymine. J Phys Chem A 111:8500
101. Levine BG, Martinez TJ (2009) Ab initio multiple spawning dynamics of excited butadiene: role of charge transfer. J Phys Chem A 113:12815
102. Ong MT, Leiding J, Tao HL, Virshup AM, Martinez TJ (2009) First principles dynamics and minimum energy pathways for mechanochemical ring opening of cyclobutene. J Am Chem Soc 131:6377

103. Smith B, Bearpark M, Robb M, Bernardi F, Olivucci M (1995) Classical wavepacket dynamics through a conical intersection – application to the S1/S0 photochemistry of benzene. Chem Phys Lett 242:27
104. Bearpark MJ, Bernardi F, Clifford S, Olivucci M, Robb MA, Smith BR, Vreven T (1996) The azulene S1 state decays via a conical intersection: a CASSCF study with MMVB dynamics. J Am Chem Soc 118:169
105. Boggio-Pasqua M, Ravaglia M, Bearpark M, Garavelli M, Robb M (2003) Can diarylethene photochromism be explained by a reaction path alone? A CASSCF study with model MMVB dynamics. J Phys Chem A 107:11139
106. Barbatti M, Ruckenbauer M, Lischka H (2005) The photodynamics of ethylene: a surface-hopping study on structural aspects. J Chem Phys 122:174307
107. Groenhof G, Bouxin-Cademartory M, Hess B, De Visser S, Berendsen H, Olivucci M, Mark A, Robb M (2004) Photoactivation of the photoactive yellow protein: why photon absorption triggers a trans-to-cis isomerization of the chromophore in the protein. J Am Chem Soc 126:4228
108. Groenhof G, Schaefer LV, Boggio-Pasqua M, Grubmueller H, Robb MA (2008) Arginine52 controls the photoisomerization process in photoactive yellow protein. J Am Chem Soc 130:3250
109. Szymczak JJ, Barbatti M, Lischka H (2009) Is the photoinduced isomerization in retinal 4 protonated Schiff bases a single- or double-torsional process? J Phys Chem A 113:11907
110. Lan ZG, Fabiano E, Thiel W (2009) Photoinduced nonadiabatic dynamics of 9H-guanine. ChemPhysChem 10:1225
111. Asturiol D, Lasorne B, Robb MA, Blancafort L (2009) Photophysics of the pi, pi* and n,pi* states of thymine: MS-CASPT2 minimum-energy paths and CASSCF on-the-y dynamics. J Phys Chem A 113:10211

The Interplay of Nuclear and Electron Wavepacket Motion in the Control of Molecular Processes: A Theoretical Perspective

8

Sebastian Thallmair, Robert Siemering, Patrick Kölle, Matthias Kling, Matthias Wollenhaupt, Thomas Baumert, and Regina de Vivie-Riedle

Abstract

The concept of coherent control of molecular processes with light is introduced, sketching the way from single parameter to the multiparameter control in the time domain. Optimal control theory is by now a widespread and well-recognized method to solve a variety of control tasks ranging from chemical to physical applications. The underlying concepts and tools with their links to the experiment will be introduced with the focus on chemical reactions. As they include the motion of the nuclei, their time scale ranges from femtoseconds to picoseconds and longer and requires the solution of the time-dependent Schrödinger equation for the nuclear motion. Recent developments that enter the sub-femtosecond domain and open the prospect for direct control of the faster electron motion will be addressed. Two strategies—already realized experimentally—are presented: control of electron dynamics via the carrier envelope phase (CEP) in few-cycle pulses and via the temporal phase of a femtosecond laser pulse with attosecond precision. The issue of nuclear and electronic wavepacket synchronization to

S. Thallmair • R. Siemering • P. Kölle • R. de Vivie-Riedle (✉)
Department Chemie, Ludwig-Maximilians-Universität München, Butenandtstr. 11, Haus E, 81377 München, Germany
e-mail: Regina.de_Vivie@cup.uni-muenchen.de

M. Kling
Max-Planck-Institut für Quantenoptik, Hans-Kopfermann-Str. 1, 85748 Garching, Germany

T. Baumert
Institut für Physik und CINSaT, Universität Kassel, Heinrich-Plett-Str. 40, 34132 Kassel, Germany

M. Wollenhaupt
Institut für Physik und CINSaT, Universität Kassel, Heinrich-Plett-Str. 40, 34132 Kassel, Germany

Institut für Physik, Carl von Ossietzky Universität Oldenburg, Carl-von-Ossietzky-Straße 9-11, 26129 Oldenburg, Germany

F. Gatti (ed.), *Molecular Quantum Dynamics*, Physical Chemistry in Action,
DOI 10.1007/978-3-642-45290-1_8,

achieve control on a chemical reaction is raised. A theoretical method to answer these questions is presented. Finally, a proposal how the electron dynamics can be used as an additional control parameter for a chemical reaction is made.

8.1 Introduction

Laser chemistry stands for the long-standing dream to control bond breaking and formation in chemical reactions by light and started with the first experimental realization of a laser in the 1960s. The basic idea was that energy is supplied only to frequency selected bonds in a molecule, leaving the other bonds unaffected [1–3]. However, it became evident that even a light source well tuned to one vibrational mode heats the molecule uniformly, and all vibrations reach equilibrium in accordance with the laws of statistical thermodynamics. This phenomenon was explained by intramolecular vibrational relaxation, which can be rapid in large molecules [2]. The result is that the weakest bond will break. For selective bond chemistry this situation has to be avoided. One solution is the separation of time scales. Ultrashort laser pulses of some ten femtoseconds ($1\ \text{fs} = 10^{-15}\ \text{s}$) are able to deposit energy to one degree of freedom on a time scale much faster than the energy can be redistributed to the other modes and are more appropriate to achieve mode-specific bond breaking. Alternatively, bond rearrangements can also be induced via localized vibrational wavepackets in electronically excited states. These first ideas of control of chemical reactions are part of the much wider field of femtochemistry [3] dealing with the real time observation of complex molecular reactions [4–12, 20, 21].

The realization of light controlled reactions faces further challenges. One example is the anharmonicity inherent in any potential energy describing a molecular bond. Bond breaking in the electronic ground state includes vibrational ladder climbing and the energy gap between adjacent vibrational levels will steadily decrease. To secure resonant transitions up to the dissociation limit, pulse modulation is required to offer the right frequency at the right time. To guide even more complex reactions specially adapted pulse forms, in amplitude and phase, are required. Along this line several ideas were developed. The first theoretical proposals discussed three different approaches using single parameter control in the 1980s. In the Brumer–Shapiro control scheme, the interference between different light-induced reaction pathways is used for the control of state-to-state transitions [13, 14]. The stimulated Raman adiabatic passage (STIRAP) uses two suitably timed laser interactions to achieve complete population transfer in Λ-type quantum systems [15, 16]. In the Tannor–Kosloff–Rice pump–dump scheme, laser light is used to create and steer nuclear wavepackets to control a molecular reaction [17, 18]. First experimental realization of the Tannor–Kosloff–Rice scheme was already demonstrated in the early 1990s [3, 19, 22, 23].

The extension of this concept to multiparameter control [17, 18, 24–30] constitutes the concept of coherent control and was again proposed by theory as well as its transfer to the experiment. Under the slogan “Let the molecule solve its own Schrödinger equation” the concept of closed loop control was introduced from

theory to experiment [31]. Realization has come within reach due to the development of femtosecond laser pulses in combination with elaborate pulse shaping techniques [32]. Successful demonstrations opened the field from the control of molecular reactions [33–37] to the field of quantum information [38] and quantum optics [39, 40]. In molecular experiments the yield of a predefined reaction product was optimized by tailoring the driving laser field in a pulse shaping device. In the visible frequency range liquid crystal optical modulators are often used. They work in the frequency domain and are able to control the laser parameters amplitude, phase, and polarization in quantum control experiments [41–44]. The optimal pulse shape for the desired task is found by using sophisticated search algorithms, in most cases genetic algorithms. The resulting optimized electric fields are often very complex and would not lead to physical insight. To reduce the complexity of the shaped laser fields in optimal control experiments (OCEs), analytic, parameterized phase functions for phase modulation were tested [45–53].

From the theory side, the optimal pulses for reaction control can be found by using the powerful approach of optimal control theory (OCT) [24–29]. OCT works in the time domain and uses the known Hamiltonian of the quantum system to iteratively calculate the electromagnetic field, which drives the system most efficiently from a given initial state to the desired target state. For chemical reaction control the underlying equation of motion is the Schrödinger equation for the nuclei. Numerous examples for molecular control, like molecular switches [58, 83, 85], molecular motors [54], and quantum information [38, 39] have been presented. Issues like controllability and control landscapes [55–57] are lively discussed. The comparability of results from OCT and OCE is of high interest and the issues arising thereby were discussed in detail in [58].

Evidently, also the electrons move during chemical reactions. A recent theoretical illustration is given in [59]. The Born–Oppenheimer approximation tells us that they are typically fast enough to instantaneously adapt to the nuclear motion. With the development of strong few-cycle near-infrared (NIR) and mid-infrared (MIR) light pulses as well as their conversion to ultrashort extreme ultraviolet light pulses by high-harmonic generation (HHG) the control of electronic motion came into reach. The term attochemistry ($1\ \text{as} = 10^{-18}\ \text{s}$) emerged with the claim to steer a chemical reaction by forming and guiding an electronic wavepacket along a molecular reaction pathway. The formation of electronic wavepackets as a result of the removal of an electron (through ionization) on attosecond time scales was recently considered [60–62]. The reported response times in the range of 50 as to less than one femtosecond are much too fast for the nuclei to react and this strategy is not suited to control a chemical reaction. An alternative to create and guide electronic wavepackets is to superimpose preselected electronic states in a coherent way by laser radiation. To gain full control, it is also required to control and steer the phase of the electronic wavepackets. Two strategies have been realized. One uses the carrier envelope phase (CEP) of a few-cycle pulse as control parameter [63], another utilizes strong electric fields to shift electronic states in energy in order to steer the molecular reactions. The resonant Stark effect acts on the time scale of the electron dynamics and leads to the second concept, which is known as selective population

of dressed states (SPODS), a strategy which nicely combines both routes of phase and strong field control [64, 65].

Regardless of the way the electronic wavepackets are prepared an effective control of a molecular reaction can only be obtained when the time scale of nuclear and electronic motion is synchronized. Learning from first examples on diatomics criteria could be formulated for which the control of a molecular process through the steering of the electronic motion is possible [58, 64, 66, 68, 69]. For larger molecules more elaborated control strategies are needed. Their design requires the knowledge of the intramolecular processes critical for the time evolution and the life time of the electronic wavepacket. Depending on the vibrational dynamics the induced electron wavepacket dynamics is damped or stopped. This loss of electronic coherence can be of intermediate nature, but certainly defines the time window for efficient control via electronic wavepacket dynamics.

The chapter is organized as follows: first, the concepts of coherent control in the femtosecond to picosecond domain are outlined together with a short introduction into the theoretical framework of the OCT formalism. Second two different concepts of sub-femtosecond control are discussed and their realization in theory. Examples of controlled molecular quantum dynamics including implicit and explicit control of electron motion are presented. We conclude with an outlook how the control of complex reactions in large molecules could be assisted by steered electronic wavepackets.

8.2 Concepts of Coherent Control for Molecular Motion

As outlined in the introduction several very efficient single parameter quantum control schemes have been developed and experimentally verified. In this section we will concentrate on the proposals in the time domain. The main idea here is to steer the time evolution of a vibrational wavepacket—either on one potential energy surface or via multiple potential energy surfaces—from the reactant to the product. We will sketch from the theoretical point of view the way from single parameter to multiparameter control.

8.2.1 Theory for Single Parameter Control

The time evolution of a vibrational wavepacket $\psi(t)$ is governed by the time-dependent, nuclear Schrödinger equation:

$$i\hbar\frac{\partial}{\partial t}\psi(t) = H\psi(t) \tag{8.1}$$

with $H = H_{\mathrm{mol}} - \mu E(t)$ the total Hamiltonian comprising the molecular Hamiltonian $H_{\mathrm{mol}} = T + V$ and the interaction with an external light field $E(t)$. The interaction is mediated by the molecular dipole moment μ. In the framework of the

Born–Oppenheimer approach T corresponds to the kinetic Hamiltonian for the nuclei described by the wavefunction $\psi(t)$ and $V = V(R)$ to the electronic potential as obtained by solving the time-independent electronic Schrödinger equation at different geometries R. Integrating the time-dependent, nuclear Schrödinger equation [Eq. (8.1)] determines the equations of motion as the action of a propagator on the nuclear wavefunction:

$$\psi\left(t+\Delta t\right) = U\left(t+\Delta t, t\right)\psi(t) = \mathrm{e}^{-iH\Delta t}\psi(t) \tag{8.2}$$

where the propagator of the time-dependent Hamiltonian $H(t)$ is $U(t+\Delta t, t)$. The propagation has to be performed in sufficiently small time steps, so the perturbation can be regarded as constant during the time interval Δt. The numerical evaluation of the term $\mathrm{e}^{-iH\Delta t}\psi(t)$ can be performed efficiently with different techniques. For our examples the Chebychev polynomial expansion [70] is applied.

In case several potential energy surfaces are involved in the molecular process Eq. (8.1) changes to:

$$i\hbar\frac{\partial}{\partial t}\begin{pmatrix} a_1(t)\psi_1(t) \\ \vdots \\ a_n(t)\Psi_n(t) \end{pmatrix} = \begin{pmatrix} H_{11} & \cdots & H_{1n} \\ \vdots & \ddots & \vdots \\ H_{n1} & \cdots & H_{nn} \end{pmatrix}\begin{pmatrix} a_1(t)\psi_1(t) \\ \vdots \\ a_n(t)\Psi_n(t) \end{pmatrix} \tag{8.3}$$

The nuclear wavefunction can now be distributed over several potential energy surfaces. The distribution is given by the time-dependent expansion coefficients $a_n(t)$. The entries on the diagonal of the Hamiltonian matrix describe the uncoupled dynamics on the individual potential energy surfaces, i.e., on $H_{11} = T + V_1(R)$ with $V_1(R)$ the pre-calculated potential energy surface of state 1. Coupling between the different electronic states can be induced by the off-diagonal elements. They may reflect the interaction with the laser light mediated by the molecular transition dipole μ_{mn} ($H_{mn} = -\mu_{mn}E(t)$) or by intramolecular coupling, like non-adiabatic coupling (NAC), or by both.

8.2.2 Single Parameter Control

The pump–dump control concept [17, 18] has been realized in different experiments in the gas and the condensed phase (see review [71] and references therein, [30]). The concept includes three successive steps. First step: excitation of the system from the ground state (reactant) to an excited state with a femtosecond pump pulse short enough to create a wavepacket in the excited state. Second step: field free evolution of the system. Third step: interaction with a second pulse to dump the vibrational wavepacket to the target state/region on the electronic ground state.

In general, the energy gap between the electronic states is different in the Franck–Condon (FC) region of the reactants and the products and the wavelengths for pump and dump pulse should be suitably adapted. The optimal delay time Δt between pump and dump pulse must match the reaction time, in this scenario the time

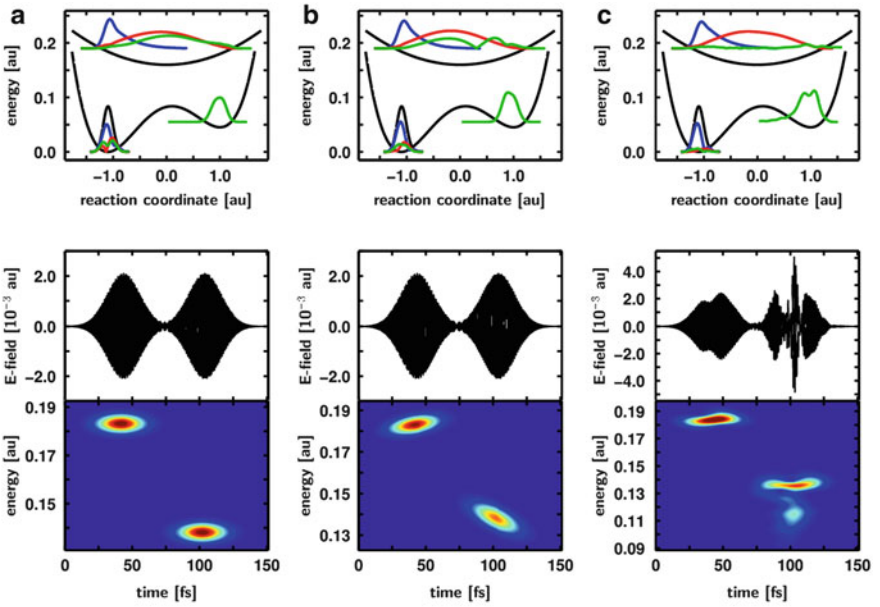

Fig. 8.1 Three different control scenarios for the population transfer from the left to the right minimum via an excited state. Panel **a** shows a pump–dump sequence, panel **b** a pump–dump sequence including chirp, and panel **c** a freely optimized sequence. The *top row* shows snapshots at 0 (*black*), 44 (*blue*), 70 (*red*), and 140 fs (*green*) from the controlled wavepacket dynamics. The initial wavepacket is shown in *black*, the excitation process in *blue*, the freely evolving wavepacket in *red*, and the final wavepacket in *green*. In the *middle row* the temporal laser fields are depicted and below their time versus frequency representation. The population transfer increases from left to right and can be followed in the amplitude of the "green" wavefunction. In **c** close to 100 % of the initial (*black*) wavefunction has been transferred to the target minimum. Nothing remains on the reactant side or in the excited state

needed for the excited state wavepacket to propagate from the reactant to the product region. Or in other words the time needed for the structural rearrangement from reactant to product on the excited state. A typical pulse sequence with the delay time $\Delta t = t_2 - t_1$ is

$$\begin{aligned} E(t) = {} & E_1 \exp\left[-2\left(\frac{t-t_1}{\mathrm{FWHM}/\sqrt{2\ln 2}}\right)^2\right] \cos\left(\omega_1 (t-t_1)\right) \\ & + E_2 \exp\left[-2\left(\frac{t-t_2}{\mathrm{FWHM}/\sqrt{2\ln 2}}\right)^2\right] \cos\left(\omega_2 (t-t_2)\right) \end{aligned} \tag{8.4}$$

For the simulation we used one-dimensional model potentials and pulses with a full width at half maximum (FWHM) of 20 fs and a maximum electric field E of 0.0021 a.u. for pump and dump. The delay time for the given system can be optimized manually. The control aim is to transfer the population from the reactant (left ground state minimum, Fig. 8.1) via the excited state to the product

Table 8.1 Pulse parameters for the pump–dump, pump–dump with chirp sequence, and for the OCT optimized pulse

	E_1/E_2 (a.u.)	Δt (fs)	ω_1/ω_2 (eV)	c_1 (eV/fs)	c_2 (eV/fs)	Reactant (%)	Excited state (%)	Target (%)
Pump–dump	0.0021	60.5	4.98/3.64	0	0	8.3	48.4	43.4
Pump–dump with chirp	0.0021	60.5	4.98/3.64	0.0046	−0.012	3.9	30.0	66.1
Optimal pump–dump	0.0024/0.0051	54.3		$\alpha_1 = 5$	$\alpha_2 = 1$	0.6	1.9	97.5

E_i is the maximum pulse amplitude, ω_i the carrier frequency, c_i the chirp parameter, and Δt the time delay between the subpulses. The indices refer to the pump (1) and dump (2) pulse

(right ground state minimum). The simulation parameters are given in Table 8.1. The pump–dump scheme is illustrated in Fig. 8.1a, where the time evolution of the wavepackets in ground and excited state is color coded. Black is the initial wavepacket, blue the wavepacket prepared by the pump pulse, red the free evolving wavepackets, and green the wavepacket transferred by the dump pulse. The pump–dump sequence is shown in the middle and its two-dimensional XFROG (crossed frequency resolved optical gating) spectrum below. The XFROG representation contains in addition to the temporal information also the information about the frequency ordering in the light pulse. In case of Fourier limited (FL) pulses all frequencies occur at the same time. The shift in the central frequencies ω_i is reflected in the shift of the two pulse maxima along the frequency axis. In case the excited state surface connects reactants and product states almost barrierless, the pump–dump scheme is quite efficient, see Table 8.1, nevertheless it can be improved.

One way of improvement is to adapt the temporal sequence of the spectral frequencies to the difference potential of the electronic states involved, which changes for the propagating wavepacket. Introducing a temporal phase $\Phi_t = \frac{c(t-t_i)^2}{2}$ by non-linear optical processes like self-phase modulation [72] leads to a change in the frequency spectrum of the pulse and introduces a so-called chirp. Note that this is usually not the approach taken by the experimentalist, as chirps are commonly realized by modulations in the frequency domain keeping the spectral width unchanged. For consistency we use the same maximum value for the electric field and keep the FWHM of 20 fs. The pump–dump pulse sequence including chirp reads:

$$\begin{aligned} E(t) = {} & E_1 \exp\left[-2\left(\frac{t-t_1}{\mathrm{FWHM}/\sqrt{2\ln 2}}\right)^2\right] \cos\left[\left(\omega_1 + \frac{c_1(t-t_1)}{2}\right)(t-t_1)\right] \\ & + E_2 \exp\left[-2\left(\frac{t-t_2}{\mathrm{FWHM}/\sqrt{2\ln 2}}\right)^2\right] \cos\left[\left(\omega_2 + \frac{c_2(t-t_2)}{2}\right)(t-t_2)\right] \end{aligned} \tag{8.5}$$

In our example a slight up chirp of the pump pulse and a stronger down chirp of the dump pulse (Fig. 8.1b) increase the product yield from 43.4 to 66.1 %, by improving both steps.

Additional control parameters like pulse intensity, wavelength, or polarization are conceivable. The simultaneous optimization of such a multiparameter scenario can be efficiently treated with OCT. A short introduction to OCT is given below. We optimized a pump–dump sequence for our model potentials with OCT. The corresponding results are given in Fig. 8.1c. The pump pulse has a similar chirp as in Fig. 8.1b. The main changes occur in the dump pulse. It is much more structured and shows strong amplitude modulation in addition to phase modulation. Again the yield for both processes, especially the dump process increase significantly leading to a final target population of 97.5 %.

8.2.3 Multiparameter Control: OCT

In the following section the basic formalism of OCT will be introduced. A summary of the various extensions of OCT can be found in [58]. The original OCT concepts for quantum control investigations were developed, predominantly in the groups of Rabitz [26, 27], Tannor and Rice [17, 18] based on the calculus of variations. In general, the following OCT functional [Eq. (8.6)] has to be maximized:

$$\begin{aligned} J\left(\psi_{ik}(t), \psi_{jk}(t), E(t)\right) &= F\left(\tau\right) - \int_0^T \alpha(t)|E(t)|^2 dt \\ - 2\Re\sum_{k=1}^{N}\left[C\int_0^T \left\langle\psi_{fk}(t)\right| i\left[H_{\mathrm{mol}} - \mu E(t)\right] + \frac{\partial}{\partial t}\left|\psi_{ik}(t)\right\rangle dt\right] \end{aligned} \tag{8.6}$$

It includes three terms, the optimization aim $F(\tau)$, an integral over the laser field penalizing the pulse fluence, and the time-dependent Schrödinger equation as an ancillary constraint. In our model case $k = 1$, the optimization aim $F(\tau)$ is to transfer an initial state wavefunction $\psi_i(t)$ into a final state ϕ_f after the laser excitation time T. In a more general fashion, the algorithm is asked to fulfill several transitions starting from various initial states to predefined target states or target regions with the same laser pulse. This formulation is known as multi-target optimal control theory (MTOCT) [73]. In MTOCT $F(\tau)$ is formulated as the sum over the absolute squares of the scalar products between the initial states $\psi_{ik}(t)$, propagated in time with the target states ϕ_{fk}:

$$F\left(\tau\right) = \sum_{k=1}^{N}\left|\left\langle\psi_{ik}(T)|\phi_{fk}\right\rangle\right|^2 \tag{8.7}$$

The second term of Eq. (8.6) is an integral over the laser field $E(t)$ with a time-dependent factor $\alpha(t)$, known as the penalty factor or Krotov change parameter. High values of α assure low field intensities and, given that a solution is found, less complex structures. With the choice of $\alpha(t) = \alpha_0/s(t)$ and, e.g., a sinusoidal

shape function $s(t)$, an envelope function can be impressed on the laser field [29, 74], which guarantees smooth switching on and off behavior of the pulse, crucial for the experimental feasibility. In order to avoid unrealistic frequency components further extensions [58] are necessary. The last term of the functional [Eq. (8.6)], the constraint, contains accordingly the Lagrange multiplier $\psi_{fk}(t)$. Separable differential equations can be derived with a suitable choice of the factor C in dependence on the definition of the optimization aim. For multi-target population transfer C is set to $C = \langle \psi_{ik}(T) | \phi_{fk} \rangle$.

The calculation of the optimal laser fields now relies on finding the extreme of the functional $J(\psi_{ik}(t), \psi_{jk}(t), E(t))$ [Eq. (8.6)] with respect to the functions $\psi_{ik}(t), \psi_{jk}(t)$ and $E(t)$. The derivative of the functional with respect to these functions leads to the following coupled equations of motion:

$$\begin{aligned} i \tfrac{\partial}{\partial t} \psi_{ik}(t) &= [H - \mu E(t)]\, \psi_{ik}(t) \\ i \tfrac{\partial}{\partial t} \psi_{fk}(t) &= [H - \mu E(t)]\, \psi_{fk}(t) \\ E(t) &= -\tfrac{s(t)}{\alpha_0 N} \Im \left[\sum_{k=1}^{N} \left\langle \psi_{ik}(t) | \psi_{fk}(t) \right\rangle \langle \psi_{ik}(t) |\, \mu \, | \psi_{fk}(t) \rangle \right] \end{aligned} \tag{8.8}$$

with the corresponding boundary conditions $\psi_{ik}(0) = \phi_{ik}$ and $\psi_{fk}(T) = \phi_{fk}$. The last equation gives the improved electric field of the current iteration. The coupled Eqs. (8.8) can be interpreted in different ways and different methods to obtain the optimal field were proposed. The schemes can be based on gradient-type optimization of the laser fields [75, 76]. Alternatively, the Krotov method, which is a global iterative procedure, was developed [28, 77, 78]. OCEs are often realized in a closed loop scenario as proposed in [31].

8.2.4 Coherent Control in the Sub-femtosecond Domain: Theory for Coupled Electron Nuclear Motion

Direct control on the electron dynamics has become a hot topic. It requires changes in the electric field on a further shorter time. Two different strategies relying either on the CEP or on the temporal phase in a modulated light field are shortly presented. In the first strategy the CEP of a few-cycle pulse is varied to control the electron dynamics. The second strategy relies on the highly precise temporal phase control in a multi-pulse sequence [79]. The theoretical treatment requires the simultaneous description of electronic and vibrational wavepacket motion. The fundamental steps of our approach [80] for molecular systems are shortly reviewed.

The approach [80] starts with the time-dependent Schrödinger equation for the total wavefunction $\Psi_{\text{tot}}(r,R,t)$:

$$
\begin{aligned}
i\,\tfrac{\partial}{\partial t}\Psi_{\mathrm{tot}}\,(r,R,t) &= H\,\Psi_{\mathrm{tot}}\,(r,R,t)\\
&\text{with}\\
\Psi_{\mathrm{tot}}\,(r,R,t) &= \begin{pmatrix} a_1(t)\psi_1\,(R,t)\,\varphi_1\,(r,t;R)\\ a_2(t)\psi_2\,(R,t)\,\varphi_2\,(r,t;R)\\ \vdots \end{pmatrix}
\end{aligned}
\tag{8.9}
$$

The total wavefunction $\Psi_{\mathrm{tot}}(r,R,t)$ is written as the product function of the nuclear wavefunction $\psi_n(R,t)$ and the electronic wavefunction $\varphi_n(r,t;R)$, now indicating the time dependence of electronic and nuclear wavefunction explicitly. Multiplying Eq. (8.9) from left by $\tilde{\varphi}_i^*\,(r;R)$ and integration over the electron coordinate r results for a multi-state problem to Eq. (8.3) and a total nuclear wavefunction $\psi_{\mathrm{tot}}(R,t)$ propagating on several electronic states V_n. To extract the time-dependent electronic wavefunction $\phi_{\mathrm{tot}}(r,t;R(t))$, we now multiply the total wavefunction $\Psi_{\mathrm{tot}}(r,R,t)$ in analogy to the BO approximation, from left with the complex conjugate of the total nuclear wavefunction $\psi_{\mathrm{tot}}^*(R,t)$ and subsequently integrate over the nuclear coordinates R:

$$
\begin{aligned}
\phi_{\mathrm{tot}}\,(r,t;R(t)) &= \int \psi_{\mathrm{tot}}^*\,(R,t)\,\Psi_{\mathrm{tot}}\,(r,R,t)\,dR\\
&= \begin{pmatrix} \phi_1\,(r,t;R(t))\\ \phi_2\,(r,t;R(t))\\ \vdots \end{pmatrix}
\end{aligned}
\tag{8.10}
$$

The components $\phi_i(r,t;R(t))$ correspond to coupled electronic wavefunctions and are given by:

$$
\begin{aligned}
\phi_i\,(r,t;R(t)) &= a_i\,(t)^2\varphi_i\,(r,t;R(t))\\
&+ \sum_{j\neq \grave{\imath}} a_i\,(t)^*\,a_j\,(t)\left\langle\psi_i\,(R,t)\,|\psi_j\,(R,t)\right\rangle_R\;\varphi_j\,(r,t;R(t))
\end{aligned}
\tag{8.11}
$$

with $a_i(t)^2$ the population of the electronic state i. The pre-factor $a_i(t)^*a_j(t)\langle\psi_i(R,t)|\psi_j(R,t)\rangle_R$ is the time-dependent overlap between the nuclear wavefunctions propagating on the potential energy surfaces i and j and defines the degree of mixing achieved for the electronic states. $\varphi_i\,(r,t;R(t))$ denotes the electronic wavefunction of state i, which parametrically depends on the nuclear coordinates R. Per construction the Hamiltonian for the electron dynamics is diagonal in the basis $\phi_i(r,t;R(t))$. Now the time-dependent electronic density $\rho_{\mathrm{tot}}(r,t;R(t))$ is calculated as a function of the electron coordinate r_1. This is done by integrating the absolute value square of the total wavefunction over the nuclear coordinates and over the $N-1$ electronic coordinates:

$$
\begin{aligned}
\rho_{\text{tot}}(r,t;R(t)) &= \int \Psi^*_{\text{tot}}\Psi_{\text{tot}}\, dR dr_2 \ldots dr_N \\
&= \sum_i a_i(t)^2 \int \varphi_i^*(r,t;R(t))\,\varphi_i(r,t;R(t)) dr_2 \ldots dr_N \\
&\quad + \sum_i \sum_{j>i} 2\Re \left\{ \sum_{j\neq i} a_i(t)^* a_j(t) \langle \psi_i(R,t) | \psi_j(R,t) \rangle_R \right. \\
&\qquad \left. \times \int \varphi_i^*(r,t;R(t))\,\varphi_j(r,t;R(t)) dr_2 \ldots dr_N \right\} \\
&= \sum_i a_i(t)^2 \int \varphi^*_{i,0}(r;R(t))\,\varphi_{i,0}(r;R(t)) dr_2 \ldots dr_N \\
&\quad + \sum_i \sum_{j>i} 2\Re \left\{ \sum_{j\neq i} a_i(t)^* a_j(t) \langle \psi_i(R,t) | \psi_j(R,t) \rangle_R \right. \\
&\qquad \left. \times \int \varphi^*_{i,0}(r;R(t))\,\varphi_{j,0}(r;R(t))\, dr_2 \ldots dr_N \times \mathrm{e}^{-i\theta_{ij}(t)} \right\}
\end{aligned}
\tag{8.12}
$$

The time dependence of the electronic wavefunction is now expressed in the eigenstate basis, i.e.,

$$
\varphi_i(r,t;R(t)) = \varphi_i(r,t=0;R(t))\,\mathrm{e}^{-iE_i(R(t))t} = \varphi_i(r,0;R(t))\,\mathrm{e}^{-iE_i(R(t))t} \tag{8.13}
$$

The time evolution of the electronic eigenfunctions φ_i obtained at "time t = 0" from a quantum chemical code is given by their phase factor $\mathrm{e}^{-iE_i(R(t))t}$. The corresponding eigenenergies $E_i(R(t))$ are functions of the nuclear coordinates due to the propagating nuclear wavefunctions. To keep track of the actual phase factor of the electronic wavefunction from time step to time step this phase factor needs to be calculated recursively by utilizing the phase of the previous time step:

$$
\theta_{ij}(t) = \theta_{ij}\left(t - \Delta t'\right) + \left(E_j(t) - E_i(t)\right)\Delta t' \tag{8.14}
$$

As the evolution of the electronic phase is much faster than the dynamics of the nuclei, the time step $\Delta t'$ needs to be adjusted relative to the time step Δt of the nuclear dynamics. The time-dependent expectation value of the nuclear coordinates $R(t) = \langle \psi_{\text{tot}}(R,t)|R|\psi_{\text{tot}}(R,t)\rangle$ is evaluated using the solution of Eq. (8.3). Subsequent quantum chemical calculations are performed at the nuclear geometries $R(t)$ to obtain the electronic wavefunctions $\varphi_{i,0}(r;R(t))$. The quantities $a_i(t)^2$, $a_i(t)^* a_j(t)\langle\psi_i(R,t)|\psi_j(R,t)\rangle_R$ are also obtained from Eq. (8.3). The integrals over the electronic wavefunctions $\int \varphi^*_{i,0}(r;R(t))\,\varphi_{i,0}(r;R(t)) dr_2 \ldots dr_N$ and $\int \varphi^*_{i,0}(r;R(t))\,\varphi_{j,0}(r;R(t))\, dr_2 \ldots dr_N$ are solved numerically. With this approach

the time evolution of an electronic wavepacket in the presence of vibrational motion can be followed.

8.3 Molecular Control Including the Electron Motion Implicitly and Explicitly

In the preceding sections quantum dynamical methods to describe the propagation of electronic and vibrational wavepackets have been outlined as well as a summary of the OCT. In the next sections we demonstrate the potential of OCT to guide vibrational wavepackets on coupled electronic potential energy surfaces. We will extend the control strategies to include the steering of electronic wavepackets explicitly.

8.3.1 Photoreactions Mediated via Conical Intersections

Many fast photoreactions in chemistry as well as in biology are mediated via conical intersection seams [81, 82]. They mark the regions where different potential energy surfaces (of the same symmetry and spin multiplicity) become degenerate and can cross. When these regions are energetically accessible after light excitation, the conical intersections mediate the fast non-radiative decay from the excited electronic state to the lower lying states and eventually to the ground state. The typical time scale is in the femto- to picosecond range. Likewise the conical intersections function as branching points towards different reaction channels.

As an example to demonstrate control of reactions governed by conical intersections we consider molecular switches. Molecular switches such as azo-benzene, fulgides or hemithioindigo derivates [8, 11, 83–87] can be used as versatile devices in nanotechnology and for logic gates in molecular computation. The active center in fulgides is a cyclohexadiene/all-*cis* hexatriene subunit [central six-membered ring, Fig. 8.2 (bottom)]. In the following we focus on this subunit. Its photochemical reaction is a text book example and well studied experimentally [88–90] as well as theoretically [91–95]. Its electrocyclic ring-opening and ring-closure reaction constitutes the switching operation from one stable isomer to the other (see Fig. 8.2). After excitation the system returns to the ground state through various conical intersections (CoIns) leading to a branching into both ground state isomers, the all-*cis* hexatriene and the cyclohexadiene, which correspond to the isomers B and A in Fig. 8.2. Femtosecond excitation of the closed isomer A yields a product ratio of 60:40 of A:B in below 200 fs [89]. Possible control strategies that optimize the switching efficiency for the cyclohexadiene/all-*cis* hexatriene subunit are discussed for two different target examples.

The most important molecular rearrangements of this photoreaction can be described in two reactive coordinates r and φ (Fig. 8.2) introduced in [93]. The asymmetric squeezing of the ring is described by the internuclear distance r and the angle between the two indicated diagonals φ. The corresponding ab initio potential

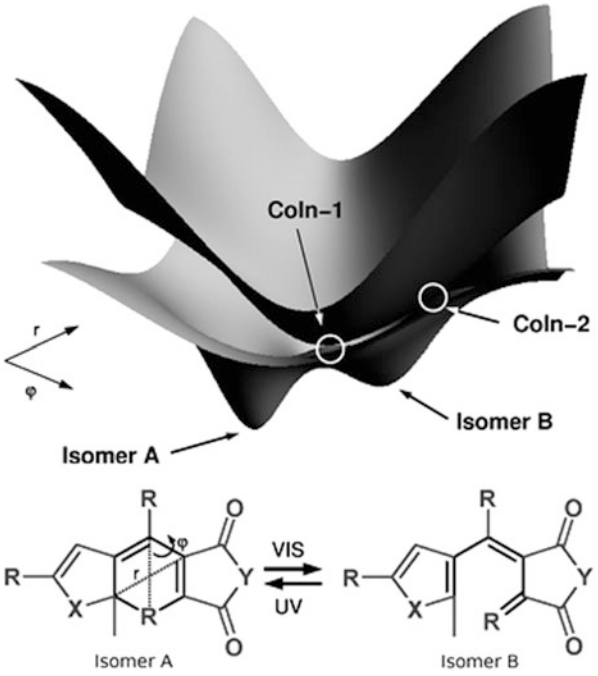

Fig. 8.2 The switching process of fulgides is driven by the electrocyclic reaction of a cyclohexadiene/all-*cis* hexatriene subunit. The reactive coordinates r and φ used for the quantum dynamics simulation are indicated. The corresponding potential energy surfaces include both minima and two conical intersections (CoIn-1 and CoIn-2) connecting the excited state and the ground state. Adapted from [58] with copyright permission of PCCP

energy surfaces of ground and excited states comprising the minima of isomers A and B and the two relevant CoIns between S_1 and S_0 are shown in Fig. 8.2 and are used for the quantum dynamics calculation. The details for the calculation can be found in [94, 96]. The effect of the CoIns is calculated non-adiabatically with the coupling elements derived by quantum chemical calculations as described in [94]. To describe the nuclear quantum dynamics beyond the BO approximation the NAC terms have to be included in the equations of motion and Eq. (8.3) becomes

$$i\frac{\partial}{\partial t}\begin{pmatrix} a_1(t)\psi_1(t) \\ a_2(t)\psi_2(t) \end{pmatrix} = \begin{pmatrix} T+V_1 & K_{ij} \\ -K_{ji} & T+V_2 \end{pmatrix}\begin{pmatrix} a_1(t)\psi_1(t) \\ a_2(t)\psi_2(t) \end{pmatrix} \tag{8.15}$$

with K_{ij} the NAC term between the electronic states $\varphi_i(r;R)$ and $\varphi_j(r;R)$. This NAC is given by (see [94, 96], for example)

$$K_{ij} = -\sum_l \frac{1}{m_l}\left(f_{ij}^{(l)}\partial_{x_l} + \frac{1}{2}g_{ij}^{(l)}\right) \tag{8.16}$$

with m_l the mass of the lth atom, x_l the Cartesian nuclear coordinates and $f_{ij}^{(l)}$ and $g_{ij}^{(l)}$ the first- and second-order derivative (non-adiabatic) coupling elements between the electronic wavefunctions i and j.

To demonstrate different control scenarios that optimize the switching, we concentrate on the backward reaction, i.e., the ring closure from isomer B to isomer A, driven by a laser excitation in the UV/VIS regime. The control of the active subunit exhibits several challenges as parts of the reaction occur in a region which only weakly couples to the laser light. One promising strategy is to prepare an excited state wavepacket in the FC region with well-defined shape and momentum, which subsequently evolves on the excited state to the target region. Possible targets are the region of the selected conical intersection on the excited state or more directly the desired ground state isomer. Control through selected conical intersections requires a corresponding projection operator in the control aim $F(\tau)$ [Eq. (8.6)] and could be achieved with a modulated light field [96]. The resulting overall quantum yield for the desired isomer was about 40 %. The switching time of about 100 fs is in the range of the experimentally observed reaction time. This optimal solution relies on a fast transfer through the selected CoIn. In general, this transfer is not completed in one step. The system has to reach the relevant CoIn several times and a loss of control is inevitable for CoIns located in an optically dark region. Further control with a shaped light pulse is not possible [96].

In case a ground state isomer is directly selected as target state, vibrationally hot molecules are formed during the control simulation. Their numerical treatment becomes challenging in the OCT algorithm, as forward and backward propagations are needed [95]. However, this process is very appropriate for a control experiment, as it relies on optical processes and targets directly accessible. The control target is realized by defining an area around the ground state geometry of the desired product (here isomer A) as the target. As in the first scenario the initial wavefunction is the vibrational ground state of isomer B. The optimal field returned by the algorithm is an all optical pump–dump process, neglecting the existence of conical intersections. The requirement for success is that the pump pulse prepares an excited state wavepacket that can reach the region where the transition to the target isomer can happen. For the matching delay time the dump pulse can transfer the wavepacket to the target isomer A. The optimization leads to a laser pulse with the following features (see Fig. 8.3): a short pump pulse with an up-chirped frequency progression is followed by an intense dump pulse which consists of two main frequencies. The mechanism can be followed in the temporal evolution of the population in the states involved. During the excitation 81 % of the population is transferred to the excited state (see Fig. 8.3a, green line) where the wavefunction evolves towards the FC region of isomer A and localizes. The dump pulse transfers 84 % of the excited state population to isomer A. The switching is completed within only 30 fs with an overall yield of 0.66 (see Fig. 8.3a, red line). This second control scenario is not only faster but also superior in efficiency to the first one with the intermediate target, as the complete switching process is now controllable. The main optimization task is performed by the pump pulse, i.e., first subpulse of the optimal field. It generates

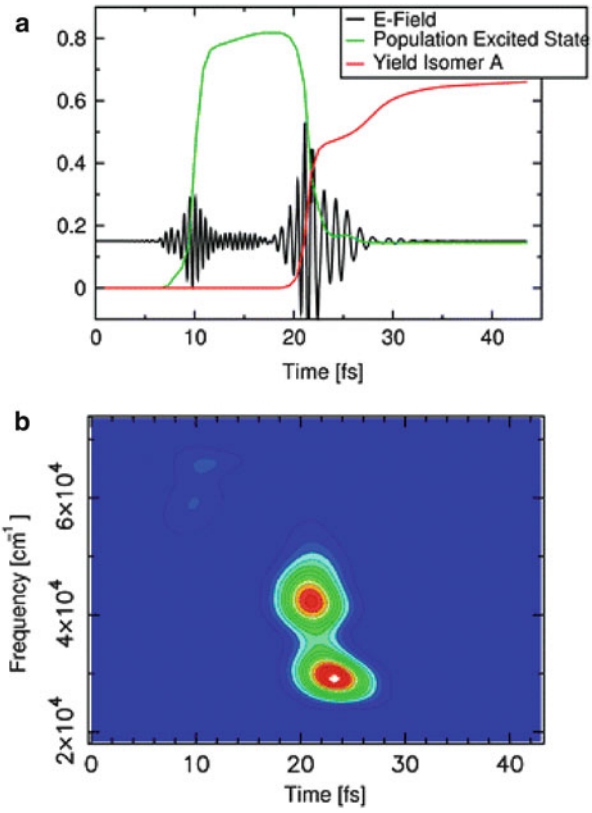

Fig. 8.3 Optimized pulse for isomer A as ground state target. *Top*: temporal evolution of the optimized field (*black*), intermediate population in the excited state (*green*), and in the target isomer A (*red*). *Bottom*: XFROG of the optimized light field. Adapted from [58] with copyright permission of PCCP

an enhanced momentum in φ, which is required to reach the target region on the excited state.

The sub-5-fs substructure in the optimized field points to the implicit impact of electronic motion in the control mechanism and to the implicit assistance of additional control knobs from the electronic wavefunction. How these can be used to control chemical reactions will be addressed in the next section.

8.3.2 Control of Electron Motion in Diatomics

Control of electron localization is regarded as the most direct way to intervene in a chemical reaction. Two different strategies already realized in experiments are shortly presented. In the first strategy control over the electron dynamics is

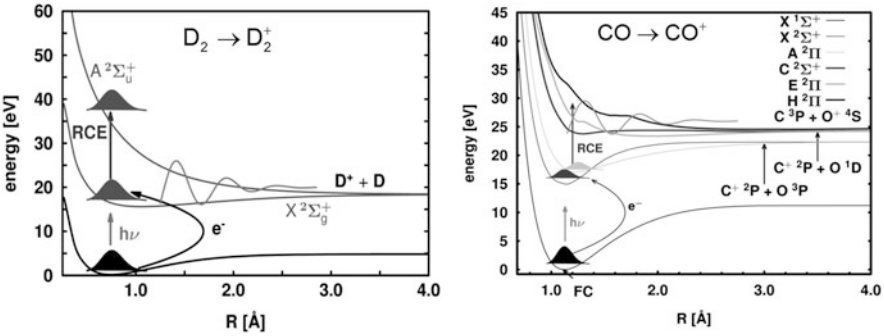

Fig. 8.4 Potential energy curves for D_2, D_2^+ (*left*) and CO, CO^+ (*right*). The pathways for the formation of ions by dissociation of the molecular ions after recollision excitation are indicated. The remaining laser field (*solid gray line*) indicates the coupling between the electronic states. Adapted from [67] with copyright permission of Elsevier B.V.

gained by variation of the CEP in a strong few-cycle pulse, typically in the NIR and MIR range. The second strategy relies on the highly precise temporal phase control in a multi-pulse sequence whose carrier frequency is typically tunable in a wide range. For a successful control of a chemical reaction, the synchronization of the electron and nuclear motion is needed. The theoretical method summarized in Sect. 8.2.4 is able to treat electron and nuclear dynamics simultaneously and to address these questions. Three different examples exhibiting the requirements for control of chemical reactions through direct control of electronic motion will be given. The extracted decisive factors for control are strongly supported by the outcome of three experiments on the diatomics D_2 [63], CO [66], and K_2 [69, 101] demonstrating control of the electron dynamics.

8.3.2.1 CEP Control

In D_2 and CO the dissociative ionization with high intense few-cycle pulses of 760 and 740 nm was investigated. The overall process consists of three steps [depicted in Fig. 8.4 for D_2 (left) and CO (right)].

The first step is the ionization, which is assumed to occur at the maximum pulse intensity, the second step is the excitation of the ion due to the recolliding electron 1.7 fs later, and the third step is the interaction with the remaining light field. The coupling with the remaining light field can generate an electronic wavepacket whose phase can be manipulated directly with the CEP of the few-cycle pulse. For illustration the superposition of the Σ_g and Σ_u electronic wavefunctions of D_2^+ is shown in Fig. 8.5. Depending on the value of the CEP the initial sign in the superposition can be set to "+," e.g., for CEP = 0, to "−," e.g., for a CEP = π, or any phase relation in between. The bottom row sketches the subsequent free evolution of the prepared electronic wavepacket.

In D_2^+ as well as in CO^+ recollision excitation (RCE) induces the dissociation. In the related experiments, the ionic fragments were recorded using a velocity

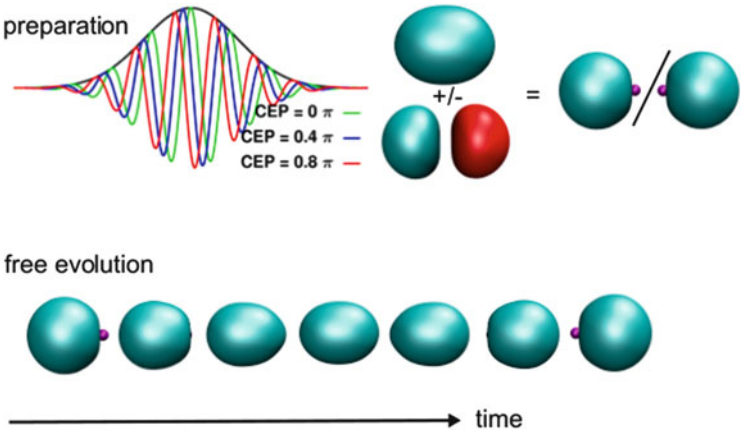

Fig. 8.5 Preparation of an electronic wavepacket by a few-cycle pulse (*top*, *left*) and its free evolution (*bottom*). The relative sign of the initial superposition is directly controllable by the CEP. A CEP of 0 π can introduce a positive sign and leads to a localization on the left, while a CEP of 1 π introduces a negative sign and a localization of the wavepacket on the right or vice versa (*top*, *right*). The localized wavepacket then starts to oscillate from one side to the other along the molecular bond

map imaging (VMI) spectrometer. Inversion of the recorded projections using an iterative procedure [97] allowed reconstruction of the original 3D ion momentum distributions. With CEP stabilization, a pronounced phase dependence on the directional ion emission of the ionic fragments ($P_{\text{left}}, P_{\text{right}}$) is found, which could be quantified by the angle-integrated asymmetry

$$A\left(W,\phi\right) = \frac{P_{\text{left}}\left(W,\phi\right) - P_{\text{right}}\left(W,\phi\right)}{P_{\text{left}}\left(W,\phi\right) + P_{\text{right}}\left(W,\phi\right)}$$

as a function of the kinetic energy W and the CEP ϕ. The asymmetry is directly linked to the localization of electron density on one of the two fragments. In $D_2{}^+$ this translates to the enhancement of electron density on either the "left" or the "right" D-atom, in CO it means the preferential formation of either C^+ or O^+.

From the experiments it is clear that the RCE channel contributes to the observed asymmetry. In case of $D_2{}^+$ it is the only source, in case of CO the tunnel ionization process also contributes to the total asymmetry [66]. In the following we concentrate the discussion on the RCE reaction channel as here the interplay between electron and nuclear wavepacket dynamics is decisive. In $D_2{}^+$ and CO^+ the RCE starts the dissociation process. During dissociation the interaction with the remaining light field transfers population between the electronic states and prepares an electronic wavepacket whose "left–right" localization can be controlled by the CEP. The simulation starts after the recollision of the electron with the parent ion. The molecules are assumed to be aligned along the laser polarization axis. The relevant potential energy surfaces (Fig. 8.4) together with the corresponding

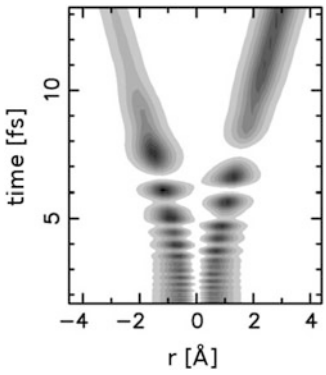

Fig. 8.6 Electron density as a function of time and the electron coordinate *r*. Adapted from [80] with copyright permission of J. Phys. B.

transition dipole moments are calculated on the CASSCF level of theory (for details see [66, 80]). After the RCE the system is excited from its ionic ground state to the higher lying states reachable for the given collision energy. In D_2^+ only the $A^2\Sigma_u^+$ state is reached, in case of CO^+ the situation is more complex since multiple electronic states are reachable.

In D_2^+ the remaining laser field couples the $A^2\Sigma_u^+$ back to the $X^2\Sigma_g^+$and thus induces a coupled electron and nuclear motion. The time evolution of the electron density is shown in Fig. 8.6.

In the beginning (1.7–5.5 fs) the superposition is built up slowly as the coupling laser light is still off-resonant. During the dissociation, the nuclear wavepacket reaches parts of the PES, where the energy difference between the $X^2\Sigma_g^+$ and the $A^2\Sigma_u^+$ state is resonant to the laser frequency, leading to a large population exchange between 6 and 9 fs and large amplitude oscillations of the electronic density from one D-atom to the other. The electron dynamics stops after about 11 fs. The overall dynamics comprising the interplay between the light pulse, the time evolution of the prepared superposition, and the nuclear quantum dynamics results in the observed asymmetry. Scanning the CEP ϕ between 0 and 2π leads to the sinusoidal behavior of the final asymmetry in the electron density which is shown in Fig. 8.7. The amplitude of the asymmetry exhibits excellent agreement with the experiment [63, 80, 98].

The decay in the dynamics of the electronic wavepacket can be explained by the interference term (double sum) in Eq. (8.12) in which the dynamical behavior is encoded. In D_2^+ the overlap of the nuclear wavefunctions $a_i(t)^* a_j(t)\langle\psi_i(R,t)|\psi_j(R,t)\rangle_R$ stays nearly constant, as well as the integral over the electronic wavefunctions $\int \varphi_{i,0}^*(r;R(t))\varphi_{i,0}(r;R(t))dr_2 \ldots dr_N$. The oscillation frequency of the electronic wavepacket is dominated by the phase term $e^{-i\theta_{ij}(t)}$ and thus by the energy difference $E_{ji}(t) = (E_j(t) - E_i(t))$ between the electronic states involved. The energy difference $E_{ji}(t)$ falls to zero during the reaction entailing a decrease in oscillation frequency of the electron density (see also Fig. 8.6) until the oscillation stops. Thus degeneration of the electronic states involved in the electronic wavepacket is one factor that determines the time window for control.

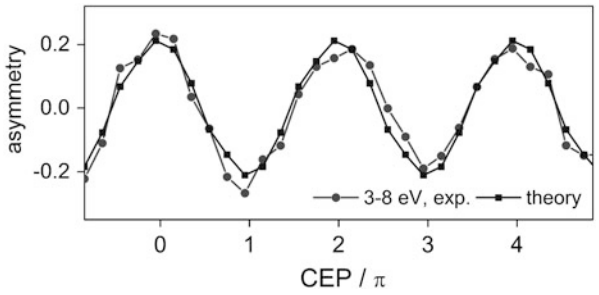

Fig. 8.7 Integrated asymmetry over several energy ranges versus carrier envelope phase ϕ and theoretical prediction. Adapted from [63, 80]

In CO^+ the situation is more complex as many electrons contribute to the time dependence of the electron density. This is reflected in the increased number of electronic states populated in the RCE and forming an electronic wavepacket already in this step. The choice of electronic states for the simulation is more demanding and guidance from the experiment is needed. Selection criteria are the energy distribution of the recolliding electron and the kinetic energy distribution of the ionic fragments. The 13 eV cut-off energy for the recolliding electron defines an upper energy limit for the excited states. Besides the CO electronic ground state, the first three $^2\Sigma$ states and the first six $^2\Pi$ states for the CO^+ ion are reachable and calculated on the CASSCF level of theory. From the excited state manifold three potential curves are selected according to the selection criteria to represent the induced nuclear dynamics [66]. The states are the $C^2\Sigma^+$ state representing the weakly bound state character and two repulsive states $E^2\Pi$ and $H^2\Pi$. The $E^2\Pi$ state correlates with the $C^+(^2P) + O(^1D)$ channel and the $H^2\Pi$ state is the first state that leads to the $C(^3P) + O^+(^4S)$ dissociation channel. The selected potential energy surfaces are depicted in Fig. 8.4, right. Due to the Gaussian energy distribution of the recolliding electron, we assume as the initial wavepacket after the RCE a 55 ($C^2\Sigma^+$):38 ($E^2\Pi$):7 ($H^2\Pi$) linear combination, which reproduces the experimentally observed ratio between C^+ and O^+ fragments [66]. Whether the initial population of the excited states (caused by the recollision) is slightly dependent on the CEP or not is an open question, but its calculation is currently beyond the scope for larger molecules [99].

For the quantum dynamical calculations, the CO^+ ions are taken to be aligned at an angle of 45° with respect to the laser polarization. This allows all transitions between the Σ and Π states. On the other hand the 45° orientation coincides with the angle for the maximum number of experimentally detected ionic fragments. The observed overall asymmetry is depicted in Fig. 8.8.

The RCE induced electron dynamics is not as pronounced as in $D_2{}^+$ and the definition of the asymmetry is slightly more complex. In heterodiatomics orientation is an issue and the asymmetry cannot be derived directly from the electron density of a single molecule at one specific orientation. In addition contributions to the

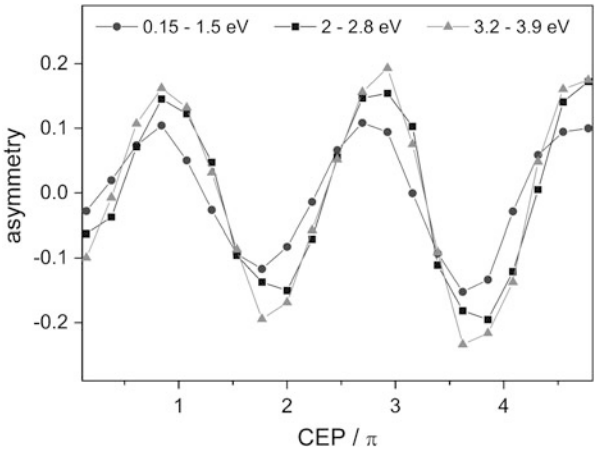

Fig. 8.8 Experimentally observed asymmetry integrated over the indicated energy ranges versus CEP. Adapted from [66] with copyright permission of APS

asymmetry arise already in the ionization step [66]. In the calculations we have direct access to the probability $P_{C^+}(t)$ of measuring a C^+ fragment for a given orientation. This probability is given by:

$$P_{C^+}(t) = \int_{x_{min}}^{x_{max}} dx \int_{y_{min}}^{y_{max}} dy \int_{z_{min}}^{0} dz \rho\left(r_1, t; R(t)\right) \tag{8.17}$$

where x, y, and z refer to the molecular frame with z pointing along the intermolecular axis and the O-atom oriented along negative z-values. The CEP-dependent asymmetry induced in the RCE can be calculated by the final $P_{C^+}(t)$ values from two different orientations, shown in Fig. 8.9c. To elucidate the mechanism the electronic state population during the interaction with the remaining light pulse and the temporal evolution of the electric field are also shown in Fig. 8.9. The population dynamics (Fig. 8.9b) shows only a weak light-induced coupling between the electronic states. Contrarily to $D_2{}^+$, the conditions for a resonance between the selected electronic states are never fulfilled. A π flip of the CEP ϕ inverts the temporal evolution of the excited states population dynamics.

The induced electron dynamics is reflected in $P_{C^+}(t)$. It starts with strong oscillations reflecting the dynamics of the electronic wavepacket prepared in the RCE step. The remaining light pulse interacts with this superposition state inducing a CEP-dependent redistribution among the electronic states involved. As soon as the light-induced population transfer stops (approximately after 8 fs, see Fig. 8.9b) the oscillation in $P_{C^+}(t)$ decreases rapidly. Its final value is directly related to the final population distribution of the electronic states leading either to the channel for C^+ or O^+ formation [66]. Their ratio is steered very precisely by the CEP. A shift of the CEP by π while keeping the molecular orientation leads to a different result

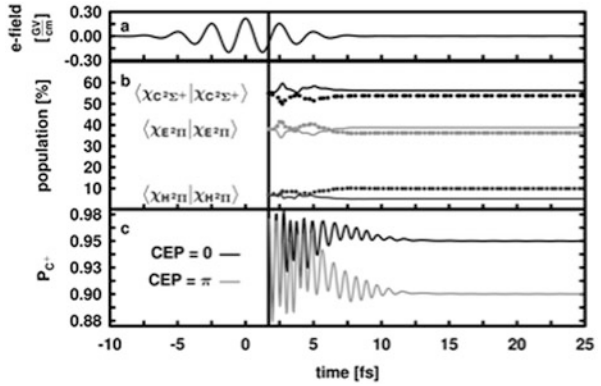

Fig. 8.9 Summary of the coupled electron and nuclear dynamics during the dissociation. The *black vertical line* indicates the time of recollision, 1.7 fs after ionization at the maximum electric field. (*a*) Temporal evolution of the electric field. (*b*) Time-dependent populations of the $C^2\Sigma^+$, $E^2\Pi$, and $H^2\Pi$ states of CO^+ after recollision excitation (*solid* CEP = 0, *dotted* CEP = π). (*c*) Temporal evolution of the probability of measuring a C^+ fragment P_{C+} for the dissociative ionization of CO^+ after recollision (*black* CEP = 0, *gray* CEP = π). Reprinted from [66] with copyright permission of APS

(gray curve in Fig. 8.9c). Changing the orientation of the molecule by 180° is equal to shifting the CEP by π, as the transition dipole moment changes the sign. Thus in practice, the CEP-dependent asymmetry can be calculated from $P_{C+}(t)$ obtained for two CEP values shifted by π. The damping of the oscillations in $P_{C+}(t)$ reflects the decay of the initially prepared electronic coherence. The reason for the decay in this example is a vanishing value of the integral

$$\int \varphi^*_{i,0}(r; R(t))\, \varphi_{j,0}(r; R(t))\, dr_2 \ldots dr_N$$

again one of the factors in the interference term of Eq. (8.12). In CO^+ the molecular orbitals become localized on either the O- or C-atom and consequently their overlap integral vanishes. This is the second factor that determines the time window for control via electron motion.

8.3.2.2 Strong Field Temporal Control

In K_2 the electron dynamics is steered via the temporal phase of a femtosecond laser pulse resonant to the electronic transition and controllable with attosecond precision (see Fig. 8.10, inset). The underlying excitation scheme is the non-adiabatic SPODS mechanism [65, 101], a strong-field resonant interaction in which the initial part of the laser pulse creates a coherent superposition between two electronic states inducing an oscillating charge distribution with maximum amplitude. After evolution on the coherently coupled PES, a later part of the laser pulse is timed

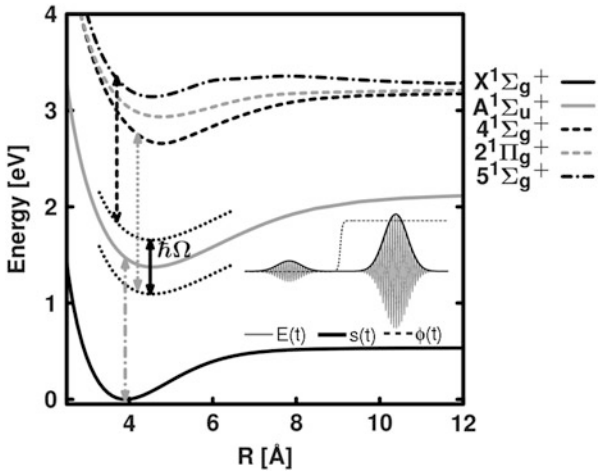

Fig. 8.10 SPODS scheme of K_2. A sketch of the SPODS pulse sequence is shown in the *inset*. The first subpulse creates a superposition between the $X^1\Sigma_g^+$ and $A^1\Sigma_u^+$ states (*gray dash–dotted arrow*). During the second pulse the X − A subsystem is "photon locked." The optical phase controls which of the dressed states (indicated as *black dotted lines*) energetically separated by Ω is selectively populated. Absorption of another photon leads to population transfer to either the lower target states, represented by the $4^1\Sigma_g^+$ (*gray dotted arrow*) or to the upper target states, represented by the $5^1\Sigma_g^+$ (*black dashed arrow*)

with high precision [79] to adjust the phase of the field to the oscillating dipole. The control strategy is schematized in Fig. 8.10 (inset).

A straightforward realization for K_2 would be a double pulse sequence consisting of a moderately strong preparation pulse followed by a more intense main pulse [101], both resonant with the bare $X^1\Sigma_g^+ - A^1\Sigma_u^+$ subsystem (see Fig. 8.10). The preparation pulse generates an electronic coherence in the X − A subsystem, launching an oscillating electric dipole $\mu(t)$ that follows the driving field with a phase shift of $\pi/2$ (see, e.g., Fig. 8.12). The subsequent main pulse interacts with the dipole, giving rise to an interaction energy $\varepsilon(t) = -\mu(t) \cdot E(t)$. The interaction energy is controlled precisely by the phase relation in the scalar product. With a $\pm\pi/2$ shift the interaction energy $\varepsilon(t)$ is either maximized or minimized. In K_2 the in-phase situation (minimization) selectively populates the lower dressed state (see Fig. 8.10 lower dotted curve), the π shift (maximization) leads to a selective population of the upper dressed state (see Fig. 8.10 upper dotted curve). During the second pulse the bare state populations are locked due to the phase relation, preventing population transfer between the X − A subsystem, although the frequency is resonant on this transition [102, 103]. The corresponding dressed states give access to lower lying (e.g., $4^1\Sigma_g^+, 2^1\Pi_g$) or higher lying (e.g., $5^1\Sigma_g^+, 6^1\Sigma_g^+, 3^1\Pi_g$) excited target states. In the experiment, a probe pulse photoionizes the excited molecule and maps the target state populations into the photoelectron spectrum [69].

This straightforward realization serves as an optimal solution for atoms [65] or rigid molecules [100]. Recent OCT calculations on this problem revealed that additional phase and amplitude modulation enhance the efficiency of SPODS in the presence of the vibrational motion [102]. In general, the light-induced electric dipole is subject to additional phase dynamics due to vibrational wavepacket propagation during the interaction with the laser pulse.

To master this complexity, more flexible pulse shapes in terms of both temporal amplitude and phase were used in experiment as well as in theory. A sinusoidal phase modulation $\varphi(\omega) = A\ \sin[T(\omega - \omega_0) + \phi]$ was applied to the laser spectrum, yielding a highly flexible and controllable multi-pulse sequence [51, 69], adjustable by the phase parameters A for the amplitude of the subpulses, T for the temporal separation of the subpulses, and ϕ controlling the relative temporal phases between adjacent subpulses.

In the calculation the phase mask was applied to a Fourier limited pulse $E_{\mathrm{FL}}(t)$ with a Gaussian envelope and variable FWHM.

$$E_{\mathrm{FL}}(t) = E_0 \cdot \mathrm{e}^{-2\left(\frac{t-t_0}{\mathrm{FWHM}/\sqrt{2\ln 2}}\right)^2} \cdot \cos\left[\omega_{\mathrm{FL}}\,(t - t_0)\right] \tag{8.18}$$

For the dynamics simulation, we again used our approach [80] for the coupled electron and nuclear quantum dynamics. We followed the time-dependent expectation value of the induced electric dipole moment $\mu(t) = \langle\mu(t)\rangle$ which is related to the time-dependent electron density $\rho_{\mathrm{tot}}(r, t; R(t))$ of Eq. (8.12) through $\langle\mu(t)\rangle = \langle\phi_{\mathrm{tot}}(r, t; R(t))|\mu|\phi_{\mathrm{tot}}(r, t; R(t))_r\rangle$ with μ the dipole operator.

The electric field $E_{\mathrm{FL}}(t)$ is modulated in the frequency domain with the sinusoidal phase mask $\varphi(\omega)$ (for positive values of ω):

$$E_{\mathrm{mod}}(t) = F^{-1}\left(F\,(E_{\mathrm{FL}}(t)) \cdot \mathrm{e}^{-i\varphi(\omega)}\right) \tag{8.19}$$

The values for the phase mask were set in correspondence to the experiment to $A = 0.55$ and $\omega = 0.055$ a.u. For the phase offset and the interpulse delay values in the range of $\phi \in [0 : 2\pi]$ and $T \in [0 : 60]$ fs were taken. In accordance to the SPODS mechanism the low-lying versus high-lying target state population is inverted when the relative phase ϕ between preparation and main pulse is changed by π. In the absence of vibrational motion an almost constant contrast is expected with varying interpulse delay T. In the presence of vibrational motion additional dependence on T is expected as the vibrational motion influences the oscillating electric dipole $\langle\mu(t)\rangle$ [69].

To demonstrate the vibrational influence we analyze exemplarily the effect of the first part of the preparation pulse in the experimental multi-pulse sequence that optimized the transfer to the high-lying target states. A relevant section of the multi-pulse sequence is shown in red in Fig. 8.11, the first part of the preparation pulse is indicated by the red envelope (Fig. 8.11, top) and the active switching windows for the SPODS mechanism are marked by the black rectangles. The

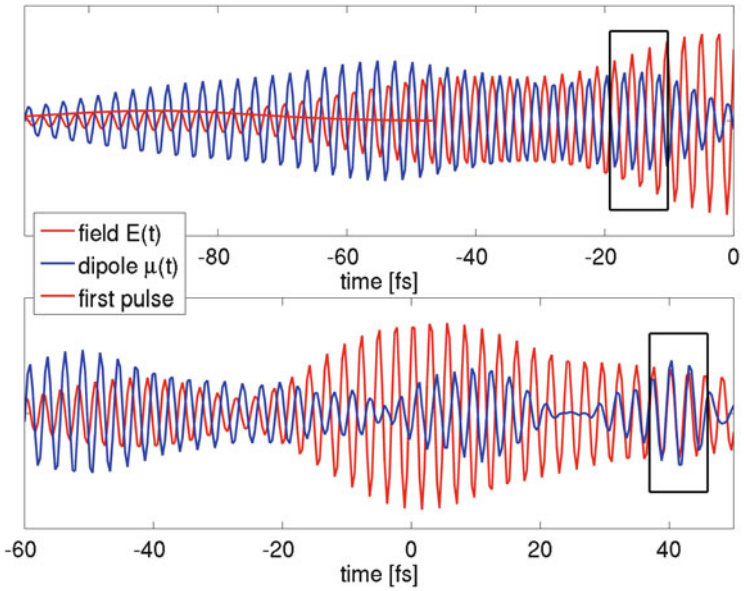

Fig. 8.11 Relevant section of the experimental multi-pulse sequence that controls the population transfer to the higher lying (*top*) or to the lower lying (*bottom*) target states. The electric light field is shown in *red* and the induced electric dipole in *blue*. The *red envelope* (*top*) indicates the first part of the preparation pulse, the *black rectangle* the respective SPODS switching time windows

induced oscillating dipole is shown in blue. A relevant section of the multi-pulse sequence that optimized the transfer to the low-lying target states is shown below. In accordance with the SPODS mechanism the dipole and the electric field are either in (bottom) or out (top) of phase in the switching window. In agreement with the OCT calculation [102], the main pulse (Fig. 8.11, top) in the optimal pulse sequence shows an upward chirp. To demonstrate how the temporal phase $\varphi(t)$ of the oscillating dipole can be extracted we concentrate exclusively on the first part of the preparation pulse (Fig. 8.11, top and Fig. 8.12, top).

The following steps are needed. First, the Fourier transform of the electric dipole is calculated:

$$\mu(\omega) = F(\mu(t)) \tag{8.20}$$

Next the negative frequencies are removed and subsequent inverse Fourier transform leads to the complex field in the time domain $\mu'(t)$:

$$\begin{aligned} \mu^{+}(\omega) &= \begin{cases} \mu(\omega) & \text{for } \omega > 0 \\ 0 & \text{for } \omega \leq 0 \end{cases} \\ \mu'(t) &= F^{-1}\left(\mu^{+}(\omega)\right) \end{aligned} \tag{8.21}$$

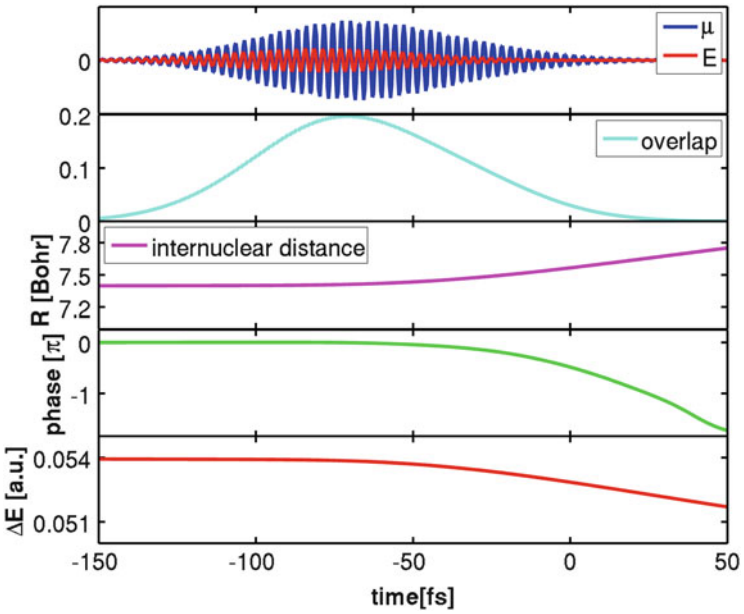

Fig. 8.12 Analysis of the impact of the vibrational motion on the induced oscillating electric dipole. *Top*: first part of the preparation pulse from Fig. 8.11 (*red*), launched dipole (*blue*). *Second row*: time-dependent overlap of the vibrational wavepackets in the X − A subsystem. *Third row*: internuclear distance changing with the propagating vibrational wavepackets. *Fourth row*: extracted phase $\varphi(t)$ of the electric dipole. *Bottom*: change in the X − A energy difference during the propagation of the vibrational wavepacket

which can be decomposed into a slowly varying envelope $s(t)$, a fast oscillation with the frequency ω_0 and the temporal phase $\varphi(t)$:

$$\mu'(t) = s(t) \cdot \mathrm{e}^{-i\omega_0(t-t_0)} \cdot \mathrm{e}^{i\varphi(t)} \tag{8.22}$$

After multiplying $\mu'(t)$ with the carrier frequency ω_0 (set to the laser frequency ω_{FL}):

$$\overline{\mu}(t) = \mu'(t) \cdot \mathrm{e}^{i\omega_0(t-t_0)} = s(t)\mathrm{e}^{i\varphi(t)} \tag{8.23}$$

the temporal phase can be extracted as the time evolution of the angle in the complex plain of $\overline{\mu}(t)$.

The phase $\varphi(t)$ in Fig. 8.12 (fourth panel) shows a quadratic shift which can be regarded as a downward chirp of the dipole oscillation frequency. It is induced because the propagating nuclear wavepackets map the variation in the X − A energy gap (Fig. 8.12, bottom) onto the electric dipole oscillation. In the dissociation dynamics of D_2^+ the energy gap converged to zero and stopped the fast electron dynamics. In the bound state dynamics of K_2 the more moderate change in the

electronic resonance introduces the dynamic detuning in the frequency of the electric dipole and has to be taken into account when selecting the interpulse delay T to match the SPODS condition.

In addition to the phase modulation an even more pronounced amplitude modulation is observed (Fig. 8.12, top). After the first pre-pulse (red), the oscillating dipole (blue) is damped simultaneously with the temporal decrease in overlap of the nuclear wavefunctions propagating on the $X^1\Sigma_g^+$ and the $A^1\Sigma_u^+$ surface (Fig. 8.12, second panel). Due to the difference in position and shape of both surfaces, the freely evolving nuclear wavepackets get out of phase. Their spatial overlap $a_i(t)^* a_j(t)\langle\psi_i(R,t)|\psi_j(R,t)\rangle_R$ is reduced, which is again a decisive factor for the electron dynamics [Eq. (8.12)]. Its decrease stops the electron dynamics as observable in the damping of the electric dipole oscillation and in the loss of control for large subpulse separations [69]. In this sense K_2 is an example for the third factor in Eq. (8.12), which determines the electron dynamics. This third factor can be regarded as time-dependent FC overlap.

Both effects—phase and amplitude modulation of the electric dipole—are observable in the experiment [69]. The strong amplitude modulation compels the short interpulse delay for optimal SPODS control. The sinusoidal mask function is flexible enough to adapt to the more subtle phase modulation. On top, it even varies the amplitude and phase modulation of the electric dipole to optimize the SPODS control. Two examples from an experimental control landscape are shown in Fig. 8.13. The upper panel shows the results for the higher lying target states (5 and $6\Sigma_g^+$, $3\Pi_g$, situation ①), the lower panel for the lower lying target states (4 Σ_g^+, 2 Π_g, situation ②). The photoelectron spectra recorded for situation ① and ② are shown on the left. The relevant section of the multi-pulse sequence and the underlying population dynamics are also shown.

In ①, the laser field between −100 and −50 fs prepares the coherent superposition in the X − A subsystem, launching the oscillating electric dipole. In the switching time window (indicated as gray area), the dipole oscillates with maximum amplitude exactly out of phase with the electric field of the main pulse. The intense central subpulse opens the upper target channel for efficient population transfer. In ②, again the X − A coherence is build up between −100 and −50 fs. A more complicated population dynamics including Rabi cycling follows. Around 45 fs, the dipole increases once more and shifts in phase with the shaped laser pulse during the switching time window and the lower target states are populated efficiently. The electron movie frames in the upper panels of Fig. 8.13 visualize the induced electronic wavepacket dynamics in form of the electron density together with the associated dipole moment $\langle\mu(t)\rangle$ (blue arrows) and the applied electric field $E(t)$ (red arrows). Starting from the ground state configuration, the movies proceed via the transient electron dynamics during the switching time window and end with the molecule in its final electronic configuration. The vertical black and green dashed lines indicate the nuclear dynamics during the interaction. In situation ①, the molecule is steered into a peanut-shaped electron configuration dominated by the $5\Sigma_g^+$ electron density distribution. In situation ② the molecule is guided

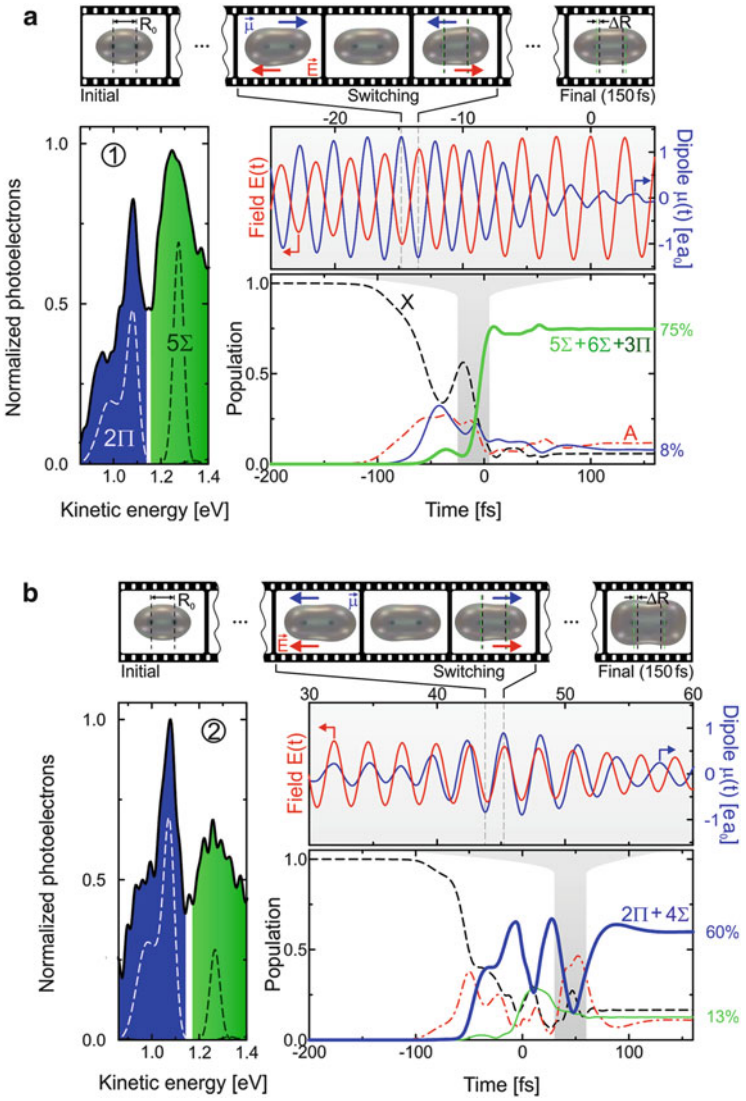

Fig. 8.13 Experimental and theoretical results for the excitation of K_2 molecules with two different pulse shapes, leading to population of **a** the upper target states and **b** the lower target states. On the left the measured photoelectron spectra (*black line*, signal contributions colored accordingly) are compared to simulations (*dashed lines*). To the right, the neutral electronic population dynamics are shown. The *blue* and *green curves* represent the accumulated populations of the lower (*blue*) and upper electronic target channels (*green*). The phase relation of the electric field $E(t)$ (*red line*) and the induced electric dipole moment $\mu(t)$ of the X − A subsystem (*blue line*) is illustrated in the *upper right frame*. The switching time window for the population transfer to the electronic target channels is indicated as *gray-shaded* background. The amplitude and phase modulation of the electronic dipole with respect to the electric field directly reflects the coupling between the nuclear and electronic motion. The movies on *top* show snapshots of the induced electron density motion for decisive moments during the laser–molecule interaction. Adapted from [69]

into a cushion like electronic configuration, reflecting the $2\ ^1\Pi_g$ electron density distribution.

8.4 What Can Be Learned for Larger Molecules?

From the theoretical and experimental results on the electron control in diatomics, three main factors are identified that define the lifetime of electronic wavepackets and thus the time window for control. This knowledge is used to design a novel scheme for the control of a photochemical reaction by guidance of an electronic wavepacket. A situation is needed in which the prepared and controlled electronic wavepacket survives long enough to determine the outcome of a chemical reaction. Such a situation is found in photo-induced reactions proceeding via CoIns. These prominent regions on the potential energy surface can serve as points of no return for the nuclear dynamics, irreversibly setting the reaction path. Already the presented OCT results on the reaction control of the cyclohexadiene/all-*cis*-hexatriene system through CoIns pointed to the impact of electronic motion. Chemists classify the reaction as electrocyclic reaction, sketching a cyclic electronic motion circling electron density from a σ-bond into the extended π-system and back.

Due to the NAC, population is switched between the intersecting electronic states. Thereby, a superposition state and hence an electronic wavepacket is formed. In the vicinity of CoIns, the time scales of the electron and nuclear dynamics are well synchronized. The energy difference between the coupled electronic states becomes very small slowing down the dynamics of the usually faster electrons to the time scale of the nuclear dynamics and below. The motion of the electronic density in the vicinity of a CoIn is visualized in Fig. 8.14 for CoIn-1 of the cyclohexadiene/all-*cis*-hexatriene system (Fig. 8.2). The underlying electronic wavepacket is created as the normalized superposition of the CASSCF-wavefunctions of ground and first excited state, keeping the nuclear geometry fixed. To describe the temporal evolution we take into account the time-dependent phase of both components.

CoIn-1 is known as a branching point towards cyclohexadiene and hexatriene. In correspondence we observe a gradual change from a more cyclohexadiene type electronic structure (snapshot 1) via the characteristic [91–93] three center bond (snapshot 2) to a more all-*cis*-hexatriene like electronic structure (snapshot 3) and back on a time scale of 1.6 ps. Directly at the intersection point, the energy gap is zero and the electron dynamics stops. Whether it stops more in the cyclohexadiene or hexatriene type configuration can be influenced by preparing an electronic wavepacket with a controllable phase relation already before the CoIn is reached. CoIn-1 lies close to the S_1 minimum (see Fig. 8.2), where the ground (S_0) and excited state (S_1) are separated by about 1.5 eV. Here the preparation of an electronic wavepacket by a resonant few-cycle IR pulse of about 800 nm is possible. In most cases the electronic wavepacket needs to be prepared close to the CoIn. If prepared far away it will not survive until the system has reached the CoIn due to the vanishing time-dependent FC-factor in Eq. (8.12). Snapshots for the motion of the electron density as inducible by an IR pulse that creates a S_1/S_0 superposition

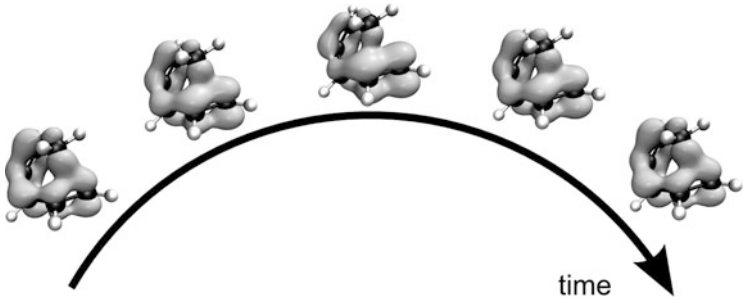

Fig. 8.14 Snapshots of the time evolution of an electronic wavepacket prepared close to CoIn-1 for fixed nuclear geometry. The underlying electronic wavepacket is created as the normalized superposition of the CASSCF-wavefunctions of ground and first excited state. The depicted motion of the electron density takes place in 1.6 ps

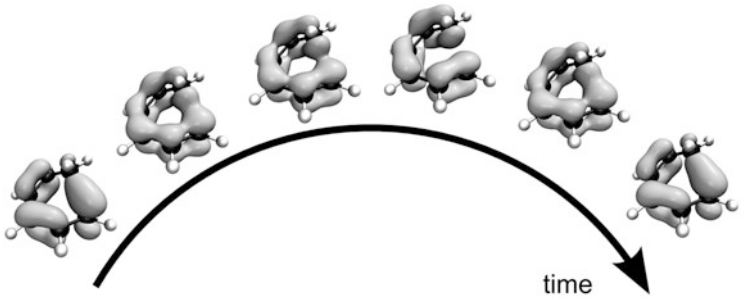

Fig. 8.15 Snapshots of the time evolution of an electronic wavepacket prepared at the S_1 minimum for fixed nuclear geometry. The underlying electronic wavepacket is created as the normalized superposition of the CASSCF-wavefunctions of ground and first excited state. The depicted motion of the electron density takes place in less than 3 fs

state at the S_1 minimum are shown in Fig. 8.15. The snapshots are given for selected non-equidistant time steps to visualize the ongoing dynamics.

The electronic wavepacket now moves on a much faster time scale, changing from the cyclohexadiene to the hexatriene and again to the cyclohexadiene configuration in less than 3 fs. In the example the initial superposition is an electronic structure close to the cyclohexadiene (first snapshot). During the time evolution, electron density is withdrawn from the σ-bond and cycles around the π-system towards an electronic structure close to hexatriene (fourth snapshot) then again along the π-system to the cyclohexadiene structure (last snapshot) and so forth. During the reaction path to the CoIn-1 the electron dynamics will be slowed down until it stops at the CoIn-1. The electronic configuration at CoIn-1 now depends on and can be controlled by the initially prepared wavepacket.

The scenario was tested for a two-dimensional model potential (Fig. 8.16), designed as first study case. Here, CoIn and NACs are chosen such that an equally distributed population between S_2 and S_1 is obtained after the wavepacket on S_2 has

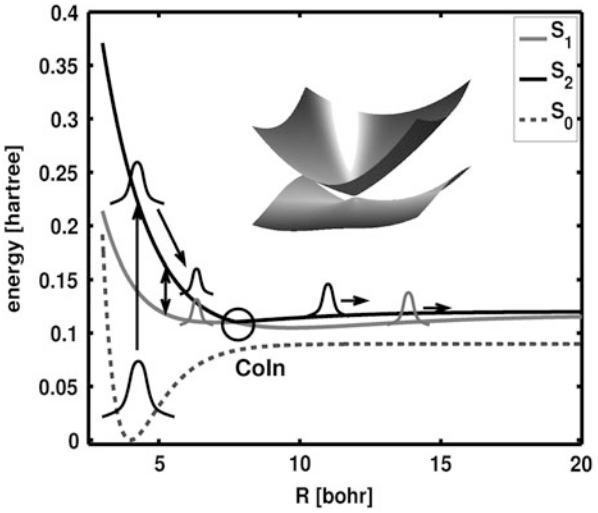

Fig. 8.16 1D cut of the 2D adiabatic potential energy surfaces S_0, S_1, and S_2. A 2D representation of the S_1 and S_2 surface at the CoIn is shown as *inset*

passed the CoIn without any control pulse. The details of the calculation are given in [68, 98]. The task is to control the branching ratio between S_2 and S_1 at the CoIn. The reaction is started by a first pulse, transferring population from the electronic ground state S_0 to the electronically excited state S_2. The system evolves on S_2 towards the CoIn S_2/S_1. Shortly before it reaches the CoIn, a second pulse, e.g., a phase stable MIR control pulse is sent in and prepares the S_1/S_2 superposition. The phase of the electronic wavepacket is imprinted by the CEP of the IR-control-field and is used to steer the passage through the CoIn.

For the model system a 3-fs (FWHM) Gaussian pulse, resonant to the $S_0 - S_2$ transition with moderate maximum electric field (100 GV/cm^2) is used as pump pulse. The pump pulse should be resonant and its time duration short compared to the systems nuclear dynamics to produce a narrow and localized vibrational wavepacket on the excited state, which later can be efficiently coupled to the S_1 state. The MIR-control-field (3.0 μm, 12 fs FWHM (100 GV/cm^2), CEP $= 0.1\ \pi$) has to follow at the right delay, here within 40 fs.

Figure 8.17 shows the final populations in the target states (S_1: gray line; S_2: black line) as a function of the CEP of the MIR control pulse. We could steer the final population ratio S_1:S_2 in limits of 27:73 and 69:31 very precisely by changing the CEP of the MIR pulse. The loss in control efficiency can be assigned to the imperfect preparation of the superposition by the MIR control pulse.

The observed control can be understood as follows: changing the phase in the MIR-control-field changes the phase of the prepared superposition, i.e., the phase of the electronic wavepacket and thus its localization. The NAC elements imprint a constant phase on the superposition state themselves. Thus, the interplay between

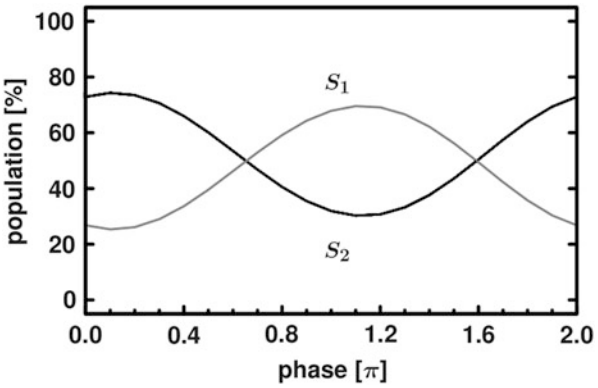

Fig. 8.17 Final population of the S_1 (*gray*) and the S_2 state as a function of the CEP of the MIR control pulse

both phases now defines the path through the CoIn, the position of the electron density and simultaneously the final branching ratio. As a consequence, the phase in a few-cycle pulse or, in a different scenario, the relative phase in a multi-pulse sequence is a highly efficient knob, which is capable of controlling electron dynamics. When timed correctly a chemical reaction can be steered very precisely combining the tools for nuclear and electron control.

In this chapter we summarized successful demonstrations on control of molecular dynamics with sophisticated light fields and reviewed the experimental and theoretical methods required to observe and describe these processes. The examples ranged from small diatomics to complex polyatomic molecules and from the femtosecond to the sub-femtosecond time scale. The special focus was on the role of the electron motion. When does control of electronic wavepackets play a role and under which circumstances can they be guided to influence the outcome of a molecular reaction in which the atoms have to move. From the diatomic examples, comprising the two different experimental realizations of CEP control and strong field temporal control, very precise requirements could be deduced as for diatomics theory and experiment can work very close together. In a theoretical proposal these requirements were transferred to the real world scenario of the photo-induced electrocyclic ring opening of cyclohexadiene. The theoretical calculations show how and when the electrocyclic motion through the π-system of the ring is involved and how it can be controlled to influence the outcome of the photoreaction. Both experimental approaches presented should be able to induce and control the respective electronic wavepacket. The future will show whether one of the famous text book examples for electrocyclic reactions can be visualized and controlled with state-of-the-art light field control.

References

1. Zewail AH (1980) Laser selective chemistry—is it possible? Phys Today 33:27
2. Robinson PJ, Holbrook KA (1972) Unimolecular reactions. Wiley-Interscience, New York
3. Zewail AH (2000) Femtochemistry: atomic-scale dynamics of the chemical bond. J Phys Chem A 104:5660–5694
4. Vierheilig A, Chen T, Waltner P, Kiefer W, Materny A, Zewail AH (1999) Femtosecond dynamics of ground-state vibrational motion and energy flow: polymers of diacetylene. Chem Phys Lett 312:349
5. Zhong D, Bernhardt TM, Zewail AH (2000) Femtosecond real-time probing of reactions. 24. Time, velocity, and orientation mapping of the dynamics of dative bonding in bimolecular electron transfer reactions. J Phys Chem A 103:10093
6. Lochbrunner S, Wurzer AJ, Riedle E (2003) Microscopic mechanism of ultrafast excited-state intramolecular proton transfer: a 30-fs study of 2-(2′-hydroxyphenyl)benzothiazole. J Phys Chem A 107:10580
7. Schriever C, Barbatti M, Stock K, Aquino AJA, Tunega D, Lochbrunner S, Riedle E, de Vivie-Riedle R, Lischka H (2008) The interplay of skeletal deformations and ultrafast excited-state intramolecular proton transfer: experimental and theoretical investigation of 10-hydroxybenzo[h]quinoline. Chem Phys 347:446
8. Brust T, Draxler S, Eicher J, Lees WJ, Rück-Braun K, Zinth W, Braun M (2010) Increasing the efficiency of the ring-opening reaction of photochromic indolylfulgides by optical pre-excitation. Chem Phys Lett 489:175
9. Langhals H, Esterbauer AJ, Walter A, Riedle E, Pugliesi I (2010) Förster resonant energy transfer in orthogonally arranged chromophores. J Am Chem Soc 132:16777
10. Haiser K, Fingerhut BP, Heil K, Glas A, Herzog TT, Pilles BM, Schreier WJ, Zinth W, de Vivie-Riedle R, Carell T (2012) Mechanism of UV-induced formation of Dewar lesions in DNA. Angew Chem Int Ed 51:408
11. Nenov A, Schreier WJ, Koller FO, Braun M, de Vivie-Riedle R, Zinth W, Pugliesi I (2012) Molecular model of the ring-opening and ring-closure reaction of a fluorinated indolylfulgide. J Phys Chem A 116:10518
12. Sailer CF, Thallmair S, Fingerhut BP, Nolte C, Ammer J, Mayr H, Pugliesi I, de Vivie-Riedle R, Riedle E (2013) A comprehensive microscopic picture of the benzhydryl radical and cation photogeneration and interconversion through electron transfer. Chem Phys Chem 14:1423
13. Brumer P, Shapiro M (1986) Control of unimolecular reactions using coherent light. Chem Phys Lett 126:541
14. Shapiro M, Hepburn JW, Brumer P (1988) Simplified laser control of unimolecular reactions: simultaneous (ω_1, ω_3) excitation. Chem Phys Lett 149:451
15. Gaubatz U, Rudecki P, Becker M, Schiemann S, Külz M, Bergmann K (1988) Population switching between vibrational levels in molecular beams. Chem Phys Lett 149:463
16. Gaubatz U, Rudecki P, Schiemann S, Bergmann K (1990) Population transfer between molecular vibrational levels by stimulated Raman scattering with partially overlapping laser fields. A new concept and experimental results. J Chem Phys 92:5363
17. Tannor DJ, Rice SA (1985) Control of selectivity of chemical reaction via control of wave packet evolution. J Chem Phys 83:5013
18. Tannor DJ, Kosloff R, Rice SA (1986) Coherent pulse sequence induced control of selectivity of reactions: exact quantum mechanical calculations. J Chem Phys 85:5805
19. Potter ED, Herek JL, Pedersen S, Liu Q, Zewail AH (1992) Femtosecond laser control of a chemical reaction. Nature 355:66
20. Baumert T, Herek JL, Zewail AH (1993) Femtosecond real-time probing of reactions. XI. The elementary OClO fragmentation. J Chem Phys 99:4430
21. Banares L, Baumert T, Bergt M, Kiefer B, Gerber G (1997) Femtosecond photodissociation dynamics of $Fe(CO)_5$ in the gas phase. Chem Phys Lett 267:141

22. Baumert T, Grosser M, Thalweiser R, Gerber G (1991) Femtosecond time-resolved molecular multiphoton ionization: the Na_2 system. Phys Rev Lett 67:3753
23. Baumert T, Helbing J, Gerber G (1997) In: Prigogine I, Rice S (eds) Advances in chemical physics-photochemistry: chemical reactions and their control on the femtosecond time scale. Wiley, New York, pp 47–77
24. Peirce AP, Dahleh MA, Rabitz H (1988) Optimal control of quantum-mechanical systems: existence, numerical approximation, and applications. Phys Rev A 37:4950
25. Kosloff R, Rice S, Gaspard P, Tersigni S, Tannor D (1989) Wavepacket dancing: achieving chemical selectivity by shaping light pulses. Chem Phys 139:201
26. Zhu W, Botina J, Rabitz H (1998) Rapidly convergent iteration methods for quantum optimal control of population. J Chem Phys 108:1953
27. Zhu W, Rabitz H (1998) A rapid monotonically convergent iteration algorithm for quantum optimal control over the expectation value of a positive definite operator. J Chem Phys 109:385
28. Tannor DJ, Kazakov V, Orlov V (1992) In: Broeckhove J, Lathouwers L (eds) Time dependent quantum molecular dynamics. Plenum, New York, pp 347–360
29. Sundermann K, de Vivie-Riedle R (1999) Extensions to quantum optimal control algorithms and applications to special problems in state selective molecular dynamics. J Chem Phys 110:1896
30. Brixner T, Pfeifer T, Gerber G, Wollenhaupt M, Baumert T (2005) In: Hannaford P (ed) Femtosecond laser spectroscopy (Chapter 9). Springer, Berlin, pp 225–266
31. Judson RS, Rabitz H (1992) Teaching lasers to control molecules. Phys Rev Lett 68:1500
32. Weiner A, Leaird D, Patel J, Wullert JI (1992) Programmable shaping of femtosecond optical pulses by use of 128-element liquid crystal phase modulator. IEEE J Quantum Electron 28:908
33. Bardeen CJ, Yakovlev VV, Wilson KR, Carpenter SD, Weber PM, Warren WS (1997) Feedback quantum control of molecular electronic population transfer. Chem Phys Lett 280:151
34. Assion A, Baumert T, Bergt M, Brixner T, Kiefer B, Seyfried V, Strehle M, Gerber G (1998) Control of chemical reactions by feedback-optimized phase-shaped femtosecond laser pulses. Science 282:919
35. Levis RJ, Rabitz H (2002) Closing the loop on bond selective chemistry using tailored strong field laser pulses. J Phys Chem A 106:6427
36. Bartels RA, Weinacht TC, Leone SR, Kapteyn HC, Murnane MM (2002) Nonresonant control of multimode molecular wave packets at room temperature. Phys Rev Lett 88:033001
37. Rabitz H, de Vivie-Riedle R, Motzkus M, Kompa KL (2000) Whither the future of controlling quantum phenomena? Science 288:824
38. de Vivie-Riedle R, Troppmann U (2007) Femtosecond lasers for quantum information technology. Chem Rev 107:5082
39. Negretti A, Benseny A, Mompart J, Calarco T (2013) Speeding up the spatial adiabatic passage of matter waves in optical microtraps by optimal control. Quantum Inf Process 12:1439
40. Goerz MH, Calarco T, Koch CP (2011) The quantum speed limit of optimal controlled phasegates for trapped neutral atoms. J Phys B 44:154011
41. Vogt G, Krampert G, Niklaus P, Nuernberger P, Gerber G (2005) Optimal control of photoisomerization. Phys Rev Lett 94:068305
42. Polachek L, Oron D, Silberberg Y (2006) Full control of the spectral polarization of ultrashort pulses. Opt Lett 31:631
43. Plewicki M, Weber S, Weise F, Lindinger A (2007) Independent control over the amplitude, phase, and polarization of femtosecond pulses. Appl Phys B 86:259
44. Brixner T, Krampert G, Pfeiffer T, Selle R, Gerber G, Wollenhaupt M, Gräfe O, Horn C, Liese D, Baumert T (2004) Quantum control by ultrafast polarization shaping. Phys Rev Lett 92:208301

45. Zeidler D, Frey S, Kompa K-L, Motzkus M (2001) Evolutionary algorithms and their application to optimal control studies. Phys Rev A 64:023420
46. Herek JL, Wohlleben W, Cogdell RJ, Zeidler D, Motzkus M (2002) Quantum control of energy flow in light harvesting. Nature 417:533
47. Hornung T, Meier R, Motzkus M (2000) Optimal control of molecular states in a learning loop with a parameterization in frequency and time domain. Chem Phys Lett 326:445
48. Meshulach D, Silberberg Y (1998) Coherent quantum control of two-photon transitions by a femtosecond laser pulse. Nature 396:239
49. Lozovoy VV, Pastirk I, Walowicz KA, Dantus M (2003) Multiphoton intrapulse interference. II. Control of two- and three-photon laser induced fluorescence with shaped pulses. J Chem Phys 118:3187
50. Bartelt A, Lindinger A, Lupulescu C, Vajda Š, Wöste L (2003) One parameter fs-pulse form control on NaK and Na_2K. Phys Chem Chem Phys 5:3610
51. Wollenhaupt M, Präkelt A, Sarpe-Tudoran C, Liese D, Bayer T, Baumert T (2006) Femtosecond strong-field quantum control with sinusoidally phase-modulated pulses. Phys Rev A 73:063409
52. Vogt G, Nuernberger P, Selle R, Dimler F, Brixner T, Gerber G (2006) Analysis of femtosecond quantum control mechanisms with colored double pulses. Phys Rev A 74:033413
53. Roslund J, Rabitz H (2009) Experimental quantum control landscapes: inherent monotonicity and artificial structure. Phys Rev A 80:013408
54. Filatov M (2013) Understanding the dynamics behind photoisomerization of light-driven molecular rotary motors. Comput Mol Sci 3:427
55. Rabitz HA, Hsieh MM, Rosenthal CM (2004) Quantum optimally controlled transition landscapes. Science 303:1998
56. Wollenhaupt M, Präkelt A, Sarpe-Tudoran C, Liese D, Baumert T (2005) Quantum control and quantum control landscapes using intense shaped femtosecond pulses. J Mod Opt 52:2187
57. Bayer T, Wollenhaupt M, Baumert T (2008) Strong-field control landscapes of coherent electronic excitation. J Phys B 41:074007
58. von den Hoff P, Thallmair S, Kowalewski M, Siemering R, de Vivie-Riedle R (2012) Optimal control theory – closing the gap between theory and experiment. Phys Chem Chem Phys 14:14460
59. Andrae D, Barth I, Bredtmann T, Hege H-C, Manz J, Marquardt F, Paulus B (2011) Electronic quantum fluxes during pericyclic reactions exemplified for the cope rearrangement of semibullvalene. J Phys Chem B 115:5476
60. Breidbach J, Cederbaum LS (2005) Universal attosecond response to the removal of an electron. Phys Rev Lett 94:033901
61. Hennig H, Breidbach J, Cederbaum LS (2005) Electron correlation as the driving force for charge transfer: charge migration following ionization in N-methyl acetamide. J Phys Chem A 109:409
62. Remacle F, Levine RD (2006) An electronic time scale in chemistry. Proc Natl Acad Sci U S A 103:6793
63. Kling MF, Siedschlag C, Verhoef AJ, Khan JI, Schultze M, Uphues T, Ni Y, Uiberacker M, Drescher M, Krausz F, Vrakking MJJ (2006) Control of electron localization in molecular dissociation. Science 312:246
64. Wollenhaupt M, Liese D, Präkelt A, Sarpe-Tudoran C, Baumert T (2006) Quantum control by ultrafast dressed states tailoring. Chem Phys Lett 419:184
65. Wollenhaupt M, Präkelt A, Sarpe-Tudoran C, Liese D, Baumert T (2005) Strong field quantum control by selective population of dressed states. J Opt B 7:S270
66. Znakovskaya I, von den Hoff P, Zherebtsov S, Wirth A, Herrwerth O, Vrakking MJJ, de Vivie-Riedle R, Kling MF (2009) Attosecond control of electron dynamics in carbon monoxide. Phys Rev Lett 103:103002
67. von den Hoff P, Znakovskaya I, Kling MF, de Vivie-Riedle R (2009) Attosecond control of the dissociative ionization via electron localization: a comparison between D_2 and CO. Chem Phys 366:139

68. von den Hoff P, Siemering R, Kowalewski M, de Vivie-Riedle R (2012) Electron dynamics and its control in molecules: from diatomics to larger molecular systems. IEEE J Sel Top Quantum Electron 18:119
69. Bayer T, Braun H, Sarpe C, Siemering R, von den Hoff P, de Vivie-Riedle R, Baumert T, Wollenhaupt M (2013) Charge oscillation controlled molecular excitation. Phys Rev Lett 110:123003
70. Ezer HT, Kosloff R (1984) An accurate and efficient scheme for propagating the time dependent Schrödinger equation. J Chem Phys 81:3967
71. Nuernberger P, Vogt G, Brixner T, Gerber G (2007) Femtosecond quantum control of molecular dynamics in the condensed phase. Phys Chem Chem Phys 9:2470
72. Wollenhaupt M, Assion A, Baumert T (2012) Short and Ultrashort Pulses In: Träger F (2nd ed) Springer Handbook of lasers and optics. Springer, Dordrecht Heidelberg London New York, pp 1047–1094
73. Tesch CM, de Vivie-Riedle R (2002) Quantum computation with vibrationally excited molecules. Phys Rev Lett 89:157901
74. Manz J, Sundermann K, de Vivie-Riedle R (1998) Quantum optimal control strategies for photoisomerization via electronically excited states. Chem Phys Lett 290:415
75. Gross P, Neuhauser D, Rabitz H (1992) Optimal control of curve-crossing systems. J Chem Phys 96:2834
76. Shi S, Woody A, Rabitz H (1988) Optimal control of selective vibrational excitation in harmonic linear chain molecules. J Chem Phys 88:6870
77. Somloi J, Kazakov VA, Tannor DJ (1993) Controlled dissociation of I_2 via optical transitions between the X and B electronic states. Chem Phys 172:85
78. Palao JP, Kosloff R (2003) Optimal control theory for unitary transformations. Phys Rev A 68:062308
79. Köhler J, Wollenhaupt M, Bayer T, Sarpe C, Baumert T (2011) Zeptosecond precision pulse shaping. Opt Express 19:11638
80. Geppert D, von den Hoff P, de Vivie-Riedle R (2008) Electron dynamics in molecules: a new combination of nuclear quantum dynamics and electronic structure theory. J Phys B 41:074006
81. Domcke W, Yarkony DR, Köppel H (eds) (2004) Advanced series in physical chemistry, vol 15: Conical intersections. World Scientific, Singapore
82. Domcke W, Yarkony DR, Köppel H (eds) (2011) Advanced series in physical chemistry, vol 17: Conical intersections. World Scientific, Singapore
83. Feringa BL (ed) (2001) Molecular switches. Wiley-VCH Verlag GmbH, Weinheim
84. Cordes T, Schadendorf T, Rück-Braun K, Zinth W (2008) Chemical control of Hemithioindigo-photoisomerization – substituent-effects on different molecular parts. Chem Phys Lett 455:197
85. Draxler S, Brust T, Malkmus S, DiGirolamo JA, Lees WJ, Zinth W, Braun M (2009) Ring-opening reaction of a trifluorinated indolylfulgide: mode-specific photochemistry after pre-excitation. Phys Chem Chem Phys 11:5019
86. Cordes T, Malkmus S, DiGirolamo J, Lees WJ, Nenov A, de Vivie-Riedle R, Braun M, Zinth W (2008) Accelerated and efficient photochemistry from higher excited electronic states in fulgide molecules. J Phys Chem A 112:13364
87. Wachtveitl J, Spörlein S, Satzger H, Fonrobert B, Renner C, Behrendt R, Oesterhelt D, Moroder L, Zinth W (2004) Ultrafast conformational dynamics in cyclic azobenzene peptides of increased flexibility. Biophys J 86:2350
88. Reid PJ, Doig SJ, Wickham SD, Mathies RA (1993) Photochemical ring-opening reactions are complete in picoseconds: a time-resolved UV resonance Raman study of 1,3-cyclohexadiene. J Am Chem Soc 115:4754
89. Lochbrunner S, Fuß W, Schmid WE, Kompa KL (1998) Electronic relaxation and ground-state dynamics of 1,3-cyclohexadiene and *cis*-hexatriene in ethanol. J Phys Chem A 102:9334
90. Pullen SH, Anderson NA, Walker LA II, Sension RJ (1998) The ultrafast photochemical ring-opening reaction of 1,3-cyclohexadiene in cyclohexane. J Chem Phys 108:556

91. Celani P, Bernardi F, Robb MA, Olivucci M (1996) Do photochemical ring-openings occur in the spectroscopic state? $^1B_2$ pathways for the cyclohexadiene/hexatriene photochemical interconversion. J Phys Chem 100:19364
92. Garavelli M, Celani P, Fato M, Bearpark MJ, Smith BR, Olivucci M, Robb MA (1997) Relaxation paths from a conical intersection: the mechanism of product formation in the cyclohexadiene/hexatriene photochemical interconversion. J Phys Chem A 101:2023
93. Hofmann A, de Vivie-Riedle R (2000) Quantum dynamics of photoexcited cyclohexadiene introducing reactive coordinates. J Chem Phys 112:5054
94. Hofmann A, de Vivie-Riedle R (2001) Adiabatic approach for ultrafast quantum dynamics mediated by simultaneously active conical intersections. Chem Phys Lett 346:299
95. Geppert D, de Vivie-Riedle R (2006) Control strategies for reactive processes involving vibrationally hot product states. J Photochem Photobiol A 180:282
96. Geppert D, Seyfarth L, de Vivie-Riedle R (2004) Laser control schemes for molecular switches. Appl Phys B 79:987
97. Vrakking MJJ (2001) An iterative procedure for the inversion of two-dimensional ion/photoelectron imaging experiments. Rev Sci Instrum 72:4084
98. Kling M, von den Hoff P, Znakovskaya I, de Vivie-Riedle R (2013) (Sub-)femtosecond control of molecular reactions via tailoring the electric field of light. Phys Chem Chem Phys 15:9448
99. Gräfe S, Ivanov MY (2007) Effective fields in laser-driven electron recollision and charge localization. Phys Rev Lett 99:163603
100. Barth I, Manz J (2006) Periodic electron circulation induced by circularly polarized laser pulses: quantum model simulations for Mg porphyrin. Angew Chem Int Ed 45:2962
101. Wollenhaupt M, Baumert T (2006) Ultrafast strong field quantum control on K_2 dimers. J Photochem Photobiol A 180:248
102. von den Hoff P, Kowalewski M, de Vivie-Riedle R (2011) Searching for pathways involving dressed states in optimal control theory. Faraday Disc 153:159
103. Wollenhaupt M, Assion A, Bazhan O, Horn C, Liese D, Sarpe-Tudoran C, Winter M, Baumert T (2003) Control of interferences in an Autler–Townes doublet: symmetry of control parameters. Phys Rev A 68:015401

The Dynamics of Quantum Computing in Molecules

9

Alex Brown and Ryan R. Zaari

Abstract

A brief introduction to quantum computing is provided and the potential use of molecules as the platform is discussed. The basic building blocks (quantum bits, quantum gates, and quantum algorithms) are described in order to emphasize the requirements for realizing a quantum computer, and, the advantages quantum computation has over its classical counterpart. We outline the three key steps to quantum computation: (1) initialization, (2) manipulation, and (3) readout. The possible use of internal molecular states as quantum bits and shaped laser fields to implement the quantum gates is introduced. The application to molecular quantum computing is connected to the more general problem of the control of quantum dynamics using tailored laser fields determined theoretically with optimal control theory or genetic algorithms.

9.1 The Advent of Quantum Computing

The rapid pace of computer technology innovation was predicted in the early 1960s by Intel co-founder Gordon Moore. His prediction, popularly known as "Moore's Law," states that transistor density on integrated circuits (a rough measure of computer processing power) doubles about every 2 years. While this "Law" has held for nearly 50 years, the end is in sight. However, more than 30 years

A. Brown (✉)
Department of Chemistry, University of Alberta, Edmonton, AB, Canada T6G 2G2
e-mail: alex.brown@ualberta.ca

R.R. Zaari
Department of Chemistry, University of Alberta, Edmonton, AB, Canada T6G 2G2

Present Address: Department of Chemistry, University of Nevada, 216, Reno, NV 89557-0216, USA
e-mail: rzaari@ualberta.ca

F. Gatti (ed.), *Molecular Quantum Dynamics*, Physical Chemistry in Action,
DOI 10.1007/978-3-642-45290-1_9,

ago, the physicist Richard Feynman proposed a potentially revolutionary idea for computation: the quantum computer [1]. By utilizing quantum mechanical phenomena, such as quantum superposition, entanglement, and interference, a quantum computer realizes a fundamentally new mode of information processing relative to classical computing [2, 3]. The quantum computing paradigm opens the avenue to vast increases in computational power relative to methods based on classical computation. Several potential applications of quantum computing are already known: cryptography, algorithmic searching, and factorizing large numbers very rapidly. Of particular interest to the field of molecular simulation, the advent of quantum computing would allow the efficient simulation of quantum-mechanical systems over unprecedented length and time scales. With the potential benefits being so great, the field of quantum computing has emerged as an intriguing and exciting research area involving the efforts of chemists, computer scientists, engineers, mathematicians, and physicists.

In the present work, a brief introduction to the basic ideas of quantum computing is provided. In particular, several problems that need to be addressed in order to realize a quantum computer are introduced: the identification of a physical system to represent the quantum bits (qubits), the implementation of mechanisms for performing quantum logic gate operations on the qubits, and the maintenance of coherence. While several different physical systems have been proposed or utilized to realize quantum computing algorithms[4–8], the focus here is on the use of molecules to store the quantum information and shaped laser pulses to carry out the quantum gate operation—ideas introduced over 10 years ago [9–11]. Here the proposals for implementing qubits in molecular systems are introduced, and the methodologies for finding the shaped laser pulses (i.e., optimal control theory (OCT) and genetic algorithms [12–14]) are discussed. Since a theoretical understanding of these problems requires solving the time-dependent Schrödinger equation (TDSE), there is a strong connection to the field of quantum dynamics and new ideas and methods developed in that area can have important applications in the field of molecular quantum computing.

9.1.1 Qubits, Quantum Gates and Quantum Algorithms

The computers that we encounter in our everyday lives operate using *classical* processing. On the most fundamental level, calculations occur by changes in the state of bits which can be in either of two states; typically represented by a “0” or “1” in binary notation. The changes in the state of bits occurs by boolean logic operations such that a specific sequence of these logic operations can carry out an algorithm. It is these algorithms that are used to perform computations. The workings of a quantum computer are (to-date) analogous to a classical computer. However, the quantum mechanical nature of a system and its interactions are utilized to represent qubits, quantum logic gate operations and quantum algorithms. As stated before, a classical bit can exist in one of the two states (0 or 1) but a qubit is a quantum 2-state system; although qudits with d quantum states could be

used, we restrict our discussion to qubits only. The resulting state of the qubit is a superposition of both "0" and "1". For example, a classical two-bit system can be in one of the four possible states, i.e., "00", "01", "10" or "11" state. A quantum two-qubit system, represented in Dirac notation as $|q_1 q_2\rangle$, can be in pure states $|00\rangle$, $|01\rangle$, $|10\rangle$ and $|11\rangle$. The critical difference to classical bits is that qubits are described by the wavefunction, $\Psi = \sum_{q_1,q_2=0}^{1} c_{q_1,q_2}|q_1 q_2\rangle$, where the coefficients c_{q_1,q_2} have the relationship $\sum_{q_1,q_2} |c_{q_1,q_2}|^2 = 1$. Therefore, the system (i.e., the quantum information) is represented by the superposition of its individual qubits—it is this fundamental difference that leads to the power of quantum computing (see Sect. 9.1.3). With respect to the representation, qubits can be structured in two different ways. The first case entails that each qubit is represented by a separate 2-level or quasi 2-level system, and then these n qubits are appropriately coupled [6,15–17]. This is the case, for example, in ion trap quantum computing examples in which a string of trapped atomic ions represents a series of qubits through excitation of two hyperfine levels from each atom, while coupling between each atom/qubit occurs through vibrational motion in the harmonic potential of the linear Paul trap [4, 17]. Alternatively, n qubits can be represented by $N = 2^n$ combinations of N quantum states [18–20]. A proposed quantum computing architecture suggests using the rovibrational states or modes of molecules as qubits and in this case each resulting qubit state,"00" to "11", would be represented as the qubits. In this case n qubits are represented by 2^n quantum states [9]. Quantum logic gates have specific requirements due to their quantum mechanical nature. Unlike classical logic gates, a quantum logic gate ($\mathbf{Q}$) must be reversible ($\mathbf{Q}\mathbf{Q}^{-1} = \mathbb{1}$), unitary ($\mathbf{Q}^\dagger = \mathbf{Q}^{-1}$) and Hermitian ($\mathbf{Q}^\dagger = \mathbf{Q}$)—if these requirements were not fulfilled, it would indicate decoherence in the system leading to the loss of quantum information. There are a number of elementary quantum logic gates such as the NOT, Controlled-NOT (CNOT), Hadamard, Toffoli and phase gates as shown in Table 9.1, which can be used for universal quantum computation (see Sect. 9.1.5). In order to illustrate the general operation of a quantum gate, consider a NOT gate acting on the general quantum state, $\Psi = c_0|0\rangle + c_1|1\rangle$, i.e.,

$$\text{NOT}\Psi = \begin{pmatrix} 0 & 1 \\ 1 & 0 \end{pmatrix} \begin{pmatrix} c_0 \\ c_1 \end{pmatrix} = \begin{pmatrix} c_1 \\ c_0 \end{pmatrix} = c_1|0\rangle + c_0|1\rangle. \tag{9.1}$$

The extension to 2-qubit and n-qubit gate operations is straightfoward.

An example algorithm is the one-bit full adder which is shown in Table 9.2 for the classical and quantum forms of the algorithm [21]. The one-bit adder adds three one-bit numbers (A, B and C_{in}) to produce output bits ($S = A + B + C_{in}$ and C_{out}). The carry (C_{in} and C_{out}) are bits from previous or future additions, respectively, as would occur if the sum of the numbers, S, is greater than or equal to two. This is analogous to addition in the decimal system, as when the number is greater than or equal to 10 then we carry a 1 to the next place value. The quantum form of the one-bit adder must include one additional input (D) and two extra

Table 9.1 Examples of elementary quantum logic gates in matrix notation

Gate	Matrix operation	Gate	Matrix operation
NOT	$\begin{pmatrix} 0 & 1 \\ 1 & 0 \end{pmatrix}$	CNOT	$\begin{pmatrix} 1 & 0 & 0 & 0 \\ 0 & 1 & 0 & 0 \\ 0 & 0 & 0 & 1 \\ 0 & 0 & 1 & 0 \end{pmatrix}$
Phase	$\begin{pmatrix} 1 & 0 \\ 0 & e^{i\theta} \end{pmatrix}$		
Hadamard	$\frac{1}{\sqrt{2}} \begin{pmatrix} 1 & 1 \\ 1 & -1 \end{pmatrix}$	Toffoli	$\begin{pmatrix} 1 & 0 & 0 & 0 & 0 & 0 & 0 & 0 \\ 0 & 1 & 0 & 0 & 0 & 0 & 0 & 0 \\ 0 & 0 & 1 & 0 & 0 & 0 & 0 & 0 \\ 0 & 0 & 0 & 1 & 0 & 0 & 0 & 0 \\ 0 & 0 & 0 & 0 & 1 & 0 & 0 & 0 \\ 0 & 0 & 0 & 0 & 0 & 1 & 0 & 0 \\ 0 & 0 & 0 & 0 & 0 & 0 & 0 & 1 \\ 0 & 0 & 0 & 0 & 0 & 0 & 1 & 0 \end{pmatrix}$

In general the Hadamard, Phase and NOT gates are 1-qubit operations, the CNOT gate is a 2-qubit operation, and the Toffoli is a 3-qubit operation

Table 9.2 Description of the classical and quantum one-bit full adder algorithm

Inputs				Outputs			
C_{in}	A	B	D	C_{in}	A	S	C_{out}
0	**0**	**0**	0	0	0	**0**	**0**
1	**0**	**0**	0	1	0	**1**	**0**
0	**1**	**0**	0	0	1	**1**	**0**
1	**1**	**0**	0	1	1	**0**	**1**
0	**0**	**1**	0	0	0	**1**	**0**
1	**0**	**1**	0	1	0	**0**	**1**
0	**1**	**1**	0	0	1	**0**	**1**
1	**1**	**1**	0	1	1	**1**	**1**

The input binary numbers (C_{in}, A, B) are added to produce the output numbers (S, C_{out}). The carry (C_{in}, C_{out}) represent the bits being carried over from previous and future additions, respectively. Additional input (D) and output (A, C_{in}) binary numbers are included in the quantum form of the algorithm to ensure reversibility. The inputs and outputs for the classical one-bit adder are given in bold while the quantum algorithm requires all four inputs to produce all four outputs

output (A, C_{in}) qubits to ensure reversibility. In order to illustrate the concept of irreversibility in the classical form of the algorithm, consider the following three inputs (C_{in},A,B) = (**100**), (**010**) and (**001**), see Table 9.2. All three produce the same final state (S, C_{out}) = (**10**), and hence, one could not reversibly return from this output to the correct initial state. If the input (D) and output (A, C_{in}) qubits are included in the quantum algorithm, the input states (**100**0), (**010**0) and (**001**0) now produce different final states (10**10**), (01**10**) and (00**10**), respectively, albeit all with the same values of (S, C_{out}) = (**10**). However, since the final states are distinct, the process could be reversed to return to the corresponding initial state. The quantum

Table 9.3 An example of the general phase imposed after the NOT_2 quantum gate is applied

Gate	Matrix operation	Global phase alignment
NOT_2	$\begin{pmatrix} 0 & 1 & 0 & 0 \\ 1 & 0 & 0 & 0 \\ 0 & 0 & 0 & 1 \\ 0 & 0 & 1 & 0 \end{pmatrix}$	$\|00\rangle \rightarrow \|01\rangle e^{i\phi_1}$ $\|01\rangle \rightarrow \|00\rangle e^{i\phi_2}$ $\|10\rangle \rightarrow \|11\rangle e^{i\phi_3}$ $\|11\rangle \rightarrow \|10\rangle e^{i\phi_4}$

Each gate operation on each qubit acquires an arbitrary phase, $e^{i\phi_n}$

one-bit full adder algorithm can be implemented with the elementary Toffoli and CNOT quantum logic gates [21]. A finite number of elementary boolean logic gates provides the means to produce a vast number of algorithms. This is similar to the finite set of letters in an alphabet (logic gates) which produce a vast number of words, sentences and books in a language (algorithm).

9.1.2 Global Phase Alignment

In order to implement a quantum algorithm, a series of quantum gates must be applied in a specific order. Therefore, besides causing the required qubit excitations, there is an extra requirement imposed on the laser pulse quantum gate operation. That is, the laser pulse quantum gate operation must also align the relative phases of all the qubits by the end of the laser pulse interaction. This is termed *global phase alignment*. Thus subsequent application of quantum gates will impose the appropriate qubit transformation, since the qubits will all be in phase. An example of this is shown in Table 9.3 for the 2-qubit NOT gate or NOT_2 quantum logic gate. If a laser pulse were applied that does not impart a global alignment in qubit phase, then there would be an arbitrary resultant phase associated with each qubit. Subsequent quantum gate transformations would impart even more phase uncertainty. Global phase alignment requires that all resultant phases are the same and in the case of the example NOT_2 gate, $e^{i\phi_1} = e^{i\phi_2} = e^{i\phi_3} = e^{i\phi_4}$. The control of qubit phase is important within many quantum algorithms and some quantum logic gates.

9.1.3 Quantum Superpositions and Quantum Parallelism

It may now seem apparent that an advantage of a quantum computer is in its ability to construct superpositions of qubits, something not possible on a classical computer. During each computation the system's wavefunction consisting of superpositions of the qubits (in reality the wavefunction likely also contains some other non-qubit states) is manipulated according to the necessary quantum logic gates required by the algorithm. Thus every qubit experiences each quantum gate operation, in turn each qubit is manipulated by the entire quantum algorithm and at the end of the computation the wavefunction exists which describes every

possible solution from each initial condition. By contrast, in order to attempt representing this on a classical computer would require one processor for each qubit and then run in parallel to produce all possible solutions to all possible initial conditions. Thus *quantum parallelism* is not the same as classical parallelism since classical parallelism refers to using multiple processors and on a quantum computer this is done on the single processor. Quantum parallelism was first described by Deutsch [22].

9.1.4 Advantages of a Quantum Computer

By utilizing quantum behaviour, algorithms can be constructed on a quantum computer which in some cases take exponentially less computational time as compared to classical computers. The most recognized quantum algorithm is Shor's algorithm [23] for factoring prime numbers. It was shown that a quantum computer implementing Shor's algorithm could determine the factors of a prime number in a polynomial amount of time; the classical counterpart requires an exponential amount of time with respect to the size of the prime number. Even though it is relatively straightforward to generate very large valued prime numbers, it is exceptionally difficult to determine their resulting factors on a classical computer. It is this key classical computing limitation that allows Internet RSA encryption to function. Using Shor's algorithm, the prime factors of 15 were calculated through Nuclear Magnetic Resonance (NMR) using 7 spin 1/2 nuclei of a perfluorobutadienyl iron complex as the qubits [6]. This is the largest number of qubits used in an NMR quantum computation. The Deutsch–Jozsa algorithm, an example quantum algorithm which performs exponentially faster on a quantum computer, has also been applied as a benchmark to many quantum computer systems [17, 19].

Recent developments in quantum algorithms showcase specific uses in mathematics, physics and chemistry with much improved calculation times compared to our current classical computers. In current electronic structure calculations, the CPU time required to compute molecular energies scales exponentially with the system size but it has been shown to take only a polynomial amount of time on a quantum computer [24]. Chemical reactions could also be simulated exactly on a quantum computer in polynomial time with respect to the system size [25]. Other example studies have deduced quantum algorithms for determining the dynamics of open quantum systems [26] and also molecular properties and geometry optimizations [27]. With respect to molecular dynamics simulations, a true quantum Metropolis algorithm has been developed [28] and also a quantum algorithm for exact Monte Carlo sampling [29]. Quantum algorithms within mathematics have also been developed for systems of linear equation [30] and for solving the Poisson equation [31]. These select examples of the implementation of quantum algorithms in science and mathematics showcase the inherent and valuable use a quantum computer would have for scientific research.

9.1.5 Universal Quantum Computer and Quantum Simulator

Thus far, the largest universal quantum computer controlled 14 qubits represented by 14 $^{40}Ca^{+}$ cations (one for each qubit) in a linear Paul ion trap [32], but it has been suggested that thousands or even millions of qubits would be needed to perform a practical calculation [33, 34]. On this 14-qubit quantum computer, the authors investigated entanglement and the effect of noise, but being a universal quantum computer they could have examined other simple quantum algorithms. The most recent applicable progress has been made by utilizing a quantum algorithm on a linear optical quantum simulator for determining eigenvalues of a molecule and the hydrogen molecule was used as the simplest test case [35]. A universal quantum computer would have the capability of solving general quantum algorithms whereas a quantum simulator would solve a problem specific to the system being "simulated" [21]. Using the previously described one-bit full adder as an example, a universal quantum computer would utilize a specific set of universal quantum logic gates to represent the quantum analogue of the one-bit full adder, whereas a quantum simulator would be designed strictly to carry out the one-bit full addition operation only.

9.1.6 Experimentally Realized and Proposed Quantum Computer Architectures

Besides the inherent properties that a quantum computer, including the quantum gates, must have, there are technical issues regarding implemented and proposed architectures. These issues include scalability, decoherence and computational speed. Scalability refers to the ability to increase the number of qubits for calculation. Coherence is the ability for the qubit to retain its encoded information and thus decoherence is a loss of encoded information. Computational speed refers to the general number of quantum gates that can be applied before decoherence destroys the quantum state information. As will be alluded to below, it is not so much the difference between atoms and molecules in quantum computing architectures that determines feasibility but more so the choice of quantum state for qubit representation.

The current implementation of a quantum computing architecture utilizing atoms comes in the form of linear Paul ion traps [4], though there are suggestions of performing quantum algorithms on atomic ions that are trapped in a 2-D or 3-D lattice [5]. The qubits are represented by two hyperfine atomic levels, generally chosen to be the ground state and some metastable state. With these choices of quantum states, information encoded in the qubits can be long lived with respect to the quantum operation being performed, and qubit preparation (see Sect. 9.2.1) is straightforward through known atomic "cooling" techniques. Just as important, the system is scalable simply by adding more atomic ions to the linear Paul trap. The qubit excitations correspond to frequencies in the microwave region and qubit

coupling occurs through vibrational mode coupling in the linear Paul harmonic trap. Due to this, the application of a series of laser pulses to represent quantum logic gates combined with the slow harmonic vibrational coupling could lead to decoherence before the end of the quantum computation.

Alternatively a quantum computing architecture that has shown promise but uses molecules is that of NMR [6–8]. The qubits are represented by the nuclear spin of specific atoms within the molecule. Again the lifetimes for such states are long lived and qubit state preparation is done through familiar NMR techniques. Scalability is an issue for NMR quantum computing since increasing the number of qubits requires increasing the number of nuclei in the molecule (i.e. increasing the size of the molecule). In conjunction with scalability, the molecules used in NMR quantum computing are specifically designed such that the nuclear spin excitations occur in distinctly separate regions of the energy spectrum for detection purposes. The qubit excitations occur through application of radiofrequency pulses and the qubits are coupled through J-coupling of nuclei. Again very long radiowaves could lead to decoherence before application of the entire quantum algorithm.

In order to attempt at circumventing some of the problems encountered in current quantum computer implementations, it was proposed that rovibrational states or vibrational modes of molecules could be used to represent the qubits [9]. Qubits are coupled through strong intermolecular dipole–dipole coupling and/or intermolecular vibrational mode coupling. Respective qubit excitations occur in the mid-infrared using femtosecond laser pulses. The results are very quick excitations by quantum gates represented by shaped laser pulses such that possibly thousands of gates can be applied before decoherence becomes an issue. Unfortunately, n qubits are represented each by a specific rovibrational state or mode, utilizing 2^n states and posing a problem with scalability. Further suggestions include adopting this method but specifically trapping diatomic molecules in a linear optical trap or optical lattice [36], thus eliminating the issue of scalability. Theoretical research is aimed at providing information regarding laser pulse shaping of the quantum gate, control of the qubit excitations and indication of candidate molecules for such architectures. Experimental investigations are mostly concerned with the preparation of such diatomics and the ability for optical trapping of them.

9.2 Procedure for Performing a Quantum Computation

Quantum computer processing can be broken down into three chronological procedures: (1) system preparation, (2) system manipulation and (3) system readout. Before an algorithm can be implemented, the system must be prepared in the desired initial qubit state arrangement. The qubit states are then manipulated through application of quantum logic gates to carry out the desired algorithm. After the algorithm is complete, the system must be read to determine the solution to the problem. The three general steps are summarized in the following sections. Emphasis is placed on and further details are provided for the system manipulation

step in subsequent sections, since understanding this step theoretically involves the utilization of quantum dynamics techniques.

9.2.1 System Preparation: Qubit Initialization

With respect to implementing a quantum algorithm, the set of n qubits must be initialized. This requires preparing the quantum system into a known configuration or, more specifically, preparing the qubits into a known and desired state. The initial state of the qubits depends on the problem being studied. Generally this is carried out through common atomic or, more recently, molecular [37] "cooling" techniques, where the system is brought ideally to its ground quantum state with respect to the qubit representation. Thus, after cooling, the system is prepared into a state where all qubits have been initialized, for instance a register reading as $|000\ldots0\rangle$, depending on how many qubits are used. If the ground state is not a qubit representation, then further excitations must occur in order to create an initialized qubit register. There are clearly obvious advantages to having the initial qubit representation being that of the ground quantum state.

9.2.2 System Manipulation: Apply Quantum Algorithms

After the qubits have been specifically prepared, the quantum algorithm is then applied via qubit manipulation through the necessary quantum logic gates. Laser pulses, or more generally electromagnetic fields, provide a practical means to implement the quantum logic gates and manipulate the quantum states of atoms and molecules. Such experimental implementations include NMR [6–8] and ion trap quantum computing [17, 38], with applied laser pulses using radiowave and microwave frequencies, respectively. An alternative quantum computer architecture proposed suggests using the rovibrational states of molecules as qubits and producing mid-infrared laser pulses to represent the quantum logic gates [9]. Within the mid-IR frequency region, laser pulses can be generated which are ultrafast (fs to ps duration) and whose time-domain (spectral) properties are well controlled. These properties allow the precise implementation of quantum gates and application of quantum algorithms in time frames before decoherence becomes problematic. Much of the theoretical work within molecular quantum computing has focused on the quantum dynamics involved during the qubit manipulation step. The primary concern is to obtain insight with respect to the laser pulse representation of quantum logic gates, the controllability of the qubits, issues governing decoherence and the sensitivity to the choice of molecular system. The effect of shaping laser pulses to represent quantum logic gates, qubit controllability and the choice of molecular system will be covered in Sect. 9.3, for the proposed quantum computing architecture using the rovibrational states of diatomics (or polyatomics) as qubits and shaped laser pulses as quantum logic gates.

9.2.3 System Readout: Determine the Solution

Once the quantum algorithm has been implemented on the qubits, the solution to the problem must be determined. This amounts to determining (i.e. measuring) the final quantum state of the qubits. Unlike in classical computing, the act of measuring the quantum system destroys the qubit arrangement and so readout can only occur once per calculation. In theory, this is sufficient since we do not need to carry out identical calculations to determine a solution. In practice, measurements are not without error and generally there is an error associated with determining the state of the qubits. Thus far, the simple quantum algorithms that have been carried out to show quantum computation have in general relied on repeat measurements to improve the probability of the solution. In the case of NMR quantum computing, the qubit states are superimposed on an ensemble rather than individual molecules, and thus measuring the nuclear spin qubit state occurs over a statistical average [6]. Readout on ion trap quantum computers has been carried out by exciting to a higher lying electronic state and, by monitoring the fluorescence, the original qubit states can be determined [32]. In classical computer systems, there are also associated errors but their probability has been dramatically decreased through fault tolerance techniques and improved technology. Analogous quantum error correction and fault tolerant techniques [39] as well as new readout methods, see for example [40], to improve quantum computing are being developed, proposed and researched.

9.3 Molecular Quantum Computing Using Shaped Laser Pulses

In an attempt to expand the search for quantum computing architectures, it was suggested that the rovibrational states or modes of molecules could be used as the qubit representation and laser pulses could be shaped to cause the required quantum logic gate operation on the qubits [9]. This came at a time when there were emerging chemistry experiments being performed with mid-infrared shaped laser pulses on the femtosecond time scale, with control of phase and amplitude at specific frequencies [41]. It was thought that the quantum algorithm could be applied more quickly with picosecond laser pulses (mid-infrared) than with pulses used in ion traps (microwave; nanosecond) or NMR (radiowave; microsecond) quantum architectures; thus possibly minimizing decoherence issues. Internal molecular modes and rovibrational transitions are also more strongly coupled, in comparison with ion trap and NMR quantum computing implementations. Numerous theoretical studies emerged examining the use of internal vibrational modes of polyatomics (e.g. acetylene [42, 43], ammonia [44, 45], thiophosgene [18, 46, 47], vibrational [48] or rovibrational states of diatomics [49–51] and also systems using dipole–dipole coupled diatomics [52–55] as the qubits. The majority of theoretical studies determined the optimal shape of the laser pulse using OCT [56, 57], while others implemented optimization routines such as ant colony optimization [58], Simulated

Annealing [59] or, more commonly, Genetic Algorithm (GA) optimization [50, 51, 60]. In this section, we introduce the relevant dynamics equations, how OCT or GA procedures differ and how they are utilized for the required qubit transformations for logic gate representation, including global phase alignment. In general, the theory is presented for diatomic molecules, but the generalization to polyatomics is straightforward, for example, see [45] where MCTDH is utilized to examine gate operations in ammonia.

9.3.1 Quantum Dynamics: Laser/Molecule Interaction

The molecular response to the laser pulse is determined by solving the TDSE,

$$i\hbar \frac{d\Psi(t)}{dt} = \hat{H}\Psi(t). \tag{9.2}$$

The semi-classical Hamiltonian, $\hat{H}$, composed of a time-independent operator $\hat{H}_0$, describing the molecule, combined with the time-dependent term describing the interaction of the electric field, $\epsilon(t)$, with the molecular dipole moment, $\mu(r)$, is given by,

$$\hat{H} = \hat{H}_0 - \boldsymbol{\mu}(r) \cdot \boldsymbol{\epsilon}(t) = \hat{H}_0 - \mu(r)\epsilon(t)\cos\theta. \tag{9.3}$$

The wavefunction, $\Psi(t)$, composed of a linear combination of time-dependent coefficients, $c_{vJ}(t)$, with rovibrational state eigenvectors $|vJ\rangle$ is described by,

$$\Psi(t) = \sum_{vJ} c_{vJ}(t)|vJ\rangle. \tag{9.4}$$

The magnetic quantum number M is equal to zero for the closed shell diatomic molecules and linear electric field polarizations considered in our pulse optimization examples. However, in general, one may have to consider a sum over quantum number M (for open shell systems), other hyperfine constants and/or multiple vibrational states (for polyatomics).

Solving the TDSE for the time-dependent coefficients in vector notation, $\underline{c}(t)$, results in,

$$\dot{\underline{c}}(t) = -\frac{i}{\hbar}\left[\underline{\underline{E}} - \epsilon(t)\underline{\underline{\mu}}\right]\underline{c}(t). \tag{9.5}$$

Each time step along the laser pulse duration can be solved by using a numerical integrator such as the commonly used Runge–Kutta fourth order integrator. Care must be taken to ensure that the time steps are smaller than the oscillatory period of the laser pulse in order to minimize integration error. The diagonal rovibrational state energy matrix, $\underline{\underline{E}}$, is

$$\underline{\underline{E}} = \begin{pmatrix} E_{0,0} & 0 & \cdots & 0 \\ 0 & E_{0,1} & \cdots & 0 \\ \vdots & \vdots & \ddots & \vdots \\ 0 & 0 & \cdots & E_{\nu_{\max},J_{\max}} \end{pmatrix} \tag{9.6}$$

where $\nu_{\max}$ and $J_{\max}$ are the maximum vibrational and rotational states, respectively, considered when solving the problem of interest numerically. The energies can be determined directly from experimental spectroscopic excitation data, from fits of diatomic molecular constants or through numerical calculations of the quantum states from an ab initio potential energy curve. Rather than using a basis of eigenstates, one can solve the problem using the potential energy curve, $V(r)$, or surface (for polyatomics), directly [45]. An example of the transition dipole moment matrix, $\underline{\underline{\mu}}$, is shown for single photon excitations between adjacent rovibrational states,

$$\underline{\underline{\mu}} = \mu_{\nu,J}^{\nu',J'} = \begin{pmatrix} 0 & \mu_{0,J}^{1,J'} & 0 & & 0 & 0 & 0 \\ \mu_{1,J}^{0,J'} & 0 & \mu_{1,J}^{2,J'} & \cdots & & 0 & 0 \\ 0 & \mu_{2,J}^{1,J'} & 0 & & & & 0 \\ & \vdots & & \ddots & & \vdots & \\ 0 & & & & \mu_{\nu_{\max}-2,J}^{\nu_{\max}-1,J'} & 0 & \\ 0 & 0 & & \cdots & \mu_{\nu_{\max}-1,J}^{\nu_{\max}-2,J'} & 0 & \mu_{\nu_{\max}-1,J}^{\nu_{\max},J'} \\ 0 & 0 & 0 & & 0 & \mu_{\nu_{\max},J}^{\nu_{\max}-1,J'} & 0 \end{pmatrix}. \tag{9.7}$$

It is tridiagonal with zeroes along the diagonal and structured so that excitations occur via simultaneous $\Delta\nu = \pm 1$ and $\Delta J = \pm 1$ transitions as is appropriate for a relatively weak, linearly polarized laser field. The notation for $\underline{\underline{\mu}}$ is given by initial state (ν,J) as a subscript and the final state, (ν',J'), as a superscript. Equation (9.7) shows the structure for vibrational transitions and Eq. (9.8) shows the rotational transition substructure of the sample cell at $\mu_{0,J}^{1,J'}$

$$\mu_{0,J}^{1,J'} = \begin{pmatrix} 0 & \mu_{0,0}^{1,1} & 0 & & 0 & 0 & 0 \\ \mu_{1,1}^{0,0} & 0 & \mu_{0,1}^{1,2} & \cdots & & 0 & 0 \\ 0 & \mu_{1,2}^{0,1} & 0 & & & & 0 \\ & \vdots & & \ddots & & \vdots & \\ 0 & & & & \mu_{0,J_{\max}-2}^{1,J_{\max}-1} & 0 & \\ 0 & 0 & & \cdots & \mu_{1,J_{\max}-1}^{0,J_{\max}-2} & 0 & \mu_{0,J_{\max}-1}^{1,J_{\max}} \\ 0 & 0 & 0 & & 0 & \mu_{1,J_{\max}}^{0,J_{\max}-1} & 0 \end{pmatrix}. \tag{9.8}$$

The exact form of the transition dipole matrix will vary depending on the excitations involved. Initial investigations into the state population transfer are

required since the number of quantum states included in the computations involves a truncation of the complete set at $(v_{\max}, J_{\max})$. The total number of states required in the computation is dependent on the quantum states used as the qubits, the strength of the state-to-state coupling and also the strength of the laser pulse being optimized. In general, one is looking to include a minimum number of states such that insignificant population transfer occurs for higher lying quantum states and the resulting sum of the populations of the included states resembles to some error the condition if all quantum states were included.

In relation to quantum computing, Eq. (9.5) illustrates that the resulting time-dependent coefficient corresponding to each qubit at the final time needs to be determined in order to elucidate effectiveness of the laser pulse ($\epsilon(t)$) at representing the quantum logic gate. The two most common theoretical methods used to determine the optimized laser pulse to represent specific quantum logic gates will be discussed in the next sections, namely OCT and GA optimization.

9.3.2 Optimal Control Theory (OCT)

One of the most widely used theoretical laser optimization routines for molecular laser control is OCT due to its relative ease in implementation and monotonic convergence, see recent reviews [12–14] and the many references therein. Optimization of the laser pulse occurs in the time-domain. Beyond the initial implementation [61], further investigations developed important features such as constraints on the frequency spectrum[62–64] and optimization of the laser pulse duration[65–67], both of which are required to produce laser pulses comparable to those obtained experimentally. Within OCT an objective function, J, is maximized according to constraints on the required excitation, constraints on the laser pulse field and it must also satisfy the TDSE. These constraints are represented by each term in the objective function, respectively,

$$J = \sum_{k}^{z} \left| \left\langle \Psi_i^k(T) | \Phi_f^k \right\rangle \right|^2 - \int_0^T \frac{\alpha_0}{s(t)} |\epsilon(t)|^2 \, dt$$
$$-2Re \sum_{k}^{z} \left[\left\langle \Psi_i^k(T) | \Phi_f^k \right\rangle \int_0^T \left\langle \Psi_f^k(t) \left| i \left[H_0 - \mu\epsilon(t) \right] + \frac{\partial}{\partial t} \right| \Psi_i^k(t) \right\rangle dt \right]. \tag{9.9}$$

Here Ψ_i^k is the resulting wavefunction after interaction with the laser pulse (of total pulse duration T) of the ith state for the kth qubit transformation for the specific quantum logic gate. Φ_f^k is the target state of the qubit transformation for the specific quantum logic gate. The second term in the objective function contains the electric field, $\epsilon(t)$, and the penalty parameter, α_0, which is an arbitrary constant that determines the weight of the field term on the resulting objective function, J.

The penalty parameter is important for appropriate laser pulse optimization and chosen based upon numerical adjustments. The integer z corresponds to the number of multiple target qubit states that are being optimized to represent the quantum logic gate. For 1-qubit operations, $z = 2$ and for 2-qubit operations, $z = 4$.
Upon maximizing the objective function with respect to $\Psi_i^k(t)$, $\Psi_f^k(t)$ and $\epsilon(t)$, a set of resultant equations is obtained [68]:

$$i\frac{\partial}{\partial t}\Psi_i^k(t) = [H_0 - \mu\epsilon(t)]\,\Psi_i^k(t), \qquad \Psi_i^k(0) = \Phi_i^k, \quad k = 1\ldots z \tag{9.10}$$

$$i\frac{\partial}{\partial t}\Psi_f^k(t) = [H_0 - \mu\epsilon(t)]\,\Psi_f^k(t), \qquad \Psi_f^k(0) = \Phi_f^k, \quad k = 1\ldots z \tag{9.11}$$

$$\epsilon(t) = -\frac{zs(t)}{\alpha_0}\sum_k^z Im\left\{\left\langle\Psi_i^k(t)|\Psi_f^k(t)\right\rangle \times \left\langle\Psi_f^k(t)|\mu|\Psi_i^k(t)\right\rangle\right\}. \tag{9.12}$$

The first two conditions are the TDSE describing the wavefunctions $\Psi_i^k(t)$ and $\Psi_f^k(t)$, while the last equation details the form of the laser pulse, $\epsilon(t)$. There are several numerical methods that have been developed to solve for the laser pulse field using the above optimal equations, see [14]. It is important to note that the optimal pulses obtained by alternative methods for numerical optimization can differ [69] and this is a reflection that there are generally numerous pathways/solutions to the required problem.

The laser pulse envelope, $s(t)$ with amplitude s_0, is arbitrary but is usually defined by a *sine-squared* envelope or *Gaussian* envelope with pulse width σ, respectively:

$$s(t) = s_0 \sin^2(\pi t/T) \tag{9.13}$$

$$s(t) = s_0 \exp\left(-\frac{(t-\frac{T}{2})^2}{2\sigma^2}\right). \tag{9.14}$$

As stated previously, the quantum gate operation being represented by the optimized laser pulse not only induces a change in population but must also induce a global phase alignment between the qubits (see Sect. 9.1.1). We shall see that in the GA this is accomplished through an appropriately chosen fidelity function, F (Eq. (9.22)). The simplest process of including global phase alignment within OCT though, without altering the objective function and thus subsequent maximization, is to include an auxiliary transition into the optimization [68]:

$$[|\Psi_{00}\rangle + |\Psi_{01}\rangle + |\Psi_{10}\rangle + |\Psi_{11}\rangle]_{t=0} \longrightarrow \left[(|\Psi_{00}\rangle + |\Psi_{01}\rangle + |\Psi_{10}\rangle + |\Psi_{11}\rangle)e^{i\phi_5}\right]_{t=T} \tag{9.15}$$

This fifth stipulation on the requirement for the resultant optimized laser field is incorporated within the summation of the first term of the objective function

(Eq. (9.9)), now with $z = 5$ for 2-qubit operations. The qubits, after operation by the laser pulse, are then biased to shift by the same amount of phase, $e^{i\phi}$ (global phase alignment). Phase alignment is in general more difficult to optimize than population.

9.3.3 Genetic Algorithm (GA) Optimization

The Genetic Algorithm is a heuristic search optimization routine that utilizes ideas from natural selection to "breed" laser pulses, in effect optimizing the associated pulse parameters (e.g. phase and amplitude), to produce the "fittest" or optimal pulse shape [70]. In comparison with OCT, the GA optimizes the laser pulse in the frequency domain with associated pulse parameters and is constructed in the time-domain through a Fourier transform. Since OCT is monotonically convergent then a convergence criteria can be readily implemented indicating progress in locating the optimal pulse chape. Conversely, in GA optimizations since the parameter space is being searched, there is no guideline dictating how many more generations will be needed to bring the fidelity up to a specific value indicative of the optimal pulse. On the other hand, without specific OCT pulse constraints, the optimal laser pulses generated do not necessarily represent those obtainable from current experimental laser pulse shaping techniques, see, however, recent work by Shyslov and Babikov [46]. Work has been done using variations to both the GA and OCT optimizations in order to bridge the gap between optimal pulses obtained from theory and those obtained from experiment [71].

In Fig. 9.1, the general framework of a closed-loop feedback set-up using a GA is conceptualized. Initially a random set of laser pulses, experimental or theoretical, is input into the quantum dynamics procedure (Fig. 9.1; lower box) in order to start the algorithm. The upper box is the GA routine, constituting the laser pulse optimization. In the theoretical case, the quantum dynamics is determined by solving the TDSE for the applied laser pulse, from an initial state Ψ_i, over the laser pulse duration, to a final state Ψ_f. The Fidelity (see Sect. 9.3.3.2), a value between 0 and 1, is computed which describes the effectiveness of the specific laser pulse at carrying out the required quantum gate operation over the chosen rovibrational state qubits. This is repeated for all laser pulses of that generation. The Fidelity is fed back into the GA so that it can rank the laser pulses and determine the appropriate actions for "breeding". A new set of laser pulses is produced which constitutes the next generation. This process is continued for n generations. Both the GA and quantum dynamics are connected in a closed loop, providing feedback to each other in order to produce an optimal pulse for the quantum gate operation of interest.

9.3.3.1 Laser Field

In general, a laser field (electromagnetic radiation) is modelled classically as a combination of perpendicular oscillating electric and magnetic fields. The electric field interaction with the electric dipole moment is (typically) five orders-of-magnitude (10^5 times) larger than the magnetic field interaction with the magnetic dipole [72]. Therefore, effects of the magnetic dipole are omitted in theoretical investigations

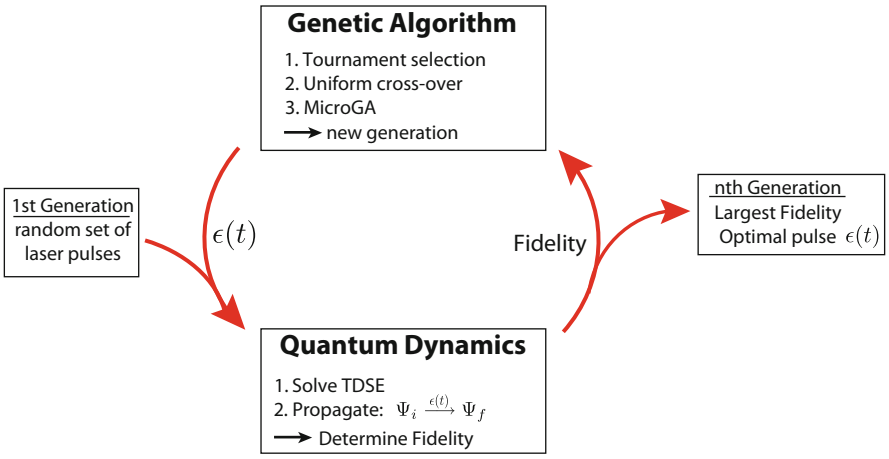

Fig. 9.1 Illustration of theoretical shaped laser pulse optimization using a genetic algorithm (GA). The first generation of laser pulses is randomly generated. The time-dependent Schrödinger equation (TDSE) for the model diatomic is solved for each input laser pulse. The system is propagated from an initial state Ψ_i to a final state Ψ_f, at which point the fidelity is calculated based upon how close the laser pulse brings the system to the desired final state. The fidelity associated with each laser pulse is used to determine the GA optimization through tournament selection and uniform cross-over. The GA produces a new generation of laser pulses related to the previous ones. The cycle is repeated for n generations; the optimal laser pulse being produced in the nth generation

and only the electric field/electric dipole moment interaction is considered. In molecular quantum computing applications, the effect of polarizability has also been considered [49] but its effects were shown to be negligible for the fields considered—fields which are typical of most theoretical simulations in this area.

As stated by Milonni [73], "An arbitrarily large number n of 'photons' may occupy the same state, and when this situation obtains, it is accurate to regard the photon wave function as defining a classical field distribution." Thus the quantum electrodynamic view of radiation for intense laser fields can be described classically. Overall, the light–matter interaction is treated semi-classically where the diatomic molecule is quantum mechanical and the laser pulse is classical in nature. The electric dipole approximation [74] is also used which reduces the form of the electric field due to the comparative size of the electric field wavelength compared to the molecule. The classical description of the laser field, $E(r,t)$, can be written in complex form according to

$$E(r,t) = \epsilon_0 \cos(\omega t - \mathbf{k}\cdot\mathbf{r}) = \epsilon_0 \Re\left[e^{i\omega t} e^{-i\mathbf{k}\cdot\mathbf{r}}\right]. \tag{9.16}$$

It is a continuous laser field of single-frequency (ω) with peak field strength (ϵ_0) being a function of space and time. The norm of the wave vector ($\mathbf{k}$) is related to the frequency of the laser field by $k = \frac{\omega}{c}$, and for example is on the order of 10^{-6} Å^{-1}

for the mid-infrared frequencies. The value of k describes the number of oscillations of the electric field in space. In this case one oscillation occurs approximately every 10^6 Å, which is much larger than the molecules studied in molecular quantum computing. Consequently the resulting value of $\mathbf{k} \cdot \mathbf{r}$ is small and the Taylor series expansion for the electric field of the laser can be truncated to the first term (i.e., unity):

$$e^{-ik\mathbf{n}\cdot\mathbf{r}} = 1 - [i\,\mathbf{k}\cdot\mathbf{r}] + \frac{1}{2}[-i\,\mathbf{k}\cdot\mathbf{r}]^2 + \cdots \approx 1. \tag{9.17}$$

The electric field can now be written strictly in terms of time,

$$E(r,t) = \epsilon_0 \Re\left[e^{i\omega t}\right] = \epsilon_0 \cos(2\pi\nu t). \tag{9.18}$$

For the example optimized laser pulses illustrated herein, only the amplitude and phase were shaped (no polarization shaping [75, 76] was considered). The pulse shaping occurs in the frequency domain which can be readily connected to the more familiar time-domain expression for the laser field. The form of the laser pulse for each component of the discretized frequency spectrum with amplitude and phase variation is [49]

$$\epsilon(\nu_j) = \epsilon_0 \sqrt{A(\nu_j)} \exp\left[-2\ln 2\left(\frac{\nu_j - \nu_0}{\Delta\nu}\right)^2\right] \exp\left[i\phi(\nu_j)\right]. \tag{9.19}$$

In Eq. (9.19), ϵ_0 is the peak field strength, ν_0 is the central frequency and ν_j represents the discrete frequencies at which the field is shaped. A Gaussian envelope is used with a full width at half-maximum (FWHM) pulse width of $\Delta\nu$. The amplitude and phase range from $0 \le A(\nu_j) \le 1$ and $0 \le \phi(\nu_j) \le 2\pi$, respectively. A transformed-limited (TL) pulse corresponds to the case when $A(\nu_j) = 1$ and $\phi(\nu_j) = 0$ for all frequency components j. The familiar time-dependent form of the laser pulse can be determined by a Fourier transform or alternatively using the analytic form for the time-dependent field [77]:

$$\epsilon(t) = \frac{\sin(\pi t d\nu)}{\pi t} \sum_{j=0}^{n} \epsilon_0 \sqrt{A_j} \exp\left[-2\ln 2\left(\frac{\nu_j - \nu_0}{\Delta\nu}\right)^2\right] \cos(2\pi\nu_j t + \phi_j), \tag{9.20}$$

with frequency resolution $d\nu$. The frequency domain laser pulse shaping shown is closely related to experimental Spatial Light Modulators using Liquid Crystal pixelated grids (LC-SLM). This requires diffraction of the incident laser pulse onto the LC-SLM, in which each pixel will be illuminated by a specific frequency band. At each pixel, there is simultaneous control over the amount of light transmitted (amplitude) and the phase of that light passing through. Once each frequency band passes through and is affected by the LC-SLM, the light is recombined to form a

new pulse shape depending on the alterations imposed by the shaper. Thus, there are numerous pulse shapes that can be generated by varying for instance: the number of frequency bands (ν_j), the resolution of the frequency bands illuminating each pixel ($d\nu$) and the variation in amplitude and phase. The GA optimization aims at modelling an LC-SLM set-up in order to reflect more closely the possible laser pulse shapes that can be experimentally produced.

9.3.3.2 Fidelity and Average Population

Within GA optimization, the degree to which the shaped laser pulse represents the quantum logic gate operation of interest is stated by a metric. Initial theoretical studies which had not yet perceived the necessity of global phase alignment used the average population $\bar{P}$, as this metric, i.e.,

$$\bar{P} = \frac{1}{N} \sum_{k=1}^{N} |\langle \Psi_k(T) | \Phi_k \rangle|^2 , \tag{9.21}$$

where $\Psi_k(T)$ is the resulting wavefunction after the laser pulse of duration T has been applied and Φ_k is the target wavefunction. The sum is over the number of qubit transformations N, which is $N = 4$ for the case of 2-qubit operations. There is clearly no phase information contained in the average population function. Population transfer combined with global phase alignment can be included in the required constraints for shaped laser pulses within the GA by using instead the fidelity function, F, where

$$F = \frac{1}{N^2} \left| \sum_{k=1}^{N} \langle \Psi_k(T) | \Phi_k \rangle \right|^2 . \tag{9.22}$$

The fidelity is a number between 0 and 1. $F = 0$ implies no excitation to the resultant qubit state (i.e., an incomplete quantum gate operation), while $F = 1$ implies a 100 % complete quantum gate operation on the qubits. Though the average population is a useful value to determine the extent of overall population transfer between the qubits, it is strictly the fidelity function values that should be used within the GA optimization procedure when dealing with quantum gate operations.

9.4 Summary and Future Directions

In the present work, the basic ideas of quantum computing have been presented by highlighting the similarities and differences to classical computing, see Sects. 9.1.1 and 9.1.2. Most important among these differences is the possibility for exponential speed-up in solving computational problems, if, and only if, suitable quantum algorithms can be designed, see Sects. 9.1.3 and 9.1.4. In addition to the development of quantum algorithms, a critical choice is the physical system on which the quantum gates, and hence algorithms, can be implemented, see Sect. 9.1.6, where

the primary focus is on atomic and molecular systems. Once a physical system has been chosen (in this work, the discussion is on molecules), there are three important steps: (i) system preparation, (ii) gate and algorithm implementation and (iii) system readout, see Sects. 9.2.1–9.2.3. The majority of the research on molecular quantum computing has emphasized step (ii), see for example [18,42–55]. Therefore, the theoretical investigation of molecular quantum computing involves several important elements: the choice of molecular (hyperfine, rovibrational, rovibronic. . .) states for the qubits and the molecule from which they are selected, the quantum gates to be implemented, and the optimization algorithm used to determine the laser field. The two most important computational challenges presented for gate implementation, i.e., step (ii), are the accurate and efficient solution of the TDSE, see Sect. 9.3.1, and the optimization techniques used to find the required laser field, see Sects. 9.3.2 and 9.3.3. Unlike control of photochemical or photo physical processes, molecular quantum computing imposes the stringent requirement of global phase alignment for quantum gate operations. While initial studies of molecular quantum computing have been promising, practical applications involving several (or many) qubits remain challenging. These will require the careful choice of a molecular system for scalability, e.g., the use of coupled polar diatomic molecules on a 1D array[36, 37, 53–55]. However, just as important will be the development of new or refined theoretical and computational techniques for dealing with quantum dynamics (most likely, for many degrees of freedom) and/or optimization algorithms for finding the best (and, hopefully, experimentally accessible) laser field. Whatever approach is taken, insight can, and will, be revealed through high-level simulations.

Acknowledgements The authors thank the Alberta Ingenuity Fund (New Faculty Award) and the Natural Sciences and Engineering Research Council of Canada (NSERC Discovery Grant) for financial support. We thank the Canadian Foundation for Innovation (New Opportunities Fund) for support of the computational infrastructure on which this work was carried out. R.R.Z. acknowledges financial support of NSERC via a PGS-D2 scholarship.

References

1. Feynman R (1982) Simulating physics with computers. Int J Theor Phys 21:467
2. Nielsen MA, Chuang IL (2000) Quantum computation and quantum information. Cambridge University Press, Cambridge
3. Benenti G, Casati G, Strini G (2004) Principles of quantum computation and information, vol I: basic concepts. World Scientific, Singapore
4. Cirac JI, Zoller P (1995) Quantum computations with cold trapped ions. Phys Rev Lett 74:4091
5. Chotia A, Neyenhuis B, Moses S, Yan B, Covey J, Foss-Feig M, Rey AM, Jin DS, Ye J (2012) Long-lived dipolar molecules and Feshbach molecules in a 3D optical lattice. Phys Rev Lett 108:080405
6. Vandersypen LMK, Steffen M, Breyta G, Yannoni CS, Sherwood MH, Chuang IL (2001) Experimental realization of Shor's quantum factoring algorithm using nuclear magnetic resonance. Nature 414:883
7. Chuang IL, Vandersypen LMK, Zhou XL, Leung DW, Lloyd S (1998) Experimental realization of a quantum algorithm. Nature 393:143

8. Jones JA, Mosca M (1998) Implementation of a quantum algorithm on a nuclear magnetic resonance quantum computer. J Chem Phys 109:1648
9. Tesch CM, de Vivie-Riedle R (2002) Quantum computation with vibrationally excited molecules. Phys Rev Lett 89:157901
10. Zadoyan R, Kohen D, Lidar DA, Apkarian VA (2001) The manipulation of massive ro-vibronic superpositions using time-frequency-resolved coherent anti-stokes Raman scattering (TFR-CARS): from quantum control to quantum computing. Chem Phys 266:323
11. Bihary Z, Glenn DR, Lidar DA, Apkarian VA (2002) An implementation of the Deutsch-Jozsa algorithm on molecular vibronic coherences through four-wave mixing: a theoretical study. Chem Phys Lett 360:459
12. Brif C, Chakrabarti R, Rabitz H (2010) Control of quantum phenomena: past, present and future. New J Phys 12:075008
13. Brif C, Chakrabarti R, Rabitz H (2012) Control of quantum phenomena. Adv Chem Phys 148:1
14. Balint-Kurti GG, Zou S, Brown A (2008) Optimal control theory for manipulating molecular processes. Adv Chem Phys 138:43
15. Knill E, Laflamme R, Martinez R, Tseng CH (2000) An algorithmic benchmark for quantum information processing. Nature 404:368
16. Schmidt-Kaler F, Häffner H, Riebe M, Gulde S, Lancaster GPT, Deuschle T, Becher C, Roos CF, Eschner J, Blatt R (2003) Realization of the Cirac–Zoller controlled-NOT quantum gate. Nature 422:408
17. Gulde S, Riebe M, Lancaster GPT, Becher C, Eschner J, Haffner H, Schmidt-Kaler F, Chuang IL, Blatt R (2003) Implementation of the Deutsch-Jozsa algorithm on an ion-trap quantum computer. Nature 421:48
18. Weidinger D, Gruebele M (2007) Quantum computation with vibrationally excited polyatomic molecules: effects of rotation, level structure, and field gradients. Mol Phys 105:1999
19. Vala J, Amitay Z, Zhang B, Leone SR, Kosloff R (2002) Experimental implementation of the Deutsch-Jozsa algorithm for three-qubit functions using pure coherent molecular superpositions. Phys Rev A 66:062316
20. Ahn J, Bucksbaum PH, Weinacht TC (2000) Information storage and retrieval through quantum phase. Science 287:463
21. Bomble L, Lauvergnat D, Remacle F, Desouter-Lecomte M (2008) Vibrational computing: simulation of a full adder by optimal control. J Chem Phys 128:064110
22. Deutsch D (1985) Quantum theory, the Church-Turing principle and the universal quantum computer. Proc R Soc Lond Ser A 400:97
23. Shor PW (1997) Polynomial-time algorithms for prime factorization and discrete logarithms on a quantum computer. SIAM J Comput 26:1484
24. Aspuru-Guzik A, Dutoi AD, Love PJ, Head-Gordon M (2005) Simulated quantum computation of molecular energies. Science 309:1704
25. Kassal I, Jordan SP, Love PJ, Mohseni M, Aspuru-Guzik A (2008) Polynomial-time quantum algorithm for the simulation of chemical dynamics. Proc Natl Acad Sci 105:18681
26. Wang H, Ashhab S, Nori F (2011) Quantum algorithm for simulating the dynamics of an open quantum system. Phys Rev A 83:062317
27. Kassal I, Aspuru-Guzik A (2009) Quantum algorithm for molecular properties and geometry optimization. J Chem Phys 131:224102
28. Yung MH, Aspuru-Guzik A (2012) A quantum quantum Metropolis algorithm. Proc Natl Acad Sci 109:754
29. Destainville N, Georgeot B, Giraud O (2010) Quantum algorithm for exact Monte Carlo sampling. Phys Rev Lett 104:250502
30. Harrow AW, Hassidim A, Lloyd S (2009) Quantum algorithm for linear systems of equations. Phys Rev Lett 103:150502
31. Cao Y, Papageorgiou A, Petras I, Traub J, Kais S (2013) Quantum algorithm and circuit design solving the Poisson equation. New J Phys 15:013021
32. Monz T, Schindler P, Barreiro JT, Chwalla M, Nigg D, Coish WA, Harlander M, Hänsel W, Hennrich M, Blatt R (2011) 14-Qubit entanglement: creation and coherence. Phys Rev Lett 106:130506

33. DiVincenzo DP, Loss D (1998) Quantum information is physical. Superlattice Microstruct 23:419
34. Kielpinski D, Monroe C, Wineland DJ (2002) Architecture for a large-scale ion-trap quantum computer. Nature 417:709
35. Lanyon BP, Whitfield JD, Gillett GG, Goggin ME, Almeida MP, Kassal I, Biamonte JD, Mohseni M, Powell BJ, Barbieri M, Aspuru-Guzik A, White AG (2010) Towards quantum chemistry on a quantum computer. Nat Chem 2:106
36. DeMille D (2002) Quantum computation with trapped polar molecules. Phys Rev Lett 88:067901
37. Carr LD, Demille D, Krems RV, Ye J (2009) Cold and ultracold molecules: science, technology and applications. New J Phys 11:055049
38. Sackett CA, Kielpinski D, King BE, Langer C, Meyer V, Myatt CJ, Rowe M, Turchette QA, Itano WM, Wineland DJ, Monroe C (2000) Experimental entanglement of four particles. Nature 404:256
39. Devitt SJ, Munro WJ, Naemoto K (2013) Quantum error correction for beginners. Rep Prog Phys 76:076001
40. Vincent R, Klyatskaya S, Ruben M, Wernsdorfer W, Balestro F (2012) Electronic readout of a single nuclear spin using a molecular spin transistor. Nature 488:357
41. Nuernberger P, Vogt G, Brixner T, Gerber G (2007) Femtosecond quantum control of molecular dynamics in the condensed phase. Phys Chem Chem Phys 9:2470
42. Tesch CM, Kurtz L, de Vivie-Riedle R (2001) Applying optimal control theory for elements of quantum computation in molecular systems. Chem Phys Lett 343:633
43. Troppmann U, Tesch CM, de Vivie-Riedle R (2003) Preparation and addressability of molecular vibrational qubits in the presence of anharmonic resonance. Chem Phys Lett 378:273
44. Suzuki S, Mishima K, Yamashita K (2005) Ab initio study of optimal control of ammonia molecular vibrational wavepackets: towards molecular quantum computing. Chem Phys Lett 410:358
45. Schroeder M, Brown A (2009) Realization of the CNOT quantum gate operation in 6D ammonia using the OCT-MCTDH approach. J Chem Phys 131:034101
46. Shyshlov D, Babikov D (2012) Complexity and simplicity of optimal control theory pulses shaped for controlling vibrational qubits. J Chem Phys 137:194318
47. Berrios E, Gruebele M, Shyshlov D, Wang L, Babikov D (2012) High fidelity quantum gates with vibrational qubits. J Phys Chem A 116:11347
48. Babikov D (2004) Accuracy of gates in a quantum computer based on vibrational eigenstates. J Chem Phys 121:7577
49. Tsubouchi M, Momose T (2008) Rovibrational wave-packet manipulation using shaped midinfrared femtosecond pulses toward quantum computation: optimization of pulse shape by a genetic algorithm. Phys Rev A 77:052326
50. Zaari RR, Brown A (2011) Effect of diatomic molecular properties on binary laser pulse optimizations of quantum gate operations. J Chem Phys 135:044317
51. Zaari RR, Brown A (2010) Quantum gate operations using midinfrared binary shaped pulses on the rovibrational states of carbon monoxide. J Chem Phys 132:014307
52. Mishima K, Yamashita K (2009) Quantum computing using rotational modes of two polar molecules. Chem Phys 361:106
53. Jaouadi A, Barrez E, Justum Y, Desouter-Lecomte M (2013) Quantum gates in hyperfine levels of ultracold alkali dimers by revisiting constrained-phase optimal control design. J Chem Phys 139:014310
54. Pellegrini P, Vranckx S, Desouter-Lecomte M (2011) Implementing quantum algorithms in hyperfine levels of ultracold polar molecules by optimal control. Phys Chem Chem Phys 13:18864
55. Bomble L, Pellegrini P, Ghesquière P, Desouter-Lecomte M (2010) Toward scalable information processing with ultracold polar molecules in an electric field: a numerical investigation. Phys Rev A 82:062323

56. Peirce AP, Dahleh MA, Rabitz H (1988) Optimal control of quantum-mechanical systems: existence, numerical approximation, and applications. Phys Rev A 37:4950
57. Zhu WS, Botina J, Rabitz H (1998) Rapidly convergent iteration methods for quantum optimal control of population. J Chem Phys 108:1953
58. Gollub C, de Vivie-Riedle R (2009) Modified ant-colony-optimization algorithm as an alternative to genetic algorithms. Phys Rev A 79:021401
59. Guha S, Mukherjee N, Chaudhury P (2012) A simulated annealing based study to design optimum pulses for selective target excitation in vibrational levels. Indian J Phys 86:245
60. Gollub C, de Vivie-Riedle R (2009) Multi-objective genetic algorithm optimization of 2d- and 3d-pareto fronts for vibrational quantum processes. New J Phys 11:013019
61. Zhu WS, Rabitz H (1998) A rapid monotonically convergent iteration algorithm for quantum optimal control over the expectation value of a positive definite operator. J Chem Phys 109:385
62. Gollub C, Kowalewski M, de Vivie-Riedle R (2008) Monotonic convergent optimal control theory with strict limitations on the spectrum of optimized laser fields. Phys Rev Lett 101:073002
63. Schroeder M, Brown A (2009) Generalized filtering of fields in optimal control theory: application to symmetry filtering for quantum gate operations. New J Phys 11:105031
64. Cheng T, Brown A (2006) Pulse shaping for optimal control of molecular processes. J Chem Phys 124:144109
65. Mishima K, Yamashita K (2011) Free-time and fixed end-point multi-target optimal control theory: application to quantum computing. Chem Phys 379:13
66. Mishima K, Yamashita K (2009) Free-time and fixed end-point optimal control theory in quantum mechanics: application to entanglement generation. J Chem Phys 130:034108
67. Tibbetts KWM, Brif C, Grace MD, Donovan A, Hocker DL, Ho TS, Wu RB, Rabitz H (2012) Exploring the tradeoff between fidelity and time optimal control of quantum unitary transformations. Phys Rev A 86:062309
68. Tesch CM, de Vivie-Riedle R (2004) Vibrational molecular quantum computing: basis set independence and theoretical realization of the Deutsch-Josza algorithm. J Chem Phys 121:12158
69. Sola IR, Santamaria J, Tannor DJ (1998) Optimal control of multiphoton excitation: a black box or a flexible toolkit? J Phys Chem A 102:4301
70. Carroll DL (2004) Genetic Algorithm driver v1.7.0. http://www.cuaerospace.com/carroll/ga.html
71. van der Hoff P, Thallmair S, Kowalewski M, Siemering R, de Vivie-Riedle R (2012) Optimal control theory - closing the gap between theory and experiment. Phys Chem Chem Phys 14:14460
72. Brown JM, Carrington A (2003) Rotational spectroscopy of diatomic molecules. Cambridge University Press, Cambridge
73. Milonni PW (1976) Semiclassical and quantum-electrodynamical approaches in nonrelativistic radiation theory. Phys Rep 25:1
74. Bethe HA, Salpeter EE (1957) Quantum mechanics of one- and two-electron atoms. Springer, Berlin
75. Brixner T, Krampert G, Pfeifer T, Selle R, Gerber G, Wollenhaupt M, Graefe O, Horn C, Liese D, Baumert T (2004) Quantum control by ultrafast polarization shaping. Phys Rev Lett 92:208301
76. Brixner T, Gerber G (2001) Femtosecond polarization pulse shaping. Opt Lett 26:557
77. Zaari RR, Brown A (2012) Effect of laser pulse shaping parameters on the fidelity of quantum logic gates. J Chem Phys 137:104306

Conclusions

10

Fabien Gatti and Benjamin Lasorne

The first stage in the history of molecular quantum dynamics has been dedicated mainly to the development of numerical methods for solving the Schrödinger equation. Nowadays, the main challenge is to reproduce experimental data at a very high level of accuracy for small molecular systems in the gas phase. Many examples have been given in the present book. The systems contain up to 4–10 atoms in full dimensionality depending on their complexity. When a process is strongly impacted by quantum effects, an excellent agreement between theory and experiments is the only way to prove that a perfect control of these effects has been achieved. This constitutes an essential test before transposing these studies to larger systems. However, quantum effects do not always imply a very high accuracy. Biological materials use quantum effects, such as conversion of light into chemical energy through a conical intersection: these processes are very fast and then correspond to a low level of accuracy on the energy according to the Heisenberg principle. Generally speaking, the quantum effects occur not only in small molecules in the gas phase but also for large systems in an environment.

Consequently, the main challenge that molecular quantum dynamics will have to face in the future is probably the description of molecules entangled in a complex and large environment [1, 2]: solute–solvent systems, chromophore–protein, chromophore–nanomaterial, etc. How do the quantum effects behave due to the interplay of the system with structured and dynamically responding environments? In particular, is quantum coherence destroyed very fast by the environment's non-equilibrium dynamics? Can quantum coherence be preserved under particular conditions ? If yes, which ones precisely? Can we exploit this quantum coherence?

F. Gatti (✉) • B. Lasorne
Institut Charles Gerhardt Montpellier - CNRS - Université Montpellier 2,
CC 15001 Place Eugène Bataillon, 34095 Montpellier, France
e-mail: gatti@univ-montp2.fr; blasorne@univ-montp2.fr

F. Gatti (ed.), *Molecular Quantum Dynamics*, Physical Chemistry in Action,
DOI 10.1007/978-3-642-45290-1_10, © Springer-Verlag Berlin Heidelberg 2014

The recent development of novel algorithms such as the Multi-layer MCTDH approach of Haobing Wang, Michael Thoss, and co-workers will allow us to treat much larger systems [3–7]. This approach is very promising for the description of reactions in a condensed phase environment. However, having an algorithm that allows one to solve the time-dependent Schrödinger equation for a large number of degrees of freedom is not sufficient since the description of the electronic potential poses a considerable challenge. System-bath partitioning methods can then be used such as those devised by Irene Burghardt and co-workers [8–11]. Several approximations for the description of the bath's potential can be invoked that greatly simplify the calculation of the potential energy surface. In principle, the scope of these approaches is very large and might greatly help for a systematic description of quantum effects in condensed-phase media. However, it should be emphasized that the dynamics has in general a markedly non-Markovian behavior precluding the use of standard system-bath methods. In other words, the role of the bath is not only to rapidly dissipate the energy and the quantum coherence of the subsystem. It may also change the very nature of the process.

In conclusion, molecular quantum dynamics is a field of fundamental research that prepares the chemistry of the future. A chemistry that will control reactivity at its most fundamental level including the quantum effects that govern the microscopic realm. Of course, we are still very far from the level of complexity and efficiency in the control of quantum effects that can be found in biological processes, but it is to be expected that the understanding of quantum effects in molecular systems will allow the development of highly desirable materials and controlled processes in technological applications.

References

1. Ashkenazi G, Kosloff R, Ruhman S, Tal-Ezer H (1995) Newtonian propagation methods applied to the photodissociation dynamics of I_3^-. J Chem Phys 103:10005
2. Ashkenazi G, Banin U, Bartana A, Kosloff R, Ruhman S (1997) Quantum description of the impulsive photodissociation dynamics of I_3^- in solution. Adv Chem Phys 100:229
3. Wang H, Thoss M (2003) Multilayer formulation of the multiconfiguration time-dependent Hartree theory. J Chem Phys 119:1289–1299
4. Wang H, Thoss M (2007) Quantum dynamical simulation of electron-transfer reactions in an anharmonic environment. J Phys Chem A 111:10369
5. Manthe U (2009) Layered discrete variable representations and their application within the multiconfigurational time-dependent hartree approach. J Chem Phys 130:054109
6. Wang H, Thoss M (2010) From coherent motion to localization: II. Dynamics of the spin-boson model with sub-Ohmic spectral density at zero temperature. Chem Phys 370:78–86
7. Vendrell O, Meyer H-D (2011) Multilayer multiconfiguration time-dependent Hartree method: implementation and applications to a Henon-Heiles Hamiltonian and to pyrazine. J Chem Phys 134:044135
8. Cederbaum LS, Gindensperger E, Burghardt I (2005) Short-time dynamics through conical intersections in macrosystems. Phys Rev Lett 94:113003
9. Burghardt I, Hynes JT, Gindensperger E, Cederbaum LS (2006) Ultrafast excited-state dynamics at a conical intersection: the role of environmental effects. Phys Scr 73:C42

10. Burghardt I, Hughes KH, Martinazzo R, Tamura H, Gindensperger E, Köppel H, Cederbaum LS (2011) Conical intersections coupled to an environment. In: Koppel H, Domcke W, Yarkony DR (eds) Advanced series in physical chemistry: conical intersections: theory, computation, and experiment, vol 17. World Scientific, Singapore, p 301
11. Bonfanti M, Tantardini GF, Hughes KH, Martinazzo R, Burghardt I (2012) Compact MCTDH wave functions for high-dimensional system-bath quantum dynamics. J Phys Chem A 116(46):11406–11413